Journal of Materials Research and Technology 33 (2024) 3550–3618

Contents lists available at ScienceDirect

Journal of Materials Research and Technology

journal homepage: www.elsevier.com/locate/jmrt

# Findings and perspectives of β-Ti alloys with biomedical applications: Exploring beyond biomechanical and biofunctional behaviour

Amir A. Elhadad [a], L. Romero-Resendiz [b], M.C. Rossi [c], L.M. Rodríguez-Albelo [d], Sheila Lascano [e], Conrado R.M. Afonso [c], A. Alcudia [f], V. Amigó [g], Y. Torres [d,*]

[a] Department of Pre-Clinical Oral Health Sciences, College of Dental Medicine, QU-Health, Qatar University, Qatar
[b] Facultad de Química, Departamento de Ingeniería Metalúrgica, Universidad Nacional Autónoma de México, Mexico City, 04510, Mexico
[c] Materials Engineering Department (DEMa), Universidade Federal de São Carlos (UFSCar), 13.565-905, São Carlos, SP, Brazil
[d] Departamento de Ingeniería y Ciencia de los Materiales y del Transporte, Escuela Politécnica Superior, Universidad de Sevilla, 41011, Seville, Spain
[e] Departamento de Ingeniería Mecánica, Universidad Técnica Federico Santa María, Avda. Vicuña Mackenna Poniente N 3939- San Joaquín, 8320000, Santiago, Chile
[f] Departamento de Química Orgánica y Farmacéutica, Facultad de Farmacia, Universidad de Sevilla, 41012, Seville, Spain
[g] Instituto de Tecnología de Materiales, Universitat Politècnica de València, Camino de Vera s/n, 46022, Valencia, Spain

ARTICLE INFO

Handling editor: P.Y. Chen

*Keywords:*
Beta-titanium alloys
Novel manufacturing routes
Surface modification treatments
Bio-functional and tribomechanical behaviour
Cellular and bacterial response

ABSTRACT

Early implant failure and bone resorption may occur in load-bearing conditions as a result of stress shielding brought on by a mismatch in the bone-Ti-implant modulus. A review with a novel multidisciplinary perspective is proposed in this work, which considers recent developments of β-Titanium alloys and new trends in novel microstructures, processing techniques, properties of dense and porous substrates, as well as the relationship between all these aspects and performance in service, in terms of improved its biomechanical and bio-functional balance. In addition to highlighting several modern and historical uses for Ti alloys, this review covers many cutting-edge novel β-Ti alloys and uses that promise to exceed historical standards. Also, it deepens through several important properties of these alloys, including toxicity of alloying elements, phase stability, thermo-mechanical processing, heat treatment, surface, and stress-induced modifications. The stiffness, hardness, fatigue and wear resistance, corrosion behaviour, biocompatibility, and manufacturing and surface modification effects on these parameters are also emphasized. *In-vitro* and *in-vivo* assays have been added to highlight important aspects of bioactivity and antibacterial behaviour, and future significant research areas are suggested along with new techniques to ensure the successful clinical application of β-Ti alloys.

## 1. Introduction

In the US and Europe, 500,000 individuals undergo bone restoration operations each year [1]. In 2012, the market for biomaterials was at $94.1 billion USD; as of 2017, it is worth $134.3 billion USD [2]. Whereas the entire cost of expenses related to bone repair is expected to be US$ 17 billion annually, the annual global expenditures on bone fractures and orthopaedics are estimated to be 6.5 billion USD and 4.7 billion USD, respectively [3]. Several diseases or accidental bone fractures lead to the requirement to repair the specific damaged organs. Biological activity is unfortunately limited at the region of the damaged bone tissue, making implantation necessary. Once tissue is lost due to severe trauma or injury in an ageing population, it has a major clinical and socioeconomic impact on many people's quality of life [4,5]. Additionally, the ageing of populations in developed nations and patients' desire to retain their normal level of physical activity have also contributed to a remarkable rise in the usage of implants during the last few years [6]. Choosing the appropriate implant materials that can serve as a bridge and support and, having the proper mechanical and bone induction capabilities, is crucial [7]. Treatments for bone repair relies on autografts, allografts, xenografts, and synthetic scaffolds [8]. Due to their osteoinductive and osteoconductive capabilities, autografts are widely recommended; yet, they have significant downsides, including a limited availability and donor-site morbidity [9,10]. While successfully resolving the mentioned drawbacks, allografts and xenografts are nevertheless susceptible to immune rejection, and transmission of infection [9]. Use of synthetic biomaterials, such as metals, ceramics, and polymers, is another potential treatment approach [11]. However,

* Corresponding author.
*E-mail address:* ytorres@us.es (Y. Torres).

https://doi.org/10.1016/j.jmrt.2024.09.248
Received 15 July 2024; Received in revised form 20 September 2024; Accepted 28 September 2024
Available online 5 October 2024

due to a variety of issues, such as low support strength and the brittleness of inorganic ceramics, biocompatible metals have emerged as the ideal material for implants [12]. In addition, the criteria for specialized designs, such as load transmission, stress distribution, and implant articulation to facilitate movement in prosthetic knee joint applications, are likewise satisfied by metal-based implants [13]. Stainless steels, commercially pure titanium (CP–Ti), Ti–6Al–4V, and cobalt-chromium-molybdenum (Co–Cr–Mo), alloys are one of the most commonly employed metallic implants [5]. The Ti–6Al–4V alloy is an ideal choice for biomedical implants due to its biocompatibility, ease of manufacture, and superior corrosion resistance when compared to other alloys [5,14–16]. So far, one of the primary drawbacks of implants made of standard materials is the apparent mismatch between the mechanical characteristics of the implant and those of bone. The merely linear stress-strain attributes of metallic implants, which are considerably stiffer and do not match the plateau-like hysteretic activity of bones, causes implant loosening [17]. Accordingly, metallic implants have the downside of stress shielding due to their high elastic modulus, which might lead to bone resorption and eventually the early failure of the implant under load-bearing conditions [17]. Another major issue that could have an impact on the biological environment is the harmful consequences of the V and Al ions that are released by metallic implants when they are implanted *in-vivo* [18,19]. More research data indicate the possibility that vanadium (V) ions may alter the kinetics of an enzyme activity related to inflammatory response cells in human tissues. Aluminium (Al), on the other hand, raises the risk of Alzheimer's disease [20]. Another major downside of the Ti–6Al–4V alloy is the implant-associated infection (IAI) continues to be a major clinical concern despite advances in the life expectancy of Ti alloy (Ti–6Al–4V) implants used in applications including joint and tooth replacement [21,22]. The implant may get infected directly during surgery by contamination, indirectly by a contiguous route in which bacteria are transferred to the implant from the surgical site, an open traumatic wound, an infection at a nearby site, or through haematogenous seeding [23].

There has been a great deal of research in the field of super elastic β-Ti alloys driven primarily by the desire to develop an implant based on metallic materials that would combine super elasticity with a biocompatibility comparable to pure Ti. The β-Ti alloys have received a lot of attention over the recent decades due to the use of other biocompatible chemical elements that replace V and Al as a reasonable solution to obtain Ti alloys with a stiffness quite similar to that of the cortical bone tissue that they intend to replace as well as long-term implant rejection [24–26]. The usage of non-toxic, low elastic modulus β-Ti alloys is envisaged for the development of the next generation of implanted devices [27]. Such an alloy is completely biocompatible and possesses amazing mechanical, chemical, and electrochemical properties for the manufacture of bio implants. Despite numerous reviews of β-Ti alloys for biomedical applications in the literature, many of them omit or do not go into detail about specific aspects of the microstructure, manufacturing processes, and characteristics of this type of alloy, considering the real-world requirements in customer experience and the problems that negatively affect the clinical success of this type of metal alloys for replacing damaged bone tissues. For instance, among the most crucial measures affecting the strength of the bone-to-implant contact is surface roughness [28]. The implant's surface roughness affords the bone a chance to grow and interlock with the implant. Cell distribution is affected by the geometry of the pores, their internal structure, and their pattern of connectivity. When the implant has a porous structure over its whole volume, the rate of osseointegration may be considerably higher [29]. The use of surface modifications, such as anodizing, grit-blasting, acid-etching, and resorbable blast media, has proven effective in improving bone regeneration around dense implants [30]. However, in individuals with poor bone density and osteoporosis, acid-etched and sandblasted Ti surfaces contributed to lower implant stability [31,32].

An implant with a porous structure will facilitate the attachment of biological bone to the implant [11]. Studies have demonstrated that porous titanium implants significantly enhance the rate of tissue ingrowth as well as the strength of the implant's attachment to the bone [30]. Stress shielding brought on by a bone-Ti-implant modulus mismatch leads to poor osseointegration and bone formation [33]. Pore introduction is one approach for lowering the elastic modulus of pure bulk Ti to a value closer to that of human bone [33]. To reduce the impacts of stress shielding and boost porosity for bone tissue ingrowth, another strategy of implant surface treatment is the creation of porous structures [30]. Porous metal, also described as trabecular metal in the field of orthopaedic use, is a type of metal structure having a 3D network of interconnecting pores. When compared to dense metal, porous metal shows less rigidity and strength [12]. Its Young's modulus is within or close to that of the characteristics of human bone (from 0.4 GPa of trabecular bone to 17.9 GPa of cortical bone) [34]. High friction coefficients improve the porous metal's initial stability, and connected porosities and bone growth into the porous Ti implant provide long-term stability [12]. Porous Ti implants have larger surface areas compared to solid Ti implants, which enhances bone cell attachment and growth, allows bone ingrowth into the implant, and accelerates osseointegration [35]. Thus, porous Ti appeared to be useful choice for usage in biomedical field, such as prosthetics and scaffolds for tissue engineering. However, more than 50 GPa is the elastic modulus of β-Ti, exceeding the elastic modulus of human bone [36]. Due to the stiffness mismatch, the implants are subjected to most of the stress. The majority of the stress is placed on the implants as a result of the mismatch in stiffness. While going through the healing process, human bone regenerates and grows. As a result, the bone density around the implants may diminish over time due to a lack of load, which can lead to bone resorption, a stress shielding phenomenon, and slowed-down healing times [37]. Contrarily, a material with a low elastic modulus will deform substantially under stress and cease to have a supporting function [38]. Moreover, implanted Ti alloys are difficult to deeply bind to biological tissue, which increases the risk of implant fracture and tissue loss [5]. Consequently, research into the correlations between elastic modulus and chemical composition, hardness, and porosity is crucial. Various chemical compositions and microstructures of β-Ti alloys were designed to address the concern of stress shielding; some of them have been applied to the biomedical field.

Even though there are many works reviewing β-Ti alloys for biomedical applications in the literature, large number them avoid mentioning or do not go into considerable detail regarding specific aspects of the microstructural features, manufacturing processes, and characteristics of this type of alloy, taking into consideration the practical needs in service and the issues that adversely impact the clinical success of this type of metal alloys replacing damaged bone tissues. In this context, the review on β-Ti alloys attached offers a multidisciplinary perspective, emphasizing the balance between biomechanical and biofunctional properties, which is a unique approach compared to previous literature. It covers recent developments in microstructures, processing techniques, and the service performance of both dense and porous β-Ti alloys. This comprehensive view, which includes *in-vitro* and *in-vivo* assays for bioactivity and antibacterial behaviour, and the discussion on the toxicity of alloying elements, phase stability, and surface modifications, sets it apart from existing reviews that may not delve into these aspects in detail. Additionally, the review suggests future research directions and new techniques for clinical application, highlighting a forward-looking perspective on β-Ti alloy development. The scope of this review is outlined schematically in Fig. 1.

## 2. Effect of alloying elements in β-Ti alloys

This section describes the impact of different alloying elements on the crystal structure stability, toxicity, reactivity, and cost. The design of new and improved β-Ti alloys is under intense worldwide research.

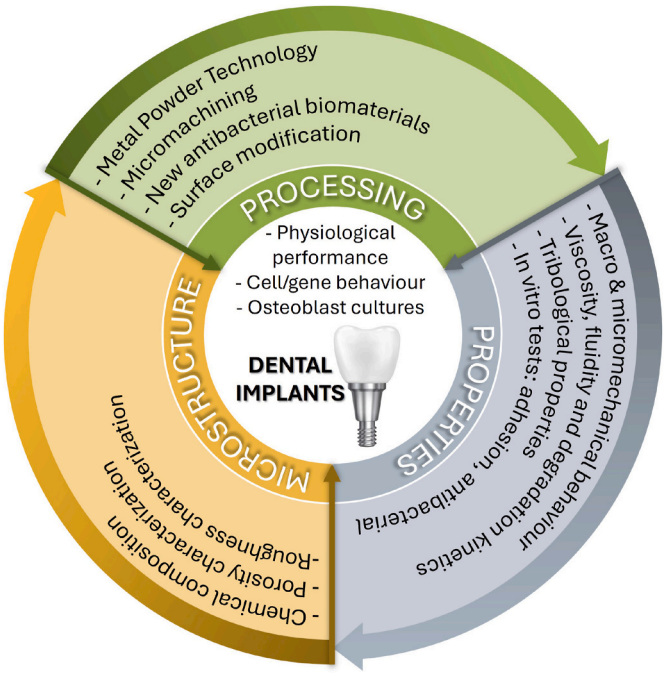


**Fig. 1.** Overview of alloy processing, microstructure and performance evaluation that make up the scope of this review.

### 2.1. Selection and toxicity of alloying elements

One of the primary concerns when using metallic implants *in-vivo* is the toxicity of the ions that are released [18,19]. As explained in the introduction, CP-Ti and Ti–6Al–4V are preferred compared to other metallic implants used in joint replacement since the 1940s [39]. Nevertheless, study findings and long-term clinical applications revealed that adding Al and V to a Ti–6Al–4V alloy would have significant negative physiological impacts [20]. Al has been associated with a variety of diseases, including brain damage, digestive issues, neurotoxicity, contact dermatitis, breast cancer, osteomalacia, anaemia, and encephalopathy [40]. Al can also damage the brain and cause encephalopathy, Parkinson's disease, Alzheimer's disease, neurotoxicity, and male infertility [41,42] In very large doses, aluminium (Al), changes the mineralization of the bone system, leading to pathological fractures, which can have a deleterious impact on bone metabolism [43]. Vanadium (V) is present in extremely small amounts in the human body [44]. Although it seems to not generate substantial toxic reactions when present in low concentrations (1–4%) in the Ti–6Al–4V alloy, it does exhibit some toxic phenomena that, over time, may have negative effects on human health [45,46]. Diarrhea, vomiting, weight loss, glomerulonephritis, pyelonephritis, seminiferous epithelium degradation, male Infertility, and cell viability are some of the severe symptoms [45,46]. The toxicity of Cobalt (Co) can affect several neurologically connected organ systems, (tinnitus, vision loss, vertigo), depression, lack of concentration, headaches, impaired reflexes, vibration/position sense, as well as limb paraesthesia [47,48]. Chronic exposure to Co was related to lung cancer, some respiratory system cancers, DNA damage in sperm, and the activation of DNA repair genes in the testes, fertility reductions in male and female individuals by lowering sperm production and ova quality, and signs of reduced reproductive success [48,49]. Molybdenum (Mo) at low levels might irritate the skin and eyes while ingesting excessive amounts can result in diarrhea, infertility, liver, kidney, and lung damage [50,51]. A significant amount of copper (Cu) exposure can result in tissue damage, haemolytic anaemia, gastrointestinal bleeding, liver and kidney failure, Wilson's disease, Alzheimer's disease, mortality, nausea, vomiting, headaches, lethargy, diarrhea, tachycardia, and other symptoms [52,53].

Given aforementioned, it is evident that there is a critical need to enhance the characteristics of current implant materials or to develop new ones. Findings suggest that metals like zirconium (Zr), titanium (Ti), niobium (Nb), tantalum (Ta), and tin (Sn) are safe for use as metallic implants and have good biocompatibility [42]. Several scientists have been working to develop implant-grade titanium alloys that only contain the aforementioned biocompatibility constituents, such as the Ti–Zr series [54],Ti–Nb series [55], Ti–Zr–Nb series [56], Ti–Nb–Ta–Zr series [57], Ti–Zr–Nb–Sn series [58], and others. However, the exploration of new alloying systems is necessary to maximize the synergy between non-toxicity, biocompatibility and mechanical performance. Thus, understanding the criteria for selecting alloying elements is crucial for future implant materials development.

The chemical composition and stoichiometry are key factors in the toxicity of Ti alloys. The chemical composition determines the chemical species released from the implant material during service. Commonly, the elements are released in an ionic state. Numerous reports on developing biomaterials for dental implants include an ion release test [59–61]. This test measures the remaining ionic concentration in a corrosive media (commonly buffer solution or artificial saliva) after immersion of the implant material at specific times and temperatures [62]. The ion release concentration can be correlated to the recommended daily intake from local or international health authorities. An example of the above is the annual Dietary Reference Intakes (DRIs) from the National Academies of Sciences, Engineering, and Medicine in the USA [63]. The DRIs include recommended dietary allowances and adequate intakes of chemical elements that can be compared to the ion release concentrations by dental implant materials. An example of the above was the Ti–34Nb–6Sn, in which ion release concentrations of Nb (1.4–2.9 μg $cm^{-2}$ $day^{-1}$) and Sn (0.89–1.45 μg $cm^{-2}$ $day^{-1}$) were compared to the dietary recommended intake of 620 μg and 200 mg/kg of food, respectively [60]. The ion release concentration can also be compared to reports of TC50, i.e., the concentration of certain elements that cause 50% cell death [64]. For example, a TC50 of 2310 μM for ionic indium (In) has been reported [65]. A development of Ti–In alloys compared the indium released to the reported TC50 [61], concluding the non-toxicity due to indium content of those alloys. From the literature, the cytotoxicity of some elements can be ordered from the most to the less cytotoxic against L-929 cells as follows: $Ag^{+}$, $Zn^{2+}$, $Au^{3+}$, $Pt^{4+}$, $Co^{2+}$, $Cu^{2+}$, $Ni^{2+}$, $Pd^{2+}$, $Mn^{2+}$, $Nb^{5+}$, $Mo^{5+}$, $Cr^{3+}$, $In^{3+}$, $Sn^{2+}$ [65].

The use of the TC50 for toxicity comparative purposes should consider the multiple parameters influencing *in-vitro* cell testing, such as parent cells kind, protein concentration in the culture media, initial cell concentration, and testing parameters like time, temperature, presence of $CO_2$, pH, among others [65,66]. Fig. 2 presents an overview of how alloying elements can be harmful to human health.

The cytotoxicity is also relevant for orthopedic and dental implant materials. Cytotoxicity refers to the cell adhesion and proliferation occurrence on the surface of the implant material [67]. Among the key parameters that influence cytotoxicity are surface roughness, chemical composition, and hydrophobicity [67]. The plate counting method is one of the most useful for counting the cell colonies remaining at the surface of the implant material after contact for specific times and temperatures [68]. Commonly, a temperature that is close to that of the human body is selected for this test, i.e., about 37 °C [68]. The influencing parameters for *in-vitro* cell testing described from the TC50 testing also influence cell adhesion and proliferation testing [67]. Moreover, the literature contains numerous examples of newly developed or improved implant materials with cytotoxicity analyses, and these approaches are further explained in section 8.3.2 [59].

### 2.2. Physicochemical properties

Electronegativity, defined as an atom's capacity to attract valence electrons, plays an important role in determining the multiplicity of chemical bonding and physicochemical properties of the material [69].

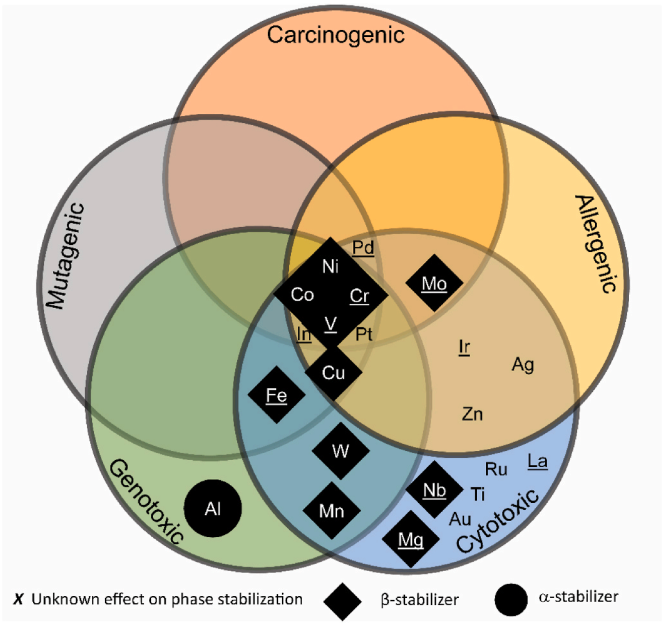


**Fig. 2.** Overview of the negative effect of alloying element in human health.

Thus, electronegativity strongly influences the corrosion susceptibility and ion release of Ti alloys. The electronegativity of noble, low reactive elements such as platinum (Pt), gold (Au), palladium (Pd), etc., tends to be higher than elements with high chemical activity like Mg [70–77]. Furthermore, high electronegativity differences between phases at the same alloy [70–77] or different materials in contact [78–80] might encourage high electrochemical potential disparities (micro-galvanic or macro-galvanic couples) and boost corrosion processes (more details in section 8.2.) [81]. Considering that V triggers the breakout of passive surface films in V-bearing Ti alloys, the β-Ti phase is more prone to corrosion than the α-Ti phase [70]. However, the β-phase has been reported to be more corrosion resistant than the α-Ti phase when Nb, Mo, and Zr β-stabilizers are present [77]. Lanthanum (La) also creates micro-galvanic cells in Ti–Zr–Mo alloys, reducing corrosion resistance [75]. Other examples are Cu and Ag, which add antimicrobial properties to the Ti matrix, but also galvanic pairs when found as segregates or intermetallic phases [82]. Thus, the expected better corrosion performance of β-Ti with respect to α-Ti is based on the obtaining of a fully single-β microstructure without galvanic couplings [83].

Using pre-alloyed β-Ti powders or heat treatments to promote homogeneity and/or single-phase microstructures decrease the formation of micro-galvanic couples through the material [70,76,77]. The solubility of the alloying elements on the Ti matrix should also be considered to decrease the risk of immiscible particles or intermetallic phases. The formation kinetics of the surface passivation layer also plays a key factor in the kinetics of corrosion due to micro-galvanic couplings [84]. For last, the ratio between anodic (where oxidation occurs) and cathodic (where reduction occurs) also impacts the galvanic corrosion occurrence [80]. Thus, electronegativity between phases, including elements segregation in the microstructure, should also be considered for the chemical performance of biomedical implant materials. Fig. 3 compares the four key criteria—biocompatibility, electronegativity, autoignition temperature, and cost to be considered when choosing alloying elements.

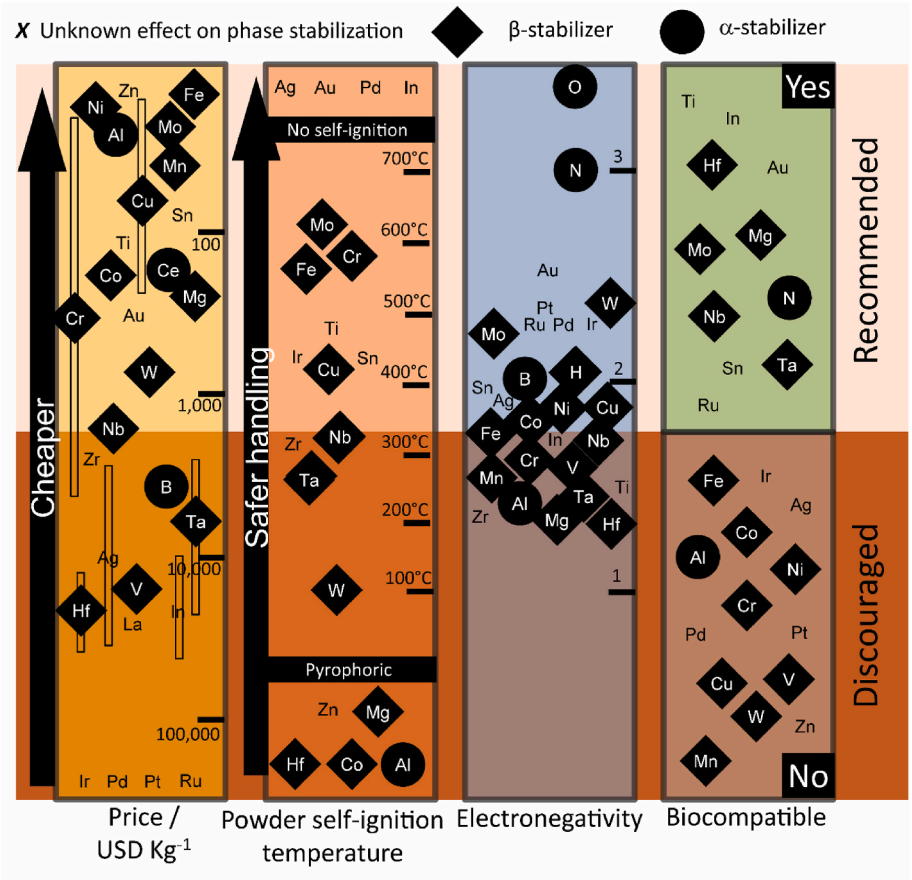


**Fig. 3.** Comparison of main factors to consider for alloying elements selection; biocompatibility, electronegativity, autoignition temperature, and cost (variable depending on the size and purity of the powder).

### 2.3. Reactivity and fabrication safety

The high surface contact area of powders increases the chemical reactivity of raw materials compared to their micrometric counterparts [85,86]. Thus, the management of elemental powders for additive manufacturing (AM) and powder metallurgy techniques requires higher safety measurements than the rods or chunks usually used for melting routes. The autoignition temperature, i.e., the temperature for a 50% thermal-induced phase conversion rate, is a useful parameter to consider during the methodology planning [87]. Fig. 3 includes the autoignition temperatures of different metallic powders. It also mentions the pyrophoric powders, i.e., materials with spontaneous ignition, to assist in the fabrication measurements consideration. Moreover, it should be considered that reducing the particle size might abruptly change the autoignition temperature of the elements. For instance, it has been reported a pyrophoric risk on nano-powder of Ti, which was not observable in the micrometric order [85]. Additionally, the oxidant media also plays a key role in the ignition temperature, which tends to be lower in the air (mostly $N_2$ and $O_2$) compared to $CO_2$ or $N_2$ [88]. Another useful parameter to identify the expected pyrophoric activity of metallic powders is the activation energy [85,89]. The activation energy is the required energy for undergoing a chemical transformation and it is closely related to the occurrence of combustion processes and their exothermic energy releases [85,89]. Typically, higher activation energies were associated with a higher self-ignition likelihood [85]. For example, Yavor et al. reported the activation energy of some elements according to their activation energies when reacting with water [90]. The activation energies of those elements can be ordered from the highest to the lowest as follows; Mg, Al, Mo, W, Ti, Zn, Zr, Cr, Sn, B, Ni, Mn, Cu, and Fe [90]. Finally, it should be remarked that the activation energy is higher in processes implying chemical bonding changes, such as combustion processes [91].

For practical purposes, an empirical explosibility index related to ignition sensitivity and explosion severity has been reported [88]. This index is a function of the ignition temperature and energy, the critical concentration of explosive material, and the explosion pressure. Specifically, the index of explosibility classifies some of the elements as follows; **i)** severe hazard: Al, Mg, Zr, and Ti, **ii)** strong hazard: C and Fe, **iii)** moderate hazard: B, Cr, Mn, and Sn, **iv)** weak hazard: Zn, V, Mo, Co, W, and Cu, and v) none hazard: Ni. Additionally, the mentioned report considered the effect of decreasing particle size on the increment of explosibility hazard; however, only micrometric particles were considered [88]. The severity of an explosion can be assessed by a fuel's explosivity index (Ks), which is a function of the maximum pressure during combustion [86]. Finally, the concept of the explosion pentagon should be carefully considered. The pentagon includes the necessary conditions to join for the occurrence of an explosion, i.e., fuel, oxidant, ignition source, confinement, and dispersion of the fuel. A guideline for safety measurements during the handling of explosive powders can be found in the literature [86].

### 2.4. Powder cost

The development of production techniques that result in final net-shape parts with no need for machining, such as additive manufacturing (AM) and powder metallurgy, have considerably decreased the manufacturing cost of metallic materials [92–94], including implant materials. The net-shape devices have been very useful considering that each patient has unique anatomy that frequently requires customized biomedical implants [94]. However, the cost of raw materials greatly impacts the final price, especially when using elements with low concentrations in nature or difficult to extract and refine.

The price of biomedical implants might be unaffordable for a big percentage of the population. For example, the invoiced prices of some hip, knee, dental, and stents biomedical devices was reported from 249 to 2308 USD in Mississippi, USA [94]. Additionally, statistics from the same report mentioned demand for hip, knee, dental and stent implants of at least 154, 326, 342, and 560 in Mississippi during 2010 [94]. Contrastingly, the annual median individual income in 2010 in Mississippi was about 20,000 USD. Thus, an average patient in Mississippi required from 0.1 to 1.4 salary months to acquire a biomedical implant in 2010. Despite the cost of implants already including raw materials, manufacturing process, and supply chain 92, there are other complementary costs for patients, such as medical diagnoses, clinical procedures, hospital stays, and recovery [94]. In addition, the Mississippi state reported average hospital charges of 24,751 USD. Thus, the annual average income could be insufficient to cover biomedical implant expenses in Mississippi in 2010. Furthermore, in the case of infection, a cost higher than 50,000 USD is estimated to treat infected arthroplasty [95]. Astoundingly, the demand for biomedical implants is large enough to be in the USA's top ten medical diagnoses. Moreover, previous numbers might be more critical for patients in low-income countries. Thus, the accessibility to biomedical implants is a worldwide burden. In this context, the authors of this review suggest considering the economic burden for the end users when designing new biomedical materials. To support this recommendation, Fig. 3 compares the cost of different elemental powders to be considered during new implant materials development.

### 2.5. Phase-stabilization

The stable room-temperature α-Ti phase corresponds to hexagonal close-packed (HCP) structure. However, the β-Ti phase (BCC structure) is more advantageous than the α-Ti phase in terms of lower elastic modulus, adequate strength, and biocompatibility [59,60]. Moreover, β-Ti alloys can be encouraged by tailoring the chemical composition of the alloys. The addition of β-stabilizers decreases the β-transus temperature, expands the β region in the phase diagram, and increases the β-phase stability. Thus, metastable β-microstructures will be formed if a critical concentration of β-stabilizers is met. The β and α stabilizer equivalencies, also called molybdenum ($Mo_{eq}$) and aluminium ($Al_{eq}$) equivalencies, allow estimating the content of β ($Mo_{eq}$ *wt.*%) and α ($Al_{eq}$ *wt.*%) phases in the microstructure. Some authors define the $Mo_{eq}$ as the amount of different β-, α-, and neutral elements necessary to retain a fully β-phase quenched microstructure [96]. The $Mo_{eq}$ and $Al_{eq}$ can be calculated from Eqs. (1) and (2) [81].

$$Mo_{eq}\ wt.\% = [Mo] + \frac{[Ta]}{5} + \frac{[Nb]}{3.6} + \frac{[W]}{2.5} + \frac{[V]}{1.5} + 1.25\,[Cr] + 1.25\,[Ni] + 1.7\,[Mn] + 1.7\,[Co] + 2.5\,[Fe] - [Al] \quad (1)$$

$$Al_{eq}\ wt.\% = [Al] + \frac{[Zr]}{5.9} + \frac{[Sn]}{3} + \frac{[O+N]}{0.1} \quad (2)$$

where [x] refers to the alloying elements content in wt.%. $Mo_{eq}$ and $Al_{eq}$ consider the effect of the main β- and α stabilizers. Thus, β-transus temperature decreases with the increment of $Mo_{eq}$. Different corrected coefficients have been introduced in Eqs. (1) and (2) [81,97]. Table 1 contains the $MO_{eq}$ calculations for various β-Ti alloys.

The metastable β-phase can be transformed under the application of an energetic stimulus, whether thermal or plastic stress [108]. These phenomena are also known as stress-induced and strain-induced phase transformations, respectively. The first one is given when no plastic deformation is applied [108], e.g., during heat treatments.

On the other hand, the strain-induced phase transformation occurs during the plastic strain regime [109]. The stress-induced transformation is the most studied in biomedical materials because they are subjected to lower loads than structural materials, which are more susceptible to strain-induced phase transformation. Moreover, the stress-induced phase transformation is affected by the alloying elements [110]. Thus, the β-Ti alloys can be obtained from heat treatments designed to retain the β phase (with cooling out of equilibrium) or by

**Table 1**
Mo equivalency ($MO_{eq}$) for several β- or near β-Ti alloys.

| Alloy | Fabrication technique | $MO_{EQ}$ | Reference |
|---|---|---|---|
| **Ti-13 Nb–13Zr** | Cast + Aging | 3.6 | [98] |
| **Ti–15Mo** | Cast + Annealing | 15.0 | [98] |
| **Ti–10Zr–5Ta–5Nb** | – | 2.4 | [20] |
| **Ti–12Cr** | – | 15.0 | [83] |
| **Ti–12Mo–5Ta** | – | 13.0 | [20] |
| **Ti–12Mo–5Zr** | – | 12.0 | [20] |
| **Ti–12Mo–6Zr–2Fe** | Aast + Annealing | 17.0 | [98] |
| **Ti–12Mo–6Zr–2Fe** | LPBF, chess- scanned | 17.0 | [99] |
| **Ti–12Mo–6Zr–2Fe** | LPBF, simple-scanned | 17.0 | [99] |
| **Ti–12Nb–12Zr–3Ta** | SLM + SSol | 3.9 | [100] |
| **Ti–12Nb–12Zr–8Ta** | SLM + SSol | 4.9 | [100] |
| **Ti–12Nb–13Zr–4Ta** | SLM + SSol | 4.1 | [100] |
| **Ti–12Nb–13Zr–6Ta** | SLM + SSol | 4.5 | [100] |
| **Ti–13Nb–12Mo** | P&S + Laser surface modification with laser power of 1000 W | 15.6 | [101] |
| **Ti–13Nb–13Zr** | – | 3.6 | [20] |
| **Ti–13Nb–13Zr** | SLM + SSol | 3.6 | [100] |
| **Ti–15Mo** | Press & Sintering | −3.3 | [102] |
| **Ti–15Mo** | Press & Sintering | 15.0 | [102] |
| **Ti–15Mo** | Press & Sintering | 15.0 | [102] |
| **Ti–15Mo** | Press & Sintering | 15.0 | [102] |
| **Ti–15Mo-0.1O** | Melting + Hot Forging + Hot Rolling | 15.0 | [103] |
| **Ti–15Mo-0.2O** | Melting + Hot Forging + Hot Rolling | 15.0 | [103] |
| **Ti–15Mo-0.3O** | Melting + Hot Forging + Hot Rolling | 15.0 | [103] |
| **Ti–15Mo-0.4O** | Melting + Hot Forging + Hot Rolling | 15.0 | [103] |
| **Ti–15Mo-0.5O** | Melting + Hot Forging + Hot Rolling | 15.0 | [103] |
| **Ti–15Mo–2.8Nb–0.2Si–0.26O** | (Annealed) | 15.8 | [83] |
| **Ti–15Mo-2.8Nb–3Al** | – | 12.8 | [20] |
| **Ti–15Mo–3Nb** | Cast + Annealing | 15.8 | [98] |
| **Ti–15Mo–5Zr–3Al** | Press & Sintering | 12.0 | [104] |
| **Ti–15Mo–5Zr–3Al** | Press & Sintering | 12.0 | [104] |
| **Ti–15Mo–5Zr–3Al** | Press & Sintering | 12.0 | [104] |
| **Ti–15Mo–5Zr–3Al** | Press & Sintering | 12.0 | [104] |
| **Ti–15Mo–5Zr–3Al** | Press & Sintering | 12.0 | [104] |
| **Ti–15Mo–5Zr–3Al** | Cast | 12.0 | [105] |
| **Ti–16Nb-10Hf** | Cast + Aging | 4.4 | [98] |
| **Ti–19Nb–14Zr** | – | 5.3 | [20] |
| **Ti–20Nb–10Mo** | P&S + Laser surface modification with laser power of 1000 W | 15.6 | [101] |
| **Ti–23Nb–0.7Ta–2Zr** | – | 6.5 | [83] |
| **Ti–23Nb–0.7Ta–2Zr–1.2O** | – | 6.5 | [83] |
| **Ti–24Nb–0.5N** | – | 6.7 | [83] |
| **Ti–24Nb–0.5O** | – | 6.7 | [83] |
| **Ti–24Nb–4Zr–7.9Sn** | – | 6.7 | [20] |
| **Ti–24Nb–4Zr–8Sn** | Hot rolling | 6.7 | [106] |
| **Ti–24Nb–4Zr–8Sn** | Hot forging | 6.7 | [106] |
| **Ti–25Nb–2Mo–4Sn** | – | 8.9 | [20] |
| **Ti–25Ta–25Nb** | – | 11.9 | [20] |
| **Ti–27Nb–8Mo** | P&S + Laser surface modification with laser power of 1000 W | 15.5 | [101] |
| **Ti–28Nb–13Zr–0.5Fe** | – | 9.0 | [20] |
| **Ti–28Nb–13Zr–2Fe** | – | 12.8 | [20] |
| **Ti–29Nb–11Ta–5Zr** | – | 10.3 | [20] |
| **Ti–29Nb–13Ta–2Sn** | – | 10.7 | [20] |
| **Ti–29Nb–13Ta-4.5Zr** | – | 10.7 | [20] |
| **Ti–29Nb–13Ta-4.6Sn** | – | 10.7 | [20] |
| **Ti–29Nb–13Ta–4.6Zr** | (Aged) | 10.7 | [83] |
| **Ti–29Nb–13Ta–4Mo** | – | 14.7 | [20] |
| **Ti–29Nb–13Ta–6Sn** | – | 10.7 | [20] |
| **Ti–29Nb–13Ta-7.1Zr** | – | 10.7 | [20] |
| **Ti–29Nb–6Ta–5Zr** | – | 9.3 | [20] |
| **Ti–34Nb–6Sn** | P&S 100 MPa | 9.4 | [60] |
| **Ti–34Nb–6Sn** | P&S 200 MPa | 9.4 | [60] |
| **Ti–35.5Nb–7.3Zr–5.7Ta** | – | 11.0 | [83] |
| **Ti–35Nb–4Sn** | – | 9.7 | [20] |
| **Ti–35Nb–5.7Ta–7.2Zr** | – | 10.9 | [20] |
| **Ti–35Nb–5ta–7Zr–0.4O** | – | 10.7 | [20] |
| **Ti–35Nb–6Mo** | P&S + Laser surface modification with laser power of 1000 W | 15.7 | [101] |
| **Ti–35Nb–7Zr–5Ta** | – | 10.7 | [20] |
| **TI–36Nb–2Ta–3Zr–0.3O** | – | 10.4 | [83] |
| **TI-40Nb** | P&S 1-h sintering at 1200 °C | 11.1 | [107] |
| **TI–6Mn–4Mo** | – | 14.2 | [83] |
| **Ti-7.5Mo–3Fe** | – | 15.0 | [20] |
| **Ti–9Mn** | – | 15.3 | [83] |

- Unknown thermomechanical route.

tailoring the chemical composition [96].

Transformations from the metastable β phase might occur to the HCP Ti-α′, orthorhombic Ti-α′′, or HCP Ti-ω phases during straining (tensile, compressive, or creep) or heat treatments. The formation of each phase is a function of the β stability, as is predicted by $Mo_{eq}$. The β-stabilizers dependence for the β, Ti-α, Ti-α′, and Ti-α′′phase transformations in Ti alloys. One example of stress-induced phase transformation is the β-type Ti–Hf alloys, which transformed to mainly HCP-α' martensite after water quenching from solution treatment [111]. For more details, Kolli et al. reviewed the phase transformation (including the Ti-ω) as a function of the $Mo_{eq}$ for several Ti alloys [96,112]. The critical concentrations of β-stabilizers, mainly Mo, Nb, Ta, V, W, Co, Cu, Cr, Fe, Mn, and Ni, to retain a fully β-phase microstructure in binary Ti-alloys can also be found in the literature [96]. Thus, chemical composition, temperature, and cooling rate have a significant impact on the phase transformation of Ti-alloys once a minimum critical strain is applied [113].

### 2.6. Effect of Fe and Cr contents

Segregation defects, particularly β-flecks, are critical phenomena impacting the microstructural integrity and mechanical properties of β-Ti alloys, especially those with higher contents of transition elements such as Fe and Cr. In addition, the heterogeneous distribution of these β-stabilizers during solidification can lead to the formation of localized, enriched regions known as β-flecks [114].

In alloys with higher Fe and Cr contents, the solidification range is extended, increasing the susceptibility to microsegregation. As the alloy solidifies, the solute elements (Fe and Cr) tend to segregate towards the interdendritic regions, which solidify later. Therefore, this segregation leads to the enrichment of β-stabilizing elements in these regions, promoting the formation of localized β-phase areas known as β-flecks. These flecks are typically harder and more brittle than the surrounding matrix, presenting as distinct, often darker, spots in the microstructure due to their different chemical composition and phase structure.

The mechanism of β-fleck formation is influenced by several factors, including the cooling rate, alloy composition, and the presence of other alloying elements [114–116]. A slower cooling rate tends to exacerbate segregation by allowing more time for the β-stabilizing elements to migrate towards the interdendritic regions. Moreover, the overall alloy composition also plays a significant role; higher concentrations of Fe and Cr not only promote the stability of the β-phase but also increase the tendency for segregation. Furthermore, the interaction of Fe and Cr with other alloying elements can influence the kinetics of segregation and the resulting microstructure.

To mitigate the formation of β-flecks, several strategies can be employed. These include optimizing the alloy composition to minimize the content of segregating elements, refining the microstructure through thermomechanical processing to disrupt the segregated regions, and employing rapid solidification techniques to reduce the time available for segregation. For example, additive manufacturing has been used to

reduceβ-flecks formation [117,118]. Additionally, post-solidification heat treatments can be used to homogenize the microstructure, dissolving β-flecks and redistributing the β-stabilizing elements more uniformly.

### 2.7. Compositional alloy design

The design β-Ti alloys involves sophisticated strategies to achieve a desirable balance between high strength, ductility, and other mechanical properties, which are essential for biomedical as well as other applications like aerospace and high-performance engineering fields. Among these strategies, two prominent approaches in the compositional design of β-Ti alloys are the d-electron theory and the Bo-Md diagram. Each of these methods offers a framework for understanding and predicting the phase stability and mechanical properties of these alloys but also comes with certain limitations.

#### 2.7.1. D-electron concept

The d-electron concept, developed by Morinaga is based on the electronic structure theory [119]. It focuses on the role of d-electrons in determining the phase stability of titanium alloys. In this concept, the number of d-electrons (*e/a* ratio, where *e* represents the number of valence electrons and *a represents* the number of atoms) is a critical parameter. The theory posits that the e/a ratio influences the phase stability of the alloys, where a higher *e/a* ratio tends to stabilize the β phase, while a lower ratio favors the α phase. This approach allows alloy designers to predict the phase stability and, to some extent, the mechanical properties of β-Ti alloys by adjusting the alloying elements to achieve the desired *e/a* ratio.

#### 2.7.2. Bo-Md diagram

The Bo-Md diagram, named after the Bonding (Bo) and Metal d-orbital energy level (Md) parameters, is another approach used in the design of β-Ti alloys. It offers a visual tool for understanding the effects of alloying elements on the stability of β-Ti alloys. This diagram plots the bond order (Bo), indicative of the strength of the metal-metal bonds, against the d-orbital energy level (Md), which represents the energy level of the d-orbitals of the metal atoms. The positioning of an alloy on this diagram can predict its phase stability, with specific regions corresponding to the stability of α, β, and other phases. By targeting a position within the β-stable region, alloy designers can tailor the composition of β-Ti alloys to achieve desired properties. For example, the Bo-Md diagram has been used to correlate the instability of the β-phase with lower Young's modulus [120]. A detailed discussion of the d-electron theory and the use of Bo-Md diagrams can be found in the literature [121,122].

#### 2.7.3. Limitations

The d-electron concept, while useful in predicting phase stability, does not account for all factors influencing the properties of alloys, such as microstructural effects and the influence of interstitial elements like oxygen and nitrogen. Moreover, it primarily focuses on electronic factors and overlooks other crucial aspects such as atomic size and lattice distortion.

On the other hand, the Bo-Md diagram, on the other hand, provides a more visual and intuitive way of understanding alloy behavior. However, it simplifies complex alloy systems to two-dimensional representations, potentially overlooking the multidimensional nature of alloy properties. Additionally, this diagram also does not directly account for kinetic factors and the effects of processing conditions on the final alloy properties.

In conclusion, while the d-electron concept and Bo-Md diagram offer valuable insights into the design of β-Ti alloys, their effectiveness is constrained by their inherent assumptions and the complexity of alloy systems. Future research and development in this field will likely integrate these theoretical frameworks with empirical data, advanced computational models, and considerations of processing-structure-property relationships, sustainability and health impact to develop the next generation of β-Ti alloys.

## 3. Powder production methods

Powder metals are essential raw materials for neat-net-shape processing technologies such as powder metallurgy (PM), metal injection molding (MIM), hot isostatic pressing (HIP) and additive manufacturing (AM) [123].

In terms of how the powder is produced, chemical, physical, and mechanical methods can be distinguished [124], as is shown in Fig. 4. Most industrial processes combine the above types. Choosing the route, however, depends on the desired properties of the powder, along with its application-specific characteristics. Powders of Ti and its alloys have been processed commercially by chemical reduction, hydrogenation/dehydrogenation, gas atomization, plasma-rotating electrode, and plasma atomization [125]. In addition, low quantities of titanium powder can also be obtained by hydrolysis of melted titanium compounds ($TiCl_4$, $TiO_2$), centrifugal atomization, and others. Here, we provide an overview of the commercial methods used to process titanium powder.

### 3.1. Chemical methods

In general, typically, chemical methods can be categorized into two groups based on the processes involved: chemical reductions and chemical decompositions. In chemical reduction, a variety of chemical compounds are employed, including oxides, halides, or various metal salts. The following are some examples of such processes: 1) reducing tungsten oxide with hydrogen from a solid state; 2) reducing titanium tetrachloride with melted magnesium, the Kroll process [126]; or 3) reducing copper sulfate and iron from an aqueous solution. CP-Ti can be produced by chlorinating natural or synthetic rutile ($TiO_2$) [125,127]. A series of reduction processes are used to reduce titanium tetrachloride (TiCl4) into metallic titanium, including the Hunter process (reduction of sodium), Kroll process (reduction of magnesium), and the reduction of calcium hydride, which has been used in Russia for years [128]. Fig. 5 illustrates the chemical methods used to produce CP-Ti.

#### 3.1.1. Hunter process

Hunter process could be performed in a one-step or two-step procedure. A stoichiometric amount of sodium metal is employed in the one-step procedure to convert $TiCl_4$ directly to Ti metal in a single reaction container. In one-step procedure, $TiCl_4$ is directly converted to Ti metal in a single reaction container by the use of a stoichiometric amount of sodium metal (Eq. 3). A two-stage reaction, on the other hand, begins with TiCl4 being reduced to TiCl2 using half stoichiometric sodium, followed by the transfer of TiCl2 into another vessel to undergo a second reaction with sodium metal to obtain Ti metal (Eq. 4 and 5). The two-step operation offers the advantages of separating the sodium reduction process into two parts to reduce the amount of heat generated as well as to control the vapor pressure of sodium metal more effectively than a one-step process. Although, the Hunter process is attractive because the purity of the Ti produced, compared to the Kroll process. Even so, the Hunter method for commercial applications has been abandoned since 1993 due to the difficulty of effectively separating NaCl, which requires leaching in an aqueous solution and requires additional energy [125].

One-step operation:

$$TiCl_4(g) + 4Na(l) \rightarrow Ti(s) + 4NaCl\ (l) \quad (3)$$

Two-step operation:

$$TiCl_4(g) + 2Na(l) \rightarrow TiCl_2(l, in\ NaCl) + 2\ NaCl\ (l) \quad (4)$$

$$TiCl_2(l, in\ NaCl) + 2\ NaCl\ (l) \rightarrow Ti(s) + 4NaCl(l) \quad (5)$$

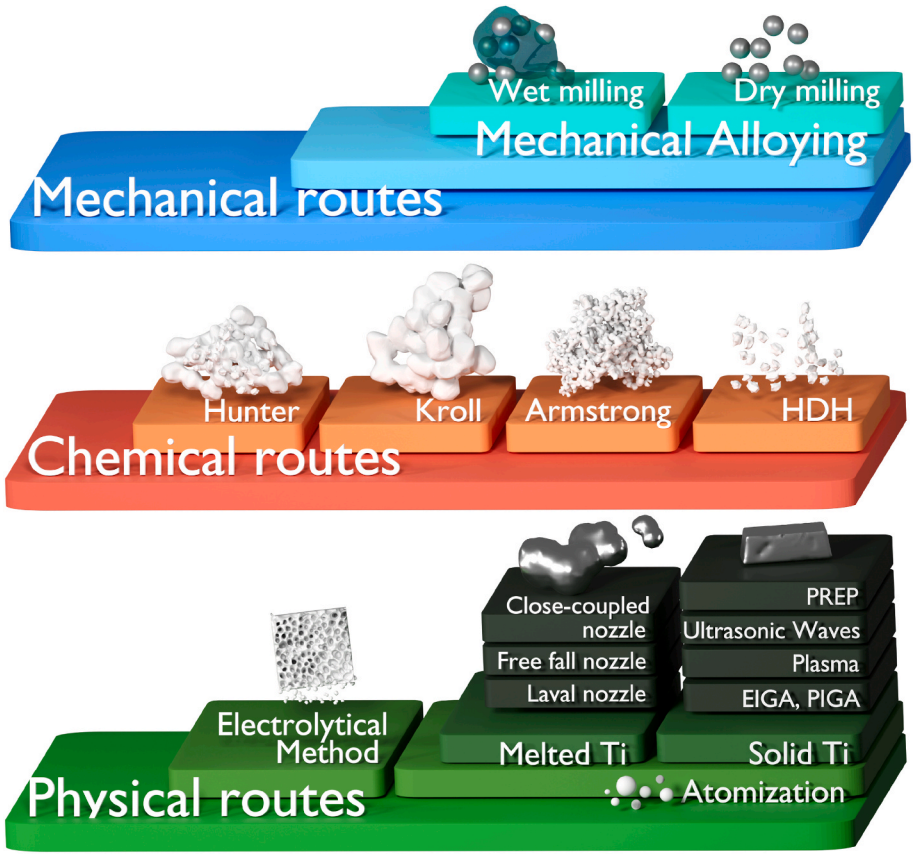


**Fig. 4.** Manufacturing techniques for Ti- powder and its alloys.

### 3.1.2. *Kroll process*

The Magnesium reduction method or Kroll process is one most used via to obtain Ti from $TiCl_4$. Due to the extensive heat treatment required to isolate pure Ti from Ti sponge obtained, this process is extremely energy intensive [129]. Kroll process occurs at 1073–1123K and its similar to the Hunter process but, magnesium is used instead NaCl to reduce $TiCl_4$ (Eq. 5) [125]. It is important to note that the reduction of Ti produces an exothermic reaction, releasing 412 kJ/mol, or even 686 kJ/mol if magnesium is added to the reaction in a gaseous state [129, 130]. Kroll process involves four stages [131], represented in Fig. 5: (1) **chlorination**, where $TiO_2$ (s) is chlorinated with carbon, obtaining $TiCl_4$ (Eq. 6); (2) **reduction and separation**, which involves the reduction of $TiCl_4$ with Mg metal to form Ti sponge (Eq. 7); (3) **crushing and melting,** where Ti the sponge is crushed and melted in vacuum arc or electron beam melting furnaces in order to reduce the impurities; and (4) **the electrolysis process**, magnesium chloride ($MgCl_2$) is electrolyzed to obtain Mg and $Cl_2$ gas (Eq. 8) [131].

$$TiO_2(s) + 2Cl_2(g) + C(s) \rightarrow TiCl_4(g) + CO_2\ (g) \quad (6)$$

$$TiCl_4(g) + 2Mg(l) \rightarrow Ti(s) + 2MgCl_2\ (l) \quad \text{(Reduction)} \quad (7)$$

$$2MgCl_2\ (l) \rightarrow\ Mg + Cl_2\ (g)\ \text{(electrolysis)} \quad (8)$$

As a disadvantage of the Kroll process, the time required for processing is lengthy. In step 2, the sponge's impurities are eliminated through vacuum distillation over 4–5 days, depending on the size of the sponge block. The high crush resistance of the sponge difficult its size reduction. In this case, prior to the crushing, Ti sponge is oxidized or hydrogenated to make it fragile.

When the reduction and separation process end, the reactor is cooled down for 4 days, and opened. The sponge obtained is pressed, and then the reaction products are eliminated from its surface. Since, the quality of the obtained Ti sponge is not homogeneous (variable grades of Ti within sponge), thus, this is grinded and classified and the high-purity grade Ti is analyzed and post processed by vacuum arc re-melting to obtain CP-Ti [129]. More effective technology process is necessary to reduce cost of Ti extraction, to improve the cycle time of the process and to increase the quality of Ti obtained [130,132,133].

### 3.1.3. *Armstrong process*

The technique is a derivative of the Hunter process and produces Ti powder with oxygen levels below 1000 ppm and chlorine levels below 50 ppm. Using the reduction of $TiCl_4$ and other metal halides by sodium, this method produces CP-Ti and Ti–6Al–4V with a unique "coral-like" morphology [134,135] (Fig. 5). Enhanced particle size distribution and tap density are achieved by employing post-processing methods like ball milling. Due to their irregular shapes, porous surfaces, and ease of compression, the resultant powder is suitable for conventional powder metallurgy, producing compacts with high green resistance, even when cold uniaxial compaction is used [135].

### 3.1.4. *Hydride-dehydride process (HDH)*

In this process, Ti (powder, sponge, milled products, or scrap) is introduced into a batch furnace at pressures of 1 atm. and temperatures up to 800 °C, in a vacuum/hydrogen atmosphere. Then, the Ti sponge is milled, and the resultant powder is sieved to produce a fine powder from titanium hydride. After that, the classified powders are re-introduced into the batch furnace under a vacuum or argon atmosphere (dehydride process) in order to remove the hydrogen. After being magnetically screened, the powders are then acid washed to remove ferromagnetic impurities. Pure powders with irregular morphologies are produced. In the case of scrap being used as raw material, this process cannot be used for modifying the alloy composition [135].

We have already discussed the basic methods for obtaining CP-Ti

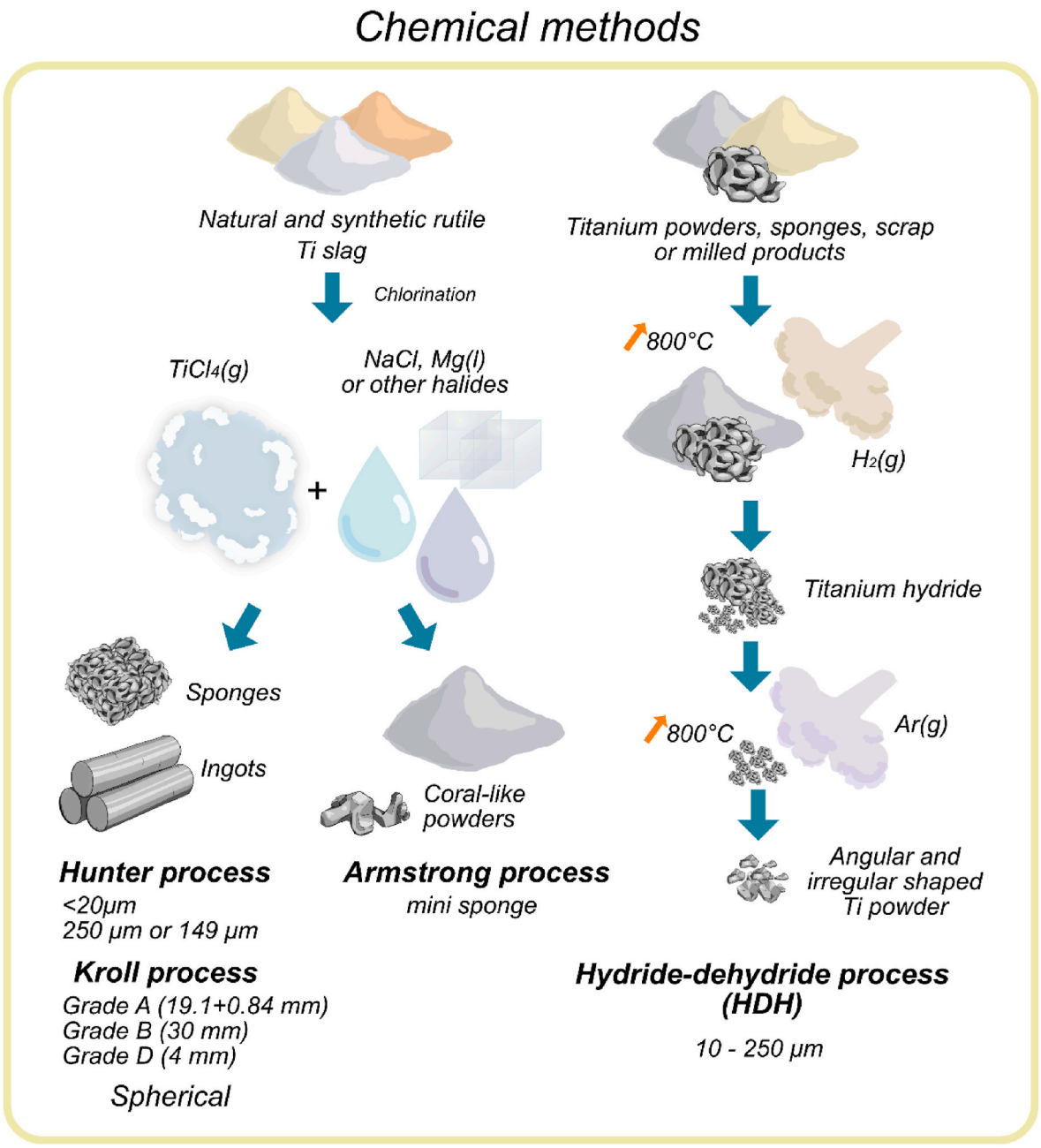


**Fig. 5.** Techniques for the production of Ti powders and its alloys by chemical methods.

metal powders via chemical methods. Some companies also use cutting-edge technology, such as atomization, to produce better quality powders. However, powders of Ti alloys are commonly obtained by blending and mechanical alloying [136]. During mechanical alloying, constituent powders are ground in a vessel containing grinding media [137]. The diffusion process over solid-state media produces homogeneous metal powders [137]. Next, we give an overview of the most common fabrication techniques for Ti alloys, which can be categorized into physical and mechanical methods.

### 3.2. Physical methods

The most relevant physical methods to obtain Ti powders are the electrolytic and atomization methods. Fig. 6 shows an illustration of physical methods used to obtain Ti powders. The shape is more spherical in atomization process; in particular, plasma atomization and ultrasonic techniques produce more spherical particles.

#### 3.2.1. Electrolytic method

Electrolysis of Ti is an ionizable process for producing high purity Ti. It involves the preparation of an electrolyte, the electro-refining of the Ti, and the collection of the Ti alloy. The electrolyte is prepared by reacting $TiCl_4$ and high-purity Ti to obtain molten salts containing low-valent Ti ions ($Ti^{2+}$ and $Ti^{3+}$) [138]. Thus, the salt contains Ti ions in solution, which are necessary to facilitate the hydrolysis process at a voltage below that required to decompose alkali and alkaline earth metals at the cathode [139]. During electro-refining, Ti sponge obtained by Kroll process acts as an anode, while high purity Ti plates serve as cathodes on which Ti ions are deposited. As an electrolyte, alkali and alkaline earth halides are utilized because of their eutectic composition, which can melt at temperatures as low as 350 °C. The final product collected is Ti of high purity. Table 2 shows possible reactions involved

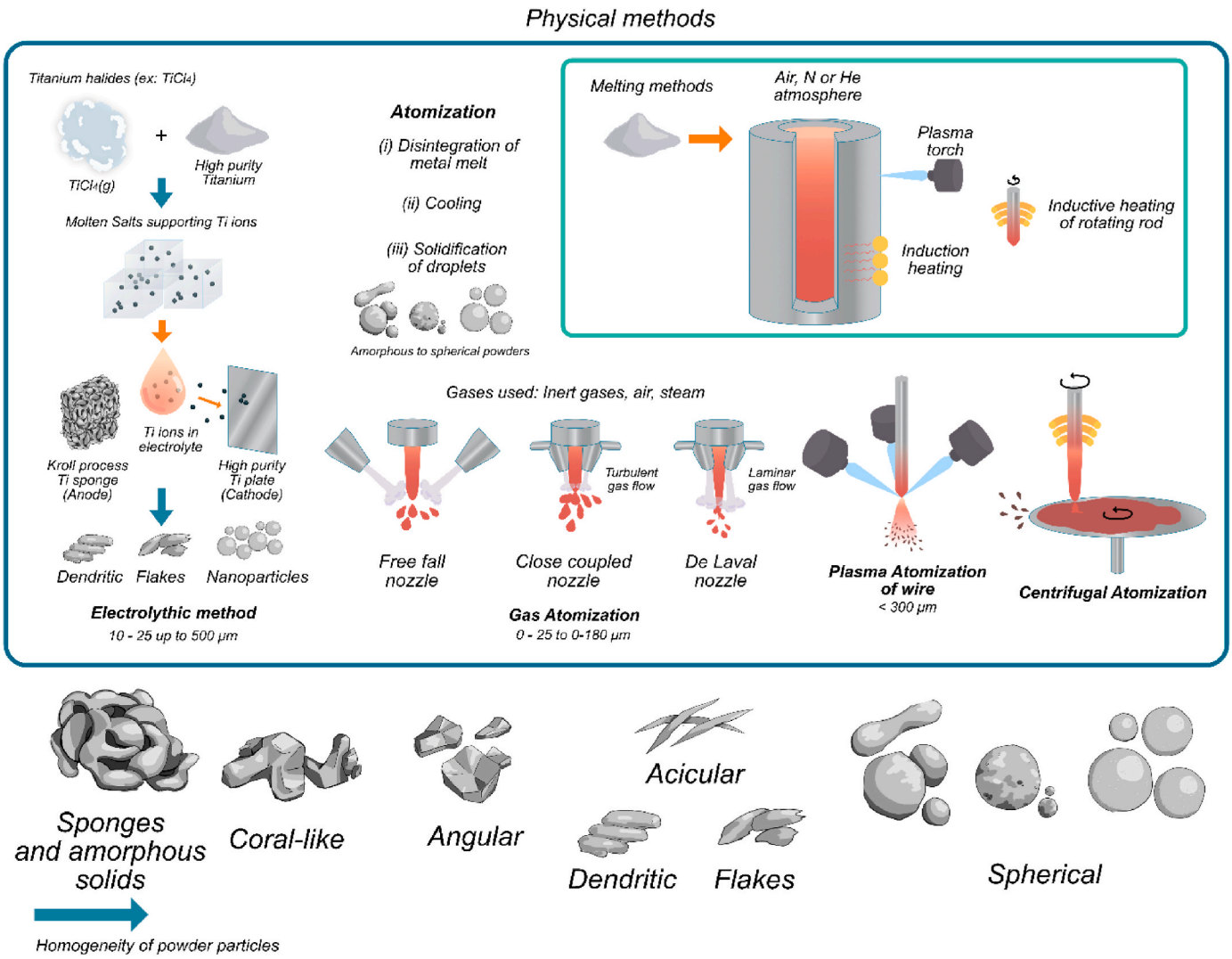


**Fig. 6.** Techniques for the production of Ti powders and its alloys by physical methods and evolution of powder morphology.

**Table 2**
Possible reactions involved in the stages of the production of high-purity Ti obtained via electrolysis.

| | |
|---|---|
| Possible reactions in the electrolyte preparation in case of $TiCl_4$ | $TiCl_4 + Ti = 2TiCl_2$<br>$TiCl_4 + TiCl_2 = 2TiCl_3$<br>$2TiCl_3 + Ti = 3TiCl_2$ |
| Ionized state, reversible reactions | $2Ti^{3+} \leftrightarrow Ti^{4+} + Ti^{2+}$<br>$4Ti^{3+} \leftrightarrow 3Ti^{4+} + Ti^{+}$<br>$2Ti^{2+} \leftrightarrow Ti^{4+} + Ti$<br>$3Ti^{2+} \leftrightarrow 2Ti^{3+} + Ti$ |
| The following reactions can occur as a result of applying a potential | $Ti^{4+} + e^- \rightarrow Ti^{3+}$<br>$Ti^{3+} + e^- \rightarrow Ti^{2+}$<br>$Ti^{2+} + 2e^- \rightarrow Ti$ |

in the stages of the production of high-purity Ti obtained via electrolysis. It was reported that Ti powders could be produced from halide salt electrolytes which contain $Ti^{2+}$ ions [139]. Ti produced by electrolytic method can take on a variety of morphologies, including nanoparticles, flakes, and dendrites (Fig. 7), depending on the processing parameters such as the concentration of metallic Ti ions in the electrolyte or the fused salt electrolyte. Different methods for electrolysis of titanium compounds are discussed by Neikov et al. [125].

### 3.2.2. Atomization

The atomization process is the most commonly used method in the PM industry to produce high quality powders, due to its applicability to different alloys, high productivity (0.5–50 kg/min), spherical shape of powder particles with particle size between 10 μm and 100 μm [140], and low oxygen content (<500 ppm for reactive metals). During the atomization of molten metal, three steps are involved: the disintegration of the metal melt, (ii) cooling with a suitable medium (solid such as melt spinning, liquid (water, cryogenic argon or nitrogen, or gas), and (iii) solidification of the droplets [141].

In disintegration, molten metal is injected into a tiny hole to produce a jet of liquid metal. The metal is melted at high temperature in a furnace in air, nitrogen or helium atmosphere [140]. The stream is disintegrated using gas, air, or water jets. Disintegration of liquid metal is achieved by transferring kinetic energy. The size and morphology of the particles depend on the temperature of the molten metal, the flow rate, the size and shape of the nozzle, and the characteristics of the stream [142]. During the formation of the particles, different stages of the process occur. The first stage involves disruption of the laminar flow regime when the atomizing medium (gas or liquid) contacts the molten metal at the nozzle outlet. Then in the second stage the formation of filament and film occurs. Disintegration mechanisms are then determined by surface tension and cooling rate. Generally speaking, a low cooling rate combined with a high surface tension will result in more spherical particles,

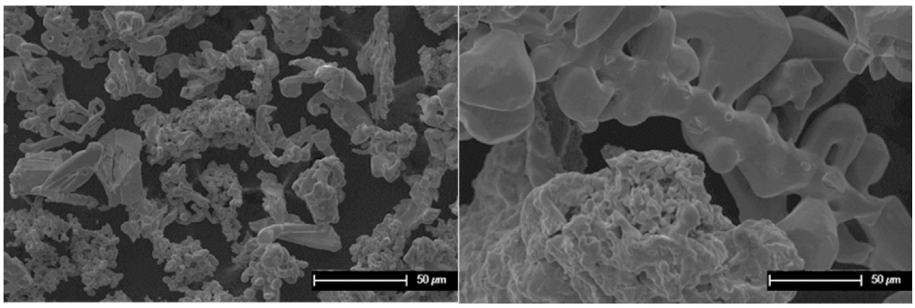


**Fig. 7.** SEM image of Ti metal powder 99.5% pure, −325 mesh, produced via electrolytic method, supplied by NOAH chemicals (San Antonio, Texas).

while a low surface tension combined with a high cooling rate will result in fewer spherical particles. Thus, in the third stage, the disintegration of the film or filament is generated, called primary atomization. Followed by the fourth stage that consists of a second stage of atomization [143].

Yule et al. [144], studied the mechanisms of first stage, considering that the fundamental mechanisms of fragmentation or primary rupture could be: drop formation by dripping mode from orifice, liquid column break, liquid ligament rupture in a flat sheet, liquid film break and the rupture of the free surface in liquids [143].

There are currently several metal powder atomization routes, depends on the cooling and solidification steps. The atomization process could be classified according to the method of obtaining the molten particle: water atomization, gas atomization, plasma atomization and centrifugal atomization [145,146]. Those are commercially established processes for the production of metal powders. In addition, hybrid processes, such as gas/centrifugal atomization, combines different methods to obtain finer particles sizes and highly spherical shape [147].

i. Water atomization

In water atomization, high-pressure water is forced through nozzles in order to produce a dispersion of droplets that collide with a stream of molten metal. The water must be supplied at a high pressure, which uses a considerable amount of energy. According to estimates, the total efficiency of the process is less than or equal to 4%. Stainless steel, as well as low and high alloy steels, can be processed using this method. Water spray is not recommended for highly reactive metals such as titanium and super alloys due to oxide formation. Water atomized powders usually have irregular shapes and rough surfaces due to their oxidation [148,149].

ii. Gas atomization.

In gas atomization, a stream of air, steam, or an inert gas is used to collide with molten metal, resulting in a fine spherical powder ranging in size from 0 to 300 μm [150,151]. Nitrogen, argon, or air are usually employed as media for atomization. In general, the morphology of powders is highly spherical (Fig. 8), with surfaces relatively smooth. It is challenging to prevent satellite formation during gas atomization, which makes it difficult to achieve high flow-ability. The particle size depends on the pressure and spray distance. High pressure and/or short spray distances produce finer powders. The atomization pressures ranged between $14 \times 10^5 - 42 \times 10^5\ Pa$ and flow rate ranging $50\ m/\ s - 150\ m/s$. Inert gas atomization is the primary method for producing additive manufacturing powder [152].

iii. Plasma atomization.

In this process, Ti wire is used as a precursor material for producing spherical Ti powder [151,153]. Feeding the wire into the apex of three plasma torches causes them to melt and atomize it in an argon atmosphere [125]. During their stay in argon, the droplets are subsequently

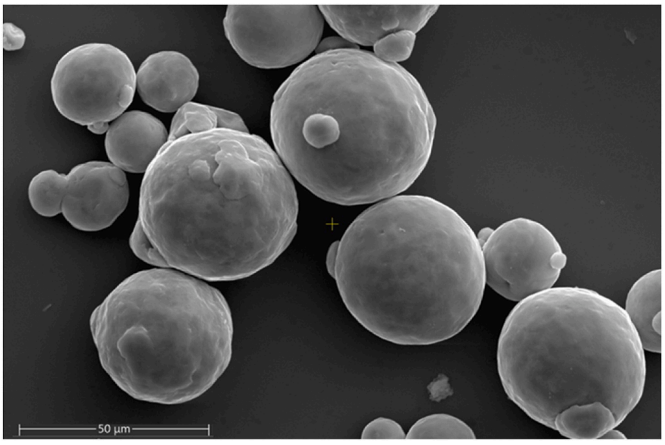


**Fig. 8.** SEM image Ti spherical powder, particle size 14–45 μm, produced via gas atomization, supplied by AEM deposition (Hunan, China).

cooled at $10^2$–$10^3$ K/s, solidifying into spherical powder particles. Different particle sizes of Ti and Ti–6Al–4V powders have been commercially available, ranging from 5 to 150–250 μm. Depending on the particle size, oxygen content varies between 0.1 and 0.3 wt% [125].

PyroGenesis and Hydro-Quebec have developed plasma atomization, which is employed to create very pure spherical particles of molybdenum, copper, and Inconel in a range of sizes [154]. A plasma torch that receives power from an electric source creates a jet of highly hot, rapidly moving ionized inert gas as part of this process. The extended high temperature region and high velocity of the impacting ions led to atomization and spheroidization. This procedure requires pricey equipment and personnel who have undergone specialized training. Plasma atomized Ti powders were proposed by PyroGenesis Inc. for the production of porous filters, applications in thermal spray and injection processes, as well as in biomedical applications [151].

iv. Centrifugal atomization

The centrifugal atomization method involves ejecting molten metal from a fast-rotating container, plate, or disk. A good example of centrifugal atomization is the Rotating Electrode Process (REP) [155]. The powder particles exhibit a smooth, spherical morphology, averaging 200 μm in diameter, and ranging in size from 50 μm to 400 μm. It has been found that tungsten contamination from the stationary electrode is a limitation of powders produced via REP. One method of overcoming this limitation is called PREP (Plasma Rotating Electrode Process), which has been developed in the United States for the production of titanium alloy powders. PREP uses electrodes that consist of pre-alloyed bars of 60–65 mm in diameter that rotate at speeds of up to 15,000 rpm in helium plasma [146,156]. A variety of factors influence the particle size, including chemical composition, electrode diameter, and rotation speed. PREP powders are spherical, high pure, fewer satellite particles,

almost no hollow particle, and relatively narrow particle size distribution than that obtained by gas atomization [157–159]. The typical Ti–6Al–4V powder size ranges from 50 μm to 350 μm with an average diameter closer to 175 μm [160]. The PREP powder is spherical, with a good flowability and density that is approximately 65% that of its solid counterpart. High purity metal powders can be created using the plasma rotating electrode method, although the final product is not as fine as sought for most applications, PREP powder is suitable for biomedicine. In order to produce finer powder, several modifications have been made to the process [146,157,161]. It is possible to produce fine spherical powder using hybrid atomization methods, such as electrode induction gas atomization (EIGA), which combines gas atomization with centrifugal atomization [162]. This process involves the atomization of liquid melt using a gas stream. As the gas atomized droplets impact the rotating disk, a thin liquid film is generated, which is ejected by centrifugal forces, resulting in fine powders [147]. At present, Electrode Induction Gas Atomization (EIGA) is the most common technology used to produce Ti alloys for additive manufacturing industries [151]. ALD Vacuum Technologies are the main suppliers of hardware in this method [146].

v. Plasma melting induction guiding gas atomization (PIGA).

PIGA is an additional variation of the gas atomization method devised by the GKSS Research Center, located in Geesthacht, Germany, to produce ceramic-free Ti alloy powders [163]. It consists of inserting an alloyed bar into a conical induction coil, heating the tip until it melts, and then allowing the liquid to fall into the center of the nozzle [125]. As a result, powders finer than 45 μm with spherical shape are obtained. The PIGA powders are suitable to be used in metal injection molding (MIM) [125,164].

vi. Gas Atomization by liquid gas

During this process, molten metal is atomized by exposure to a cryogenic liquid gas, such as argon or nitrogen, at −200 °C. When cryogenic liquid is forced out of the opening of a jet, a cooling unit prevents temperature rises due to compression and prevents the rapid vaporization of cryogenic liquid during the expulsion process. This raises the pressure of the liquid gas up to 300 bar.

Due to the atomization of the liquid, the liquid is completely vaporized and separated from the gas in the cyclone. As the resultant powder is purer than water-sprayed powders, it can be compared with gas-sprayed powders. In addition to having a cooling rate ten times greater than gas-sprayed powders, the product has quality almost as good as water-sprayed powders, and it maintains a spherical shape with an average size between 6 μm and 125 μm, just like gas atomization. This technique was developed by Messer Greisheim in collaboration with the University of Erlangen-Institute Nürnberg's of Material Science and Messrs Leybold AG [141].

vii. Ultrasonic atomization

Another process to produce high spherical powders is the ultrasonic atomization (UA). In this method, ultrasonic vibrations break molten metal into fine droplets and then drying them to powder [162]. Fig. 9 shows Ti–6Al–4V powder with spherical shape produced via UA by ATO system. Compared with gas atomization, no satellite particles are shown (compared to Fig. 8), the ATO system run at low pressure (1.1 bar vs. 16–60 bar), and rapid processing (production of high-quality metal powders in less than one day). The ATO system works, by means of an ultrasonic horn (Sonotrode) ejecting fine droplets, while ultrasonic vibrations are directed at the molten metal. Applications of this technology comprehend laser powder bed fusion (LPBF), Direct Energy Deposition (DED), Brazing (soldering), powder spraying, filters and foams, conventional powder metallurgy sintering, other powder metallurgy methods, and laser cladding.

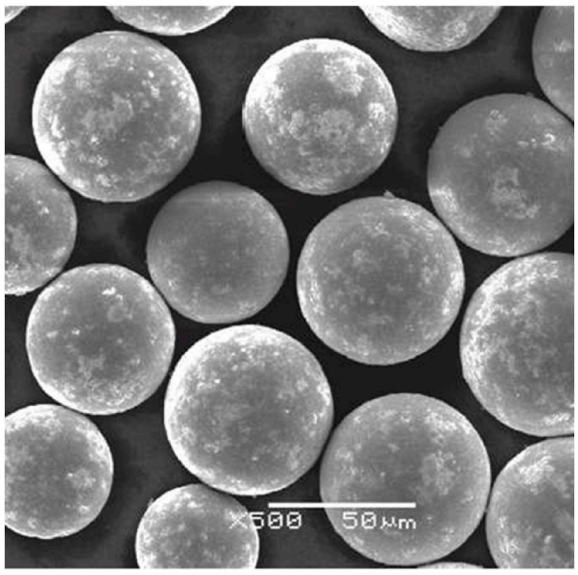


**Fig. 9.** Ultrasonic atomization. Courtesy of 3DLab ATO [165].

### 3.3. Mechanical methods

In recent years, Ti-based alloys have been manufactured by mechanical alloying (MA). In this method, fine metallic powders with controllable microstructure are produced using a high energy ball mill [125]. A mixture of metallic and non-metallic particles is repeatedly welded and fractured in a highly activated ball mill during this procedure. In response to the severe applied stress, the brittle material undergoes a high level of plastic strain before breaking. During the process of breaking and welding, the metal powder continuously refines its internal structure as the operation continues on [166,167]. This method can be used to produce composite materials and metallic alloys (mechanical alloying) or the reduction of particle size (mechanical milling). MA is used to obtain alloyed powders with unique characteristics such as supersaturated solid solutions [168], metastable solid solutions [169], nanostructured Ti-based alloys and compounds [170–172], high-entropy alloys and cermets [173–175], intermetallic alloys [176], amorphous phase Ti alloys [175,177,178], reinforced intermetallic matrix nanocomposites [179] and α+β phase Ti-based alloys [180–182]. Additionally, high-energy ball milling is commonly used to mechanically alloy elemental powders [183]. This can reduce the particle size and improve plastic deformation into the powder particles [184]. It is illustrated in Fig. 10 how particle size of titanium powder changes after high-energy ball milling in a planetary ball mill for 10 h (Fig. 10 (b)) and 20 h (Fig. 10 (c)).

In order to achieve the desired quality and microstructure, mechanical alloying requires the control of certain parameters. During mechanical alloying, the repeated fracturing, cold welding, and refracturing of material produces new chemically active surfaces that can react with the grinding atmosphere or with other materials within the grinding bowl. Through the welding of particles through these surfaces, the chemical composition of the material can be altered and solid-state interdiffusion and supersaturation beyond the equilibrium limit could take place [185]. For these changes to occur during mechanical alloying, a minimum amount of energy must be applied during grinding. There are several factors that influence the grinding process, including the type of mill, the container or the grinding bowl, the grinding atmosphere, the speed of rotation of the rotor, the amount of process controlling agent used, the size and density of the balls, the ball to powder mass ratio, and the feed charge [183]. However, it should be noted that each factor has a certain degree of interdependence. As an example, the optimal milling time depends on the type of mill, the size of

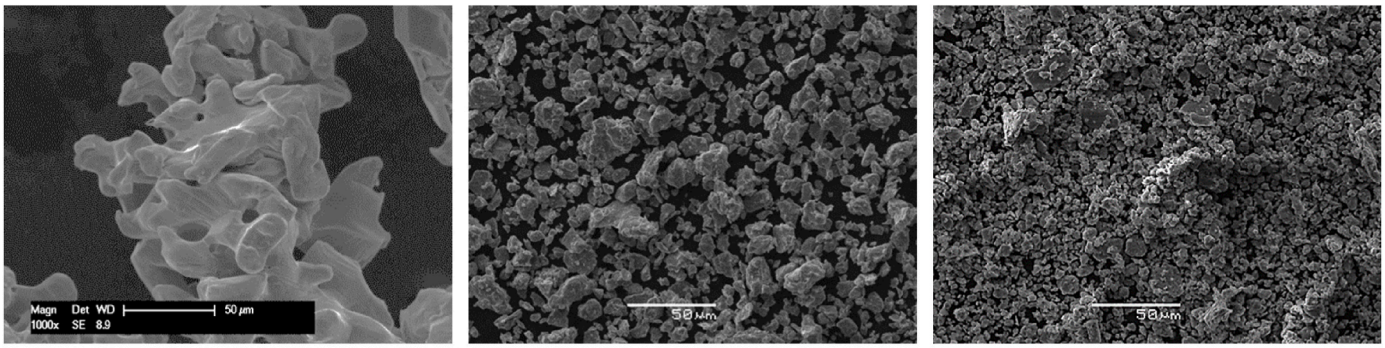


**Fig. 10.** SEM image Ti: (a) As received powder supplied by Alpha Aesar®; powder synthesized by high-energy ball milling in a planetary ball mill for (b) 10 h, and (c) 20 h.

the balls, the temperature of the grinding process, the mass ratio of the balls to the powder, and many other factors. Fig. 11 illustrates the factors that could affect the mechanical alloying processes, and the more common ball mills used to process Ti particles.

A brief description of the grinding parameters and how they impact the end product is provided below.

The type of mill determines how much mechanical energy is transferred to the powder at each impact, thus determining how long the grinding process takes. A variety of mill types are available today, but the following are the most common:

- Attritor-type ball mill (vertical or horizontal). This device allows for the processing of moderate amounts of powder, typically in the range of kg, within a reasonable amount of time (usually in the range of hours). The balls and powder charge are kept in a stationary container and are agitated by a rotor with radial arms.
- Planetary mill. In terms of material it can handle, it falls between what SPEX and Attritor can handle. An arrangement of containers,

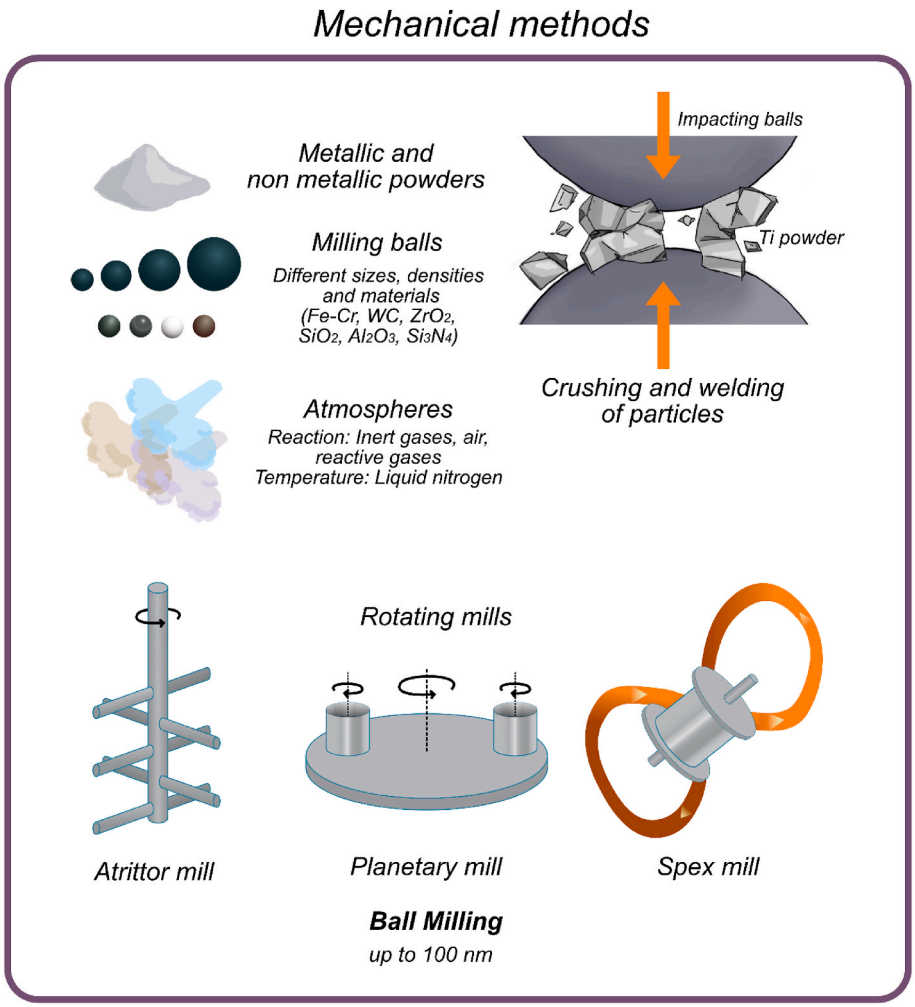


**Fig. 11.** Illustration of processing of powders via mechanical alloying methods.

arranged on a rotating platform, contains a load of balls and powder. Base rotates in one direction, while containers, rotating on their axes, rotate in the opposite direction. Consequently, the two movements combine to create centrifugal forces, which are transferred to the powder. One of its drawbacks is the impossibility of using controlled grinding atmospheres. However, certain vendors provide tools for fast and securely grinding in inert gas for mechanical alloying. As an illustration, Fritsch's planetary Micro Mill PULVERISETTE 7 premium line gassing covers enable the measurement of temperature and pressure inside the bowl.

- Vibratory mill. It is capable of processing small volumes of powder (typically between 10 and 20 g) within a relatively short timeframe. In order to generate intense G forces, a small vial containing a sample and at least one milling ball is shaken at high frequency in a complex pattern that combines forward, backward, and sideways movements. An example is SPEX (registered trademark of SYSTECH Co.).
- Conventional horizontal ball mill. Balls and powder are placed in a grinding bowl with a diameter greater than 1 m that rotates on its horizontal axis. Because of centrifugal force, the rotational speed is less than critical, causing the balls to adhere to the mill wall. It is used for processing large quantities of powder, but it can take a long time (on the order of a day or more).

The selection of the type of mill is important since this determines the energy available for the grinding. In addition, the *rotor speed* affects the grinding energy and, therefore, the strain introduced into the powder. However, the *grinding time* is the most significant parameter of the mechanical milling, because determines the balance between fractures and cold-welding of the particles. According to the desired characteristics, the grinding time can vary from a few minutes to several days, depending on the type of mill, the intensity of the grinding, the ball-to-powder ratio, and the grinding temperature. However, it is important to consider that using grinding times longer than those required can lead to an increase in contamination and that some undesired phases may result [186]. A similar phenomenon occurs when the rotation speed of the rotor is increased during grinding.

Another important parameter is the *ball to powder ratio (BPR)*, which is defined as the proportion between the mass of the balls and the mass of the powder introduced into the vessel. Fundamentally, it affects the time required to complete the grinding process and, in addition to that, it controls the distribution of particle sizes. Increasing the ball to powder ratio results in a reduction in the final particle size distribution and grain size [187]. It plays a significant role in the time required to complete the milling process. A higher BPR allows the powder to be ground faster and achieve a particular phase in less time. When the BPR is increased, there are more collisions per unit time, resulting in a greater energy transfer to the powder particles [183]. Nevertheless, if the vessel is overfilled, the average path that the balls can travel without colliding decreases, which reduces the impact energy. Thus, it is important to control the BPR in order to achieve the desired phases.

Hardened stainless steel (Fe–Cr), tungsten carbide (WC) and zirconium oxide ($ZrO_2$) are materials commonly used as grinding media (grinding bowls/balls), because their higher density (7.7, 14.3 and 5.2 g/cm$^3$, respectively), good abrasion resistance, and are recommended for abrasive, hard or medium-hard samples. Another material is agate ($SiO_2$), sintered corundum ($Al_2O_3$ 99.7%) and silicon nitride ($Si_3N_4$), which exhibit a low density (2.65, 3.8 and 3.25 g/cm$^3$, respectively) and could be used for soft to medium hard samples, medium hard and fibrous samples, and abrasive samples, respectively. In general, grinding bowls and balls of the same materials are used. The *density of the balls* affects their impact energy, and may lead to the appearance of reactions during grinding. In this regard, the density of the balls must be high enough to produce the necessary impact energy on the powder. By increasing the ball size, more particles are involved in collisions during mechanical alloying. In this way, grinding can be completed in a shorter period of time. This factor also impacts the efficiency of grinding. According to some research, the size of the grinding media determines the final composition of the powder. For example, when a mixture of Ti–Al powders is ground with 15 mm diameter balls, a solid solution of aluminum in Ti is produced. As an alternative, a mixture of aluminum and titanium phases can be obtained after prolonged grinding time when 20 or 25 mm diameter balls are used [188]. In general, smaller grinding balls produce finer grinding results.

The grinding temperature plays an important role on the mechanical alloying process, because an increase of temperature inner the grinding bowl could allow reaching the activation energy of possible reactions. By contrast, at low temperatures, the plastic deformation is limited producing a finer grain size. For example, when the grinding bowl or material is cooled with dry ice or liquid nitrogen [189]. During ball milling at cryogenic temperatures, recovery and recrystallization processes are suppressed, thereby promoting grain refinement [183,190]. However, Ti can be embrittled when subjected to cryogenic processing with nitrogen [191]. In this regard, to prevent contamination, cryogenic milling in liquid argon is suitable for Ti processing, for achieving ultra-fine α+β Ti alloys [184,191].

The grinding atmosphere and the percentage of process control agent (PCA) are two other important factors that influence the composition of the ground material, with the grinding atmosphere having the greatest impact. A grinding atmosphere may be either inert (vacuum or inert gases, such as Ar or He) or composed of gases that can react with the material, depending on the desired effect. High purity argon is commonly used to prevent oxidation and contamination of powders. On the other hand, nitrogen cannot be used as an inert atmosphere because it reacts with reactive metals such as Ti, causing oxidation and contamination [183]. As part of the grinding process, it is essential to control the atmosphere in order to ensure the chemical composition of the ground product. In addition, PCA favor the recoating the powder particles, slowing down cold welding, and controlling the proportion of fracture-welding events. Particularly, stearic acid could be used as PCA to avoid the cold welding in the milling of Ti powders [183,191]. Moreover, since most PCA are organic compounds, oxides, carbides, and hydrides may be incorporated into the material during grinding, or during subsequent heating during consolidation, which can contribute to undesired contamination of the product.

For particle sizes below 10 μm, wet grinding is required. The problem with this small particle size is that the particles tend to agglomerate because of the electrostatic charges on their surfaces. In order to keep those powder particles separated from each other, the use of a dispersion liquid could be used, such as water, buffer, alcohol, or long-chain molecules. Buffer neutralizes the charges on the surfaces, achieving so lower particle sizes up to 100 nm. In wet grinding, is recommended the use of small grinding balls (3 mm), to get a lot of friction; therefore, the grinding tools used are from wear-resistant materials ($ZrO_2$ or WC) and jars and balls of the same materials. When the initial particle size is higher than 1 mm, is recommendable to perform dry milling, and then wet milling when the particle size is below 10 μm. The grinding ball size must be 3 times bigger than the biggest particle in the sample. For safety uses a closure device to seal the jars, because during grinding the pressure increases caused by frictional heat and the low boiling point of the dispersant. For Ti, the wet grinding is denominated reactive milling. Reactive milling has been used to produce nanocrystalline Ti and $TiO_2$ powders [192,193]. The dispersion liquid used could be distilled water, deionized DI water, hexane [192,194,195]. It has been demonstrated that low energy wet ball milling can be used to manufacture homogeneous TiO nanoparticles from commercial TiO powder [195].

When selecting the appropriate powder, it is necessary to consider particle size and distribution, morphology, chemical composition, oxygen content, and flowability. The production method determines these aspects (Table 3).

**Table 3**
Metal particle characteristics by manufacturing methods.

| Processing | Principle or mechanism | Particle size | Morphology | Oxygen content | Advantages | References |
|---|---|---|---|---|---|---|
| **Hunter process** | Reduces $TiCl_4$ with Na reductant to produce Ti | <20 μm 250 μm or 149 μm | Sponge fines | (0.05–0.30) wt.% | In powder metallurgy, the Ti obtained is beneficial as a low-cost raw material. | [128,139, 160,196] |
| **Armstrong** | Reduces $TiCl_4$ and other metal halides by sodium to produce CP-Ti and Ti–6Al–4V | Mini sponge | Dendritic "coral-like" morphology | <1000 ppm | The operation of pumping liquid sodium to the reactor's gaseous $TiCl_4$ is continuous. | [134,160] |
| **Kroll** | $TiCl_4$ and Mg metal are reduced to produce Ti sponge. | Grade A (19.1 + 0.84 mm) Grade B (30 mm) Grade D (4 mm) | Ti sponge | | At the beginning of the melting process, impurities like oxygen and iron are fully and effectively removed from the feed ore. | [197,198] |
| **Hydride-dehydride process (HDH)** | The feedstock is hydrided to induce embrittlement, followed by washing and crushing, and finally dehydrided. | (10–250) μm | Angular shape | (0.15–0.30) wt.% | Good compressibility during compaction | [128,146, 199] |
| **Electrolytic** | Involves the preparation of an electrolyte, the electro-refining of the Ti, and the harvesting of Ti. | (10–25) μm up to 500 μm | Angular shape | <100 ppm | $3,50/kg for Pure Ti. Less $CO_2$ emission than Kroll route | [139] |
| **Gas atomization (GA)** | A gas jet transfers kinetic energy to a liquid metal stream at high velocity | (0-25) μm to (0–180) μm | Spherical shape | Low content (<500 ppm for reactive materials) 0.1–0.3 wt% | Flexible to produce different alloys and feedstock options | [125] |
| **Energy Inert Gas Atomization (EIGA)** | Inductive heating is used to preheat a rotating prealloyed bar, and molten titanium is then atomized using a high-pressure inert gas. | <200 μm | Spherical shape | | Finner-mesh powder than PREP. | [160,200] |
| **Plasma atomization (PA)** | High-velocity arc plasma melts the Ti wire, causing the liquid to break up into tiny droplets that solidify in flight [199] | <300 μm | Highly spherical shape | 0.11–0.19% | Satellite free Low yield strength | [160,199, 201] |
| **Plasma Rotating Electrode Process (PREP)** | A consumable bar's end melts as it is spun about its longitudinal axis. Centrifugal atomization creates droplets of the molten metal that crystallize in an environment of inert gas. | (50–350) μm (100–300) μm[a] | High spherical shape | | High purity, fewer satellites and fewer pores compared with GA | [125,160, 202] |
| **Ultrasonic atomization (UA)** | Ultrasonic vibrations break molten metal into fine droplets and then drying them to powder. | <100 μm | Highly spherical, satellite free | 0.0039 wt% | High production yield of useful fine powder (production batch) and low consumption or argon gas. UA process runs at low pressure (~1 bar). Better flowability, higher density, and lower porosity than GA and PA. | [162] |
| **Mechanical processes** | A mixture of metallic and non-metallic particles are repeatedly welded and fractured in a highly activated ball mill | Up to 100 nm | Irregular | Powder contamination | Simplicity and low cost | [170] |

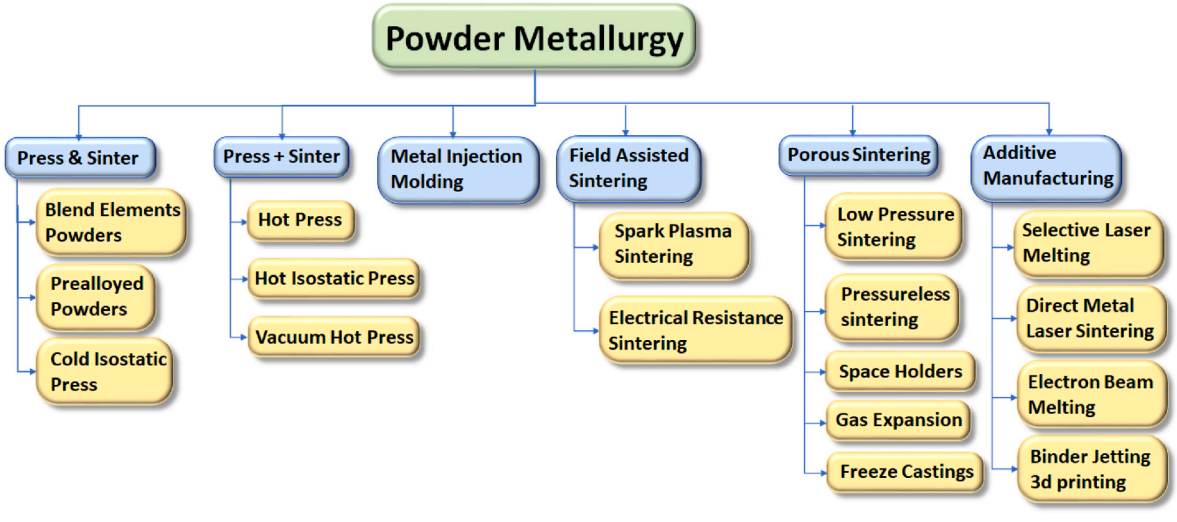


**Fig. 12.** Diagram of the different techniques applied in the manufacture of dense and porous Ti alloys.

## 4. Manufacturing of porous Ti alloys

Porous metal implants have been manufactured using different routes. On the one hand, the conventional techniques include conventional powder metallurgy [203], spark plasma sintering [204], metal injection molding (MIM) [205], pressureless sintering [206], low pressure sintering [60], the use of space holders [207], expansion of pressurized bubbles (injection of gas into the metal melt) [208], freeze casting techniques [209]. On the other hand, more sophisticated technologies referred as additive manufacturing (AM) technologies [210], which include three-dimensional printing (3DP) [211], electron beam melting (EBM) [212], selective laser melting (SLM) [213], direct metal deposit (DMD) [214], and selective laser sintering (SLS) [213], Fig. 12.

### 4.1. Powder metallurgy

#### 4.1.1. Press and sinter

Powder metallurgy has a variety of well-known advantages when it comes to the manufacturing of β-Ti alloys. The powder metallurgic approach offers a substantial financial advantage over the conventional route [203]. Due to the efficiency in manufacturing final shapes that it offers over other technologies, as well as the capability to blend a variety of alloys using both elemental powders mixing and pre-added powder mixing. The simplest process is press-and-sinter method, which allows pieces to be manufactured from an elementary mixture of the constituent particles of a certain alloy. Since Kroll first began sintering spiky Ti with low argon pressure in 1937, the conventional press-and-sinter method for Ti alloys has been evolving rapidly, along with new processes that have been incorporated into the processing of various materials, including the production of powders (Kroll, Amstrong, Hydrogen-assisted magnesium reduction HAMR, and electrochemical reduction) as in the densification of the same (Hot pressing HP, Hot isostatic pressing HIP, Field Assisted Sintering Technologies/Spark Plasma Sintering (FAST/SPS) or Electrical Resistance sintering ERS) [160]. Use of $TiH_2$ as a primary material that can dehydrate in a phase prior to the sintering cycle is one option for obtaining alloys while minimizing the impact of oxygen on the Ti. In this regard, Ti–Nb and Ti–Nb–Fe β-Ti alloys were developed from $TiH_2$ powders by Chirico et al. [215]. Furthermore, they studied the role that alloying elements play in the transformation of $TiH_2$ into β-Ti alloys [216].

Several alloys combining α and β phases of Ti have been developed in recent years for various industrial sectors. However, different methodologies have been used for powder technology. The majority of the work has been done on the CP-Ti or the Ti–6Al–4V alloy, both in the elemental mixture and the pre-alloying [217]. To address these last issues, it is necessary or preferable to turn to high-density processing (HIP or VHP: vacuum hot pressing). This final process was developed in 1980 and has primarily only been used in CP-Ti and Ti–6Al–4V, however it has been used to sinter both blending elements (BE) and prealloying (PA) powders [218]. Regarding β-Ti alloys, several alloys have been designed adjusting their molybdenum equivalent for various industries, such as aerospace, automotive, athletics, chemistry, or biomedicine [219].

One of the primary concerns with these alloys is their large concentration of alloying elements, which may make them unstable in the future, because β stability begins at a $Mo_{eq}$ of 25, with β-Ti alloys metastable for $Mo_{eq}$ ranging from 10 to 20, [220]. As a response, Bolzoni et al., developed low-cost alloys, including Fe as a alloying element as it is one of the elements with the greatest effect on β-phase stability [221]. Furthermore, the use of refractory metals as additives, such as molybdenum, niobium, or tantalium, causes diffusion problems in a solid state, allowing for a significant amount of alpha phase on the grain boundary that modifies not only the microstructure, but also affects powder metallurgy alloys in terms of their mechanical properties and corrosion resistance [222]. These mechanical characteristics are also influenced by the porosity obtained during the conventional press-and-sinter process [223,224] which mostly affects fatigue properties. However, one of the primary concerns is the high reactivity of Ti, which requires working in controlled atmospheres or in vacuum, yet despite this, certain oxygen contents (about 0.8–1.0 w%) are added, which reduces the plasticity of the alloys while increasing strength [225]. Luo et al. investigated the impact of high oxygen content on alloys produced by powder metallurgy technique such as α-Ti, α + β Ti, and finally β-Ti in the presence of a critical oxygen content that maintains a 6% elongation [226]. As a result, solubilization routes and thermal treatment methods play a significant role on final mechanical properties, particularly plasticity [227]. With an oxygen content of 0.34%, an alloy Ti–31Ta–12Nb–2V–8Zr obtained by cold isostatic pressing (CIP), vacuum sintering (VS), hot forging (HF), hot rolling (HR), solution treatment (ST), and cold work (CW) maintains a plasticity of 13% with a UTS of 1170 MPa, achieving a porosity close to 0%. In a similar processing conditions, Furuta et al. evaluate the influence of Niobium content in the alloys Ti-(30–36)Nb–2Ta–3Zr, with oxygen content of around 0.49%, resulting in tensile properties decreasing and elongation increasing [228]. The mechanism in which oxygen is presented also has a significant impact, as shown by Málek et al. that studied the impact of oxygen being in solution, homogeneous, or concentrated at the granular boundary [229]. This oxygen content is proportional to the mean particle size of the powder, increasing as the size decreases, and can range from 0.1% for particle sizes of 100–120 μm to 0.6% for particle sizes less than 25 μm for irregular HDH powder of Ti–6Al–4V [230] whereas the oxygen concentration of powder atomized by the same gas remained between 0.07 and 0.10% [199].

Accordingly, mechanical properties are determined by the parameters of the powder metallurgy press-and-sinter process, the most influential of which are temperature and sintering time. Many authors have observed that increasing the sinter temperature increases the properties slightly in all instances, since increasing the size of the grain decreases the porosity and changes the morphology of the pores [231]. However, there is a significant concern, when large amounts of alloying elements are added, microstructures of β phase with a large amount of α phase in the grain border that extends into the grain interior are formed. This could affect mechanical properties and weaken the grains in the same way that precipitated ω phase is observed in transmission microscopy. As a result, some researchers have returned to mechanical alloying, which allows for more chemical homogeneity and microstructural change in alloys. Amigó Mata et al., demonstrated that the effects of adding low Fe and Cr contents in a Ti–15Nb base alloy allow for close to 80% phase in its microstructure for 3% contents that provide a $Mo_{eq}$ of close to 12%, however, the mechanical properties of flexion of 700 MPa for these conditions are significantly reduced when P&S of elemental powder blends is performed compared to the 220 MPa obtained with mechanical alloying powders [232]. Fig. 13 shows the microstructure of Ti–Nb alloys obtained by P/M press & sinter at 1250 °C. They obtain two alloys with similar $Mo_{eq}$, Ti–40Nb and Ti–25Nb–5Fe, through P/M. Mohan et al. used the same conditions to study the impact of Fe addition in Ti–Mo alloys with Mo contents of 12 and 15%, with similar outcomes [233]. Elshalakany et al. developed quaternary alloys Ti–15Mo-6-Zr-(1–4) Cr, which were obtained by P&S of blend element powders and sintered at 1250 °C after a 3-h dwell time, and obtained compressive properties and bending strength between 1200 and 1600 MPa, with elongations of less than 5%. Plasticity is reduced primarily by the porosity obtained around 4–5% and the stabilization of the β phase up to 98.9% when Cr is added to the base alloy Ti–15Mo–6Zr [234]. It is nevertheless feasible to obtain a chemically homogeneous alloy with 15% Mo, which does not occur when the addition is more, as in Ti–Nb alloys, as concluded by Caha et al. [235].

The first exhibits a lack of diffusion of larger Nb particles, even when the sintering cycle is extended to 4 h, whereas the alloying with Fe exhibit a high porosity due to the different velocities of diffusion of Fe to Ti, which results in porosity similar to that of the Fe particles, and which appears to decrease when the cycle is extended to 4 h, as the porosity decreases to 1% [235]. These alloys, which were tested for their

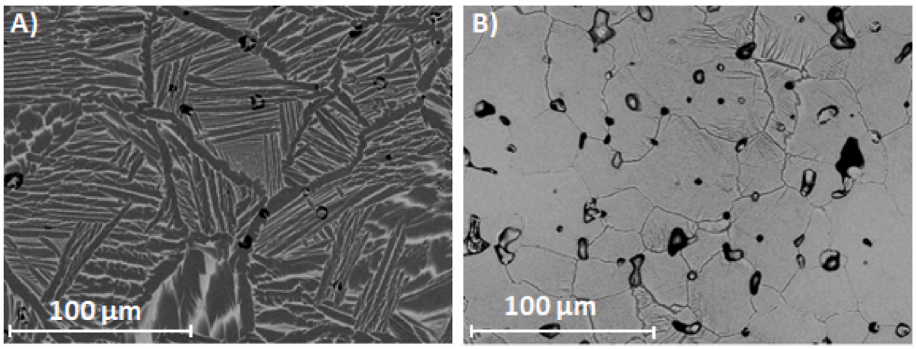


**Fig. 13.** Microstructure of Ti–Nb alloys obtained by P/M press & sinter at 1250 °C: a) Ti–15Nb, b) Ti–35Nb [233].

resistance to corrosion and tribocorrosion, demonstrated excellent resistance, allowing them to be used as biomedical alloys. Mohan et al. investigated the same effect of Fe addition on alloy porosity [236]. Despite a Fe addition of up to 4 w% in the Ti–Mo–Zr–Fe alloys with this addition, the β phase is completely stabilized; however, the bending strength increases when the temperature rises from 1250 to 1300 °C for additions of 1 and 2% Fe, whereas for higher proportions, the properties decrease [236]. They sinter elemental blend powders and mechanical alloying powders, obtaining lower mechanical properties ranging from 1000 MPa to 400–600 MPa, because the ultimate porosity in mechanical alloys is higher and the pores have a larger size. The microstructure obtained in these mechanical alloys is bimodal in all cases, with better distribution and lower porosity as the compacting pressure increases from 600 MPa to 900 MPa. In these conditions, plasticity is low, which is one of the limitations of using this technology to create products that may be used in the biomedical field, which requires an elongation minimum of 8%. However, there are other properties that should be considered for its application in this field, as well as mechanical resistance and corrosion resistance, as analyzed by Çaha et al., particularly when TiN coatings or TiN particle additions are performed in the alloys, as performed by Çaha et al. and Chirico et al. with the evaluation of the tribocorrosion behavior of the Ti–40Nb P/M [237,238]. This superficial modification is used not only to increase resistance to degradation, but also to significantly modify the surface properties that allow for greater interaction with organic tissues. To that purpose, various laser modification techniques have been used, yielding a reduction in elastic modulus in some cases due to microstructural transformations caused by rapid heating and cooling. Tendero et al. investigated the microstructural changes observed in P/M Ti–Nb–Mo alloys, observing a slight increase in bending strength but, more importantly, an increase in overall length without reaching the previously mentioned limits [101]. Rossi et al. studied the impact of different alloying elements on the mechanical characteristics of the Ti–35Nb–10Ta and Ti–30Nb–4Sn alloys, obtaining, according to process parameters, a slight increase in hardness in both alloys and a slight decrease in elastic modulus in the Ti–30Nb–4Sn alloy [239]. On this family of Ti–Nb–Sn alloys, biological studies by Batibay et al. (2023) revealed antibacterial properties against *Staphylococcus aureus* (*S. aureus*) and were not cytotoxic to healthy cells, irrespective of their compositions [240]. Despite improvements in mechanical behavior of P/M alloys following laser treatment, particularly in material plasticity, the decrease of fatigue properties with respect to forging products remains an issue.

On the other hand, Yang et al. (2024) analyze the corrosion behavior and antibacterial properties of Ti–15Mo-xCu alloys with copper contents from 3 to 15%, using low-pressure techniques to obtain functionally graded porous Ti–Mo–Cu alloys. By forming the $Ti_2Cu$ phase mainly at the grain boundary, they obtain a micro-galvanic cell effect which slightly decreases their corrosion resistance compared to Ti–15Mo alloy. However, the antibacterial properties increased with Cu content [241].

As a result, for greater β-Ti alloys's consolidation and elemental solubility, P&S Hot Isostatic Pressing (HIP) processes are introduced along with P&S processes, as demonstrated by Lario et al. (2021), who assessed the evolution of mechanical characteristics of Ti–35Nb–2Sn after HIP (1200 °C 2 h) after 3 h of sintering at 1350 °C and with temperature controls of 100 and 500 °C/min. Post-treatments can reduce porosity while increasing grain size from 19 to 57 µm. As a result, there is no lasting effect, and there is even a slight decrease in length and an increase in elastic modulus, especially when the material's cooling is slow [242]. However, this alloy results in a 10% increase in bending strength in the fast cycle and a 30% increase in bending strength in the slow cycle. In both cases, there was an increase in length that reached 4.2% and a decrease in elastic modulus from 79.8 GPa as-sintered to 76.8 GPa as-HIPed [243]. These HIP treatments maintain the excellent corrosion resistance demonstrated by the alloy Ti–35Nb–7Zr–5Ta and extend the passivation potential from 0.1V to 3V for the rapid cooling condition that exhibits the best mechanical and plastic properties. Other authors, however, refer to high-density processes such as HP, HIP, FAST/SPS, or ERS, which will be discussed further. However, these processes require the use of pre-alloyed atomized powders by various processes or mechanical alloying, as discussed in subsequent chapters. Guo et al., used direct hot pressing to obtain near- β-Ti 5553 alloys from machining swarf. Thermal aging treatments cause the formation of a content in phase that reaches values of 36.5% with acicular and globular morphology [244]. When this occurred, the UTS for HT-600°C-4h + 700°C-0.5h is 1400 MPa with a 2.5% deformation and 2500 MPa in three-point bending strength for a 1.6 mm deflection. Properties that are comparable to, and even greater to, those obtained from hot forging + solution treatment, but with a shorter elongation.

Other authors use two-step pressureless sintering consisting of cold isostatic press of the powder mixture for sintering, then sintering at different temperatures. Sun et al. (2024) use a 250 MPa cold isostatic press with pressureless sintering at 1250 °C of Ti–6Al–4V, obtaining a densification of 99% and a grain size around 90 µm. These two-step sintered samples show a maximum tensile strength of 968 MPa, yield strength of 871 MPa and elongation of 16.1%, thus maintaining ductility [245]. Kuang et al. (2023) obtain highly densified Ti–6Al–4V alloy by pressureless sintering and hot extrusion, after cold isostatic press. After extrusion they obtain an ultimate tensile strength of the rod of 1213 MPa and the elongation increases up to 14 % [246].

Chen et al. (2023) also perform two-step pressureless sintering on TiC-reinforced Ti–6Al–4V, by a first step of mechanical alloying of Ti CP and 60Al40V master alloy. This results in a composite with ultrastrong hierarchical microstructure [247].

Furthermore, Guo et al. (2024) use a hot forging post-processing after two-step pressureless sintering of Ti–6Cr–5Mo–5V–4Al for high performance, using as a first step CIP with a pressure of 200 MPa. After forging and solution treatment and ageing, the sample exhibited a high maximum tensile strength of 1211 MPa and an elongation of 13.8 %, considering very interesting properties for this PM Ti6554 alloy [248]. Similarly, Franco et al. Using a similar two-step pressureless sintering

process, they obtain the Ti–35Nb–7Zr–5Ta alloy with a final density of 98%, although the oxygen content increases to 0.96%. This high oxygen content allows obtaining a fatigue resistance higher than 88 MPa after subsequent heat treatment, together with the formation of coarse α-phase precipitates at the grain boundaries [249].

In contrast, Cai et al. (2023) obtained Ti–20Al–19Nb (at.%) dense alloy by $TiH_2$-assisted pressureless sintering; although its densification remains problematic. They found that $TiH_2$ participated in the reverse eutectoid transformation, α-Ti + δ-$TiH_2$ → β-Ti, improving the density and mechanical properties [250].

#### 4.1.2. Metal injection molding

These mechanical characteristics are also found in P&S products, but to a lesser extent when techniques such as metal injection molding are used (MIM). Specifically, the technical basis and properties, as well as the many steps to obtain MIM pieces, are described in various German Works [205]. For instance, in terms of β-Ti alloy sintering, Kafkas and Ebel sintered Ti–24Nb–4Zr–8Sn dog-bone specimens at various temperatures and times, yielding elastic moduli ranging from 53 to 61 GPa and yield strengths of 650 MPa for 0.5% oxygen contents [251]. Similarly, zhao et al. investigated the sintering behavior and mechanical characteristics of a metal injection molded Ti–16Nb alloy, requiring a temperature of 1500 °C to minimize porosity to 5%, whereas Nb diffusion is nearly complete at 1300 °C. However, due to the use of an organic binder, TiC precipitates appeared. Furthermore, this same effect of TiC precipitation is described by Xu et al., who observed the formation of particles in the alloy Ti–10Zr–20Nb with O content less than 0.28% and carbon content less than 0.04% [252]. Moreover, despite having a porosity of 5–6% and grain sizes greater than 300 μm, analyzing the mechanical properties according to the distribution of these particles, since they decrease the elongation although it is still greater than 4%, maintaining the elastic limit between 700 and 750 MPa. Eventually, the same authors (Xu et al.) investigated the impact of yttrium (0.3–1 w %) addition on the same Ti–10Zr–20Nb alloy by MIM processing. The alloys are sintered at 1500 °C for 4 h. Despite the control over grain size, which drops to 170 μm for the addition of 1% Y, mechanical properties decrease to values of yield strength of 612 MPa, resulting in a decrease in ductility of 4.0%–3.3%, as does the elastic modulus, which ranges from 71 GPa to 61 GPa.

Santos et al., also obtained a low-cost β -type Ti-(8–17 w%) Mn using MIM, reporting phase stabilization and observing phase formation in TEM. However, the obtained plastic properties are inferior to the Ti–6Al–4V alloy, whereas the Ti–Mn hipo-eutectoids exhibit greater resistance to the Ti–6Al–4V alloy [253]. Furthermore, these same authors produced alloys with low Mn (5–6 w%) content with the addition of Mo (3-4w%) contents manufactured by MIM and sintered at 1100 °C for 8 h. Notably, it continues to work around a $Mo_{eq}$ of 15, achieving tensile strengths of 1000 MPa and elongations of 2–5%, owing mostly to the hardness and fragility that ω phase provides as detected by the TEM [254]. Moreover, this transition from press & sinter to MIM is justified despite the fact that MIM does not achieve the same tolerances as axial pressing, but the improvement of mechanical properties and, more importantly, fatigue resistance is very important in these alloys, even though there are still some limitations in the amount of additives available for alloying development. In addition, Zhao et al., investigated the possibility of Ti–Nb mixture with Nb content ranging from 10% to 22% via MIM, evaluating porosities as high as 6% in different alloys but with a TiC content of 2% in Ti–22Nb. These properties and microstructures are compared to HIP-treated alloys in which the porosity has been completely closed. Even with this treatment, mechanical properties only slightly increase, from 649 MPa for as-sintered Ti–22Nb to 687 MPa for HIP Ti–22Nb, and elongation shows a slight decrease, from 1.43% for as-sintered Ti–22Nb to 1.30% for HIP Ti–22Nb, as well as an increase in elastic modulus from 70 to 75 GPa following HIP treatment [255]. Similarly, Xu et al., evaluated the alloy Ti–20Nb–10Zr generated by employing an elemental powder mixture and the MIM process to get samples for tensile and fatigue testing with porosities of 2.7%. (average pore diameter 7.3 μm), considering two different levels of material purity based on vacuum conditions used during sintering. In their fatigue tests, they obtained a greater number of life cycles than Ti–6Al–4V or Ti–6Al–7Nb, which are also processed and tested under the same conditions, as well as a certain amortiguation in their behavior, which may indicate the fatigue limit. Additionally, the study of two lots with different levels of purity found that for $10^7$ cycles of life, there is no noticeable difference between them, and that only when stress applied is more than 780 MPa the sintered more clean allow for more than $10^6$ cycles of life [256].

#### 4.1.3. Porous alloys

One technique to minimize the weight and rigidity of materials is to obtain them with a given porosity and employ one of the disadvantages of powder metallurgy, their residual porosity, to lower and manage the elastic and plastic properties. In addition to greatly increasing the specific contact surface of great significance in several applications. Consequently, powder metallurgy is one of the technologies suitable for the production of such products, and the development of porous Ti materials has included techniques such as sintering without the use of microspheres or the use of various spacers to control the quantity and size of the pores. Moreover, porosity has also been generated in the form of channels with extremely precise dimensions using trapped gas and freeze casting techniques. Finally, the incorporation of additive manufacturing techniques in the production of porous Ti allows for the design of pores and the production of porosity with various structures, whether through the use of laser, electron, or electric field [29,257,258].

i. Pressureless sintering

The sintering of microspheres without pressure has been used to obtain porous coatings of Ti on Ti alloys, as proposed by Pilliar et al., who proposed a new technology using porous coating to improve bone tissue ingrowth while simultaneously improving fixation while the bulk material provides mechanical support. As described by Pilliar et al., a new technology using porous coating to increase bone tissue ingrowth while improving fixation whereas the bulk material offers mechanical support has been obtained by sintering microspheres without pressure [206]. Moreover, the impact of these porous coatings on the fatigue resistance of Ti and Co–Cr implants was obviously evident, and this is one of the most concerning features in porous alloys. Since, sintering occurs at high temperatures and changes the microstructure of the base alloy, particularly if it has been subjected to thermal treatments, leading in granular engrossment and lamellar microstructures whether the alloy is Ti–6Al–4V or Ti–6Al–7Nb. For example, Reig et al. studied the sintering of Ti–6Al–4V alloy by microspheres [259], and they investigate the effect of temperature and sintering time, which increases from 1300 to 1400 °C and from 2 to 8 h, bending strength increases from 140 to 300 MPa for atomized particles ranging from 180 to 240 μm. However, if the microspheres are larger in size, between 425 and 600 μm, bending strength between 60 and 100 MPa are obtained, which are insufficient for the majority of applications. Fig. 14 shows the union between the microspheres of Ti–6Al–4V, with a large size 450–600 μm, pressureless sintered at 1400 °C and the microstructure of these sintered microspheres at 1300 °C for 8 h. Importantly, this particle size affects the size and number of pores that can be obtained by pressureless sintering of microspheres since the size of the pores is one-fourth of the size of the microspheres while the porosity only reaches 32% regardless of particle size [260]. To address the mechanical behavior of these materials, the authors use the Zero-Order Reaction Rate Model and Transition State Theory, which allows them to predict bending strength based on particle size and the application of different sintering temperatures and times [261]. However, because to the difficulty and high expense of obtaining Ti beta atomized powder, there are no reports describing the use of these pressureless sintering techniques in these areas.

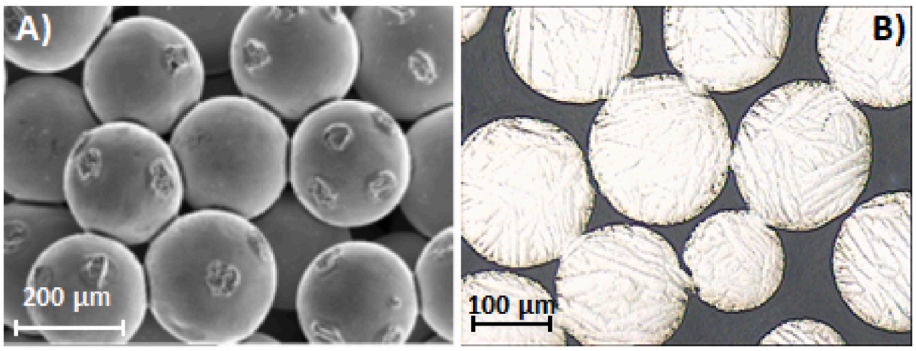


**Fig. 14.** a) the union between the microspheres of Ti–6Al–4V, with an average size of 450 µm, pressureless sintered at 1400 °C. b) Microstructure of these sintered microspheres at 1300 °C for 8 h [260].

However, due to the difficulty and high cost of obtaining atomized pre-alloyed Ti beta powders, there are no documents on the application of pressureless sintering techniques for pressureless sintering of microspheres in these alloys. Nevertheless, two-step processes with pressureless sintering after cold isostatic compaction or mechanical alloying have been used on both Ti–6Al–4V [245–247] and Ti-6554 Alloy (Guo et al., 2024), although in these processes, densities around 98% and non-porous have been obtained [248]. Zhang et al., in 2017, used pressureless spark plasma sintering to obtain Ti–Mo foams with nano and sub-micro porous. They used a solid-state dealloying method in the preparation of foam from (TiMo)1-xCux master alloys. The dealloying is performed inside Mg powders where the Cu atoms of the master alloy are selectively dissolved. As a result, this process yields pore sizes of less than 50 nm, with nano-porosities of 55–75% [262].

ii. Low pressure sintering

While conventional P/M uses high compacting pressures to provide high densification pieces, in contrast, the use of low compacting pressures, which are lower than usual, allows for greater porosity in green pieces and therefore in the sintered material. However, porosity is distributed uniformly within the finished piece. The amount of porosity depends upon the compacting pressure, particle size and shape, chemical composition, and sintering temperature and time. Rossi et al., investigated the mechanical behavior of Ti–34Nb–6Sn alloys compacted at 100 and 200 MPa and sintered at 900 °C for 2 h [60]. Additionally, they assessed the corrosion resistance using electrochemical tests and ion release. The higher Nb content generates a lack of diffusion, since the temperature has been insufficient to achieve complete chemical homogeneity, resulting in a porosity of 26% for 100 MPa compacting and 22% for 200 MPa compacting. In this manner, the elastic compression limit increases from 245 MPa for 100 MPa compacting to 320 MPa for 200 MPa compacting. Thus, the use of low powder compacting pressures, together with the use of different particle sizes, allows for the production of green pieces with very low densification and, as a result, a large number of porous in the sintered material [263]. Due to its ease of use, this technique has gained popularity in the production of materials with gradient porosity, which will be determined by the many layers with varying sizes [264]. Nevertheless, the pore size will be varied and difficult to control, making the final mechanical characteristics highly dependent on the largest size of defect obtained.

Similarly, Torres et al., obtained and characterized cylinders with gradient porosity with CP-Ti with a particle size between 10 and 70 µm of 25 µm, alternating layers with different density and therefore different porosity in such a way that they achieve a gradual longitudinal porosity with a distribution of porosities from 12 to 45 %. These materials have an elastic modulus of 25 GPa and they conclude that an optimization of the process can produce materials with a good balance of properties that can reduce the effect of stress shielding in their application as biomedical prostheses and thus avoid bone resorption [265].

iii. Space-holder technique

To obtain a larger porosity and a greater interconnection between the pores, different spacers have been used that consist of solid materials that can be removed at low temperature without excessive contaminating the Ti powder. Prior to extraction of the matrix and manipulation to eliminate the spacer thermally, the powder-spacer mixture can be compressed with the required pressure. For example, urea powder (carbamide) has been used, which can be removed at 200 °C with little CP-Ti contamination, because the oxygen content increases from 3000 to 5000 ppm [207]. However, when the porosity increases, the tensile strength decreases rapidly, from 760 MPa for 7% porosity to 68 MPa for 60% porosity and finally to 6 MPa for 77% porosity, which is also dependent on the distribution of the size of the particles used as spacers [207]. Amigó et al., employed ammonium bicarbonate ($NH_4HCO_3$), which removed at 80 °C with the formation of $CO_2$ and $H_3N$, resulting in very low contamination. Fig. 15 shows CP-Ti foams with two different spacers carbamide and $NH_4HCO_3$ with particle size between 250 and 500 µm, compacted at 300 MPa and 200 MPa respectively and vacuum sintered at 1200 °C.

Spacer sizes ranging from 250-500 µm to 500–1000 µm are used, with compacting pressures of 100 and 200 MPa. In this context, bending strength drops up to 500 MPa with 25% porosity and remains between 100 and 200 MPa with porosities ranging from 40 to 60%, depending on the size of the spacer used and the compacting pressure [266].

Similarly, Torres et al., investigated a similar material by adding 50% $NH_4HCO_3$ CP-Ti HDH, resulting in a 43% interconnected porosity [267]. Moreover, a compressive pressure of 200 MPa results in an elastic limit of 220 MPa. They evaluated the cytotoxicity of various porous samples and discover that none of them were toxic [267]. In addition, this same group developed Ti pieces with radial porosity gradients for use in orthopedic implants. In this scenario, CP-Ti combined with NaCl of 180 µm diameter, was used, after removing NaCl with water at 40 °C for 24 h, Ti samples were sintered at 1250 °C for 2 h [268]. In Fig. 16, an example of porosity obtained is shown with details of pores roughness. They employed different combinations of porosities ranging from 40 to 70% to get modulus comparable to cortical bone with a porosity of roughly 50% with experimental compression resistances ranging from 40 to 200 MPa, which are quite comparable to cortical resistance [269].

Magnesium in the form of grains is another spacer used since its melting temperature is low and its boiling temperature is high, which reduces dramatically when sintering in high vacuum [270]. They mixed CP-Ti with Mg grains (150–850 µm) in proportions of 50, 60, and 70% before compacting in circular matrices at 400 °C and 600 MPa uniaxial pressure. Removing Mg with HCl and ethanol for 24 h, and then using ethanol as a buffer solution to avoid the corrosive and damaging effects

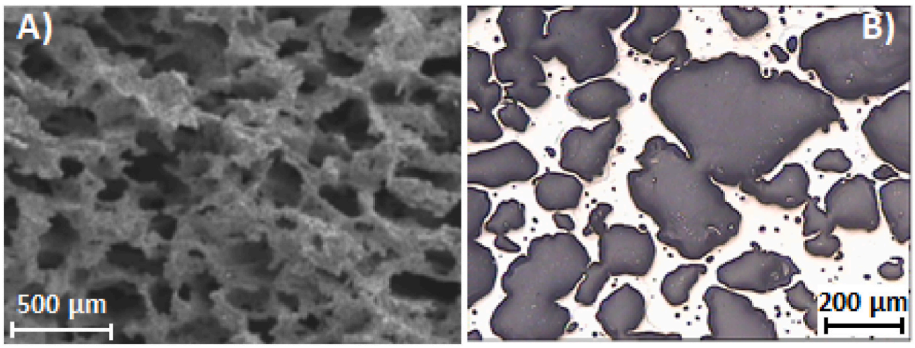


**Fig. 15.** CP-Ti foams with two different spacers (particle size 250–500 µm) compacted at 200 MPa and vacuum sintered at 1200 °C: a) Foam fracture obtained with 55 vol% with carbamide b) Microstructure of a 45 vol% foam using $NH_4HCO_3$ as spacer [266].

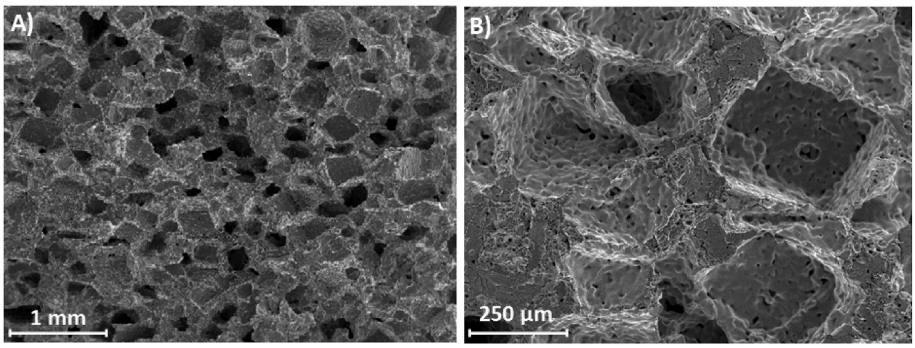


**Fig. 16.** CP-Ti foam obtained with 40 vol % NaCl as spacer a) general appearance of the tensile fracture of the foam. b) Detail of the roughness at the bottom of the pores [269].

of hydrochloric acid on Ti powder. Then, they assessed the distribution, volume, and size of the rather homogeneous pores, as well as the interior roughness caused by the hydrochloric acid attack. They have compressive properties of 100 MPa for a porosity of 60%, but close to 300 MPa for a porosity of 50%, despite the fact that these values are obtained by applying the load in a direction parallel to the plastic

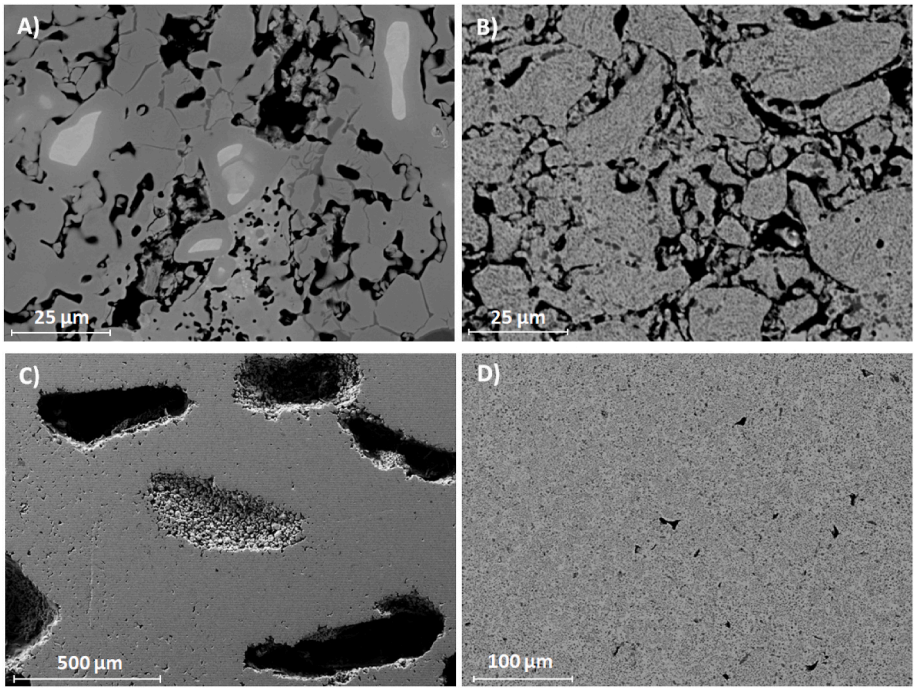


**Fig. 17.** Porosity produced by the addition of 10% Mg in the Ti–34Nb–6Sn alloy Press to 200 MPa and different sinter temperatures: A) Blend elements sinter to 900 °C. B) Mechanical alloying sinter at 900 °C. C) Porosity due to the elimination of Mg particles in mechanical alloying sinter at 1100 °C. D) Detail the sinter microstructure at 1100 °C in the inter-porous zones [271].

deformation obtained by Mg grains when compacted at 400 °C. When the application to the deformed pores is normal, these values decrease to 100 MPa and 80 MPa, respectively. Rossi et al. studied the impact of low Mg content on the properties and densification of Ti sintered at temperatures of 900 °C and 1100 °C for 2 h after compacting to a pressure of 200 MPa (Fig. 17). However, these compacts have a transverse tensile strength of 85 MPa, which ensures the ability to obtain a complex near-shape when Mg is removed, which is complicated when NaCl is used as a spacer [271].

Due to a lack of diffusion between the elemental powder used, notably Ti and Nb, less than 80% of the β phase is kept in all circumstances; therefore, the quantity of α phase retained corresponds to Ti that has not interacted to generate the β phase with Nb. Using the impulse excitation method, they observed that the elastic modulus ranged from 31 GPa to 49 GPa depending on the sintering temperature, with high hardness, and that final oxygen levels of up to 1.3% by weight were detected. They also assessed both the physical and biological properties of Ti–34Nb–6Sn/Mg, which was produced by mechanical alloying of hydrated elemental powder for 60 min. The green parts were sintered for 2 h at 700 °C and 800 °C, yielding porosities of 38 and 28% at the two sintering temperatures, respectively, and hardness of 92 and 120 HV. After 72 h, biochemical analyses of cell adhesion revealed that cells had proliferated both on the surface and within the pores, indicating that they are perfectly suitable as biomaterials [272].

iv. Expansion of pressurized bubbles

The trapped gas expansion technique is carried out in two high-temperature stages. In the first stage, the powder is placed in a container that is compressed with argon gas to a specific pressure, typically 0.33 MPa, before being subjected to HIP, which is normally 100 MPa and temperatures ranging from 900 to 1100 °C for one or 2 h. HIP-ed component is designed for long-term gas expansion treatment at temperatures between 1100 and 1250 °C, generating plastic deformation at high temperatures [208]. The most well-known Kearns technique is controlled Ar expansion in metal compacts, as the group was the first to obtain Ti–6Al–4V fumes using this approach [273]. Furthermore, the original Ti–6Al–4V alloying method has been used effectively to produce CP-Ti and Ti–Ni powders [274,275].

Davis et al. used CP-Ti 130 μm packed to a 70% relative density in a steel container, backfilled with 0.33 MPa argon gas, and soldered. The material was densified by HIP for 125 min at 890 °C and 100 MPa, then expanded in 4-min cycles between 830 and 980 °C for a total experiment time of 30 min to 24 h. After 5 h, the porosity is 38%, with ultrasonic elastic moduli of 39 GPa and yield strength to compression of 120 MPa compared the expected 160 MPa [276]. Similarly, Spoerke et al., obtained a porosity of 22% with pores with widths of 200 μm after subjecting the HIP-ed material to 960 °C for 5.25 h to obtain an argon gas expansion. They then used a rotating bioreactor to analyze the behavior of pre-osteoblasts *in-vitro*, and the results were remarkable [277].

Dunand offered an in-depth review of Ti foam fabrication, distinguishing two procedures based on pressurized bubble growth within the section [263]. The first creep expansion technique incorporates the argon expansion process developed by Kearns et al., as well as the Low-Density Core Approach (LDC), which Martin et al., developed from the Kearns approach to enable the manufacture of Ti–6Al–4V sandwich structures [278]. Boeing (USA), a leading aerospace company, has used this technology in structural components made of Ti–6Al–4V and porous Ti alloys [279], but no papers have been found where this technique is used with β-Ti alloys. The Second Superplastic Expansion Processes, as established by Dunand et al., when superplasticity is applied in the liquid state of CP-Ti and Ti–6Al–4V, are characterized by a high rate of deformation [280]. This super-plasticity generates more porosities than creep expansion which is induced by heat cycles near the CP-Ti and Ti–6Al–4V transformation, [281,282].

Additionally, Murray and Dunand investigated the influence of this thermal history on titania superplastic expansion due to argon expansion on the creation of pores. They explored chemistry and microstructure in the first half and model the chemistry in the second half [283,284]. Meanwhile, oppenheimer and Dunand used Ti–6Al–4V spherical powder with different sizes of 75, 115, and 165 μm that are encapsulated in mild steel canisters and backfilled with argon gas at 0.33 MPa of pressure before densifying by HIP at 100 MPa and 950 °C for 4 h. After the steel layer is removed, the foam is baked in a high-vacuum oven with an isothermal treatment at 1030 °C. They achieve up to 30% porosity while attaining compression limits of 500 MPa and elasticity modulus of 55 GPa by expanding pressurized argon trapped in micro-size pores during the initial stage of HIP consolidation [285].

In another study, Nugroho et al., employed this process to create Ti–29Nb–13Ta-4.5Zr emulsions, with the initial stage consisting of mixing the powders in a steel container. After filling the container with 0.68 MPa argon gas, it was subjected to a HIP at 1100 °C for 1 h under 100 MPa in an argon atmosphere. After that, the piece was subjected to 10 h of gas expansion at two temperatures, 110 and 1225 °C. This resulted in porosities ranging from 15% at 1100 °C to 27% at 1225 °C. The resistance to corrosion increases with temperature, however electrochemical corrosion demonstrates a stronger resistance to corrosion at lower temperatures, despite the notable pitting effect [286]. However, no new work has been found on porous β-Ti alloys obtained by superplastic expansion processes.

v. Freeze casting

The freeze casting technique, which was developed to manufacture ceramic products with aligned porosity, has also been applied to Ti alloys [287]. The freeze casting technique is used to prepare a solution containing the various elements that will form the alloy. Liquid $N_2$ is used to cool the slurry at a rate of less than −10 °C/min. Powder normally settles and forms canal structures with the solvent. The ice is removed from the frozen green substrate by sublimating it at low temperatures and pressure for several hours. Chino and Dunand used an aqueous slurry of Ti powders with particle sizes less than 45 μm that was solidified directly, yielding a consistent performance in ice dendrites with interdendritic areas containing a high Ti content. Following freeze-drying to remove ice dendrites and Ti sinterization, foams with 57–67% aligned holes and a length of several millimeters are obtained. Similarly, Mao and others, in a similar way achieved similar results for $TiH_2$ contents of 20, 25, and 30% by obtaining porosities ranging from 40 to 50% using elastic moduli ranging from 25 to 32 GPa [287]. Koh et al., used the freeze casting technique to produce Ti foams with varied porosity and $TiH_2$/camphene suspensions with changing hydration levels. After freeze drying, the material was exposed to a 3 h vacuum treatment at 1300 °C. This process produces layers with varying porosities of 35, 50, and 75%, with highly good union between them, depending on the $TiH_2$ amount used. Furthermore, they discovered that as the period of freezing increases, so does the number of particles suspended, generating pores ranging in size from 100 to 270 μm after 7 days [209]. Du et al., developed porous Ti scaffolds using freeze casting technology for use as structural cores of sandwiches, heat exchangers, or filters, with porosities ranging from 15% to 73% that provide compression resistances in the parallel to freezing direction of 60–86 MPa, while compression elasticity varies from 0.8 GPa to 11.2 GPa, significantly lower than those reported by Chang et al. [288].

Dunand and Li produced Ti foams using a camphene solution, finding that reducing the size of the pores improves the foam's mechanical properties [289]. Chang et al., assessed the impact of sintering temperature, sintering freeze dry Ti scaffolds from 800 to 1100 °C and varying the temperature every 50 °C, obtaining porosities ranging from 61% for 800 °C to 20% for 1100 °C that provide elastic modules ranging from 2.04 to 7.16 GPa and compression resistance ranging from 100 to more than 1100 MPa even though the pieces are tested until fracture

[290]. Jenei et al., prepared Ti foams with relative densities of 0.49, 0.37, and 0.32, assessing mechanical performance in relation to porosity and grain size after sintering treatments at 850 and 1000 °C for 4–6 h, depending on the density and grain size chosen [291]. In contrast, Jenei et al., on the other hand, use freeze casting to produce a Ti–5W foam with a porosity of 32–33% and pore diameters of 15–17 μm, resulting in an elastic modulus of 23 GPa. The addition of W to Ti raises the compression resistance from 196 MPa to 235 MPa [292]. Choi et al., examined the same alloy by producing an elemental suspension of Ti and W (about 50%) in water with 2.8 w% Poly (vinyl alcohol). By presenting an acicular microstructure Widmastäten α/β with W separated in the β phase, they obtained a 2%W solution in Ti. Ti–5W foam has a compressive yield strength of 323 MPa, which is roughly 20% larger than Ti foam, which they are testing at 256 MPa, which is significantly higher than the values reported by Jenei et al. [293]. Weaver et al., investigated the relationship between the structure and the freeze-cast processing of Ti–6Al–4V alloy using a mixture of low molecular weight chitosan and sodium carboxymethyl cellulose in water with 1% acetic acid as a filler, increasing suspension viscosity and decreasing the effect of premature powder sedimentation, which added in concentrations of 20 and 30%. Porosities of 65 and 34% are obtained. The elastic modulus is 7–29 GPa, with compression tensions of 80–400 MPa for 20% deformations, which are slightly higher than for camphene-prepared foams [294]. Li et al. obtained a volume shrinkage of 51 to 47% by combining 15–30% Ti–6Al–4V powder in an aqueous solution with 0.2 vol% Xanthan gum as a surfactant, achieving a porosity gradient of more than 20% from the foot to the head and peak values of 55–74%. As a result, when sintered at 1200 °C for 1 h, their elastic compression modulus ranges from 2 to 12 GPa, with compression resistance ranging between 40 and 300 MPa, and they later endure with the addition of SiC fiber to the suspension [295]. Additionally, they noted that the addition of SiC (2, 4.5, and 10 vol%) increases compressive strength to 400 MPa, but larger amounts of SiC fiber generate small amounts of $Ti_5Si_3$ and TiC precipitates, which can reduce compressive strength and modulus to values less than those of Ti without the use of force [296,297]. Similar properties to those reported by Chen et al., control porosity, porosity size, and porosity distribution by using gelatin as a binder and polyvinylpyrrolidone as a dispersant. They obtained compression resistances ranging from 57 to 142 MPa and elastic moduli ranging from 2.8 to 5.1 GPa [298]. The addition of zirconium acetate to the solution influences the composition of the pore structure and mechanical properties of porous Ti. As a result, the structure of the pores can be customized to resemble honeycomb structures [298,299].

Trueba et al., analyzed the influence of the freeze-casting process parameters (diameter, mold material and temperature gradient) on the porosity and mechanical behavior of cylinders with elongated porosity obtained using a 5 w% of polyethylene glycol in binder demineralized $H_2O$. They confirm the formation of a higher gradient porosity in the top, as the resistance to compression and the elastic modulus decrease with the higher porosity [300]. However, the freeze casting technique has not been applied so far to obtain porous β-Ti alloys.

### 4.2. Spark plasma sintering (FAST/SPS)

Nowadays, there is a growing demand in using rapid sintering techniques such as Spark plasma sintering also called Field Assisted Sintering Technologies (FAST/SPS) to manufacture various forms of Ti alloys with a fine-grained microstructure attain outstanding mechanical characteristics [301–303]. In FAST/SPS, a compact powder is subjected to high pressure when sintering by applying an electric current passing thought the pressing die to the powders, which improves densification and lowers the sintering temperature and holding time. The grain growth rate was also revealed to be lowered by this technique, producing grains with outstanding mechanical features [304]. The advantages of this approach over ordinary PM include the quick sintering in SPS and the outcomes of a smooth size process. When applying the SPS technique to manufacture porous structures, there are two common approaches. The first approach involves partially sintering loose particles or fibre at low temperature. The SPS involves loading Ti powders into a graphite die, which is then subjected to a uniaxial force during the sintering. Spark discharges in the spaces between the particles are used to heat the material. This discharge refines and excites the particle surface, and the electric current produces a joule heating between the particles as a consequence and plasma is generated as a result [305]. Regarding both conductive and nonconductive powder, densification is accomplished in a brief period of time during the sintering cycle owing to the electric current delivery, which also decreases the rate of grain growth [305]. Due to its rapid heating rate, SPS is used to produce nanocrystalline materials by minimizing the grain size [306].

A low voltage is used in the SPS system, which leads it to produce high electric current. The process uses graphite tools that allow to apply high cooling rates varying from 150 °C/min to 400 °C/min and auxiliary gas cooling can produce temperatures of roughly 2400 °C [307]. SPS employs loads around 50 and 250 KN while running under vacuum, thereby accelerates the densification process [308]. According to studies, the SPS can heat up fast (at a rate of 1000 °C/min), allowing for shorter material manufacturing cycles [309]. The flow of electric current between the powder particles affords the SPS's mechanism a quite special quality. Plasma is produced when the particle surfaces are heated.

The temperature refines and energies the particle surface, which leads the impurities on the powder particles to evaporate. The heated particles later melt and merged to form a neck. By directing an electrical current through the particles in the neck during the second stage, joule heat is generated. The diffusion of the particles in the neck is increased by joule heat, promoting their growth. Eventually, when the heated material has turned soft under pressure, plastic deformation occurs. Furthermore, the compact is obtained due to densification [306,307]. Since there are no intermediate ingredients used in this approach, it has the advantage of minimizing time, energy, and expense while reducing the chance of contamination.

### 4.3. Additive manufacturing (AM)

Typically, powder metallurgy, foaming, and casting technologies are used for manufacturing titanium alloys [310,311]. Nevertheless, these conventional methods need additional time, energy, and material resources due to their various processing stages [312]. Furthermore, there are a lot of issues with these approaches. For instance, titanium's low elastic modulus, rapid oxidation rate, and limited heat conductivity make it difficult to deform over a high temperature [312]. Oxygen and titanium will react throughout the machining process to create a tough oxide coating on the surface. Tool wear will also be accelerated because excessive heat accumulation will result from the machining process's heat generation not dissipating rapidly enough [313]. With the aid of moulds, large-scale components may be effectively formed by casting. Nevertheless, specific tools are needed for titanium alloys, which are quickly oxidized at high temperatures. Therefore, components with various forms are typically in demand for unique moulds. As a result, the cost of production will rise dramatically because of these extra tools and processes. Additionally, molten titanium alloys have very high viscosities as compared to other metals, which results in poor filling fluidity properties. When they solidify, they are susceptible to flaws like porosity [314]. As a result, cast Ti parts frequently fall short of performance standards. Likewise casting, forging similarly necessitates the use of expensive specialist equipment. Furthermore, forging large-scale components with intricate forms is challenging. Titanium alloys made using the aforementioned traditional techniques are therefore more expensive than many other metal alloys due to their difficult extraction process, difficult melting and manufacturing process, and mechanical imperfections [314].

Conversely, additive manufacturing features easy processing steps

and inexpensive equipment. Without the need for moulds or specialized tools, it may immediately create components with almost net shapes. Therefore, AM may be a more affordable option than casting and forging. The manufacturing of items with intricate forms requires the use of the porous structure approach. The advancement of additive manufacturing (AM) technology in the last few decades have accelerated and enhanced implant innovation [9,315,316]. Lacking the need for a separate processing program, the AM technology is capable of producing the porous implants instantly. The apparent benefits of these implants include their light weight and low Young's modulus, that can encourage the formation of new bone cells. The ability of AM to precisely machine the pore structure of complex unit structures in comparison to traditional techniques has raised serious concerns.

The term additive manufacturing (AM) describes a wide range of methods that convert 3D digital drawings into real, working components in a manner similar to how an office printer prints 2D digital data onto paper. "A process of joining materials to make objects from 3D model data, usually layer upon layer, as opposed to subtractive manufacturing methodologies," is how ASTM F2792 describes additive manufacturing [317]. The process begins with slicing a 3D solid computer assisted design (CAD) model into layers. Then, digital data is generated according to the geometry of each layer [316]. The selected layer-by-layer combining of unit materials—usually sheets, wires, and powders—into final (near) net-shaped structures is subsequently accomplished using this digital information as the tool path. The enhanced versatility of AM technology is provided by this working concept [9]. By carefully applying material just where it is required, complex structures that are not achievable by machining, such interior cooling channels, may be easily made. Instantaneous local manufacturing on a global scale is made feasible by the digital models' freedom and worldwide shareability. Furthermore, AM technology eliminates the need for fixtures, moulds, and tooling, which significantly cuts down on the lengthy lead times associated with the design and manufacture of moulds and/or tools [9]. Another key component of AM technology is near-net shaping, which drastically reduces waste and material consumption [316].

The latest innovation in the realm of metal fabrication is additive manufacturing (AM), frequently referred to as three-dimensional printing (3D printing) [318]. The near-net-shape forming capability of AM is one of its most important material-related benefits [319]. Due to the fact that AM has been recognized as a promising technology offering significant geometric design flexibility [320], a great deal of effort has gone into developing an appropriate AM method for producing titanium alloy components with enhanced mechanical qualities. Metallic items with complicated geometries may be created in a single step without requiring time-consuming and costly machining processes by layer-by-layer assembly of the component based on the digital model. 3D printing, is a technology which produces products from 3D model data via melting a layer of powder with an electron or laser beam under computer control to create intricate component structures [316]. Aerospace and biomedicine have shown a great deal of interest in additive manufacturing because of its ability to precisely, quickly, and efficiently regulate the intricate interior pore structure and form of the components that are manufactured.

In recent years, different alloys have been incorporated for additive manufacturing techniques by obtaining different pre-alloyed powders of suitable quality and price. Cheng et al. (2024) analyze the manufacturability and mechanical properties of Ti–35Nb–7Zr–5Ta porous titanium alloys produced by laser powder-bed fusion, requiring lower energy than for dense materials. These alloys were topologically optimized considering the compressive strength of cortical bone, achieving minimal defects in the material [321].

#### 4.3.1. The foundations of metal AM techniques

Despite beginning with organic materials, AM technology has a unique niche in the production of metallic materials because it can fulfil performance criteria and improve manufacturing efficiency, sustainability, and expenditures as well as energy savings. Various AM methods have been devised to leverage these significant advantages. A number of these processes have been particularly created for the manufacture of metallic components, or they have been modified from polymer-based procedures. These including sheet lamination (SL), directed energy deposition (DED), material extrusion (ME), material jetting (MJ), binder jetting (BJ), and VAT photopolymerization (VP). For Ti-based materials used in medical applications, powder bed fusion (PBF) and DED are the most used AM methods [318]. PBF and DED laser-based technologies operate in an inert atmosphere, whereas electron beam technologies operate in a vacuum [322]. Selective laser melting and electron beam melting are the two most common additive manufacturing processes [316].

#### 4.3.2. Powder bed fusion (PBF)

The basis of PBF technologies is the deposition of a layer of metal powder on the build plate. The laser/e-beam scanning of the powder layer is driven by the section drawing (slice of the 3D object model), which causes the powders to melt partially or completely. Each model slice goes through the process once again until the product is produced. The bonding between the various layers is controlled by the powders' melting and re-solidification [323]. Selective Laser Melting (SLM) and Electron Beam Melting (EBM), the two basic PBF procedures, use laser or electron beams as heating sources, respectively, for powder fusion. SLM technology, which employs a laser that melts metal powder, is the technology most metal 3D printer's use.

i. Selective Laser Melting (SLM)

The initial report on the selective laser melting system was published in 1995 in Germany by the Fraunhofer Institute ILT in Aachen. SLM is an AM approach that accounts for more than 80% of the market for metal 3D printers [324]. SLM is unique from other powder bed fusion processes, such as selective laser sintering (SLS) and direct metal laser sintering (DMLS), in that it completely melts metal rather than sintering it [324]. Prior to using an SLM printer, a 3D model needs to be translated into a format [Stereolithography (STL)] files that is compatible with it [325]. Using so-called slicing software, the model is then divided into layers, with each cross-section of the model representing a layer that will be printed by the SLM printer [326]. The proper metal powder is added to the powder stock through a hopper or automated cartridge once the model has been placed into the printer [326]. To protect the metal from oxidation while subjected to the intense laser beam, argon gas is fed into the sealed manufacturing chamber [327]. These lasers are usually focused high-power ytterbium fibre lasers, (Ytterbium fibre/Nd:YAG, $\lambda \approx 1$ μm and power <200 W) which are hot enough to completely melt the metal powder but also produce significant temperature differences. The sealed chamber is heated to reduce temperature fluctuations between the laser and powder in order to take these variances into account [327]. A computer-aided-designed (CAD) 3D model that has been sliced into slices of a specific thickness serves as the toolpath for the AM equipment, which is used to fabricate the product [328].

In a building chamber, a substrate plate is covered with a thin layer of metal powder to start the construction process. Once the powder has been placed, a high-power laser is employed to melt and fuse specific areas in accordance with the processed data [328]. After the laser scanning is done, a new layer of powder is added on top, the building platform is lowered, and the beam scans a second layer [328]. This procedure is then repeated for other powder layers until all necessary components have been fully assembled. After the laser scanning task is performed, the construction chamber is cleared of loose powders, and the product can either be manually or electrically separated from the substrate plate [329].

SLM is therefore a viable technology for the net-shape production of parts employing a wide range of high-quality engineered metals that are difficult to build using other traditional processing techniques. With the

assistance of this technology, devices with fully interconnected porosity needed to mimic the mechanical modulus and structure of cancellous bone could be manufactured. Table 4 classifies the many defect types that frequently influence the nodes and struts that comprise the microstructure of metallic implants produced through additive manufacturing in terms of their sources, impacted components, and effects. In contrast, Table 5 displays a classification of techniques for reducing AM defects.

ii. Electron Beam Melting (EBM)

Due to its simplicity of use in producing flawless metallic components, EBM has lately gained interest in the industrial industries. EBM, one of the metal AM technologies, has apparently been capable of fabricating complex products with no defects, especially when manufacturing porous structures with full density, specified external shapes, and interior designs based on Ti materials [330,331]. EBM is an established technology for producing metallic parts via a layer-by-layer approach as compared to other AM techniques [332]. In the production process, a quick-moving high-energy beam of electrons is used as a heating element [332]. It sweeps the powder bed and immediately melts powder, producing fully dense metallic components. Electromagnetic lenses are employed to guide the electron beam, ensuring that it is inertia-free. As a result, scanning velocities on the powder bed can increase to $10^5$ m $s^{-1}$ [213]. Considering Ti and aluminium metals have a high reactivity in contact with oxygen and nitrogen, the EBM manufacturing procedure is carried out in a vacuum chamber ($10^{-4}$–$10^{-5}$ mbar), which is particularly crucial for these metals [212]. Layer by layer, the sample is constructed with each layer passing through four procedures: Preheating, melting, dropping the construction plate, and 5) deposition a fresh layer of powder [212]. The samples are cooled to room temperature inside the equipment chamber after completion of the final layer [212].

#### 4.3.3. Directed energy deposition (DED)

While employing directed energy deposition (DED), a substance is introduced into the laser or electron beam's nozzles in order to melt and deposit it in accordance with the 3D design on the substrate. In the case of lasers or e-beams, the material is fed from a coaxial nozzle in the form of metallic granules or metallic wires. DED techniques allow greater compositional and design flexibility by utilizing different feeding nozzles within a single building project. Furthermore, with this approach, new components can be constructed as well as damaged components can be repaired [333]. In comparison to DED technologies (2000–4000 μm of beam size and 300–1000 μm for Laser Metal Deposition), PBF techniques are distinguished by a smaller beam size (50–500 μm for SLM and 140–250 μm for EBM) and smaller layer thickness (15–150 μm for SLM and 50–200 μm for EBM) [333]. Due to these advantages, PBF technologies enable an improved surface finish, but their application requires longer processing times. Thus, PBF is more recommended for small parts requiring high levels of precision and complexity while DED is better suited to large parts with a coarser finish [323].

Significant research has recently been conducted on metal additive manufacturing (AM) for a variety of alloy systems, particularly Ti alloys [11,334]. The majority of the studies on titanium alloys has gone into improving the processing conditions and powder feed stock, especially for Ti–6Al–4V (wt.%) as well as a few additional commercial alloys. The literature presently in publication has limited data on AM fabrication of metastable beta Ti alloys; however, a few recent investigations employing selective laser melting (SLM) and electron beam melting (e-beam) have been published [11,257,312,335,336]. The majority of this study has been devoted to enhancing processing parameters or assessing the associations between processing, structure, and properties of Ti–24Nb–4Zr–8Sn (wt.%) alloys, often referred to as Ti2448 alloy [257,258,335,337]. Due to its low modulus of elasticity and absence of components considered to be hazardous to humans, this alloy was designed for applications involving biomedical implants. Even though the Ti2448 alloy has a low modulus of elasticity that is about between 42 and 50 GPa, it is nevertheless higher than cortical bone and might potentially lead to stress shielding from an implant. A significant facet of this investigation is the creation of scaffolds with a high strength to elastic modulus. Scaffolds have the potential to further reduce the elastic modulus, becoming close to that of cortical bone. Nevertheless, the presence of Sn results in poor tensile and fatigue attributes since it may evaporate and cause defects to occur, such as porosity. In addition, studies conducted on this alloy showed that SLM and EBM need distinct ways to optimize and provide different microstructures and characteristics. This example shows how challenging it is to modify current beta Ti alloys for use in metal additive manufacturing. For Ti–Nb alloys, it was also demonstrated how mechanical characteristics might be tuned based on phase volume fraction and composition [336].

There are still many unanswered questions concerning metastable beta Ti alloys produced by metal AM, and it is expected that this will be a focus of substantial future study. To better comprehend the relationship between processing, structure, and property in metal AM, more study must be undertaken. The existing lack of understanding regarding the microstructure and characteristics of AM-processed metastable beta Ti

**Table 4**
Structural defects in metallic additively manufactured implants.

| | | | |
|---|---|---|---|
| **Geometric type** | Dimensional Inaccuracy | On the Strut | Waviness<br>Thickness<br>Varying Cross-section shape<br>Cross-section eccentricity<br>Over/under Size<br>Missing Strut |
| | | On the Node | Parasitic Node<br>Missing Node |
| | Surface Roughness | Raw Powder Particles on the Boundary of Strut | |
| | | Orientation based | Stair-stepping effect<br>Upward/downward facing surface |
| **Microstructural Type** | Porosity | Feed Stock | Pores exist in Feed stock powder<br>Pores created due to Feed stock oxidation |
| | | Processing Induced Pores | Metallurgical Pores<br>LOF and incomplete melting<br>Keyhole |
| | Material Property Imperfection | On Strut<br>On Node | |

**Table 5**
Defect minimization methods.

| | | |
|---|---|---|
| **Process parameter optimization** | Scanning Speed<br>Lase power<br>Hatching distance<br>Layer thickness<br>Powder morphology<br>Powder size<br>Powder size distribution | |
| **Post-processing** | Material Subtraction | Machining<br>Polishing<br>Chemical etching<br>Laser machining<br>Shot peening<br>Electro polishing |
| | Coating/ treatments | Heat treatment<br>HIP (Hot Isotactic Pressing)<br>Anodizing |
| **Design Strategies and defect Simulations** | Thickness Compensation Strategy<br>Design Constraints<br>Overhang elimination | |

alloys is impeding their implementation. AM causes fast cycle heating and cooling, which can lead to bulk flaws or non-equilibrium microstructures that may lack identical characteristics as traditional wrought alloys with the same composition. To have a good enough knowledge of how an alloy behaves in an application and during processing, extensive experimental characterisation is needed.

### 4.4. Additive manufacturing of beta titanium alloys

In recent years Additive Manufacturing (AM) has becoming as an innovative processing technology of materials. At the beginning, most of its main features were developed for polymeric materials due to the diversity, versatility, and low working temperatures [83,338]. However, ceramic, and metallic materials have been processing using AM despite the technological difficulties involved in forming these materials. Main studies of AM metallic materials are focused on preparation of metallic alloys powders, processing parameters of selected 3D manufacture technology, and final forming of the designed piece, which will be the determining parameter for the appropriate selection of AM technique, due to the high sintering or fusion temperatures of metals.

Nevertheless, the exponential development of metallic biomaterials for implantology, and the need to design devices with increasingly complicated and difficult to access topologies, drive the imperative use of additive manufacturing techniques as the best choice for this purpose. Titanium and its alloys continue to be the metals alloys par excellence for biomedical uses; therefore, many studies have been carried out to use commercially pure Ti and Ti–6Al–4V in different additive manufacturing technologies [83,339].

However, beta titanium alloys have been rarely used due to the high melting points of the stabilizing elements that, depending on the manufacturing technique used, will induce the formation of undesirable phases, and with it, incompatible mechanical properties for use in implantology [340]. Despite that, in 2011, Zhang et al. used Selective Laser Melting (SLM) to produce beta Ti–24Nb–4Zr–8Sn components with near full density (>99%) for the manufacture of a sample acetabular cup [106]. Shortly after, Liu et al. have used same beta Ti–24Nb–4Zr–8Sn (Ti2448) alloy to prepare scaffolds by Selective Laser Melting (SLM) technique and exploring processing parameters and final structures characterization as pores distribution, geometrical accuracy, and the mechanical properties of the produced components [312]. Furthermore, they have employed Electron Bean Melting (EBM) for the fabrication of porous scaffolds with nominal porosities of 67.9%, 72.5%, 75.0%, 77.4%, 79.5 and 91.2%, assessing mechanical properties of EBM substrates, including super-elastic properties, Young's modulus, compressive strength, and fatigue properties [337]. Additionally, same authors fabricated by EBM, Ti–24Nb–4Zr–8Sn substrates with 70 % porosity for deep understanding of processing-microstructure-property relationships of manufactured scaffolds, showing improving features compared to similar scaffolds fabricated with Ti–6Al–4V alloy [258]. In 2019, Ti–25Nb–3Zr–3Mo–2Sn was employed for the fabrication of substrates by Selective Laser Melting (SLM), achieving high strength and large tensile ductility [341]. More recently, Schaal et al. have employed Laser Powder Bed Fusion (L-PDF) fabricated beta Ti–22Zr–9Nb–2Sn samples to study mechanical properties via cyclic tensile tests that revealed an exceptionally high strain-hardening of prepared scaffolds [342].

In 2019, Hafeez et al. have used beta Ti–35Nb–2Ta–3Zr alloy for fabrication by Selective Laser Sintering (SLS) of tensile specimens for cyclic loading-unloading tensile testing, and microstructure evolution [343]. Afterwards with similar chemical composition, Yang et al. used beta Ti alloy Ti–35Nb–5Ta–7Zr (TNTZ) for the manufacture of scaffolds by Selective Electron Beam Melting (SEBM) reaching relative densities of >99.5%, and adding 2% of Si to improve wear resistance [344]. Moreover, biomedical Ti–30Nb–5Ta–8Zr (TNTZ) alloy have been studied by Luo et al., exploring mechanical properties, biocompatibility, and proteomics analyses of Selective Laser Melting (SLM) fabricated lattice structures [57]. Ti–35Nb–5Ta–7Zr scaffold was manufactured using Laser Power Bed Fusion (LPBF) which allowed simultaneous introduction of dislocations and twins into the alloy structure avoiding the strength–ductility expected relationship [345].

The group of Ackers et al. showed the potentiality of load-bearing implants fabricated by Power Bed Fusion (PBF-LB/M) of Ti-4.5Ta–4Fe-7.5Nb–6Zr (TTFNZ) alloy, studying processing parameters, mechanical and corrosion properties, as well as PVD coat-ability [346–348].

The use of Wire Arc Additive Manufacturing (WAAM) technique for the preparation of Ti–3Al–8V–6Cr–4Mo–4Zr (Beta-C or ASTM Grade 19) samples with high stability, high strength, and high quality of metastable β-titanium alloys free of segregation defects, known as β-flecks [117,349]. On the other hand, the use of Directed Energy Deposition (DED) technique for the fabrication of Ti–1Al–8V–5Fe scaffolds allow to tune the microstructure with adjustment of process parameters, to have required mechanical properties without any other processing steps [350]. Additionally, the additive manufacturing technique of Selective Laser Melting (SLM) was employed for the preparation of dense samples of Ti-X (X = Cr, Nb, Mo, Ta) with well-developed crystallographic texture, from mixture of pure metallic powders [351].

## 5. Structural and microstructural characterization

After manufacturing, and regardless of their fabrication route, the achieved microstructural characteristics must be evaluated and correlated with properties relevant to specific applications. Therefore, describing the processing-microstructure-properties relationship is crucial for designing, selecting, and improving materials, including β-Ti alloys. Among the most commonly used microstructural characterization techniques are X-ray Diffraction (XRD), Differential Scanning Calorimetry (DSC), Scanning Electron Microscopy (SEM), Electron Backscatter Diffraction (EBSD), Focused Ion Beam (FIB), Transmission Electron Microscopy (TEM), Neutron and Synchrotron Diffraction, and Atom Probe Tomography (APT). Thus, structural and microstructural characterization can be applied to β-Ti alloys produced by different fabrication routes (casting, powder metallurgy, additive manufacturing, etc.), including those where surface modification is applied to improve their biocompatibility. Fig. 18 illustrates the main techniques for structural and microstructural characterization of β-Ti alloys.

### 5.1. X-ray diffraction (XRD)

In order to characterize Ti alloys, X-ray diffraction (XRD) analysis is a crucial and fundamental tool. It allows for the identification and differentiation of potential phases that could form in alloys with a variety of compositions and β-stabilizing elements, including equilibrium α and β phases, and metastable ones: martensite α′, α″and nanoscale ω phases [352]. When using conventional XRD patterns for the analysis and characterization of Ti–35Nb–7Zr–5Ta and Ti–35Nb–7Ta alloys (TNZT) following aging heat treatments at various temperatures, the use of a broad Cu-$K_\alpha$ radiation ($\lambda = 1.54$ Å) without a monochromator can result in the superposition of peaks for β and β′ separated phases or even limit the detection of metastable nanometric ω phases when their fraction precipitated is less than 5% volume fraction reference. In the study by Ferrandini et al. [352], it can be observed that the XRD patterns mostly composed of the β -Ti phase do not significantly differ from one another when the Ti–35Nb–7Zr–5Ta alloy was aged at 200, 300, and 400 °C for 4 h after solution treatment at 1000 °C for 35 min and water quenching [352] (Fig. 19). However, when the Vickers hardness variation was evaluated for the Ti–35Nb–7Zr–5Ta alloy as a function of aging temperature (Fig. 20), it was observed that the hardness varies by 17% from the TNZT after solution (287 HV), rising to 336 HV after aging at 400 °C for 4 h. This raised the question of how the hardness was rising without a visible precipitation of metastable omega (ω) or equilibrium α phase. In order to detect phases in small volumetric fractions, such as the nanoscale metastable ω phase, one effective technique is to acquire X-ray

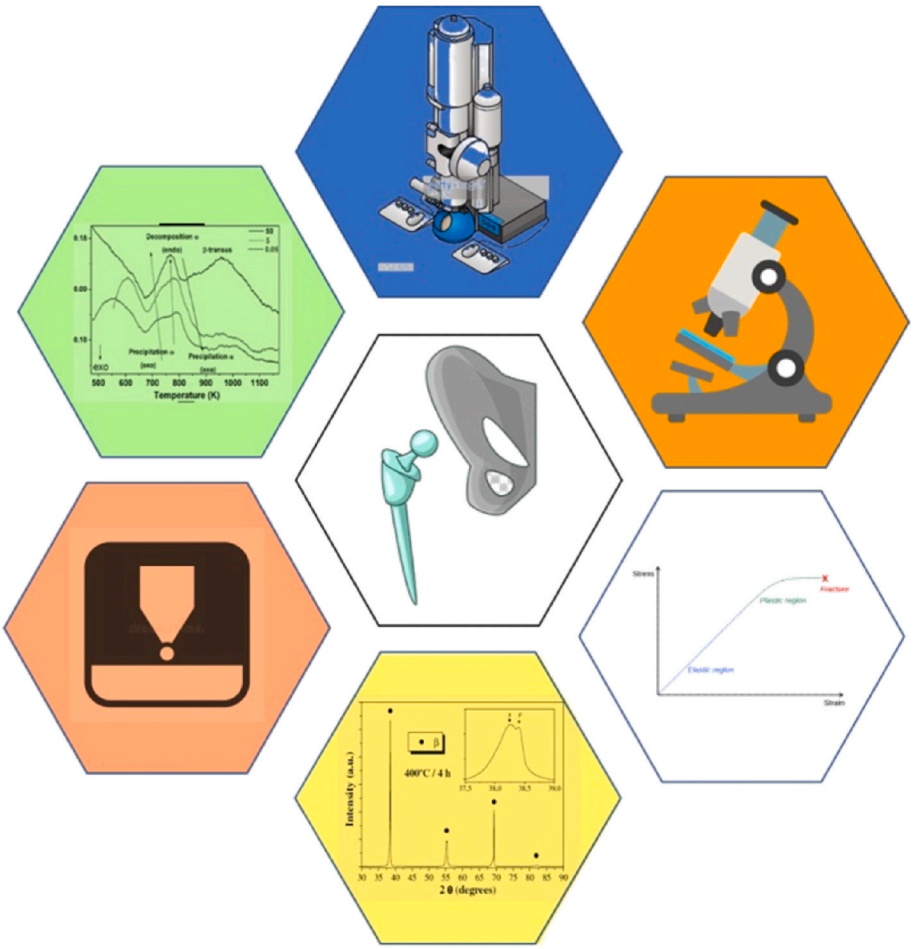


**Fig. 18.** Schematic illustration of main techniques for structural and microstructural characterization of β-Ti alloys.

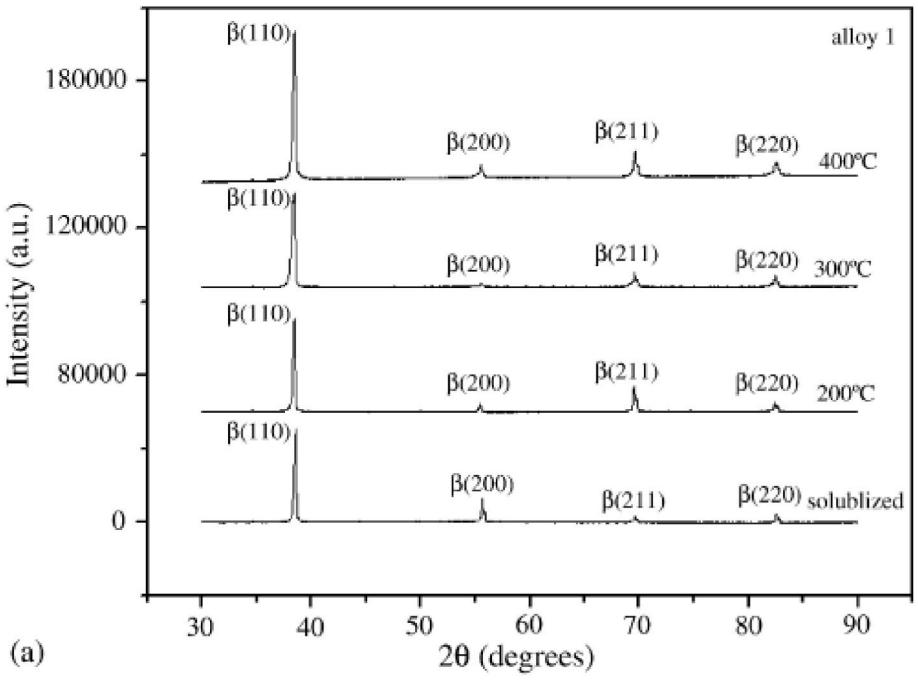


**Fig. 19.** The XRD patterns show that for samples that were aged and solubilized at certain temperatures up to 400 °C of (a) alloy I, only the β phase was developed [352].

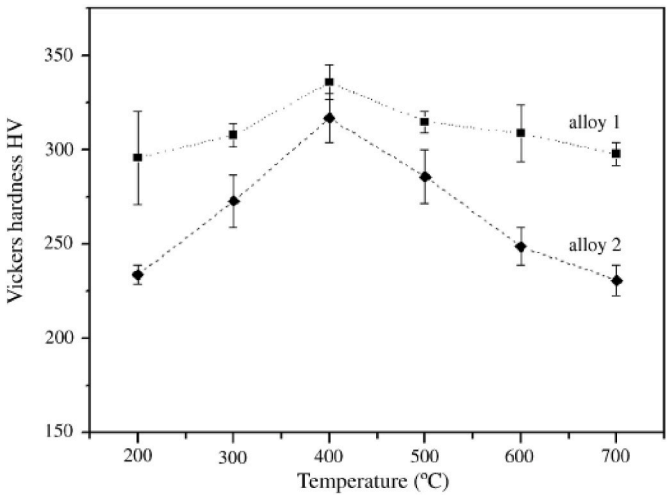


**Fig. 20.** Vickers hardness as a function of the aging temperature for Ti–35Nb–7Zr–5Ta (alloy 1) and Ti–35Nb–7Ta (alloy 2) [353].

diffraction (XRD) patterns using monochromatic synchrotron radiation Cu-$K_\alpha$ radiation ($\lambda = 1.54$ Å). Monochromatic synchrotron radiation can lower the detection limit for a given phase from the typical 5% volumetric fraction seen with traditional XRD equipment to about 1% [353].

Based on Ferrandini et al. [352], an XRD experiment was planned using monochromatic synchrotron radiation for samples after being air-quenched at 25 °C, and then aged for 4 h at 200 °C, 400 °C, and 600 °C. Using a double crystal Si (1 1 1) monochromatic radiation, the high resolution XRD studies were carried out at the D10B-XPD (polycrystalline X-ray diffraction) beamline at the old Brazilian Synchrotron Light Laboratory (LNLS) [353]. For example, a Ti–35Nb–Ta–Zr sample was aged at 400 °C for 4 h, and Fig. 21 displays the XRD pattern produced by synchrotron radiation on the sample. In the preliminary analysis, there seems to be only one phase peak per interplanar distance (or 2θ). Overall, as illustrated in detail in the right upper corner, when the peak (1 0 1) was magnified to x scale, a peak split could be seen, demonstrating β and β′ phase separation. A traditional bench Ni-filtered Cu-$K_\alpha$ XRD system was outperformed in terms of resolution by the synchrotron beamline's nearly parallel beam optics and monochromatic radiation. Furthermore, the high photon flux of the synchrotron beamline contributes to a higher signal-to-noise ratio (SNR), which facilitates the identification of small volumes of crystalline phases.

In solid solution binary diagrams, for example, the phenomena of phase separation, or spinodal decomposition, can occur when a single thermodynamic phase spontaneously splits into two phases without nucleation, each of which has a distinct phase with a different chemical composition. Neg. et al., studied the schematic binary phase diagram for a typical Ti alloy, such as the Ti–Nb diagram, with a preview of the metastable phases that will form during quenching. These phases include martensite α′ (hcp), martensite α″ (orthorrombic), nanoscale ω phase (athermal and isothermal) as well as β and β′ separated phases, depending on the amount of β-stabilizing element and heat treatment applied. As can be observed, complete stability of the β-Ti phase is also possible at high -stabilizing element content levels where spinodal decomposition occurs [354].

The work of Lopes et al. [355], produced a reduced-sized orthopedic implant of the β-Ti alloy (Ti–30Nb–2Sn) simulating an application and optimal condition with higher mechanical strength/hardness/elastic modulus in the proximal region of the implant (upper part) and lower elastic modulus/mechanical strength/hardness in the distal receptacle [355]. All of that, mapping the Vickers hardness (HV) and elastic modulus (E) in accordance with various heat treatment combinations imposed. The forged implant was then solution treated, water quenched, and aged to improve mechanical strength/hardness, resulting in stiffness graded implant. After attaining a lower elastic modulus/hardness condition, a heat treatment was performed on the proximal portion of the implant. The work of Lopes et al. [355], shows graded mechanical performance of the femoral stem, a Vickers hardness profile, and (b) X-ray diffraction patterns of the proximal and distal regions [355]. These patterns show a significant difference in elastic modulus, mechanical strength, and hardness in the different regions as a result of differential heat treatment to produce a stiffness graded implant. Regarding the use of XRD analysis in the advanced processing of Ti alloys from powder metallurgy samples with 5–10% porosity and grain sizes of tens of micrometers (50 μm), which transformed into a nanocrystalline material with just one deformation step through high pressure torsion (HPT), eliminating porosity and reaching nanoscale grain sizes in the range of 50–70 nm. The red and blue XRD patterns (after HPT) of Fig. 22 show that the peak β-Ti phase (bcc) peak intensity decreases with decreasing grain size (3 orders of magnitude), resulting in wider and lower peaks that are primarily visible at $2\theta = 56^o$ and $2\theta = 83^o$ [356,357].

In addition to bulk properties, XRD analysis is very useful for describing surface modifications made to β-Ti alloys through anodization, which result in the formation of $TiO_2$ nanotubes (NTs) and nanopores (NPs), which are initially amorphous (in the anodized condition)

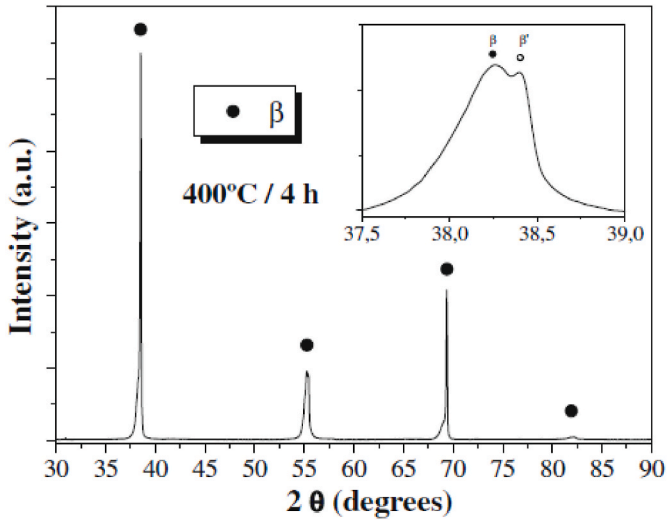


**Fig. 21.** XRD analysis performed using synchrotron radiation on a sample aged at 400° Celsius for 4 h[354].

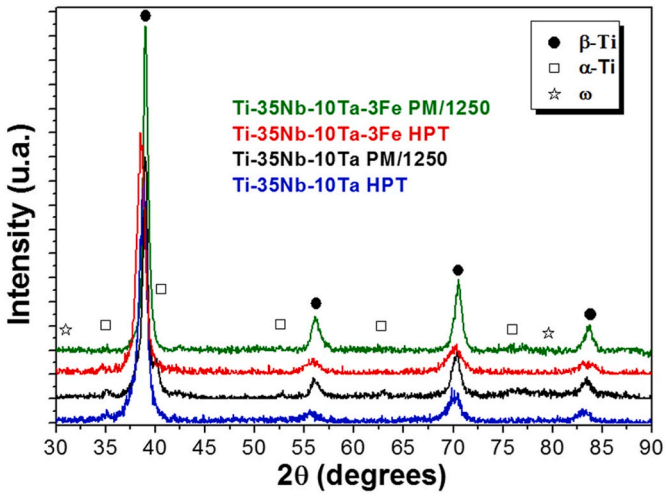


**Fig. 22.** Patterns obtained from XRD analysis of Ti35Nb10Ta and Ti35Nb10-Ta3Fe sintered at 1250 °C and then analyzed by HPT at room temperature (5 revolutions) at a pressure of 6 GPa [356].

and then crystallize into various allotropic phases of $TiO_2$ (A - anatase; R - Rutile) after heat treatment [358]. Fig. 23 shows the distinct nanostructures produced by the XRD patterns after anodizing a Ti–40Nb alloy in its as-anodized state and crystallizing at various annealing temperatures of 450, 550, and 800 °C.

Only diffraction peaks relating to the bulk Ti–40Nb alloy can be observed (α″ and β phases), as the nanostructured oxide layer that initially developed on the surface is amorphous. When $(Ti,Nb)O_2$ is annealed at 450 °C, the oxide nanostructure crystallizes as anatase. The martensite phase dissolves to generate the α" phase which is the typical for β-Ti alloys at these temperatures precipitation of metastable nanometric ω phase (2θ ~78°). The anodized layer changes to an anatase structure after annealing at 550 °C.

In Ti–40Nb alloy substrates at this temperature, only the β-Ti phase forms, indicating the dissolution of α and ω phases. At 800 °C, anatase transforms complexly into rutile, and there is the formation of $Nb_2O_5$, while in the bulk substrate, only the β-Ti phase is present in the Ti–40Nb alloy, indicating its stability at higher than T > 550 °C, suggesting that the β-transus temperature was reached and stability β phase formed.

### 5.2. Differential thermal analysis (DSC)

The DSC analysis for β-Ti alloys is a very powerful technique, which is not well applied and not frequently utilized by the researchers in this research field, and the same happens usually for metallic alloys. But, when applied in detail and optimizing operation parameters such as the sample mass (usually from 10 to 50 mg), heating and cooling hates (from 5 to 40 K/s) and the suitable extraction of the baseline, curve obtained with an empty crucible, just before analysis of the sample of interest itself, can result in very important information for the characterization of phase's precipitation, dissolution of previously precipitated phases, phase's transformation (β to α phase), among other details [359,360].

As an example, the DSC curves of Da Costa et al. shows a comparison of β Ti–30Nb and Ti–30Nb–1Fe (wt.%) alloys and the influence of Fe addition to phases formed and phase transformation temperatures. Quenched Ti–30Nb alloy typically forms β + α″ phases, and upon heating. Sample of Ti–30Nb alloy aged at 300 °C showed α″ → β transformation (endothermic) followed by another endothermic peak associated with ω → β transformation, at ~439 °C. At around 550 °C it can be seen one more peak from α phase nucleation (from ω precipitates acting as nucleation site). For sample aged at 600 °C, β-*transus* temperature was detected in the range of 614–752 °C. Comparing with Ti–30Nb–1Fe alloy, no significant α″ peak was detected, and first endothermic peak is related to isothermal ω phase precipitation at ~372 °C, while α precipitation starts around 510 °C [361].

Samples that have been solution treated (ST) and quenched are subjected to thermal analysis by DSC, which can be used as a reference to select the best aging heat treatment conditions. In this work, De Mello et al. [363]., proposed the identification of DSC peaks and phase transformations divided in temperature ranges denoted by 1, 2, 3 and 4, which makes the identification and association of phase transformations much easier. In DSC analysis of the work, the first heating cycle shows an endothermic reaction (1), corresponding to α″→ β martensitic decomposition to α″ → α + β, between 200 and 230 °C (determined by differentiating the DSC curve). Isothermal ω phase precipitation (β→$\omega_{iso}$) clearly shows an exothermic peak (2) ~300 °C. The ω phase dissolution appears as an endothermic peak between 430 and 500 °C (3), followed by α phase precipitation (4), beginning at 500 °C. Considering the Ti–Nb binary phase diagram the DSC results suggest the β-*transus* temperature around 640 °C with an inflection in the DSC curve near this temperature [362].

A recent work of Santos et al. [363], continuous cooling transformation (CCT) diagrams were obtained for β Ti–40Nb and Ti–12Mo–6Zr–2Fe (TMZF) alloys through DSC analysis combined with dilatometry test and other characterization techniques (XRD, SEM) followed by Vickers microhardness and elastic modulus measurements [363]. In the dilatometry test, the solution heat treated (at 1173 K for 10 min) cylindrical samples (∅ = 4 mm × 10 mm length) were stabilized in the β-Ti phase field, and then each sample was cooled under cooling rates (CR): 0.05, 0.5, 5.0, and 50 K/s. The heating and cooling rates adopted in the DSC analysis from 0.08 to 0.5 K/s are more limited than the ones of dilatometry test, but the DSC was used in order to compare data of phase transformations obtained by both techniques.

Fig. 24 shows DSC curves for stable β Ti–40Nb and metastable

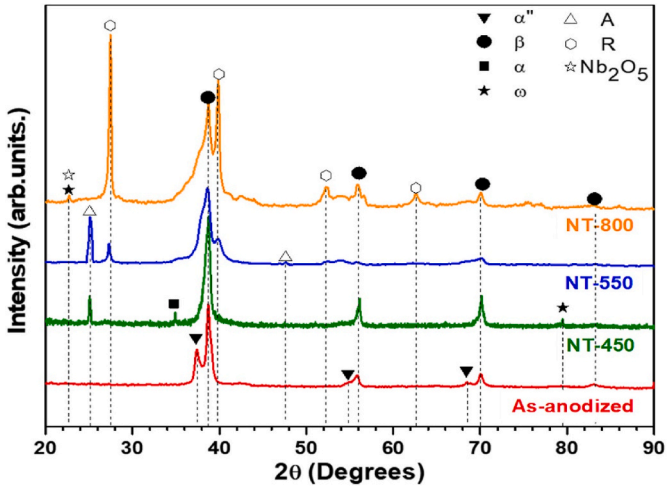


**Fig. 23.** XRD patterns of the as-anodized sample and nanostructures annealed at 450 °C, 550 °C, and 800 °C, A - Anatase; R - Rutile.

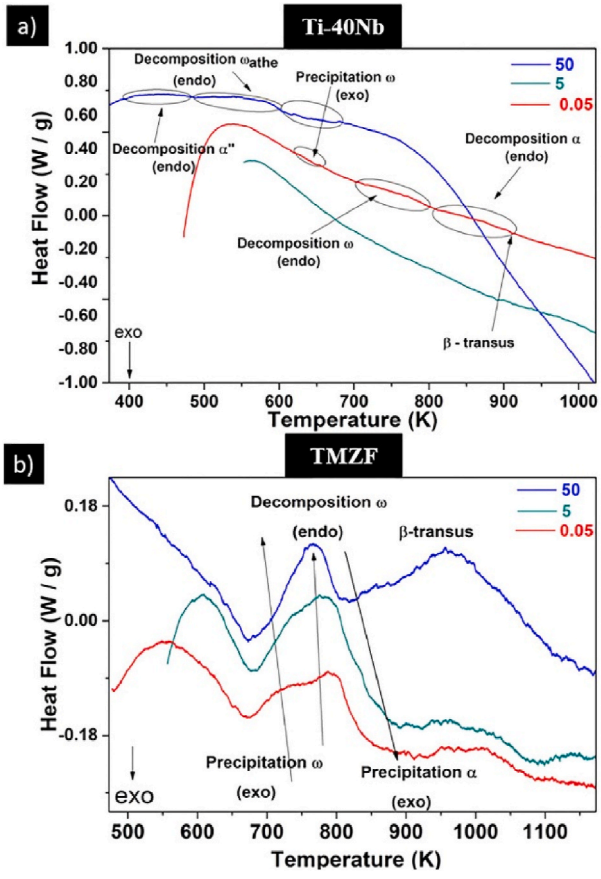


**Fig. 24.** Differential scanning calorimetry (DSC) analysis for both materials: (a) Ti–40Nb and (b) TMZF alloy. Subtle phase transformations were detected in Ti–40Nb [363].

Ti–12Mo–6Zr–2Fe (TMZF) alloys and the respective regions (temperature ranges) of phase transformations in the sequence of increasing temperature for β Ti–40Nb: decomposition of α″ martensite (α″→ β), decomposition of metastable athermal $\omega_{athe}$ nanoscale precipitates (ω → β), isothermal $\omega_{iso}$ precipitation (β → ω), decomposition of isothermal $\omega_{iso}$ ($\omega_{iso}$ → α), decomposition of α phase (α → β) and β-*transus* temperature. In this way, combining DSC analysis combined with dilatometry test and other characterization techniques, allowed the obtaining of CCT diagrams, which are very useful and rich in information regarding the phases that can be formed in β Ti alloys according with the cooling rate imposed from the high temperature filed (after solution heat treatment). It was confirmed in this work that the higher the cooling rate imposed (after heat treatment or upon solidification) the lower the elastic modulus obtained for stable and metastable β Ti alloys [363].

It is illustrated in Fig. 24b the variation of α phase precipitation according to variation of Nb from Ti–15Nb to Ti-22.5Nb (wt.%) and O additions of 0.15, 0.25 and 0.40 wt%, indicating a clear tendency of decreasing β → β + α transformation temperature.

### 5.3. Scanning electron microscopy – Electron Backscatter Diffraction (SEM-EBSD)

The scanning electron microscopy (SEM), an image technique with a resolution around ~1 nm or even lower in the modern microscopes, can provide images in secondary electrons (SE) with the best resolution for image of any kind of relief on the surface of sample (such as chemical etching). Backscattered electrons microscopy (BSE) is used to show chemical contrast of atomic number (Z) among phases with nanometric resolution Additionally, semi-quantitative chemical analysis of phases could be performed, using EDS (energy dispersive spectroscopy) down to 250–500 nm, line scan across an interface and, X-ray elemental mapping and crystallographic mapping of phases or texture combining with electron backscattered diffraction (EBSD) with resolution around 100 nm.

For β-Ti alloys, the SEM technique is very useful, and as examples of images and analysis that can be acquired: grain size measurement of β-Ti grains, α phase precipitates, α′ and α″ acicular martensite phases (usually down to 50 nm width) for bulk samples with different fractions of β-stabilizer elements such as Nb, Ta, Mo, Fe, and neutral elements such as Zr and Sn. Regarding surface treatments and modification, the SEM is very important to determine, using SE signal, pore diameter of micro-arc oxidations (MAO) treatment of β-Ti alloys generating porous oxide layer which are in the order of microns, according to Fig. 25 with MAO treatment of Ti–15Zr-xMo alloys [364].

One case of typical use of SEM-BSE images relies on α + β microstructures of the Ti-xNb-O alloys with different Nb contents: 15, 17.5, 20, and 22.5 wt% and oxygen contents: 0.15, 0.25, and 0.40 wt%), which SEM images are showed in this work of Lopes et al., where size of α phase precipitates decreases with increasing of Nb content (15–22.5 wt %) due to the higher stabilization of β-Ti phase (bcc), and size of α phase precipitates increases with increasing of O content (0.15–0.40 wt%) due to the stabilization of α phase (hcp) typical of oxygen addition [365].

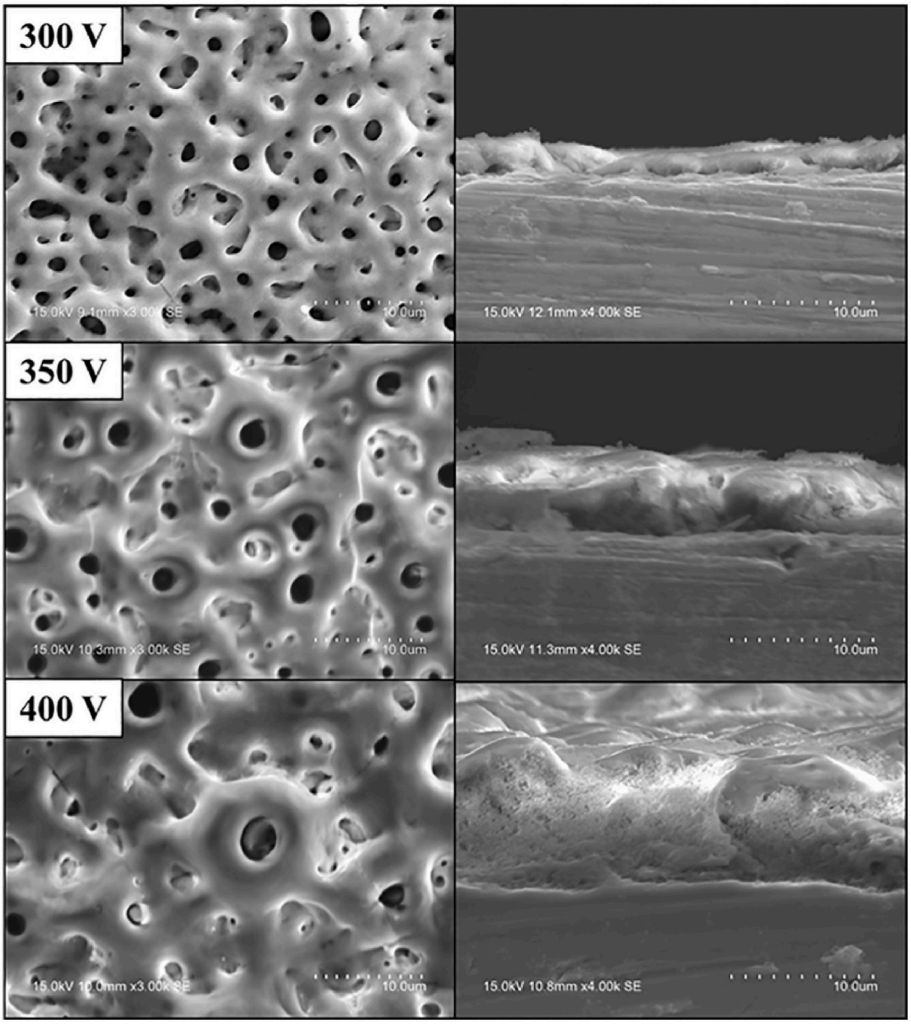


**Fig. 25.** Morphology and cross-section of MAO-treated Ti–15Zr alloy [364].

Another use of SEM in SE mode is the characterization using images and pore diameter measurement of anodization treatment of β-Ti alloys generating $TiO_2$ nanotubes of different nanostructures (nanopores or nanotubes) depending on anodization parameters such as voltage (V) and time (minutes). Usually the length (μm range) and diameter (hundreds of nm) increases with the increasing of voltage (V) and time of treatment [358]. Regarding the nature of $TiO_2$ oxide nanostructure, it is usually obtained in amorphous state in the condition as-anodized (just after anodization) and when submitted to annealing heat treatments activates the crystallization process which leads to formation of different allotropic forms of $TiO_2$ oxide (anatase and rutile) depending on heat treatment condition (time and temperature).

Related with same work and SEM images of Fig. 26, XRD patterns of Fig. 23 compares samples that have been annealed at various temperature to as-anodized samples [358]. One interesting point is that the composition of $TiO_2$ nanostructures follows in same manner, the composition of β-Ti alloy substrate, and that can be monitored with EDS analysis of nanotubes (see Fig. 27).

The resolution of EDS in the SEM (usually 0.5–1 μm) is improved a lot when it is used in the TEM (transmission electron microscope), which can reach 1 nm or even less, depending on the gun type ($LaB_6$ or FEG – field emission gun), voltage of microscope, and $C_s$ (aberration of condenser lens (depend on diameter of electron beam that can be generated) and it is strongly dependent on the TEM sample thickness. So, to measure more precisely the semi-quantitative composition of $TiO_2$ nanostructures the EDS on TEM (or STEM mode) is required, and the ideal preparation is separate the $TiO_2$ nanotubes and spread then in a carbon (5 nm amorphous layer) coated TEM copper grid in order to get just the $TiO_2$ nanotubes composition itself.

In a specific case of β Ti–Nb–Fe–Sn multicomponent ultrafine eutectic alloy, the microstructure is composed by fine intermetallic TiFe and $Ti_3Sn$ hard precipitates dispersed through a soft β-Ti matrix, generating a combination of low modulus and high strength β-Ti-based alloy, according to Fig. 28 with the microstructure, X-ray mapping of elemental distribution along the microstructure and X-ray pattern with peaks of phases described above. Regarding anodization of this type of ultrafine eutectic alloy, the $TiO_2$ nanotube produced is a multicomponent one, generating complex $(Ti,Nb,Fe,Sn)O_2$ nanotubes, confirmed by TEM image and followed by EDS analysis in Figs. 29 and 30 [366].

### 5.4. Focused ion beam (FIB)

The focused ion beam (FIB) with liquid Ga ion source (LIS) technique is a very powerful characterization tool in order to provide TEM samples (in-situ lifting method) of sample specific sites, such as interfaces between coatings and substrates, a grain boundary effect, an interface between a precipitate and a matrix, and so on. The MAO coating characterization by TEM is a very good example of FIB sample preparation application in order to characterize interface of MAO nanostructure and β-Ti alloy substrate. In the work of Correa et al. [364], a MAO-treated β Ti–15Zr–5Mo alloy sample was prepared by FIB, and the TEM analysis including HRTEM (high resolution TEM) in Fig. 31 shows a general view of MAO coating with a TEM image in bright field (BF) mode (Fig. 31 a), electron diffraction (ED) of different regions of MAO coating confirming amorphous and crystalline regions (Fig. 31 b) coexisting in the nanostructure of coating, and HRTEM micrograph of the nanocrystalline region of coating with different atomic planes delimited by nanocrystalline phases (Fig. 31 c) [364]. Finally, Fig. 31 c present EDS measurements of different coating regions (I, II and II) with Ca, Zr and Mo, confirming substrate rich composition (Mo and Zr) and Ca rich regions typical of MAO coating produced in a Ca-rich electrochemical solution.

Fig. 32 illustrates a crystallographic orientation mapping through ASTAR technique of MAO film formed in the Ti–15Zr–15Mo alloy grown with a limiting voltage of 400 V. The amorphous area I is represented as a smooth layer (~150 nm) above the substrate in the virtual brilliant field (VBF) image (Fig. 32a). The presence of the nanocrystalline region II is above the dashed lines. The same amorphous phase-related smooth layer (region III) could well be seen at the top of the image. Amorphous phases, which at the nanoscale have homogenous compositional structure, are characterized by the lack of contrast in the smooth area [367]. In Fig. 32b and c, in relation to the index quality of the phase identification, the index and reliability images, respectively, are displayed.

Fig. 33 shows another great utility for the FIB *in-situ* sample preparation for TEM analysis, is the sample preparation of cross-section of thin films, and recently the number of works in the literature of thin films of β-Ti alloys obtained by sputtering and similar techniques, increased significantly. In this way, in order to characterize such β-Ti alloys thin films, the FIB sample preparation for TEM analysis is a main issue in order to obtain grain size of nanoscale β-Ti phase, growth morphology of such grains (columnar, equiaxed or V-shaped) depending on parameters of thin films deposition and the final thickness of film obtained, which can vary from tens to hundred of nanometers up to micron scale thick. As an example, the work of Gonzalez et al. present TEM and STEM images of FIB sample of thin films cross-section for different β-Ti alloys: $Ti_{80}Nb_{15}Mg_5$, $Ti_{77}Nb_{15}Mg_8$, $Ti_{69}Nb_{15}Mg_{16}$ and $Ti_{60}Nb_{15}Mg_{25}$ coatings onto stainless steel [368].

As an additional complementary technique to TEM analysis of thin films cross-sections by FIB, ASTAR crystallographic orientation mapping can be used to characterize thin film nanoscale grains and possible presence of orientation growth textures.

Consequently, the changes in mobility and the variation in magnesium content have also a significant effect on the morphology and texture of thin film coatings. Fig. 34 displays the ACOM maps for the (a) $Ti_{80}Nb_{15}Mg_5$, (b) $Ti_{77}Nb_{15}Mg_8$, (c) $Ti_{69}Nb_{15}Mg_{16}$, and (d) $Ti_{60}Nb_{15}Mg_{25}$ coatings, showing inverse pole figure (IPF) coloring for the z-represents the coating with the lowest magnesium content ($Ti_{80}Nb_{15}Mg_5$), Fig. 34 (a) shows a crystallographic texture $\{2\ -1\ -1\ 0\}_\alpha$ for the α phase and a $\{111\}_\beta$ texture for the β phase. A change to random growth is brought about by an increase in Mg quantity, mostly for the phase and to a lesser

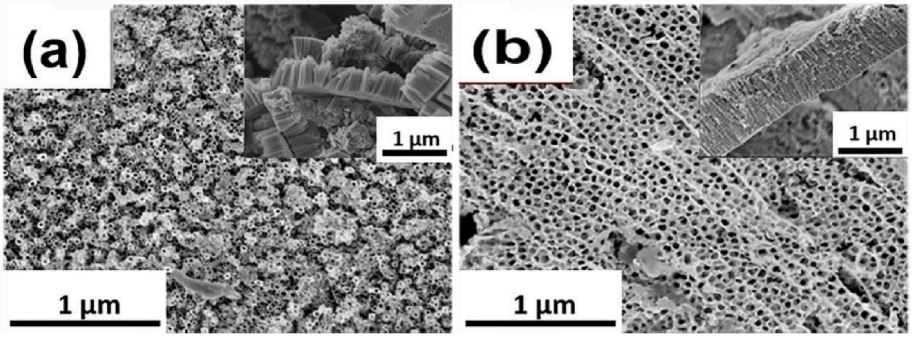


**Fig. 26.** Anodized nanostructures as viewed through a SEM (a) at 10V (NTs) and (b) at 20V (NPs). A cross-sectional view of the $(Ti,Nb)O_2$ nanostructure is shown in the insets.

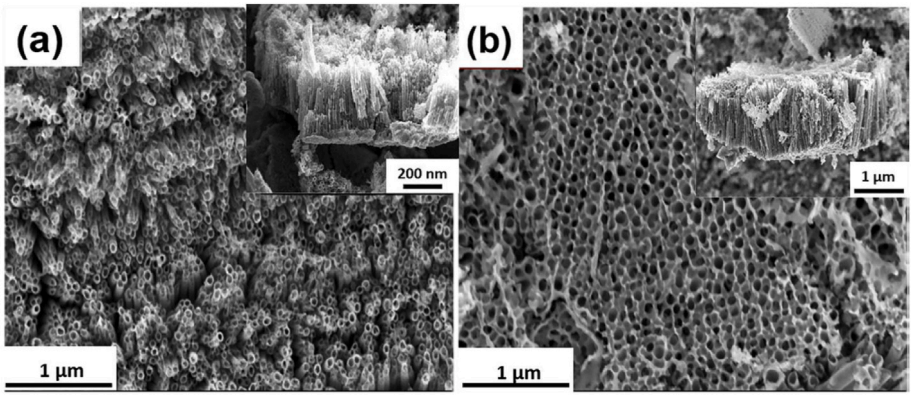


**Fig. 27.** SEM micrographs of top views of samples annealed at 550 °C (a) nanotubes (anodized at 10V) and (b) nanopores (anodized at 20V) [358].

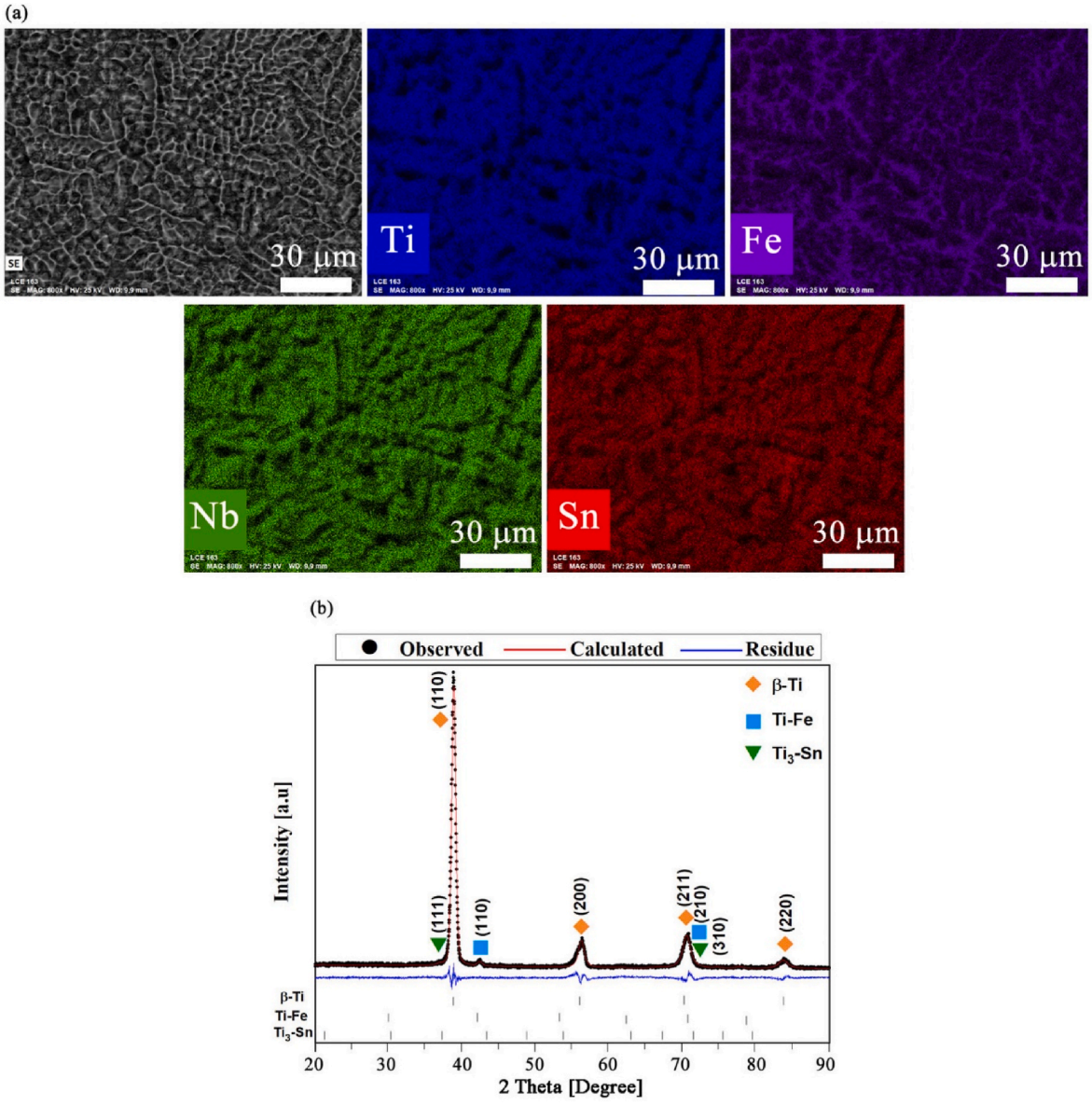


**Fig. 28.** (a) SEM micrograph in BSE mode and X-ray elemental mapping through EDS analysis showing the distribution of Ti, Fe, Nb, and Sn. (b) XRD pattern of TNFS alloy showing experimental pattern (black dotted), calculated (red line) and their difference (blue line) [366]. (For interpretation of the references to color in this figure legend, the reader is referred to the Web version of this article.)

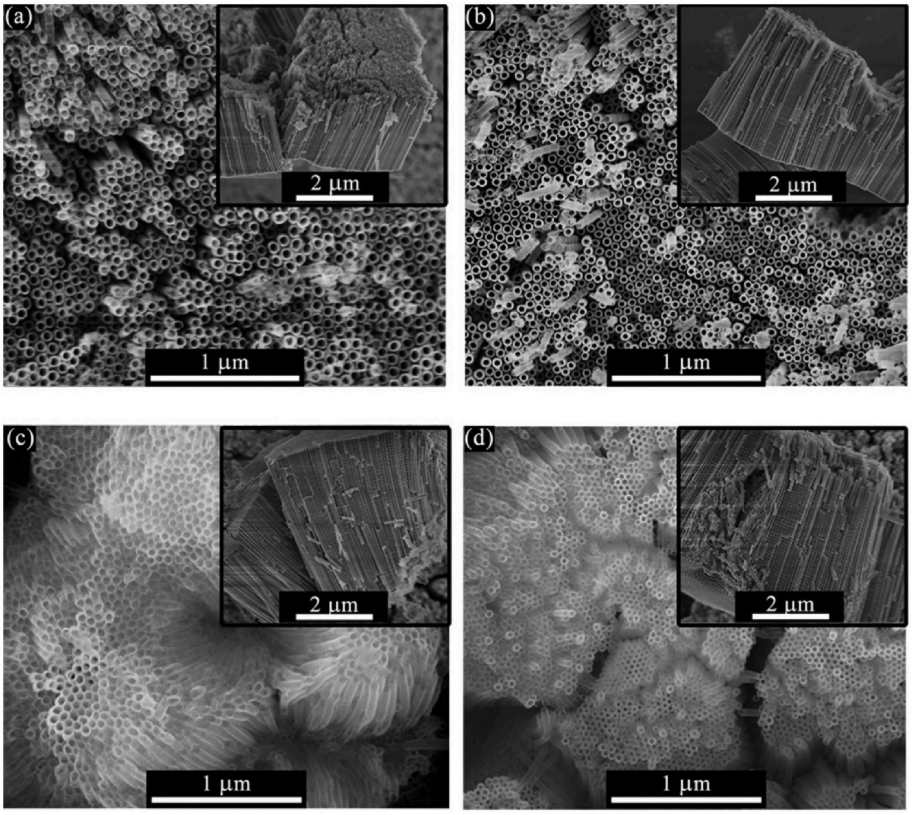


**Fig. 29.** SEM of morphology variations in the $TiO_2$ nanotubular structure as a function of anodization time at 20 V during (a) 6, (b) 12, (c) 24, and (d) 48 h [366].

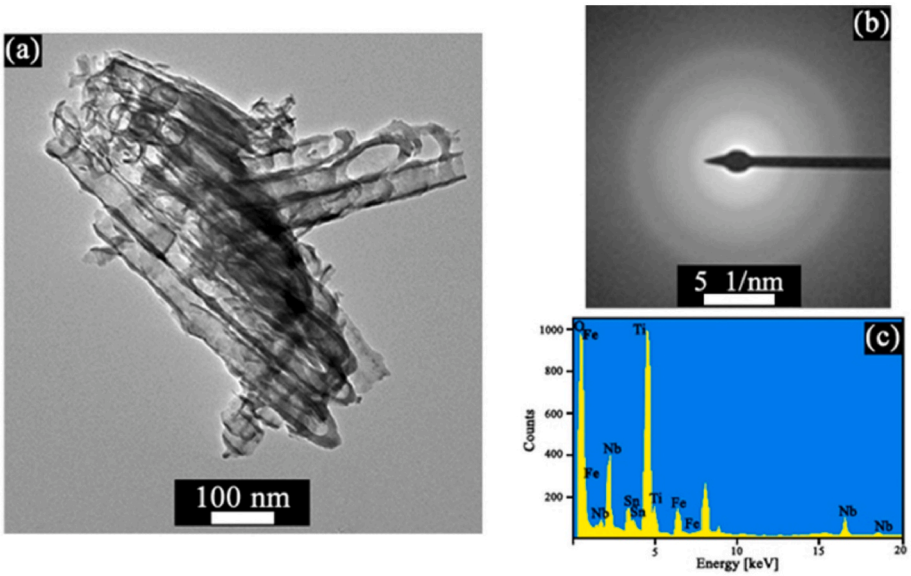


**Fig. 30.** Representative (a) TEM bright field (BF) image of $TiO_2$ NTs in the as-anodized condition at 6 h/20 V, with NTs morphology in the amorphous state and (b) the corresponding selected area diffraction (SAD) pattern typical of amorphous structure and (c) multicomponent $(Ti,Fe,Nb,Sn)O_2$ composition obtained from the EDS spectrum [366].

extent for the β phase.

### 5.5. Transmission electron microscopy TEM

The transmission electron microscopy (TEM) technique is very important in the materials science and engineering, and in the research field of β-Ti alloys it is even more important, due to nanoscale omega phase precipitation, which occurrence in β-Ti alloys can damage mechanical properties due to fragile character of ω phase in such alloys microstructure. Besides that, TEM characterization can identify α phase in micron and nanoscale, α′ martensite phase (hcp), α″ martensite phase (orthorhombic), and more complex phase transformation, such as β and β′phase separation by spinodal decomposition, which occurs in nanoscale and just can be identified with a combination of XRD and TEM

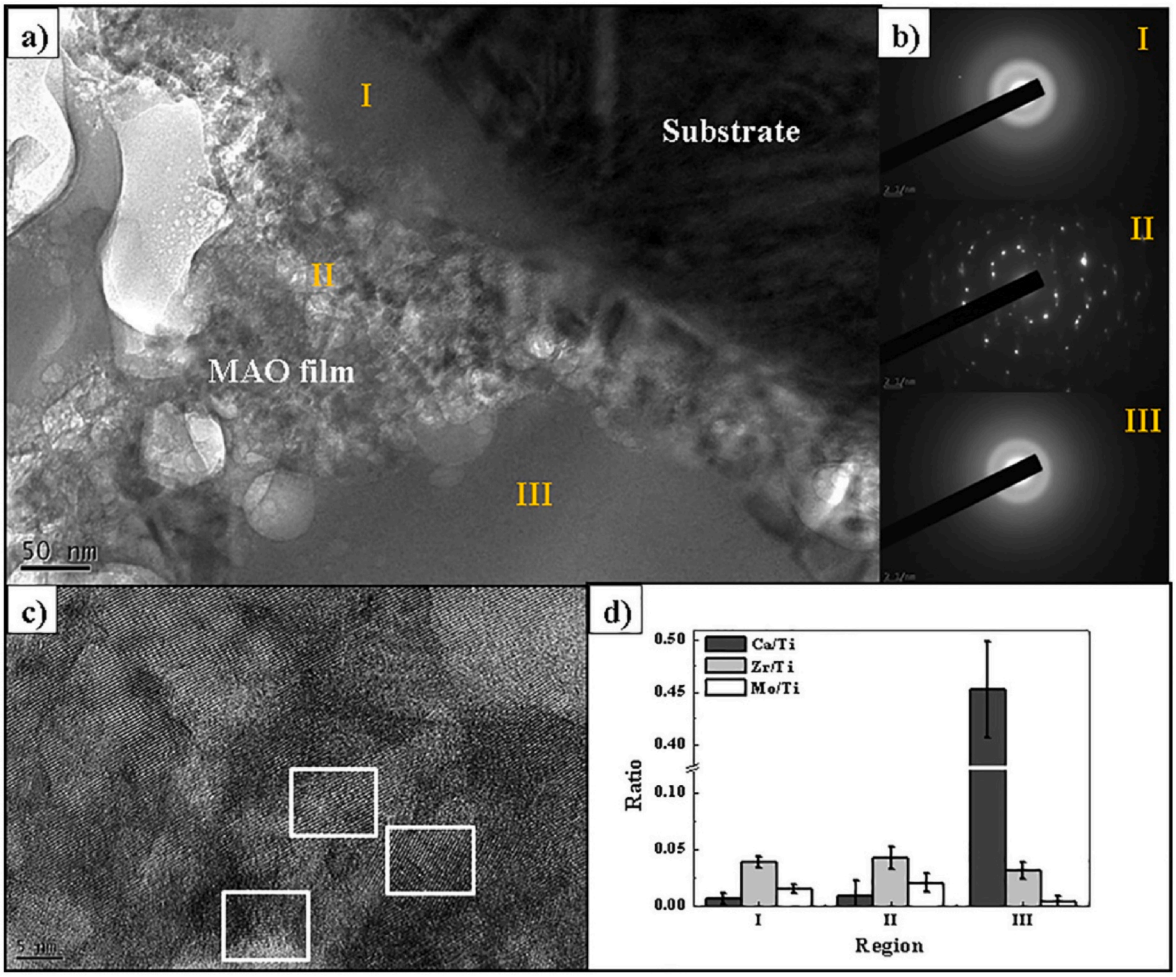


**Fig. 31.** TEM analysis of MAO-treated Ti–15Zr–5Mo alloy at 400 V: a) Interface film-substrate; b) SAED patterns of the distinct regions of the film; c) HRTEM of the nanocrystalline region of the film; d) chemical ratio of the elements along the film [364].

analyses, as showed previously in the XRD topic of this review and in the work of Afonso et al. [369].

The phase separation by spinodal decomposition in β and β′phases is displayed in Fig. 35for Ti–35Nb–7Zr–5Ta alloy aged at 400 C for 4 h. Fig. 35 a illustrates TEM image in bright field (BF) mode and the absence of α phase precipitation along the grain boundary of β-Ti grains. Fig. 35 b presents in detail the interior of β-Ti grain at the $[1\ 1\ 1]_{\beta}$ zone axis revealing diffraction contrast between the β (dark) and β′(bright) separated phases. Even in conventional TEM image, is already possible to have a good indicative of phase separation by spinodal decomposition in β-Ti alloys [369]. Increasing the magnification and reaching high-resolution transmission electron microscopy HRTEM images, as is observed in Fig. 36 for the Ti–35Nb–7Zr–5Ta alloy aged at 400 C for 4 h, is possible to detect different crystallographic phases. Fig. 36 b shows a HRTEM image along the $[1\ 1\ 1]_{\beta}$ zone axis. The respective Fourier transform (FT) reveals splitting of the $(1\ 0\ 1)_{\beta}$ reflections (white arrows). A schematic representation of the Fourier space map of the $[1\ 1\ 1]_{\beta}$ zone axis obtained from simulation using the JEMS© software includes separated phases with cubic (bcc) and tetragonal (BCT) structures [369].

In a recent work of Afonso et al. [356], Fig. 37, the conversion of porous powder metallurgy (PM) sample of β-type Ti35Nb10Ta and Ti35Nb10Ta3Fe alloys of tens of microns grain size to tens of nanometers grain size in 100% dense (no porosity) in just one step of severe plastic deformation (SPD) step through HPT (high pressure torsion). The TEM analysis combined with ASTAR crystallographic orientation mapping through ASTAR technique was a fundamental combination of characterization tools in order to determine nanoscale grain size of β-Ti alloys after HPT processing, because just TEM convention BF image can not detect neither determine clearly the grain size (and respective grain boundaries). In this way, ASTAR was used in order to determine as a more accurate way the nanoscale grain size, which is one of the main applications of ASTAR technique [356].

As can be seen in the TEM image Fig. 38 and respective SAD pattern for the PM sample of β Ti35Nb10Ta and Ti35Nb10Ta3Fe alloys, the occurrence of nanoscale metastable ω phase can be detected clearly in the right zone axis, showing an orientation relationship $[1\ 1\ 0]_{\beta\text{-Ti}}//[1\ 1\ 2\ 0]_{\omega}$ between the β-Ti matrix and metastable ω phase for both alloys. Regarding β Ti alloys after HPT processing with nanoscale grain size, the SAD pattern confirms typical ring-shaped patterns of nanocrystalline materials and in agreement with electron diffraction results, the ASTAR technique complementary determines nanoscale grain size of HPT sample.

The TEM analysis is important as well, to characterize in nanoscale and also atomic scale, the structure and nature of $TiO_2$ nanotubes (NTs) formed, amorphous or (nano) crystalline. In the work of Chaves et al. [366], TEM images, Fig. 39, is showed in bright field (BF) mode of $TiO_2$–based NTs formed in the anodization of Ti–Fe–Nb–Sn alloy anodized to 6 h/20 V and annealing at (a) 400 °C (b) 450 °C (c) 500 °C [366]. Besides that, corresponding high-resolution transmission electron microscopy HRTEM images (atomic scale) and respective selected area diffraction (SAD) patterns in each annealing condition were fundamental in order to define amorphous halo (characteristic of amorphous phase structure formation) and diffraction spots of anatase–rutile phases in the crystallized sample after heat treatment. It is worth to mention,

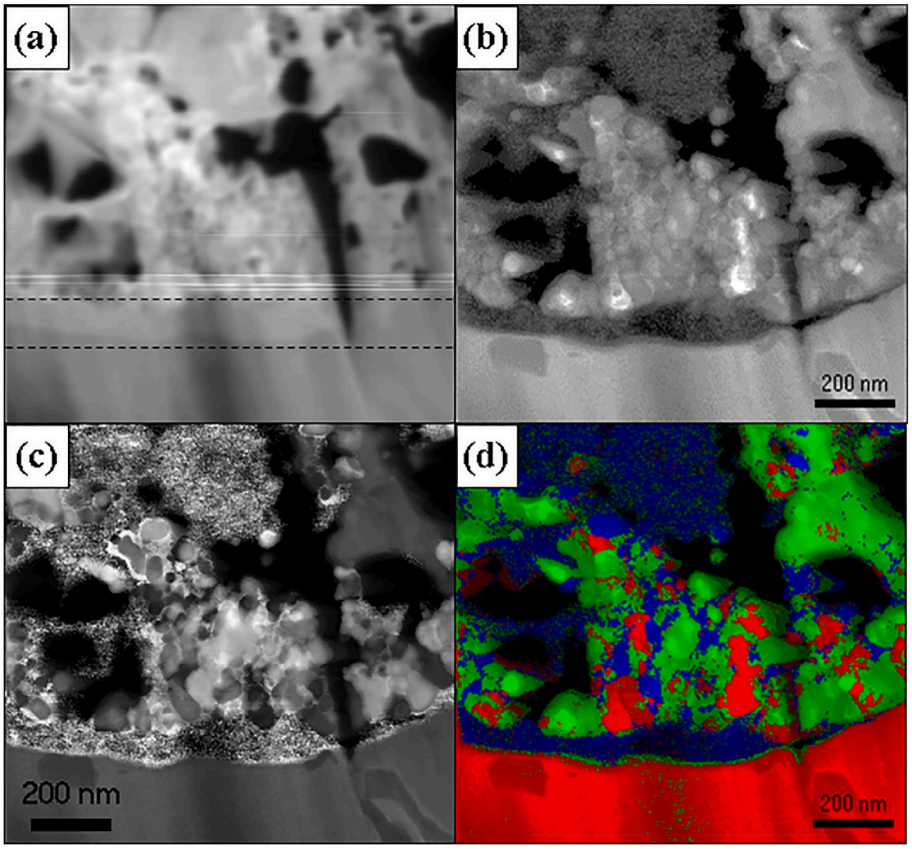


**Fig. 32.** ASTAR analysis of Ti–15Zr–15Mo alloy: a) virtual bright field (VBF) micrograph, b) Index image, c) Reliability, d) phases (red: β-Ti matrix, green: anatase $TiO_2$, blue: rutile $TiO_2$), f) mixed image of phases and index [367]. (For interpretation of the references to color in this figure legend, the reader is referred to the Web version of this article.)

that just very few works in the literature show the TEM analysis of $TiO_2$ NTs, and the sample preparation can be much easier, just spread the nanotubes from the anodized sample over the TEM carbon coated (holey carbon type) copper grid with the aid of a metal blade.

### 5.6. Neutron and Synchrotron Diffraction

Neutron and synchrotron diffraction techniques are powerful tools for investigating the structural features of materials. In particular, they provide insights into atomic-scale structures, defects, residual stress, as well as physical, chemical and mechanical behaviors of alloys, surpassing the capabilities of more conventional techniques [370–372]. Neutron diffraction is based on the interaction between neutrons and the atomic nuclei of the studied materials. Specifically, when a neutron beam interacts with a material, the neutrons are scattered by the nuclei in a pattern that depends on the crystal structure [370,371]. This means that, this scattering pattern can be analyzed to determine the crystallographic texture, lattice parameters, phase content, lattice strain, and atomic positions [370,373]. Neutrons, being uncharged particles, have high penetration depths, making neutron diffraction particularly useful for studying bulk properties and structural features of materials [371]. However, neutron diffraction may not be an appropriate selection for all β-Ti alloys. This is because, the very negative bound coherent scattering length of Ti (−3.438 fm) combined with the positive bound coherent scattering lengths of all chemical elements with atomic numbers higher than 27, may produce insufficient reflections for the scattering pattern to be analyzed. This is because the scattering cross section, i.e., the effective area interaction between the atomic nucleus and the passing neutron, is a function of the scattering length of the alloying elements [371].Weak nucleus-neutron interaction means small scattering signals. Examples of β-stabilizers with very positive scattering lengths are Fe (9.45 fm), Ni (10.3 fm), Mo (6.715 fm), Cu (7.718 fm), Nb (7.054 fm), Ta (6.91 fm), Hf (7.7 fm), etc. [370,374]. Consequently, there are limited reports of neutron diffraction on β-Ti alloys, such as Ti–10V–2Fe–3Al, Ti–12Mo, and Ti–15Mo [375–377], mainly alloyed with a limited quantity of elements with positive bound coherent scattering lengths or with other negative bound coherent scattering lengths elements (such as V of −0.3824 fm). Therefore, the rest of this section will be focused on synchrotron diffraction.

Synchrotron diffraction utilizes highly energetic X-rays generated by synchrotron light sources. Specifically, these X-rays are produced when charged particles, typically electrons, are accelerated to nearly the speed of light and forced to travel in circular paths [372]. As a result, the resulting X-rays can be tuned to specific energies by a monochromator that selects the desired wavelength. Furthermore, synchrotron X-rays interact primarily with the electron cloud surrounding atoms, providing detailed information about the electron density and atomic arrangements in the material with a high spatial resolution. In addition, this technique is especially useful for studying surface and near-surface phenomena and can detect subtle changes in electron density, such as those associated with defects, dislocations, and phase transformations [378]. Moreover, the hutches, i.e., radiation shielding, do not require a high vacuum, allowing material testing under different environments [372]. Consequently, synchrotron diffraction, with its high resolution and rapid data acquisition (faster than neutron diffraction), is well-suited for studying fine-scale features, including thin films, nanomaterials, and interfaces [372,378]. Additionally, it can also be used to study dynamic processes such as phase transformations and deformation mechanisms in real time. However, its limited penetration depth and sensitivity to surface effects can be a disadvantage when studying bulk

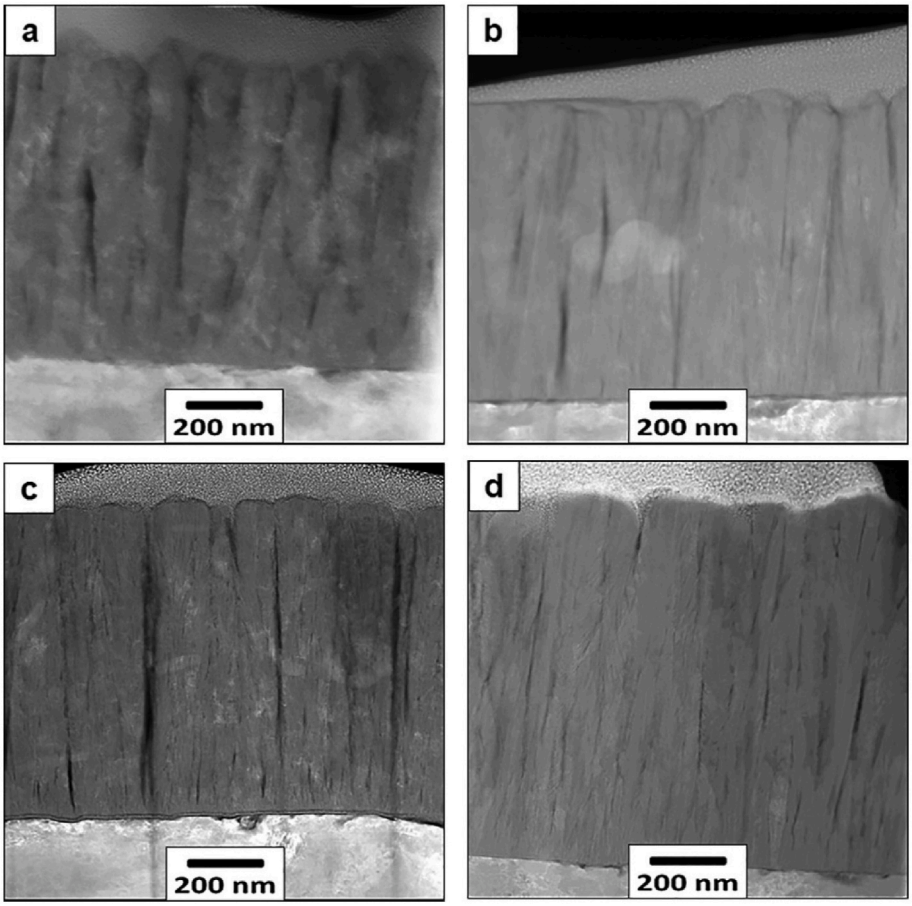


**Fig. 33.** STEM-ADF micrographs for the (a) $Ti_{80}Nb_{15}Mg_5$, (b) $Ti_{77}Nb_{15}Mg_8$, (c) $Ti_{69}Nb_{15}Mg_{16}$, and (d) $Ti_{60}Nb_{15}Mg_{25}$ coatings showing their general microstructures [368].

properties.

In particular, in-situ studies are one of the most powerful applications of synchrotron diffraction, allowing to observe real-time structural evolution under varying conditions. Several in-situ studies have focused on the β-to-α'' transformation of Ti–24Nb-0.5 N and Ti–24Nb-0.5O [379], Ti–17Nb–1Fe and Ti–17Nb–2Fe [380], Ti–17Nb [381], Ti–24Nb–4Zr–8Sn [382], Ti–30Zr–10Nb [383], Ti–12Mo [384], and Ti–5Al–5Mo–5V–3Cr β-Ti alloys [385], sometimes correlating them to the superelastic properties given by the strain-induced martensitic transformation [379,382], the high plasticity with ultra-low strain hardening [383], or with ω-phase generated during aging [380]. Furthermore, the dynamic and static mechanisms of microstructural restoration during hot working and heat treatments have been studied in Ti–6Al–4V alloy [386]. Furthermore, synchrotron X-ray computer tomography can provide imaging of bone/implant contact through their different X-ray absorption [387], as well as assist in fractography analyses of β-Ti alloys [388]. The latter one found a preferred preferential cracking starting at the β phase [388].

In addition, in-situ synchrotron diffraction has been employed to investigate the deformation mechanisms and texture evolution of β-Ti alloys under mechanical loading. These studies help in understanding the alloy's behavior at the microstructural level, including the role of dislocations, twinning, and phase transformation in enhancing mechanical properties like strength and ductility. Future research may focus on real-time studies of β-Ti alloys in simulated physiological environments or with rigs simulating the stress state received by different human body parts.

### 5.7. Atom Probe Tomography (APT)

Atom probe tomography is a nanoscale characterization technique that allows for the 3D mapping of chemical composition at the atomic scale. APT operates based on the principles of field evaporation, where atoms are ionized and then projected onto a detector to reconstruct a 3D image of the sample [389–391]. Specifically, the high electric field applied to a sharp needle-shaped specimen (tip radius <100 nm) causes surface atoms to evaporate as ions, which are then accelerated toward a detector [389]. By measuring the time of flight (TOF) of these ions, their mass-to-charge ratio can be determined, allowing the chemical identity and distribution of individual atoms to be reconstructed in 3D.

Moreover, APT is particularly advantageous for detecting and analyzing trace elements, precipitates, and solute clusters that are often critical to the performance of these alloys. APT is sensible to chemical elements in the range of parts per million, including light elements such as hydrogen, carbon or lithium [391]. However, among the limitations of APT is the requirement for specimens to be in a needle-like shape, which can be difficult to prepare [389]. Additionally, the analysis is typically confined to a small volume of material, which might not be representative of the entire sample.

In the context of biomedical Ti alloys, APT was first used to study a bone/titanium implant interface providing knowledge on the Ca-enriched chemical distribution required for osseointegration [392]. Furthermore, 4D (3D plus chemical composition) APT has also been employed to study the distribution of other elements and compounds like Ti, TiN, C, Mg, P, Na, and TiO at the bone/Ti-implant interface [393].

Additionally, APT studies have also been useful in determining that

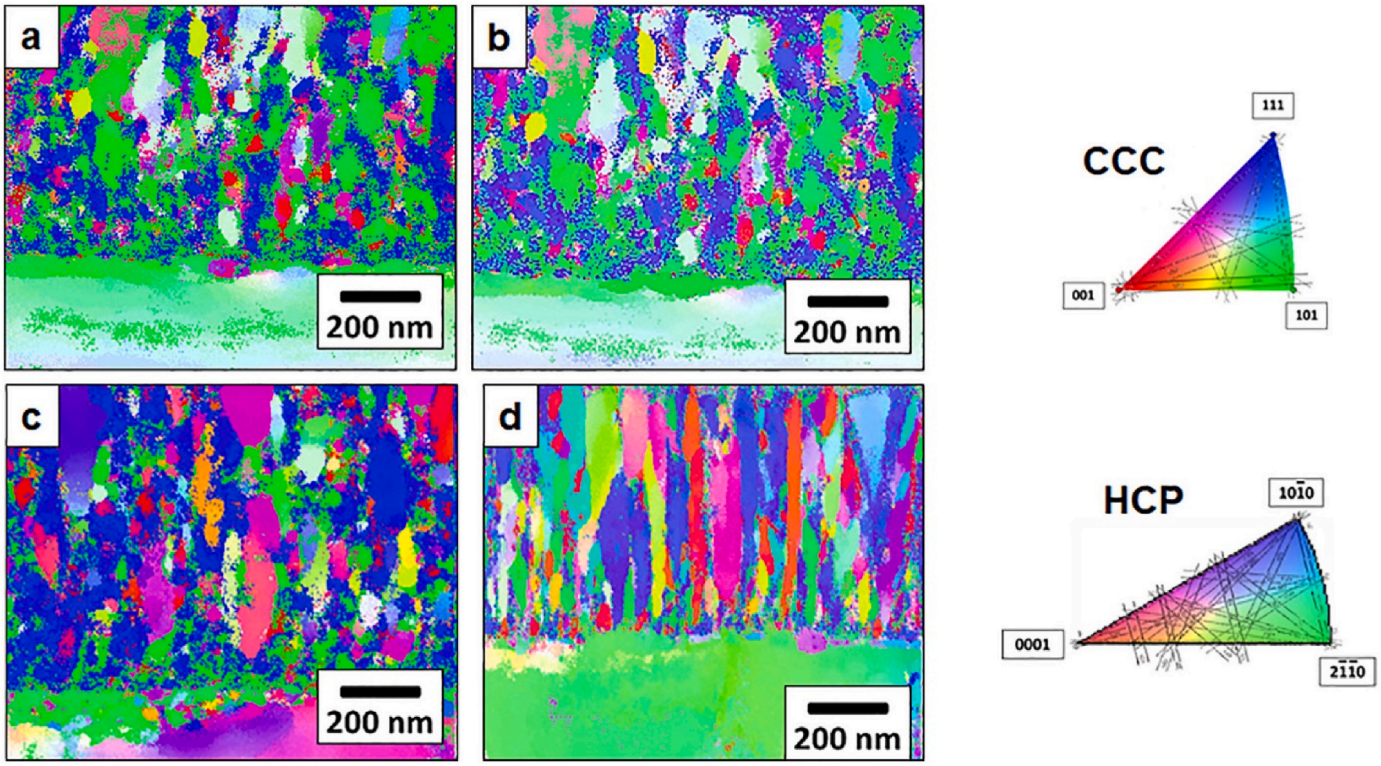


**Fig. 34.** ACOM maps obtained by ASTAR for the (a) $Ti_{80}Nb_{15}Mg_5$, (b) $Ti_{77}Nb_{15}Mg_8$, (c) $Ti_{69}Nb_{15}Mg_{16}$, and (d) $Ti_{60}Nb_{15}Mg_{25}$ coatings showing inverse pole figure (IPF) coloring for the z-axis [368].

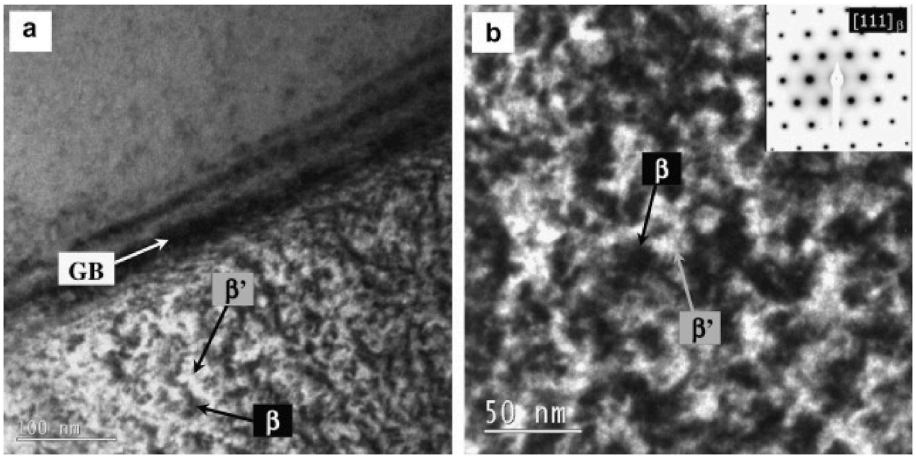


**Fig. 35.** Ti–35Nb–7Zr–5Ta alloy aged at 400 °C for 4 h. (a) TEM bright field (BF) images showing the absence of a phase precipitation along the grain boundary. (b) Detail of the grain interior at the $[1\ 1\ 1]_\beta$ zone axis revealing diffraction contrast between the β (dark) and β′(bright) phases [369].

high laser pulse energies are not appropriate for studying nanoscale precipitation in Ti-alloys because they encourage the formation of complex molecular ions, cause spectral peak overlapping, and complicate data analyses [394]. Therefore, smaller laser pulse energies are recommended to study precipitation of, for example, ω phase in β-Ti alloys. This work also elucidated that aging time increases the Al and O (α-stabilizers) enrichment at the ω-precipitate/β-matrix interface, decreasing the α nucleation barrier and acting as α nucleation site in the Ti–5Al–5Mo–5V–3Cr wt% (Ti-5553) β-Ti alloy [394]. Moreover, the formation of ω-phase embryos from compositional and structural instabilities β-Ti alloys was observed by APT and TEM, showing that β-to-ω phase transformation involves displacive and diffusional mechanisms [395].

Other works on β-Ti alloys have exploited APT to describe the chemical composition differences or evolution during thermo-mechanical processing to correlate them to different mechanical, chemical, or physical properties. For example, the chemical composition during precipitation evolution has been studied in an aged Ti-5553 β-Ti alloy, providing information on the varying chemical distribution among the isosurface, precipitate core, and matrix [396]. Similarly, the solute distribution at α-precipitates and β-matrix was also studied and correlated to the high strength of a hierarchical Ti–1Al–8V–5Fe (Ti185) alloy [397]. In addition, the microstructural evolution of biomedical Ti–24Nb–4Zr–8Sn (Ti-2448) alloy during aging has also been correlated to its elastic properties, which were negatively impacted by the dissolution of Nb-enriched domains [398]. Furthermore, a low-cost and

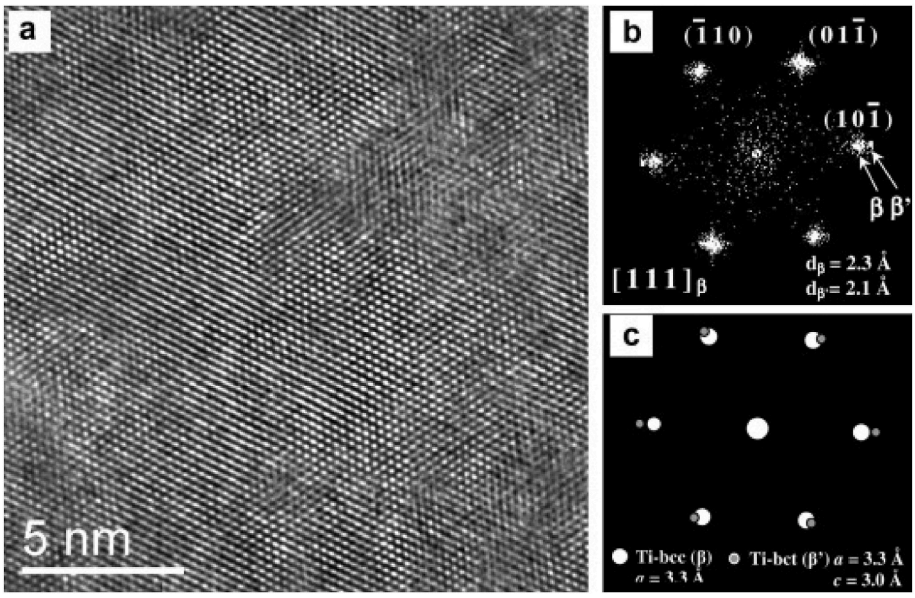


**Fig. 36.** Ti–35Nb–7Zr–5Ta alloy aged at 400 °C for 4 h. (a) HRTEM image of the region shown in Fig. 34b along the $[1\ 1\ 1]_{\beta}$ zone axis. (b) The Fourier transform (FT) reveals splitting of the (1 0 1) reflections (white arrows). (c) Schematic representation of the Fourier space map of the $[1\ 1\ 1]_{\beta}$ zone axis, considering separated phases β′ with cubic (bcc) and β′ with tetragonal (bct) structure obtained through simulation using JEMS© software [369].

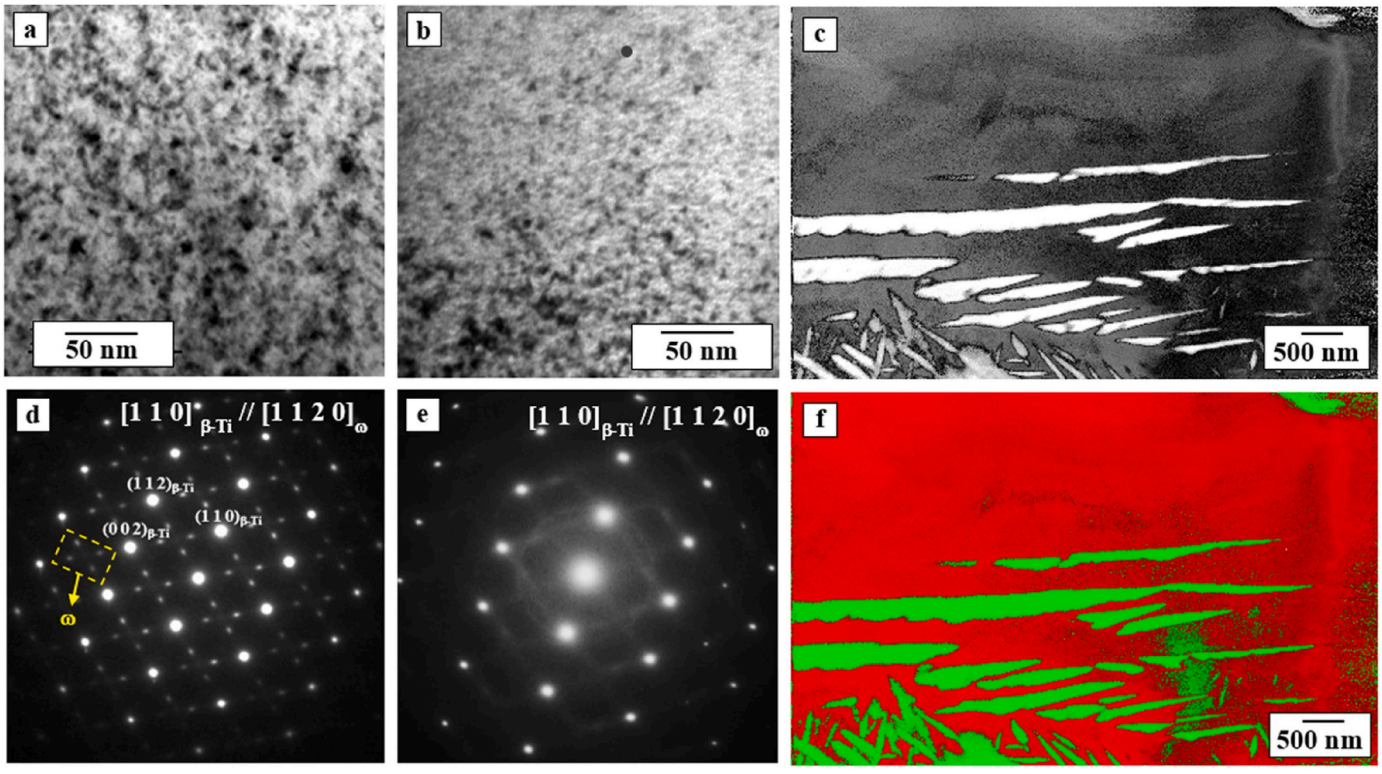


**Fig. 37.** TEM micrographs in (a) bright field (BF) mode showing the ω-Ti nanoprecipitates dispersed in β-Ti grain in the P/M samples of the Ti35Nb10Ta alloy and (c) for the Ti35Nb10Ta3Fe alloy, both sintered at 1250 °C, together with the respective (b) and (d) SAD patterns of the β-Ti region with an orientation relationship $[1\ 1\ 0]_{\beta\text{-Ti}}//[1\ 1\ 2\ 0]_{\omega}$ between the β-Ti matrix and metastable ω phase for both alloys. ACOM map of the Ti35Nb10Ta alloy sintered at 1250 °C showing (e) virtual bright field (VBF) of the α + β region and (f) Phase map combined with a Virtual-BF image of the α precipitates (green) dispersed through the β-Ti (red) matrix [356]. (For interpretation of the references to color in this figure legend, the reader is referred to the Web version of this article.)

feasible route for promoting the simultaneous enhancement of strengthening and ductility at β-Ti alloys has been proposed based on APT and synchrotron analyses, which is based on the combination of oxygen as an interstitial element and grain refinement [399].

Looking forward, the application of APT, complemented with other electron- or X-ray-based microscopies and spectroscopies, to the study of β-Ti alloys is expected to grow, particularly as advances in specimen preparation and data analysis continue to improve the accuracy and efficiency of the technique. A step forward has been made in Ti-alloys by Xe-based plasma focus ion beam (PFIB) to prepare APT specimens

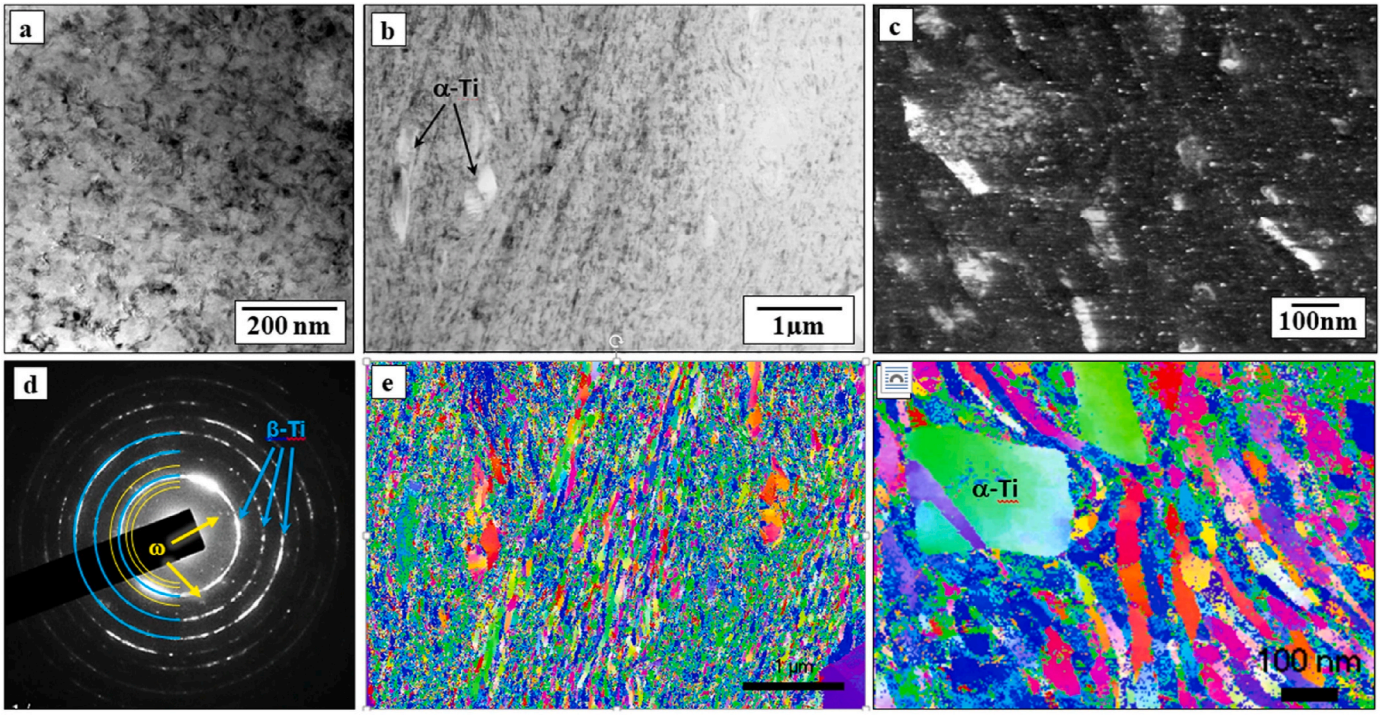


**Fig. 38.** TEM micrograph in (a) bright field (BF) mode of the nanocrystalline β Ti35Nb10Ta alloy after HPT processing and the respective (b) SAD ring pattern typical of nanostructured materials with aleatory orientation. ACOM analysis of the HPT sample of the Ti35Nb10Ta alloy with (c) virtual bright field (VBF) of the nanocrystalline α + β region and (d) IPF-z orientation image showing a general view of the nanostructure. Higher magnification ACOM analysis showing in detail (e) the virtual dark field (VDF) of the ω precipitates dispersed through the nanocrystalline β-Ti grains and (f) IPF-z orientation image showing smaller soft β nanograins and α precipitates as well [356].

without lift-out, reducing possible influence at the preparation process stage [400].

## 6. Beta BCC high (HEA) and medium entropy alloys (MEA) in Ti–Nb–Zr–Ta–Mo system as multiprincipal alloys with low elastic modulus

### 6.1. High entropy or multiprincipal alloys for biomedical applications

The concept of entropy of mixing ($\Delta S_m$) classifies metallic alloys into three categories: low entropy (1 or 2 components), medium entropy (3 or 4 components), and high entropy (5 or more components) [401]. Such an approach is based on mixing together multiple elements with the same crystalline structure in relatively high (often equiatomic) contents. Briefly, the high entropy alloys (HEA) can be composed of at least 5 main elements, which can be equiatomic (20%at. for each element in a 5 components alloy) and varying percentage from 10 to 35% [402]. Authors suggested alternative names for high (HEA) or medium entropy alloys (MEA), such as multi-component alloys, compositionally complex alloys and multiprincipal-element alloys. By incorporating multiple principal components, we can increase the mixing entropy of the system ΔSm, with the aim of creating a single-phase alloy in solid solution (e.g. BCC in the case of β Ti alloys or composed by β-stabilizing elements: Ti, Nb, Hf, Mo, V, Zr, Ta and others), which reduces the number of phases predicted by the Gibbs rule, making the structure simpler and expected to present superior and optimized properties (effect of high entropy) [402].

In HEAs the atoms are bonded to different atoms that lead to chemical bonds among them asymmetric (atoms with different atomic size and crystalline structure) unlike conventional alloys, where the majority of atoms in the matrix form bonds with atoms of the same species. Such effect, results in a distortion in the crystalline structure of the alloy, promoting changes in its mechanical properties [402]. Since diffusion in HEAs is slower than in conventional or diluted alloys, there are few gaps for the substitutional diffusion process (supersaturated solid solutions), the nucleation and growth of others phases are delayed, resulting usually in one solid solution phase (BCC, FCC or HCP). On the other hand, the slower diffusion rate, can facilitate precipitates refinement, improves grain size control and increases the recrystallization temperature of the material resulting in grain refinement of the alloy [402,403]. Despite the fact that $\Delta S_m$ is maximum when the elements are in equiatomic proportion, alloys with this composition generally have a high elastic modulus and, in the case of the Ti–Nb–Zr–Ta–Mo system, they have a high melting point (refractory alloys) since these alloys are based on Ta and Mo (when converting to weight%) due to the high atomic weight of these elements compared to the others. When just the optimization of mechanical properties of the alloy is the main goal the HEAs are very welcome, but in the case of metallic biomaterials for implant applications a lower elastic modulus (around E = 60 GPa) is highly desirable in order to avoid stress shielding. Hereupon, there is an open window for the development of HEAs or MEAs alloys with a lower elastic modulus for biomedical application (BioHEA) and, therefore, equimassic BioHEAs can be an interesting alternative [404].

New equiatomic BCC HEA alloys have been reported [404], but just a few works in the literature reportthe elastic modulus E (GPa) obtained, probably because they are higher than that of pure titanium (E = 110 GPa) and conventional Ti–6Al–4V alloy (E = 100 GPa). These works focus, for the most part, on microstructure, corrosion resistance, tensile strength limit, improvement of ductility, application of empirical parameters (such as $Mo_{eq}$, and $B_o/M_d$ diagram), and, in their minority, on biological tests. The results are promising, since the properties are more suitable than those of commonly used alloys, but there is still plenty of room for further development. But there is a strong drawback for equiatomic alloys in Ti–Nb–Zr–Ta–Mo or similar systems which is the refractory character of such alloys and resulting in elastic modulus in the range E = 116–153 GPa [358–364]. In order to circumvent it, one

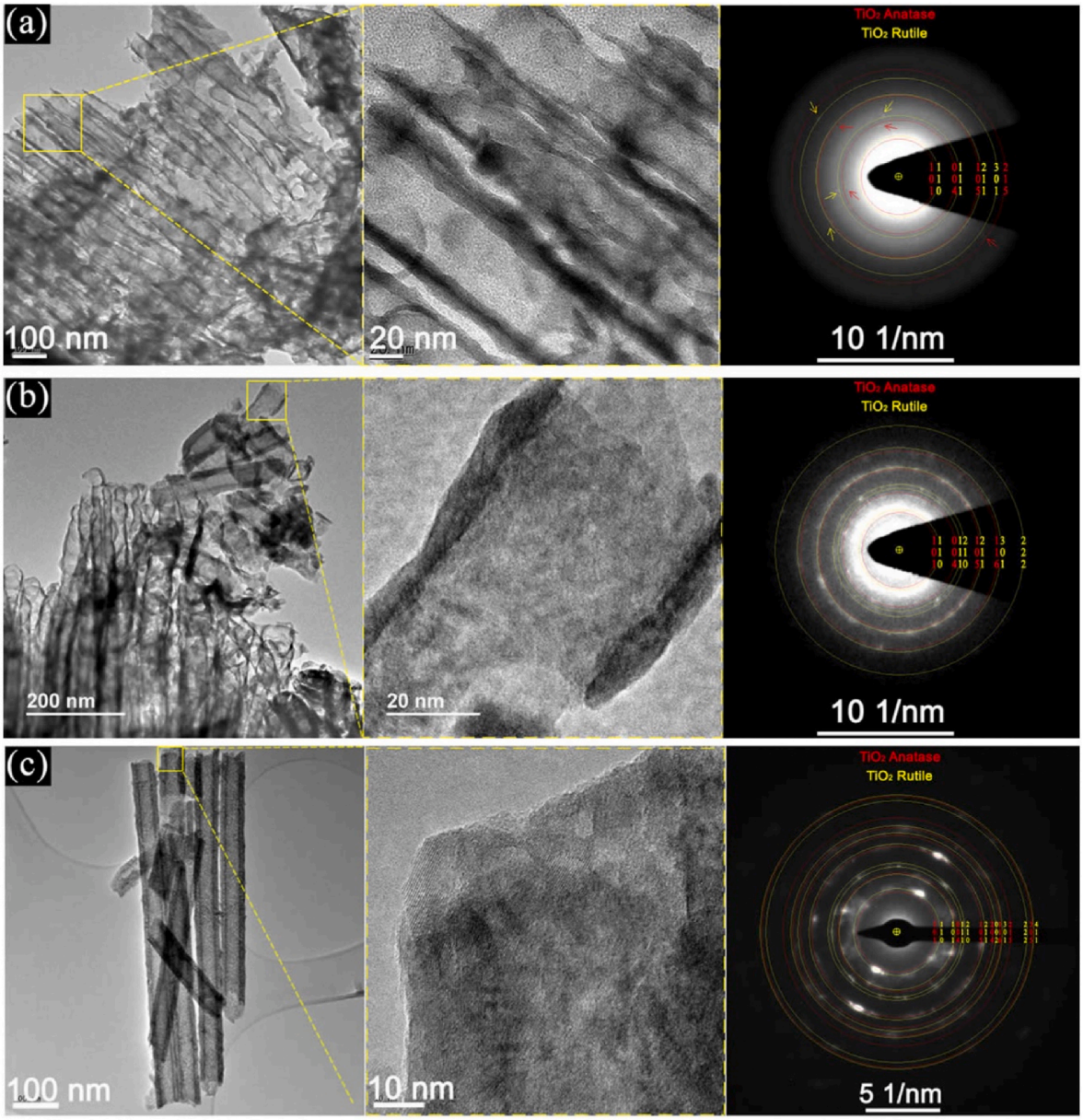


**Fig. 39.** TEM bright field (BF) images of $TiO_2$–based NTs formed from TFNS substrate anodized to 6 h/20 V and annealing at (a) 400 °C (b) 450 °C (c) 500 °C followed by corresponding HRTEM image (atomic scale) and respective SAD patterns in each annealing condition with amorphous halo and diffraction spots of anatase–rutile phases [366].

approach is to deal with medium entropy alloys (MEAs) or equimassic multiprincipal BCC alloys with 3 or more β-stabilizing alloying elements, looking for the optimal entropy range ($1.1 < \Delta S_m < 1.3R$) Such uch equimassic ternary Ti–33Nb–33Zr, quaternary Ti–25Nb–25Zr–25Ta and quinary Ti–20Nb–20Zr–20Ta–20Mo (weight%) alloys show elastic modulus E = 72–88 GPa and enhanced mechanical strength [368].

At present, the development of multicomponent, equimassic, stable β-Ti alloys with medium and high entropy of the systems Ti–33Nb–33Zr, Ti–25Nb–25Zr–25Ta, Ti–20Nb–20Zr–20Ta–20Mo (weight%), in addition to alloys from the Ti–40Nb-xZr system with high Zr fractions and based on electronic parameters Bo and Md seeking an optimal value of elastic modulus (between 40 and 60 GPa). The Ti–40Nb–40Zr alloy showed the lowest modulus of elasticity (E = 42 GPa) in the rolled condition. The Ti–25Nb–25Zr–25Ta alloy showed better results in biological tests (adhesion and cell viability assay), and better combination of low modulus (E = 72 GPa) and high mechanical strength, making it possible to reconcile these properties in β-Ti stable. Table 6 lists the chemical composition of β multiprincipal alloys as well as their elastic modulus, phases formed and processing conditions of some alloys for application with biomaterial.

## 7. Surface modification routes

Various pre-treatment methods are required for Ti alloys in order to treat implant surfaces, prepare surfaces for coating processes, and modify their surfaces. These procedures have an impact on the physical, chemical, and electrochemical surface properties (roughness, wettability, and energy surface), which improves the biological environment's response. Different kind of surface treatment or pre-treatments methods to create a functionalized surface have been investigated, such as: sandblasting, grinding, fine abrasive polishing, acid etching, electrochemical etching, anodization, and solvent degreasing [414]. Therefore, in this section, we'll describe the methods adopted to improve the surface of various β-Ti alloys to enhance their biological

**Table 6**
Chemical composition of in atomic (at.%) and weight (wt.%) Beta Multiprincipal alloys or HEA/MEA and conventional alloys, elastic modulus, phases and condition of some alloys for application as biomaterial.

| Alloy Composition | E (GPa) | Phase(s) | Condition | $\Delta S_m$xR (J/K) | Ref. |
|---|---|---|---|---|---|
| **$Ti_{34}Zr_{52}Nb_{14}$ (%at.)** | 76 | β | Co-sputtering | 0.98R | [401] |
| **TiZrNbTaMo (Equiatomic)** | – | β | Rapidly solidified (~2000K/s) | 1.609R | [404] |
| **TiZrNbTaMo (Equiatomic)** | 153 | β + β′ | Copper mold cast | 1.609R | [405] |
| **TiZrNbTaHf (Equiatomic)** | 115 | β | Copper mold cast | 1.609R | [406] |
| **$Ti_{37.5}Nb_{12.5}Zr_{25}Hf_{12.5}Ta_{12.5}$ (%at.)** | 99 | β | Copper mold cast | 1.494R | [406] |
| **TiZrNbTaHf (Equiatomic)** | 80 | β | Copper mold cast | 1.609R | [407] |
| **TiZrNbTaHf (Equiatomic)** | 66 | β | Copper mold cast | 1.609R | [407] |
| **TiZrNbTaMo (Equiatomic)** | – | β + β′ | Annealed | 1.609R | [408] |
| **TiZrNbTa (Equiatomic)** | – | β | Annealed | 1.386R | [408] |
| **$Ti_{2-X}Zr_{2-X}Nb_xTa_xMo_x$ (x = 0.6) (%at.)** | – | β | Rapidly solidified (~2000K/s) | 1.28R | [409] |
| **$Ti_{35}Zr_{27.5}Hf_{27.5}Nb_5Ta_5$ (%at.)** | 79 | β + α″ | Cold rolled and solution heat treatment. air cooled | 1.38R | [410] |
| **Ti–35Nb–2Ta–3Zr (%wt.)** | 49 | β + α″ | Cold rolled (reduction of 99% transversal section) | 1.10R | [411] |
| **$Ti_{17.5}Zr_{17}Nb_{21.5}Ta_{21.5}Mo_{22.5}$ (%at.)** | 113 | β | Homogenized | 1.60R | [412] |
| **$Ti_{17.5}Zr_{17}Nb_{21.5}Ta_{21.5}Mo_{22.5}$ (%at.)** | 87 | β | Aged at 500 °C/6 h | 1.60R | [412] |
| **$Ti_{29}Zr_{12.5}Nb_{28}Ta_{29}Mn_{1.5}$ (%at.)** | 76 | β | Homogenized | 1.38R | [412] |
| **$Ti_{29}Zr_{12.5}Nb_{28}Ta_{29}Mn_{1.5}$ (%at.)** | 80 | β | Aged at 500 °C/6 h | 1.38R | [412] |
| **Ti–33Nb–33Zr (wt.%)** | 79 | β | As-cast | 1.04R | [413] |
| **Ti–33Nb–33Zr (wt.%)** | 59 | β + α″ | Hot rolled. air cooled | 1.04R | [413] |
| **Ti–40Nb–30Zr (wt.%)** | 83 | β | As-cast | 1.06R | [413] |
| **Ti–40Nb–30Zr (wt.%)** | 65 | β + α″ | Hot rolled. air cooled | 1.06R | [413] |
| **Ti–40Nb–40Zr (wt.%)** | 63 | β | As-cast | 1.10R | [413] |
| **Ti–40Nb–40Zr (wt.%)** | 42 | β + α″ | Hot rolled. air cooled | 1.10R | [413] |
| **Ti–25Nb–25Zr–25Ta (wt.%)** | 73 | B | As-cast | 1.28R | [413] |
| **Ti–25Nb–25Zr–25Ta (wt.%)** | 59 | β + α″ | Hot rolled. air cooled | 1.28R | [413] |
| **Ti–20Nb–20Zr–20Ta–20Mo (wt.%)** | 88 | B | As-cast | 1.52R | [413] |
| **Stainless Steel 316L** | 215 | γ (FCC) | – | | [406] |
| **Co–Cr–Mo** | 252 | FCC | – | | [406] |
| **Ti-6AL-4V (wt%)** | 131 | α + β | – | 0.39R | [406] |

properties and boost their corrosion resistance in biological environments.

### 7.1. Physical (texture and roughness)

Independent of the implantation site, bone quantity, or bone quality, an ideal implant biomaterial should provide a surface that will not interfere with and may even promote the normal processes of bone healing. The procedures for modifying implant surfaces are shown in Fig. 40 and described in the section below.

#### 7.1.1. Dual-acid etching and electrochemical treatment

Acids are applied to metal surfaces during the acid etching process in order to not only clean them or disclose the grain and grain boundaries, but additionally to change how tough they are. This approach often makes use of a strong acid like hydrofluoric (HF), nitric ($HNO_3$), or sulfuric ($H_2SO_4$), or a mixture of these acids. Many studies claimed that acid-etched surfaces had boosted bone production and cell adhesion, which improved the osseointegration mechanism [415–418]. The osseointegration process may be significantly impacted by changes in surface roughness and surface parameters such as surface charge,

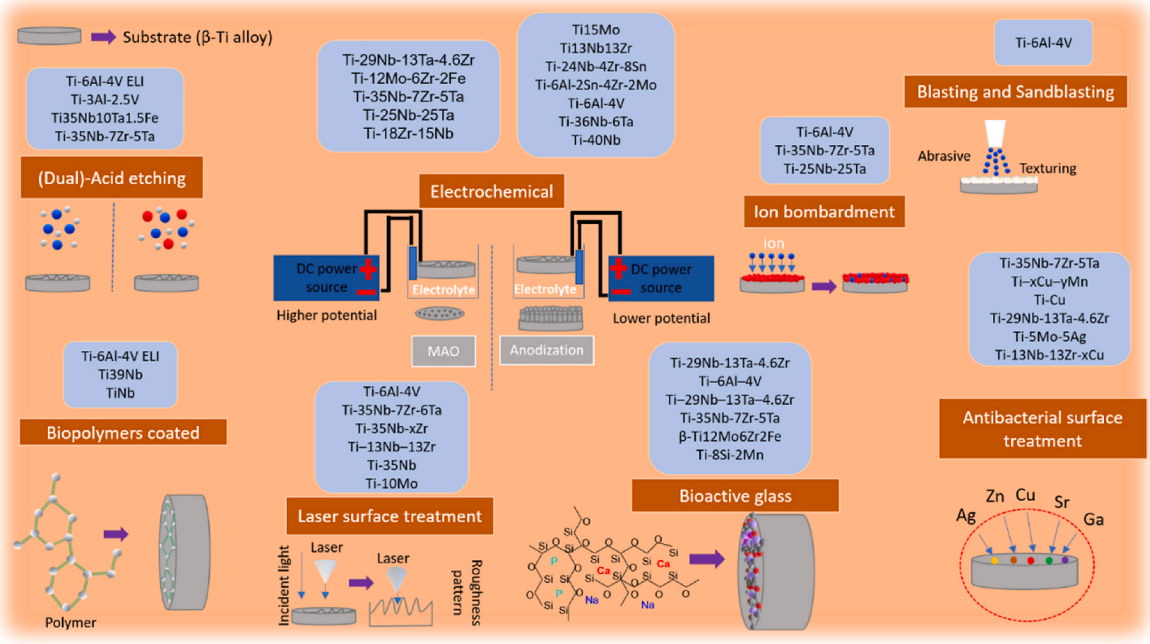


**Fig. 40.** Schematic techniques and process used for surface modification and treatment on β-Ti alloys.

surface energy, and chemical composition caused by acid etching [415–418].

This strategy's relevance also includes the homogeneous roughening it affords the substrate, independent of its sizes and shapes [419]. The durability of bone growth and resorption at the junction of bone implants is partly defined by the roughness of Ti [420].

According to Rama et al., an implant's roughness may be improved by a nano-topography that permits bone ingrowth using acid etching [421]. According to a prior study, both the type and concentration of the acid employed affect the rate of etching [422]. The appropriateness of these acids for etching, meanwhile, was not verified since they needed additional testing, notably on the bone implant interface and torque elimination. Surface roughness increased once Ti samples were etched by $H_2SO_4$ at various concentrations. Notably for biological purposes, concentrated $H_2SO_4$ has been shown to be an efficient way to roughen surfaces [421].

In a manner analogous to acid etching, dual acid etching (DAE) is likewise capable of treating the surface by chemical or acid, whether in succession [423] or with the combination of both [424,425]. By using dual etching on a micro-rough surface, rapid osseointegration can be attained [426]. An assessment of surfaces that have been machined and those that have been treated with HF and $HCl/H_2SO_4$ (DAE) has revealed that the acid-treated surface has superior osseointegration and is more resistant to reverse torque removal [426]. Yang et al. [427], implanted 15 implants into rabbits' tibias in to investigate the surface roughened by the DAE. Amazingly, implants with roughened surfaces outperformed those with machined surfaces in terms of removal torque at 2, 4, and 8 weeks.

A histomorphometric examination at the exact same time revealed that the development of peri implant bone occurred concurrently with a considerable increase in the bone-to-implant contact. Thus, the DAE can offer a surface that has a particular level of microroughness, promoting quick osseointegration [422]. Nonetheless, the procedure and acid type are very important factors in the acid etching treatment. An acid-etched Ti implant showed a surface topography that was comparable to that obtained from a sand-blasted large-grit acid etched (SLA) surface treatment, according to Juodzbalys et al. [428]. They observed that following etching with $H_2SO_4$ and then HCl, the Ti sample displayed excellent surface roughness with 1–10 μm micropits as opposed to an inferior surface microtexture by HCl and then $H_2SO_4$[429]. In general, a chemical treatment is done to Ti alloys, specifically using alkali solutions or acids, not only to improve the surface roughness but also to alter the chemical makeup and to increase the surface energy or wettability [429].

It was revealed that the acid-treated surface of the implants demonstrated superior resistance to reverse torque removal and enhanced osseointegration as compared to the machined surface implants [426]. The density of the bone implant as well as the relative potential for osseointegration have been observed to be similarly affected by acid etching the zirconia implant's surface [430]. Sadly, the usage of these acids also led to unintended consequences such porosities, which can range in size from 0.5 to 2 μm [431, 432].

In some unspecified way, it is also thought that this procedure aids with the dental implant's ability to support tissue ingrowth and cell surface contacts [432]. Reverse torque rotation was used to gauge the effectiveness of osseointegration or implant anchoring. More osseointegration was achieved as the torque rotation force value rose along with the bone-to-implant contact (BIC) [417]. By applying acid etching before coating, this value might be raised to 8.68 ± 0.37 μm [433]. However, the dual acid etching, which produced surfaces with roughness varying from 0.44 to 3.51 μm, played a significant role in producing better surfaces [422,434,435]. Due to its high composition, amount, and concentration, DAE is typically superior to a single acid etching. Depending on the type, concentration, temperature, and duration of the acid, acid etching can affect dental implants differently. It is common to see an increase in surface roughness when the acid concentration increases [424].

Acid etching is among the most commonly utilized methods for modifying the surface of dental implants as it increases the surface's bioactivity [429]. Implant bioactivity is influenced by surface chemistry, chemical composition, wettability, micro-topography, roughness, and overall increased interfacial surface area [436–438].

According to earlier studies the acid etched surface promotes greater cell attachment than implants without surface treatment [434,439,440]. Moreover, Park et al., showed that Ti surfaces subjected to dual acid etching result in an increase in fibrin and osteogenic cell adhesion [441]. For implants with acid etched surfaces compared to those with machined surfaces, Elias et al., observed a higher torque removal [442]. In the process of osseointegration, the surface topography and roughness of the implant have a significant influence on the first bone cellular response and the osseointegration process in general [422,443,444].

In order to form a fresh surface layer with a thicker coating of Ti oxide, an aggressive liquid is used on a Ti substrate to etch surface depressions. The goal of acid etching procedures is typically to change surface chemistry and micro-roughness and hence affect cell response [445]. The roughness of an implant is said to be improved by nano-topography that enables bone ingrowth by acid etching [420]. Etching is technically known as pickling, and it is typically used to remove oxide deposits to provide a smooth and even surface finish [446].

Chemical modification influences the chemical composition of the implant surface, resulting in unique interactions between molecules on the surface of cells that change not only those surface molecules but also the inner structure and function of cells [447]. These are carried out to eliminate oxide scales and contaminants in an effort to increase bioactivity and biocompatibility [448].

Chemical surface treatments have been used regularly on dental implant over the past ten years, among others. Comparing implants with Ti-plasma sprayed surfaces to those with sandblasted and acid-etched (SLA) Ti, it has been noted that the latter induces more osseous contact [449]. This is owing to the high surface roughness of SLA caused by grit blasting and acid etching, the latter of which increased the concentration of hydrogen beneath the surface and caused Ti hydride to develop [450]. By changing the treatment conditions, the SLA surface modification has also been improved [422]. These surface treatment techniques change the surface's wettability and roughness, which changes the parameters of cell adhesion and proliferation. For dental implants, osseointegration at the bone-implant contact is a requirement to achieve and preserve their long-term stability.

Understanding the biological mechanisms behind the interaction between osteoblasts and biomaterials is crucial in this context because osseointegration is the desired outcome. Titanium 's surface can be modified for use in biological applications by etching it in concentrated acid, which seems to be an appealing technique. Studies in this field are, however, hardly reported in biomaterials science. A rougher Ti surface was created by etching in concentrated sulfuric acid than by using HCl, $H_3PO_4$, HF, or $HNO_3$ according to the prior study [449].

In the research done by Lario et al., Ti–6Al–4V ELI and Ti35Nb10-Ta1.5Fe (β-Ti alloy) were used to test the effects of the acid-etching procedure in a two-step acid treatment, samples were etched [451]. The outcomes showed that the two-step acid treatment altered the alloy's morphology, increased its surface area, and modified its chemical composition. During the acid etching procedure, two distinct zones were observed in the Ti–35Nb–10Ta-1.5Fe alloy: an area with lower roughness parameters and other with greater mean roughness due to its lower chemical resistance.

Acid-etching procedures are used to produce a microroughness topography on the implant surface [422,452,453]. The surface area and roughness of implants can be adjusted in order to enhance bone regeneration and accelerate short- and midterm healing times [454,455]. Surface topography can be changed by electrochemical procedures, plasma-sprayed coatings, grit blasting, acid etching, and other

techniques [434]. The most typical pre-treatments include sandblasting, grinding, fine abrasive polishing, acid etching, electrochemical etching, anodizing, and solvent degreasing [456]. These pre-treatments serve to improve the homogeneity of the surface in terms of internal stress, shape, and specific surface area during the deposition process as well as to get rid of impurities, adsorbed species, and the unstable surface layer.

Fig. 41 demonstrates that the pre-treatments carried out by acid etching of the alloy β-Ti-35Nb–7Zr–5Ta resulted in considerable morphological changes in both the micro- and nanoscales [414]. The pre-treated surfaces had varying degrees of hydrophilicity and hydrophobicity in terms of wettability. Surface chemistry, rather than modifications in shape and roughness, was responsible for changes in contact angle. During mechanical polishing, chemical etching, and electrochemical etching, it was discovered that the Ti–35Nb–7Zr–5Ta alloy's native oxides and suboxides of alloying elements, with a predominance of $Nb_2O_5$ provided high corrosion stability. The corrosion resistance of the ion sputtered surface was drastically decreased in a physiological saline solution. The changes in surface roughness and polarization resistance are related to the declining trend in cell spreading [414].

### 7.1.2. *Blasting and sandblasting treatment*

A widely used method to promote osseointegration through surface roughness is sandblasting with different kind of abrasive materials such as: alumina ($Al_2O_3$), garnet, glass beads, crushed glass, plastic abrasive, steel shot and grit, contact protoplast and walnut shells [457]. Significant factor affecting the value of the surface roughness include the size, shape, and kinetic energy of the particles. The air pressure impulse that the sandblasting process uses to drive the particles causes an increase in kinetic energy that is inversely proportional to the density, volume, and square of the shooting velocity. The following equation illustrates the gain in kinetic energy:

$$Ec = \rho.\left(\frac{2}{3}\right).\pi.r^3.V^2 \tag{9}$$

where V, ρ, and r are the velocity, density, and particle radius, respectively.

Sandblasting is a method that produces surfaces with varying degrees of roughness and surface attributes for cell attachment. According to experiments, the type of abrasive substance employed has a greater impact on surface roughness and adhesive characteristics than do differences in pressure, as shown in equation (9) [458].

The osseointegration efficiency and biomechanical fixation of Ti implants have both been found to increase with surface roughness [459]. Several studies [457,459,460] have shown that the topography of the implant surface affects the bone response; smooth ($R_a < 0.5$ μm) and minimally rough ($R_a$ 0.5–1 μm) surfaces displayed lower bone responses than rougher surfaces. Moderately rough surfaces (Ra 1–2 mm) stimulate the bone more strongly than severely rough surfaces (Ra >2 mm). The deposition of contaminating elements on the implant's surface, which is brought on by the use of abrasive media, is one of the most significant issues in the fabrication of implants utilizing sandblasting. Sandblasted test piece failure is not a result of a flaw in the materials. The surface flaw, which acts as a crack initiator, reduces the resistance of the sandblasted stem. Reduced alloy endurance limitations can be prevented by regulating roughness with the proper sandblasting procedure [461].

The hardness and acicular shape of $Al_2O_3$ make it a suitable abrasive for sandblasting in Ti alloys, and its low manufacturing cost compared to

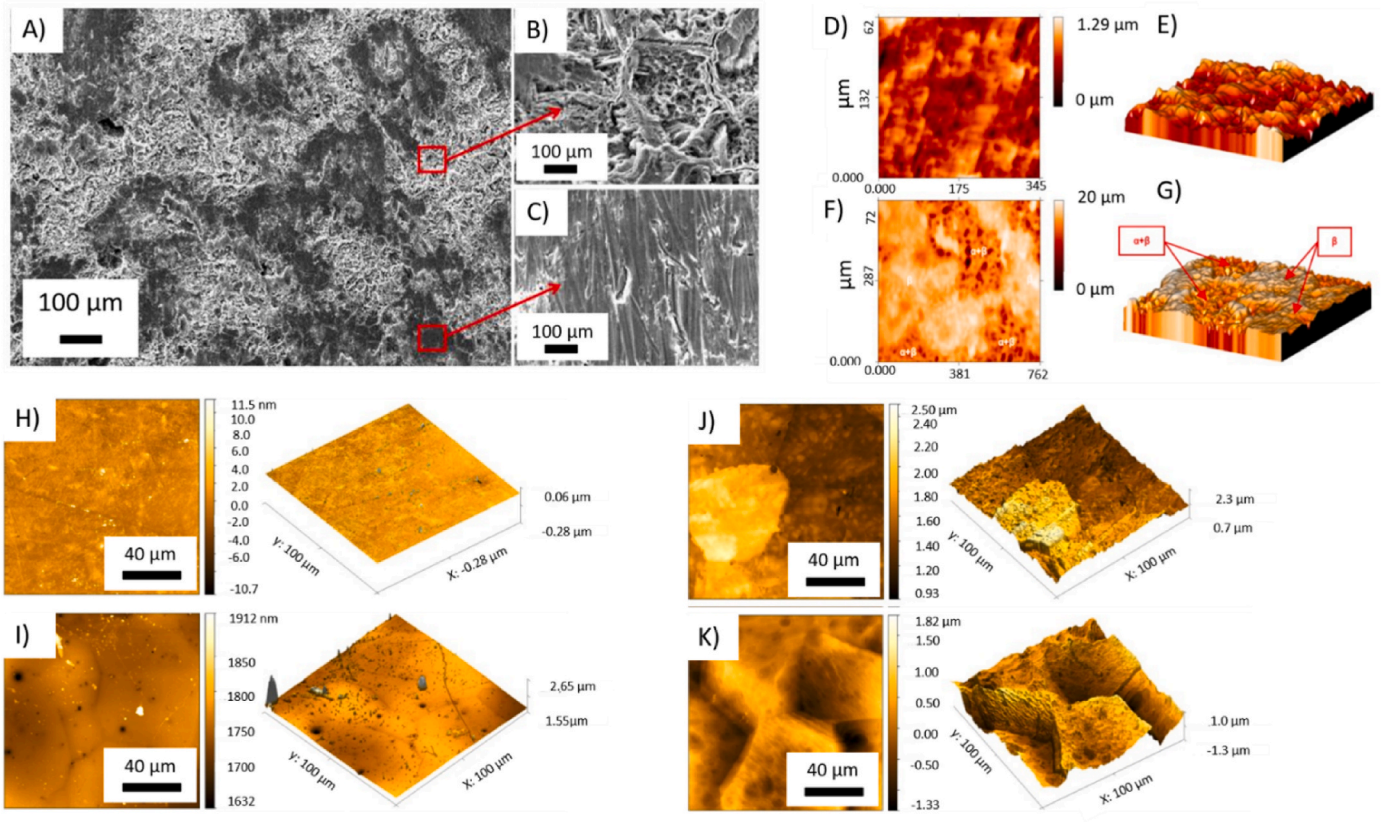


**Fig. 41.** Micrographs obtained by SEM, Confocal and AFM analyses of β Ti35Nb10Ta1.5Fe alloy posterior acid-etched and pre-treated β Ti–35Nb–7Zr–5Ta alloy surfaces. A) SEM of Ti35Nb10Ta1.5Fe microstructure. B) and C) are indicated by the arrow the α and β phase regions. D) and E) indicate the 2D and 3D topographic roughness of Ti35Nb10Ta1.5Fe posterior griding; F) and G) are indicate the 2D and 3D topographic roughness of Ti35Nb10Ta1.5Fe posterior acid-etching; H) and I) are represented AFM images of pre-treated Ti–35Nb–7Zr–5Ta by mechanical-polish and electrochemical-etched process; J) and K) are represented AFM images of pre-treated Ti–35Nb–7Zr–5Ta by chemical-etched and an ion sputter etched process [414].

other abrasives, as well as its probability of inert behavior during osseointegration make it one of the most widely used abrasives. Three different types of sandblasting abrasives (Aluminum Oxide, White Aluminum Oxide, and Glass Bead) were utilized on Ti alloy in the study by Yuda et al., [462]. Both the type of sandblasting abrasive material and the surface roughness in this experiment, were influenced by the distance between the spray gun and the surface sample. Additionally, when there was a larger level of blasting impurity, the usage of Brown Aluminum Oxide revealed a greater susceptibility to contamination. With the use of glass beads, the alloy surface's surface topography for osseointegration 368 revealed shallow and wide valleys.

Balza et al., conducted an analysis of a sandblasting procedure using $Al_2O_3$ abrasive particles (with granulometry between 420 and 600 μm) on Ti–6Al–4V surfaces. The $Al_2O_3$ particles ranged in sizes from 420 to 850 μm, with a mean particle size (d50) of 670 μm that fell to 420 μm. The surface roughness of the Ti–6Al–4V samples decreased as a result of the $Al_2O_3$ particles exhibiting ruptures during the sandblasting procedure, which led to a significant loss of their kinetic energy [457].

In the study by Stoilov et al. [463], Fig. 42, the same alloy was examined in order to assess the biocompatibility of bone cells (osteoblasts) to CP-Ti using various sandblasting techniques (different particle sizes and blasting pressure) [463]. After 7 days in contact with the Ti–6Al–4V surface, an inverse association between the blasting grain size and the development of model osteoblasts cell line (hFOB) bone cells was detected. Following 12 days of cultivation, the smaller-grain-size sandblast group showed greater biomineralization than the groups with standard-sized grains. Furthermore, although micro-roughness and other significant surface parameters were similar, hFOB adhesion and growth capabilities were reduced when treated with reduced blasting pressure at initial (2 h) and later time points for up to 7 days in comparison with standard blasting pressure-treated samples. All etched-only surfaces consistently exhibited similar or greater adhesion, proliferation, and differentiation capabilities when compared to all other sandblasted and etched surfaces. As far as surface properties are concerned, there was no difference between the CP-Ti and Ti–6Al–4V surfaces [463].

### 7.1.3. Laser surface treatment

Past few years have seen a rise in the use of lasers to modify surfaces, including surface thermal treatment [239,464], texturing of alloy surfaces with femtosecond laser [239], or coating through direct powder deposition (laser cladding) [465] to produce coatings that vary from bioactive to bio-inert. The majority of these methods for surface modification include heat transfer from a laser platform system (metal surface). Due to fast photon-electron interaction and a subsequent

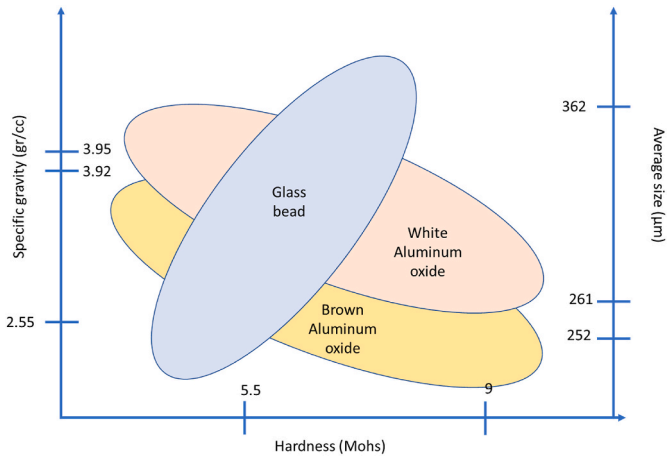


**Fig. 42.** Physical and mechanical properties of sandblasting abrasives used on Ti alloys [462].

electron-phonon energy transfer mechanism, whenever a laser beam with a high enough energy irradiates a material surface, the surface quickly approaches the melting point and melts. For the proper pretreatments, the development of the molten pool causes liquid material to re-solidify when the surface temp drops behind the laser beam, decreasing surface roughness [466]. In contrast to traditional mechanical techniques, laser surface treatment (LST) can provide a selective and localized processing capability with high automation and an ecofriendly approach. Moreover, LST is seen to be a viable technique for polishing complex three-dimensional (3D) work items while producing less pollution and tool wear. The laser treatment can offer a smoother surface, raise its density, develop new texture patterns, and enhance the mechanical, wear, and corrosion characteristics as compared to other traditional surface treatment methods discussed up to this point.

Due to its adaptability, speed of operation, and capacity for polishing complex surfaces in comparison to traditional mechanical-based methods, laser surface treatment of additively manufactured parts has garnered significant interest in recent years. This is because it can minimize surface roughness and pores that have negative effects on the fatigue behavior of additively manufactured specimens depending on its application. To extend the fatigue life of these samples, Ahmadi et al., employed a precise laser melting and recrystallization technique to seal the pores within 70 μm of the surface. They also looked at the impact of different processing variables for controlled laser surface treatments [467]. The laser treatment has been keeping an eye out for antimicrobial applications. To reduce bacterial adhesion to implant surfaces, a number of techniques have been used. Using biocides to kill germs was the first method. Nevertheless, frequent use of biocides causes increased bacterial resistance to therapeutically significant antibiotics [468]. Antibacterial metals like silver, copper, and molybdenum have also been used as a strategy [469].

The most well-known and oldest antibacterial metal is silver [469]. When silver dissolves off the surface of bio-implants, an antimicrobial effect is produced. Yet, an implant's antimicrobial effectiveness declines after the silver totally dissolves. Another strategy involves the use of photo catalytic materials like titanium dioxide ($TiO_2$), which create highly reactive species that destroy bacteria in implant environments [470]. Due to its high band gap, $TiO_2$ must be activated with UV radiation, while new research have revealed that $TiO_2$ may also be activated with visible light [471]. This method, which only requires one step and is chemical-free, is appealing because it enables localized surface treatment in both time and space. Recent research have found that bacteria are less likely to adhere to ultra-hydrophobic Ti surfaces, which limits the growth of biofilm on implants [472]. To replicate these extremely hydrophobic surfaces, a number of fabrication methods have been created, with femtosecond laser-based surface texturing being one of the more recent methods [473]. An easy way to manage the surface characteristics of Ti alloys and produce surfaces that are antibacterial is by laser-based surface treatment. To produce surfaces that are antibacterial, many laser types have been employed for surface treatment. While using nanosecond and picosecond lasers, surface shaping is still possible. Ultra-short femtosecond (fs) lasers are favored because of the numerous benefits they provide. Femtosecond laser-based surface modification is a highly accurate, repeatable method that produces little waste and heat-affected zones, limiting collateral damage.

β-type Ti–35Nb–7Zr–6Ta (TNZT) alloy's biocompatibility and antibacterial characteristics were investigated in the high-speed range between 100 and 200 mm/s 380. Throughout this study, the laser surface modification produces a surface with unique micron and nano scale features. The surface is rougher ($R_a$ value of BM is 199 nm, LT100 is 256 nm, and LT200 is 232 nm), spiky ($R_{sk} > 0$ and $R_{ku} > 3$), with homogenous elemental distribution, and decreasing peak-to-peak distance between ripples (0.63–0.315 μm). The characteristics produced by fiber laser treatments 380 are the cause of the increase in cell spreading, creation of bone-like nodules (only visible on the laser specimens), and afterwards four-fold decrease in bacterial adhesion [474].

Jeong et al. [347], examined the development of surface roughness on the beta Ti–35Nb-xZr alloy for biocompatibility using a femtosecond laser. Equiaxed β grains were present in Ti–35Nb-xZr alloys, then after treatment, the textural surface showed higher $R_p$ and $R_a$ levels of roughness than the untreated surface as well as a low contact angle [347].

CP-Ti and Ti–13Nb–13Zr alloys were studied under various laser beam energy levels under different conditions of picosecond Nd:YAG laser irradiation in air and argon atmospheres [475]. As a result of laser beam interaction with the target surface, many morphological changes were observed, such as craters, microcracks, and hydrodynamic structures. Also, numerous chemical alterations were brought about on the target materials' surfaces, which led to the production of titanium oxide in the area that was exposed to radiation, hence enhancing the absorption of radiation energy. The size of the surface damaged area grew as a result of the significant energy absorption at the place of interaction. As a result, surface roughness increased. Surface oxides are also responsible for the increased material hardness in the surface-modified area. There were significant changes in both chemical composition and morphology after laser irradiating the Ti–13Nb–13Zr alloy surface [475].

By modifying the surface of β-type Ti–Nb–Zr–Ta alloys with a laser, Chan et al., demonstrated that the material's corrosive behavior was enhanced and a hard, wear-resistant surface layer was created [476]. By using an excimer laser to modify the Ti implant alloy's surface in an argon atmosphere, elemental microstructural partitioning increases the material's corrosion resistance under artificially created physiological conditions [477]. Since the laser irradiation method is a contactless technology, no direct surface contamination can occur during the material surface modification [478,479]. Moreover, plasma frequently forms in response to the contact of the laser beam with the metallic surface, causing further surface sterilization that is advantageous for the suitability of a material for use in medical application [480].

The β-type Ti–35Nb alloy was surface-treated using laser technology in the study of Ng et al., which resulted in slight changes in the substrate's temperature [481]. The additional benefits of laser surface treatment include a quick treatment time and adjustable accuracy of treatment spot. This study assessed the effects of surface modifications made to Ti–10Mo alloy samples using a laser beam in an Ar or $N_2$ atmosphere on the parameters of cell integration and corrosion resistance. With the aid of a scanning electron microscope, energy-dispersive x-ray spectroscopy (SEM-EDX), and x-ray photoelectron spectroscopy (XPS), the surface morphology and element distributions of Ti–10Mo samples following laser surface treatments were assessed. Using x-ray diffraction (XRD), phase analysis was carried out. A cell-material interaction test was carried out utilizing the MLO-Y4 cells, and the electrochemical behavior of the Ti–10Mo samples was assessed in simulated body fluid kept at 37 ± 0.5 °C. When compared to untreated samples, laser surface modification in the Ar atmosphere improved corrosion behavior while having no effect on surface roughness, element distribution, or cell activity. When the Ti–10Mo alloy was processed in $N_2$, a significantly rougher TiN surface was created, which enhanced both corrosion resistance and cell-material integration in comparison to the other two conditions [482].

#### 7.1.4. Ion bombardment

Secondary electrons are released when energetic ions attack a surface. During ion bombardment, metals typically have secondary electron emission coefficients of less than 0.1, whereas oxide surfaces have secondary electron emission values that are greater. Compared to ion bombardment, secondary electron emission from bombardment with electrons is substantially higher. Surface material can physically sputter when an energetic ion bombardment strikes it. If the reactants from the bombardment species are not volatile, they may create a compound layer on the surface if they are chemically reactive. Arcing can occur over a surface layer if the surface layer is electrically insulating or possesses different electrical characteristics than other surfaces. Plasma etching of the surface happens when the reaction products are flammable [483]. Rare study using this method was found in the literature in the area of biomedical β-Ti alloys. According to the studies, the wear and corrosion properties as well as the adhesion and proliferative abilities of cells when in touch with this surface changed utilizing various ion bombardment types have improved.

Vlcak et al. [484], studied the corrosion behavior of a β-type Ti–35Nb–7Zr–5Ta an alloy that underwent nitriding through ion implantation. They implanted nitrogen ions at various fluences between $1{\cdot}10^{17}$ to $9{\cdot}10^{17}$ $cm^{-2}$ with a 90 kV accelerating voltage. The impacts of nitrogen fluence on the implantation zone's structural modification revealed a connection between nitrogen concentration, nitride production, and corrosion behavior. Increases in surface nitride production were seen as nitrogen fluence increased implanted, reaching a saturation fluence of $4.10^{17}$ $cm^{-2}$. In the case of oversaturation, nitrogen concentration dropped, leading to a decrease in the quantity of surface nitrides and blistering. According to the corrosion experiments performed in physiological saline solution, the implanted surfaces showed good corrosion resistance to corrosive environments, and the corrosion resistance increased with increasing fluence up to saturation fluence. When flux densities exceed saturation one, corrosion resistance decreases to the level of lower fluences. In all cases, nitrogen-implanted surfaces demonstrated greater resistance than surfaces without nitrogen [484].

The low processing temperature (50–500 °C) achieved by nitriding ion implantation (at an energy of 100 keV and at a fluence of $5.10^{17}$ $cm^{-2}$) into metastable β-Ti alloys is a significant improvement over traditional high temperature nitriding techniques using a β-type Ti–25Nb–25Ta alloy as substrate, according to Gordin et al. [485]. Together with a lower coefficient of friction, a noticeably enhanced hardness and wear resistance was noticed. A nitrogen ion implanted alloy displayed superior corrosion resistance as well as superior ion release resistance in comparison to an unmodified alloy, proving nitrogen implantation to be a useful method of material modification.

For metal alloys with body centered cubic (bcc) type-β structures, ion implantation and its derivatives are still rarely employed commercially. Ti–6Al–4V was the subject of the majority of investigations. Particularly the poor tribological and biological features of the posterior ion surface treatment of β-Ti alloys to encourage their use in the medical field.

### 7.2. Chemical surface modifications

#### 7.2.1. Bioactive glass treatment

The most diverse class of biomaterials, known as bioactive glasses (BGs), is based mostly on the structures of borate, silicate, and amorphous phosphate [486]. Hench invented the first bioactive silicate glass, known as 45S5 Bioglass, which promotes bone formation and has good bone-bonding properties [486,487]. Due to its established capacity to accelerate the regeneration of injured tissue by ion therapy and its potential to form a strong and stable chemical bond with host tissue, BG has drawn particular interest [488]. Due to the formation of a layer rich in $SiO_2$ inside the body, silicate glasses degrade slowly, but borate base glasses like 1393-B3 degrade rapidly due to their high biodegradation. It exhibits strong bioactivity within the cells in addition to a quick degradation rate. Glasses are brittle and have a low amount of strength, which limits their use in soft tissues [489]. Several types of BG were used to coat some β-Ti alloys, such as Ti–29NB–13Ta-4.6Zr, which was produced using bioactive calcium phosphate invert glass-ceramic with the following formula: $60CaO–30P_2O_5–7Na_2O–3TiO_2$. According to the investigators, the oxidized layer on Ti–29Nb–13Ta-4.6Zr alloy is substantially thinner compared to that of Ti–6Al–4V alloy [490], and the coating's tensile bonding strength to the metal is considerably higher than that of coatings to traditional metals like pure Ti or Ti–6Al–4V alloy. Similar to this, Kasuga et al. [490], produced a bioactive coating of bioactive glass (the so-called "invert glass" [491]) with a composition

of 60CaO–30$P_2O_5$–7$Na_2O$–3$TiO_2$ in mole %, which contains $PO_4^{-3}$ and $P_2O_7$ ions without $SiO_2$ [492,493].

In subsequent articles, the same scientists stated that even at 800 °C in air, heating the TNTZ alloy—on which the aforementioned mother glass powders were deposited—made it easier to mix calcium phosphate invert glass-ceramic. The development of an apatite phase that resembles bone in a simulated physiological fluid and its deposition on the coating serve as indicators of the glass ceramic layer's *in-vitro* bioactivity [494,495].

β-type Ti12Mo6Zr2Fe (TMZF) has drawn substantial interest in orthopaedic applications, since to its mechanical characteristics and biocompatibility. Ti alloys' restricted orthopedic applications are a result of their poor osseointegration, although this can be modified by coating with a bioactive layer. To enhance its biological capabilities, Da Rocha et al. [496] used the dip-coating process to develop a bioactive surface. By using the sol-gel approach, the 58S bioactive glass with 5% CaO substituted by SrO was developed and thoroughly characterized. After 24 h of immersion in SBF solution at 37 °C, the presence of bioactive coating yields an excellent bioactive response, with apatite-related deposits appearing on the samples' surfaces [496].

### 7.2.2. Biopolymeric coatings

Due to the possibility of thrombosis and thromboembolism, anticoagulation and antiplatelet pharmacologic treatments are routinely utilized on patients implanted with such devices [497,498]. Several surface coatings, including diamond-like carbon (DLC), titanium nitride (TiN), heparin, silicone, and 2-methacryloyl-oxyethel phosphorylcholine (MPC), have been developed to increase the thromboresistance of titanium alloys in interaction with the circulatory system [499]. Using biomimetic surfaces made from phospholipid polymers [phosphorylcholine (PC)], which are common on the exterior of biological cell membranes, remarkable biocompatibility and hemocompatibility have been revealed by lowering protein adsorption and platelet adhesion [500,501]. It has been demonstrated that PEO [502], PMEA [503], PEG [504], and other polymer coatings can lessen protein adsorption and platelet adhesion and aggregation.

In a study published by Stanfield and Bamberg, commercially available phosphorylcholine (PC) polymer was coated onto Ti–6Al–4V ELI to study surface modification for hemocompatibility. Changes in the concentration of the PC solution had no effect on the coating's ability to resist fouling. It was proposed that the PC-application process variables might be improved to produce good results in coating reactions to cross-linking and durability. The resulting statistical model shows that the three factors with the highest single influence on both durability and cross-linking intensity are PC solution concentration, dip rate, and cure temperature. The degree of cross-linking of the polymer surface was also improved by plasma treating the substrate with $O_2$ [505].

In order to improve the interaction of bone cells, Vandrovcova et al. published on the β-type Ti39Nb alloy that had been coated with ferroelectric barium titanate ($BaTiO_3$). Ceramic or polymeric materials are the types of materials used in ferroelectrics [506]. Lead zirconate titanate (PZT), a well-known ferroelectric ceramic material, is usually employed for industrial purposes but is extremely cytotoxic and inappropriate for biomedical applications due to its Pb concentration. $BaTiO_3$, lithium niobate ($LiNbO_3$), sodium-potassium, or potassium-sodium niobate (referred to as NKN or KNN, respectively), lithium tantalate ($LiTaO_3$), or magnesium silicate (MgSiO3) are some of the key lead-free ceramics that are better suited for biomedical applications [507,508].

After 1, 3, and 7 days of cultivating human osteoblast-like Saos-2 cells, leaching assays in a saline solution showed that Ba is released from the coating and that the Ba concentration in the material gradually decreases. On day 1, more Saos-2 cells initially attached to the $BaTiO_3$ film than to the bare alloy, although they spread out less and proliferated more slowly at first. Because the cell survival on this film was so high—it reached approximately 99%—and not because of its possible cytotoxicity, this cell behaviour was attributed to a higher surface roughness of the $BaTiO_3$ film. At day seven, the final cell population density of the $BaTiO_3$ film was higher than that of the control film. There was no difference in alkaline phosphatase levels between cells on the coated and untreated alloys. This enzyme is involved in the mineralization of bone matrix. Based on these findings, it appears that the hydrothermal ferroelectric $BaTiO_3$ film may be an effective coating for enhancing osseointegration of bone implants with the provision of a few tweaks, notably to its roughness and stability [506].

### 7.2.3. Antibacterial surface treatment

According to the National Joint Registry, aseptic loosening, infection, and unfavorable soft tissue reactivity to particle material are the three primary reasons for hip implant revision surgery [509]. Peri-implantitis can develop because dental implants, like teeth, protrude from the bone via oral soft tissue into an oral cavity that acts as a haven for a variety of microorganisms. Peri-implantitis is the term used to describe the inflammatory condition that affects the tissue around dental implants and is brought on by the presence of various bacterial species.

Due to their advantageous mechanical, physical, and chemical characteristics, titanium (Ti) and its alloys are employed in dentistry to produce implants, prosthetics, and prosthetic components. Since 1951 their use in the field of biomaterials has been facilitated by their low density, high mechanical strength, and good corrosion resistance [510]. Despite the fact, that titanium (Ti) and its alloys are extensively employed as implants to restore or enhance the function of human tissues; concerns about implant-associated infections (IAIs) and poor osseointegration limit their success.

Some strategies for improve antibacterial surfaces on biometallic alloys can be related to inhibiting the adhesion of bacterium, colonization, biofilm formation and also its proliferation over the time [511–514]. An increasingly common medical problem is surgically acquired prosthesis bacterial infection. Inflammation, interference with the healing process, inhibition of osteogenesis, and ultimately implant failure are all symptoms of pathogenic bacterial infection. Applying coatings or creating multifunctional materials (such as structural and antimicrobial) are two ways to address these problems [515].

A flowchart for producing antibacterial Ti alloys is shown in Fig. 43. The impact of Cu addition on cast Ti–Cu alloys' antibacterial efficacy against *Staphylococcus aureus* was investigated. The copper content in the Ti–Cu alloys ranged from 0.5, 1, 2, 3, 4, and 10 wt%. As a comparison, pure Ti metal was also made and tested. Colony forming unit (CFU) method killing activity test with variable contact time was used to test the antibacterial. Through time, Ti–Cu alloys were able to reduce the number of germs. However, there were no significantly different outcomes in the activity of bacteria killing over the spectrum of Cu content. Moreover, the alloy's highest bacterial kill capacity was noted. By adding 3 wt% of Cu, the alloy's highest bacterial kill capacity was observed [76,515–520].

In the study of Tsutsumi et al., the surface of beta Ti–29Nb–13Ta-4.6Zr alloy (TNTZ) was modified using the micro-arc oxidation (MAO) process to enhance both its antibacterial effect and bioactivity in bodily fluids. It was coated with the surface oxide layer that TNTZ developed after MAO treatment in a solution of calcium glycerophosphate, calcium acetate, and silver nitrate. Titanium oxide made up the majority of the porous oxide layer that resulted from the treatment, along with calcium, phosphorus, and a trace quantity of silver that were all integrated from the electrolyte. When the electrolyte included more than 0.5 mM silver ions, the MAO-treated TNTZ had a potent inhibitory effect on anaerobic Gram-negative bacteria. The bioactivity of TNTZ with significant antibacterial property was assessed based on the calcium phosphate that formed on the specimens' surfaces following immersion in Hanks' solution. As a result, the TNTZ specimen that received MAO treatment developed thick calcium phosphate layers, while TNTZ that hadn't received treatment didn't show any precipitation. As a result, it is

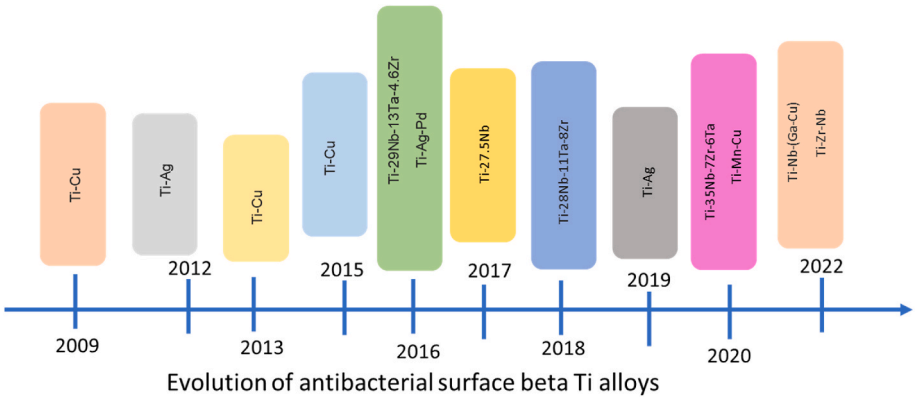


**Fig. 43.** Development flow-chart of antibacterial Ti alloys [515,521–531].

demonstrated that Ti-based alloys can effectively achieve both antibacterial and bioactive characteristics through the MAO process [532].

Implants for medical and surgical procedures frequently use β-Ti alloys. Implant-associated infections and the demands of applications under high stress, however, offer challenges for the Ti alloys now in use. In order to address these issues, we created bulk fine-grained Ti–5Mo–5Ag alloys using a mix of mechanical alloying and spark plasma sintering. Our method for achieving this was based on the combination of the stabilizing element Mo with the antimicrobial element Ag. The alloy, which was sintered at 900 °C, exhibited a network microstructure made up of 11% α-phase and micron/submicron-scale precipitates at the grain boundaries/triple junctions, with an average grain size of 8.1 (±3.2) m. This network structure displayed exceptional mechanical properties, having compressive yield strengths of 1694 (almost 8.4) and fracture strains of 23%. Compared to pure Ti, the created Ti–5Mo–5Ag alloys also demonstrated excellent antibacterial activity (with an antibacterial rate of up to 95% against *Staphylococcus aureus*) and enhanced corrosion resistance. Due to its combination of superior mechanical properties, corrosion resistance, and biological properties, Ti–5Mo–5Ag alloy is a viable candidate for load-bearing implants [533].

## 8. Biomechanical and bio-functional behavior of the implants in real service conditions

The clinical success of implants depends on their proper design, material selection, fabrication processes, and surface modification techniques, which enable the implants to meet biomechanics and bio-functional requirements under real usage conditions. In the following section, the tribo-mechanical properties of β –Ti alloys are introduced and discussed, along with the roles that the alloying elements and porosity play in this behavior. On the other hand, the most significant aspects and findings reported in the scientific literature are displayed in relation to the material's ability to osseointegrate and its behavior in the presence of bacteria.

### 8.1. Tribo-mechanical properties

Ti implants are widely applied in dental implants and load-bearing component of orthopaedic prostheses due to best specific mechanical properties, compared to austenitic stainless steel and cobalt-chromium-molybdenum (Co–Cr–Mo) alloys, as well as conventional bio ceramic and bio polymeric materials [534]. The criteria for specialized designs, such as load transmission, stress distribution, and implant articulation to facilitate movement in prosthetic knee joint applications, are likewise satisfied by metallic implants [13]. As mentioned in earlier sections, the selection of a chemical composition that allows for the manufacturing of alloys with a stabilized beta phase that reduces Young's module as well as controlling the porosity introduced must be appropriate so that the implant guarantees the performance of the bone tissue that it is designed to replace.

#### 8.1.1. Implants stiffness

The elastic modulus of human femur ranges from 6.9 to 25 GPa [535]. Contrastingly, the E for typical implant materials, such as CP-Ti and Co–Cr alloy, ranges from 100 GPa to 230 GPa [536,537]. Thus, materials with a low E near the human body are desired to increase the implant efficiency rate. The maximal elastic strain of materials used in orthopedic implants is one of their main attributes; it is approximately 1.1% for bone and roughly 3% for high-porosity Ti–Nb–Zr alloys, ensuring that the implant won't be damaged before the bone [538,539].

New Ti alloys with lower elastic modulus that are near- β and metastable- β and just comprise non-toxic metallic alloying elements like Nb, Ta, and Zr, etc. as prospective implant materials being researched with high mechanical characteristics [414]. Ta is believed to enhance mechanical efficiency and corrosion resistance while Zr is introduced to improve strength [414]. As a β stabilizing ingredient, Nb is introduced, and it also improves hot workability [414]. Due to their exceptional combination of high mechanical strength, low elastic modulus, outstanding biocorrosion resistance, no allergic issues, and good biocompatibility, β-Ti alloys containing Nb, Zr, Ta, Mo, Sn, etc. have recently attracted significant attention, particularly for orthopaedic implants applications. By altering the content of stabilizing elements, it has been discovered that their elastic modulus could be markedly reduced. Furthermore, these β-Ti alloys have exceptional resistance to corrosion in bodily fluid. This aspect is caused by the formation of a barrier-forming oxide coating that is rigid and strongly adhered [540]. Recent advancements have resulted in Ti alloy formulations that are specifically designed for biomedical uses. Some examples are Ti-In Ref. [61], Ti-Mo [234,236,541], Ti-Nb-Sn [242,542], Ti-Zr [543], and Ti–Ag alloys [544]. However, some alloying elements have not yet been extensively studied. Thus, several *in-vivo* biocompatibility tests must be performed to ensure their biological feasibility. In this context, these first-generation orthopaedic alloys included Ti–6Al–7Nb [545] and Ti–5Al-2.5Fe [546], two alloys that have Ti–6Al–4V's characteristics and were manufactured in response to issues about Vanadium 's potential cytotoxicity and unfavorable reactions with body tissues. The development of second-generation Ti orthopaedic alloys, such as Ti–12Mo–6Zr–2Fe "TMZF" [547], Ti–15Mo–5Zr–3Al [548], Ti–15Mo–3Nb–3O [549], Ti–15Zr–4Nb–2Ta-0.2Pd [550], Ti–15Sn–4Nb–2Ta-0.2Pd [551], and Ti–15Sn–4Nb–2Ta-0.2Pd alloys [551] in addition to the "totally biocompatible" Ti–13Nb–13Zr alloy [552] has further improved biocompatibility and resulted in a lower modulus. Finally, "TNZT" alloys based on the Ti–Nb–Ta–Zr system have attained lowest elastic moduli, notably through the invention of the "biocompatible" Ti35Nb5Ta7Zr alloy [344,553].

Although the bonding energy (determined by chemical composition and structure) strongly influences the elastic modulus, other parameters, such as density and crystallographic texture (especially in anisotropic materials) are also relevant. The crystal orientation has a considerable effect on the anisotropic characteristic of the elastic modulus of β-Ti alloys. Additionally, the processing method used to control the crystallographic texture affects how much Young's modulus is lowered in β-Ti alloys. According to Tane et al. [554], a single crystal of the low modulus TNTZ β-Ti alloy orientated in the 100 direction had a lower Young's modulus (35 GPa) than crystals oriented in the 111 and 110 directions. The impacts of crystal orientation on the alloy's Young's modulus were recently discussed in Wen Fang et al. [555] investigation of the texture evolution of a biomedical β-Ti alloy (Ti–28Nb–13Zr–2Fe) under 15%–85% cold rolling and 700–900 °C recrystallization annealing processing. Under a 15% drop, the Young's modulus showed the lowest value (54 GPa). After rolling (85% reduction) and annealing at 700 °C, a strong 111, 112 γ-fiber texture was produced that was advantageous for lowering Young's modulus in compared to a randomly oriented microstructure. Researchers validated that the gradual rotation of the slip plane 110 during plastic deformation encouraged the growth of the 001–110 texture component, which resulted in a significant reduction in Young's modulus.

On the other hand, porosity and pore size increase causes a reduction in the mechanical strength and stiffness, which can be crucial for the rehabilitation of load-bearing bones [556,557]. This issue can be addressed by employing an alloy whose elastic modulus is more comparable to that of bone [11]. The 3D printing of complex structures, particularly porous structures with carefully regulated micro-architecture, is made possible by the sintering or melting of Ti powders [316,558]. Therefore, the scaffold's outside shape can be tailored to resemble that of the lost bone, and its mechanical behaviour can be modified to accommodate the functional loads [558]. The long-term health issue brought on by the alloys' release of toxic ions and the stress shielding effect has been the focus of recent research efforts to find a solution [559]. On the other hand, porosity-graded materials also could avoid the drawbacks of porosity-induced strength reduction. Such a biomimetic approach for designing bone implants assures a more accurate copying of the biomaterial in accordance with its characteristics and microstructure (such as its density, modulus of elasticity), in addition to allow the bone ingrowth enhancing osseointegration and resulting in a more normal bonding between the tissue and the implant. Furthermore, an increased near-surface porosity facilitates the ability for tissue to expand into the implant's surfaces than a less porous core would [560]. An example of the above is a Ti–34Nb–6Sn that decreased the elastic modulus from 41 to 31 GPa and from 63 to 49 GPa when increasing the porosity from 23 to 30% and from 11 to 20 %, respectively [272]. Numerous Ti alloys are being developed by powder metallurgy and additive manufacturing to achieve functional porosity. Powder metallurgy can also take advantage of specific low-melting-point elements as spacers, i.e., to design functional porosity. In those cases, the toxicity of those elements should also be considered due to possible remaining traces [561]. Mg was recently applied as space holder to reduce the elastic modulus of Ti–Nb–Sn alloys [272]. With adequate ductility, as determined by the percent elongation or the percent reduction of area in a standard tensile test, strength values for orthopedic alloys are frequently acceptable, as shown in Table 7.

In Fig. 44, the influence of alloy composition by $Mo_{eq}$ on alloys stiffness is showed. Compared to the binary Ti–Nb and Ti–Mo alloys, the ternary alloys of Ti–Nb–Mo and Ti–Nb–Sn drastically lower their Young modulus, even with significant differences in the $Mo_{eq}$. Nevertheless, in terms of values similar $Mo_{eq}$ values, the ternary Ti–Nb–Fe alloys exhibit a larger E value. Meanwhile, the control of mechanical properties would be possible by the suitable design of more complex alloys with addition of β stabilizing element, as Mo, Nb or Sn, however this will come with a significantly higher cost.

In general, β-Ti alloys display a superior biomechanical equilibrium than other titanium alloys (E and YS), as is showed in Fig. 45. These enhanced tribomechanical properties of β-Ti alloys could allow the manufacture of titanium implants to replace organ tissue that has been damaged. The implementation of porosities in such alloys would let to porous titanium alloys with biomechanical performances similar to bones. The risk of the implant losing its structural integrity is reduced, since β-Ti alloys require significantly less porosities to achieve bone tissue mechanical properties, than other crystallographic phases of titanium alloys.

The method for determining Young's modulus in porous materials is controversial. Young's modulus values obtained by uniaxial compression testing are significantly lower than those acquired via dynamic tests. In the linear-elastic range of the studied materials, several scientists [274,623] related this discrepancy with super-elastic deformation; stiffness determined by the ultrasonic technique decreases with increasing porosity, in accordance with the elastic Eshelby-based hypothesis for closed spherical porosity [274,623]. Additionally, Niinomi et al. found that the instrumented micro-indentation test (P-h) offered significantly higher Young's modulus values than the free resonance or ultrasonic methods, whereas tensile testing provided slightly lower values [624]. However, a comparable tendency was noted for CP-Ti produced via a traditional powder-metallurgy method [274], as well as in more recent experiments utilizing space-holders (NaCl and $NH_4HCO_3$). The reason for these variances was determined to be the stiffness testing machine effect, which regarded the mechanical system and the sample like two springs strung together. Furthermore, the Ti matrix will vary in thickness at each cross-section of the cylindrical sample, causing the material to collapse at the point with the lowest Ti content. In the studies referred to above, and in others, the accuracy and precision of ultrasound measurements were validated by comparing them to widely recognized pore-elasticity models, such as Nielsen's [625].

### 8.1.2. Hardness

Brinell, Vickers, and nano-indentation techniques are only a few of the various ways to assess a material's hardness using its unique mechanical meanings. Unstrengthened β-Ti alloy has a substantially higher hardness than human bones [626]. It is crucial to increase hardness without lowering other qualities since it is difficult to jointly obtain, the desired combination of high hardness, low elastic modulus, and excellent biocompatibility. The most popular methods of surface modification for hardness improvement, include friction stir processing (FSP), ultrasonic nanocrystal surface modification (UNSM), laser surface treatment (LST), surface mechanical attrition treatment (SMAT), and equal channel angular pressing (ECAP).

Hardness enhancement is greatly aided by heat treatment. According to studies, air-cooling and water quenching were used to produce the Ti-xNb-3Zr–2Ta alloys (x = 33, 31, 29, 27, 25) (wt.%). With the niobium content being reduced, the hardness magnitude of both the water quenching and the air-cooling group greatly improved. Air cooling and water quenching, however, both use a distinct technique to increase the hardness. The volume fraction of the martensite phase improved the hardness for the water quenching group. The increase in hardness for the air-cooling group was attributed to the β matrix's lattice distortion [627].

Localized thermomechanical effects can be produced using the innovative solid-state surface modification technology known as friction stir processing (FSP). Wang et al. [628] studied the microhardness level of deformation stages from single pass to three passes at the exact rotation speed in order to change the surface of the newly developed Ti–35Nb–2Ta–3Zr (wt.%) alloy [629]. By using FSP, the microhardness increased from 189 HV to 208 HV. The microhardness was up to 247 HV after three passes. Additionally, to refine grains and improve mechanical properties, the Equal-Channel Angular Pressing (ECAP) technique can generate sizable uniform plastic stresses. The Ti–35Nb–3Zr–2Ta biomedical alloy reportedly obtained 216 HV in terms of hardness after

**Table 7**
Orthopaedic alloys designed for use in orthopaedic implants and their mechanical characteristics (Elastic modulus (E), yield strength (YS), and ultimate tensile strength (UTS)).

| ALLOY DESIGNATION | E (GPa) | YS (MPa) | UTS (MPa) | REFERENCE |
|---|---|---|---|---|
| **Ti–17Nb** | 84 | 640 | 768 | [562] |
| **Ti–27.5 Nb (at. %)** | 70 | 800 | 820 | [563] |
| **Ti–35Nb (wt.%)** | 75 | 343 | 555 | [564] |
| **Ti-40.5Nb** | 75.1 | – | 447 | [565] |
| **Ti–42Nb (wt.%)** | 60.51 | 674 | 683 | [566] |
| **Ti–45Nb (wt.%)** | 63 | – | 986 | [567] |
| **Ti–16Nb–10Zr** | 70 | 485 | 520 | [568] |
| **Ti–13Nb–13Zr** | 79–84 | 973–1037 | | [569] |
| **Ti–13Nb–13Zr** | 79 | 900 | 1030 | [570] |
| **Ti–34Nb–25Zr** | 62 | 810 | 839 | [565] |
| **Ti–28Nb–35.4Zr (wt.%)** | 63 | 611 | 633 | [571] |
| **Ti–31Nb-1.0Fe** | 81 | – | 477 | [572] |
| **Ti–27Nb-1.5Fe** | 94 | – | 496 | [573] |
| **Ti–23Nb-2.0Fe** | 95 | – | 604 | [572] |
| **Ti–19Nb-2.5Fe** | 90 | – | 672 | [573] |
| **Ti–15Nb-3.0Fe** | 94 | – | 695 | [573] |
| **Ti–11Nb-3.5Fe** | 97 | – | 715 | [573] |
| **Ti-38.1Nb-2.1Mo** | 54.5 | – | 663 | [574] |
| **Ti-39.9Nb-3.2Mo** | 67 | – | 535 | [574] |
| **Ti-39.3Nb-6.3Mo** | 63.6 | – | 621 | [574] |
| **Ti-38.7Nb-9.2Mo** | 55.7 | – | 634 | [574] |
| **Ti–32Nb–2Sn (wt.%)** | 93 | 870 | 930 | [575] |
| **Ti–32Nb–2Sn (wt.%)** | 82 | 900 | 1070 | [575] |
| **Ti–37Nb–6Sn (wt.%)** | 66 | – | 891 | [576] |
| **Ti-30.8Nb-9.8Sn** | 61 | – | 435 | [577] |
| **Ti-25.4Nb-10.1Sn** | 62 | – | 611 | [577] |
| **Ti-21.2Nb-10.4Sn** | 75 | – | 772 | [577] |
| **Ti-16.6Nb-10.6Sn** | 80 | – | 787 | [577] |
| **Ti–25Nb–16Hf (wt.%)** | 42 | 709 | – | [578] |
| **Ti–29Nb–13Ta–6Sn** | 65 | 523 | – | [579] |
| **Ti–29Nb–13Ta–2Sn** | 48 | 469 | – | [579] |
| **Ti–29Nb–13Ta–4.6Sn** | 78 | 513 | – | [579] |
| **Ti–30Nb–2Ta–3Zr** | 57.1 | – | 663 | [580] |
| **Ti–25Nb–2Ta–3Zr** | 75.2 | – | 864 | [581] |
| **Ti–30Nb–10Ta–5Zr** | 58 | 558 | 689 | [582] |
| **Ti–30Nb–10Ta–5Zr** | 66.9 | 804 | | [583] |
| **Ti–29Nb–13Ta–4.6Zr** | 60 | 800 | 1100 | [584] |
| **Ti–29Nb–13Ta–4.6Zr** | >80 | >1000 | >1001 | [585] |
| **Ti–29Nb–13Ta–4.6Zr** | 60 | | 549 | [586] |
| **Ti–29Nb–13Ta–4.6Zr** | 63 | 400 | | [579] |
| **Ti–29Nb–13Ta–4.6Zr (wt.%)** | ~ 80 | ~ 1000 | ~ 1100 | [571] |
| **Ti–29Nb–13Ta–4.6Zr (wt.%)** | ~ 90 | 1200 | – | [587] |
| **Ti–29Nb–13Ta–4.6Zr (wt.%)** | ~ 70 | ~ 900 | ~ 1000 | [588] |
| **Ti–29Nb–13Ta–4.6Zr (wt.%)** | 86 | – | 1375 | [589] |
| **Ti–29Nb–13Ta–4.6Zr (wt.%)** | 68 | ~400 | ~600 | [590] |
| **Ti–29Nb–13Ta–4.6Zr (wt.%)** | 70 | 900 | 1000 | [588] |
| **Ti–29Nb–13Ta–4.6Zr (wt.%)** | 50 | 490 | 740 | [591] |
| **Ti–35.3Nb–5.1Ta–7.1Zr** | 55 | 547 | 597 | [592] |
| **Ti–40Nb–2Ta–3Zr** | 57.8 | – | 589 | [580] |
| **Ti–35Nb–2Ta–3Zr** | 52 | – | 431 | [580] |
| **Ti–35Nb–2Ta–3Zr (wt.%)** | 50 | – | 896 | [411] |
| **Ti–35Nb–5Ta–7Zr (tnzt)** | 55 | 530 | 590 | [570] |
| **Ti–24Nb–4Zr–7.9Sn** | 46 | 700 | – | [579] |
| **Ti–24Nb–4Zr–7.6Sn (wt.%)** | ~75 | ~1000 | – | [593] |
| **Ti–24Nb–4Zr–7.9Sn (wt.%)** | 63.5 | 629 | 705 | [594] |
| **Ti–24Nb–4Zr–8Sn (wt.%)** | ~ 57 | – | 1050 | [595] |
| **Ti–24Nb–4Zr–8Sn (wt.%)** | 53 | 563 | 665 | [106] |
| **Ti–24Nb–4Zr–8Sn (wt.%)** | 56 | – | 1150 | [596] |
| **Ti–35Nb–7Zr–5Ta (wt.%)** | 93 | – | 2120 | [597] |
| **Ti–35Nb–7Zr–5Ta** | 55 | 823 | | [579] |
| **Ti–35Nb–3Zr–2Ta (wt.%)** | 59.3 | 389.9 | 765.4 | [598] |
| **Ti–25Nb–3Zr–3Mo–2Sn** | 80 | 946 | 1220 | [599] |
| **Ti–25Nb–3Zr–3Mo–2Sn (wt.%)** | 75 | 770 | >800 | [600] |
| **Ti–19Nb–1.5Mo–4Zr– 8Sn (wt.%)** | 55 | 823 | 973 | [601] |
| **Ti–29Nb–13Ta–4.6Zr–0.7 (wt.%)** | 80 | 1050 | 1100 | [602] |
| **Ti–32.5Nb–6.8Zr–2.7Sn (wt.%)** | 47 | – | 883 | [603] |
| **Ti–35Nb–5Ta–7Zr–0.4O** | 66 | 1010 | – | [604] |
| **Ti–35Nb–5Ta–7Zr-0.4 (TNZTO)** | 66 | 976 | 1010 | [570] |
| **Ti–35Nb–9Zr–6Mo–4Sn (wt.%)** | 65 | 925 | 950 | [605] |
| **Tiadyne 1610** | 81 | 736 | 851 | [98] |
| **Ti65.5Nb22.3Zr4.6Ta1.6Fe6 (at. %)** | 52 | 2475 | 2650 | [606] |
| **Ti–10Mo (wt.%)** | 47 | 690 | 731 | [607] |
| **Ti–12Mo–3Nb** | 105 | 450 | – | [608] |

(*continued on next page*)

**Table 7** (*continued*)

| ALLOY DESIGNATION | E (GPa) | YS (MPa) | UTS (MPa) | REFERENCE |
|---|---|---|---|---|
| **Ti–15Mo** | 78 | 544 | 874 | [98] |
| **Ti–15Mo (aged)** | 78 | 448 | | [579] |
| **Ti–4.7Mo–4.5Fe (at. %)** | 124 | – | 1390 | [572] |
| **Ti–15Mo–3Nb-0.3O (21SRx)** | 82 | 1020 | 1020 | [570] |
| **Ti–8Mo–4Nb–2Zr** | 35.4 | 798 | – | [609] |
| **Ti–8Mo–4Nb–5Zr** | 52 | 483 | – | [609] |
| **Ti–8Mo–5Nb–3Zr** | 69 | 947 | – | [609] |
| **Ti–8Mo–6Nb–4Zr** | 72 | 899 | – | [609] |
| **Ti–15Mo-2.8Nb–3Al** | 82 | 771 | 812 | [570] |
| **Ti–15Mo-2.8Nb–3Al** | 100 | 1215 | 1300 | [570] |
| **Ti–12Mo–6Zr–2Fe** | 74–85 | 1030–1100 | – | [610] |
| **Ti–15Mo–5Zr–3Al** | 75 | 838–1060 | – | [579] |
| **Ti–15Mo–5Zr–3Al** | 80 | 532 | – | [608] |
| **Ti–15Mo–5Zr–3Al** | 75 | 870–968 | 882–975 | [570] |
| **Ti–15Mo–5Zr–3Al** | 88–113 | 1087–1284 | 1099–1312 | [570] |
| **Ti–12Mo–6Zr–2Fe (TMZF)** | 74–85 | 1000–1060 | 1060–1100 | [570] |
| **Ti-4.8Mo-5.9Sn-18.5Nb-9.1Zr** | 72 | – | 519 | [572] |
| **Ti-4.9Mo–6Sn-14.2Nb-9.3Zr** | 56 | – | 701 | [577] |
| **Ti-5.2Mo-6.5Sn–10Zr-10.2Nb** | 43 | – | 577 | [436] |
| **Ti-5.3Mo-6.5Sn-10.2Nb–10Zr** | 48 | – | 715 | [580] |
| **Ti-5.3Mo-6.5Sn-15.2Nb–5Zr** | 55 | – | 692 | [572] |
| **Ti–5Mo-6.2Sn-9.7Nb-9.5Zr** | 54 | – | 715 | [572] |
| **Ti–15Mo–6zr– (1–4) Cr (wt.%)** | 86 | 1160 | – | [611] |
| **(Ti–23.72Nb4.83Zr1.74Ta)100-xSi** | 37 | 1296 | 3263 | [136] |
| **[(Mo0.5sn0.5)- (Ti13Zr1)] (Ti0.5Nb1.5)** | 56 | 566 | 701 | |
| **[(Mo0.5Sn0.5) -(Ti13Zr0.5Nb0.5)] Nb1** | 55 | 533 | 692 | |
| **[(Mo0.5Sn0.5) -(Ti13Zr1)] Nb1** | 48 | 478 | 715 | |
| **[(Mo0.5Sn0.5) -(Ti13Zr1)] Nb2** | 72 | 499 | 715 | |
| **[(Mo0.5Sn0.5)-Ti14] (Ti0.5Zr0.5Nb1)** | 59 | 275 | 762 | |
| **[(Mo0.5Sn0.5)-Ti14] (Zr1Nb1)** | 54 | 235 | 715 | |
| **Ti–30Zr–1Cr–5Mo** | 69.1 | – | 760 | [581] |
| **Ti–30Zr–2Cr–4Mo** | 64.2 | – | 780 | [581] |
| **Ti–30Zr–3Cr–3Mo** | 68.5 | – | 800 | [581] |
| **Ti–30Zr–4Cr** | 69.4 | – | 700 | [574] |
| **Ti–30Zr–5Cr** | 66.6 | – | 900 | [581] |
| **Ti–32Zr–30Nb** | 65 | 782 | 794 | [565] |
| **Ti–35.4Zr–28Nb** | 64 | 729 | 755 | [565] |
| **Ti–40.7Zr–24.8Nb** | 63 | 682 | 704 | [565] |
| **Ti–50Ta** | 88 | 380 | – | [608] |
| **Ti–25Ta–25Nb (wt.%)** | 92 | 2142 | 2423 | [612] |
| **Ti–50Ta (wt.%)** | 75.8 | 882 | 924 | [613] |
| **Ti–5Al–2.5Fe** | 110 | 1020 | – | [579] |
| **Ti–5Al—2.5Fe** | 110 | 914 | 1033 | [570] |
| **Ti-6-4 Eli** | 110 | 875 | 965 | [98] |
| **Ti–6Al–4V** | 113 | 1100 | – | [608] |
| **Ti–6Al–4V** | 110 | 850–900 | 960–970 | [570] |
| **Ti–6Al–7Nb** | 105 | 900 | – | [609] |
| **Ti–6Al–7Nb (protasul-100)** | 105 | 921 | 1024 | [570] |
| **Ti–6Al–7Nb (soln.)** | 110 | 110–1050 | – | [609] |
| **CP-Ti** | 105 | 692 | 785 | [570] |
| **Co–Cr–Mo** | 200–230 | 275–1585 | 600–1795 | [570] |
| **CP-Ti (grade 1–4)** | 102.7 | 170–485 | – | [614] |
| **Stainless steel 316L** | 200 | 170–750 | 465–950 | [570] |
| **Cp-Ti** | 109 | 607 | 758 | [565] |
| **Ti Grade IV** | 104.1 | 485 | 550 | [592] |
| **Porous titanium alloys** | | | | |
| **Ti-20.5Nb-5.6Zr 47.1 %** | 3.4 | – | [276] | [615] |
| **Ti-20.5Nb-5.6Zr 56.7 %** | 2.5 | – | [158] | [615] |
| **Ti-20.5Nb-5.6Zr 65.2 %** | 1.5 | – | [74] | [615] |
| **Ti–10Nb–10Zr 42%** | 21 | 368 | – | [616] |
| **Ti–10Nb–10Zr 50%** | 7.9 | 235 | – | [616] |
| **Ti–10Nb–10Zr 59%** | 5.6 | 137 | – | [616] |
| **Ti–10Nb–10Zr 69%** | 3.9 | 67 | – | [616] |
| **Ti–10Nb–10Zr 74%** | 1.6 | 27 | – | [616] |
| **Ti–35Nb 47.9%** | 7.7 | – | – | [617] |
| **Ti–13Nb–13Zr 39.9%** | 11.7 | – | – | [617] |
| **Ti–35Nb–7Zr–5Ta 42.5%** | 9.2 | – | – | [617] |
| **Ti–35Nb–5Ta–7Zr 40%** | 0.8 | – | – | [618] |
| **Ti–34Nb–6Sn 26%** | 14.1 | 245 | 590 | [60] |
| **Ti–34Nb–6Sn 22%** | 18.8 | 318 | 660 | [60] |
| **Ti-13-Nb-30Ta–2Mn 70.2 %** | 9.8 | 41.6 | – | [619] |
| **Ti–13Nb–30Ta–2Mn 69.2 %** | 10.1 | 52.7 | – | [619] |
| **Ti–13Nb–30Ta–4Mn 68.5 %** | 9.2 | 67.5 | – | [619] |
| **Ti–13Nb–30Ta–4Mn 68.7 %** | 8.3 | 42.3 | – | [619] |
| **Ti–13Nb–30Ta–6Mn 71.2 %** | 11.8 | 30.4 | – | [619] |
| **Ti–13Nb–30Ta–6Mn 70.8 %** | 9.8 | 43.3 | – | [619] |

(*continued on next page*)

**Table 7** (*continued*)

| ALLOY DESIGNATION | E (GPa) | YS (MPa) | UTS (MPa) | REFERENCE |
|---|---|---|---|---|
| **CP-Ti 39%** | 12.01 | – | – | [617] |
| **Ti–6Al–4V 40.6%** | 12.8 | – | – | [617] |

(–) means no available data.

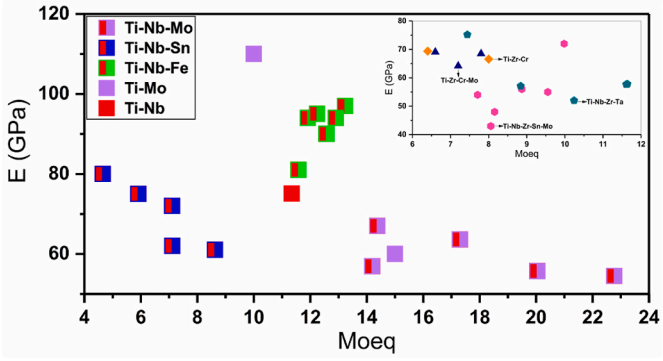


**Fig. 44.** A plot showing the modulus of elasticity, E (GPa) versus Mo equivalency (Moeq).

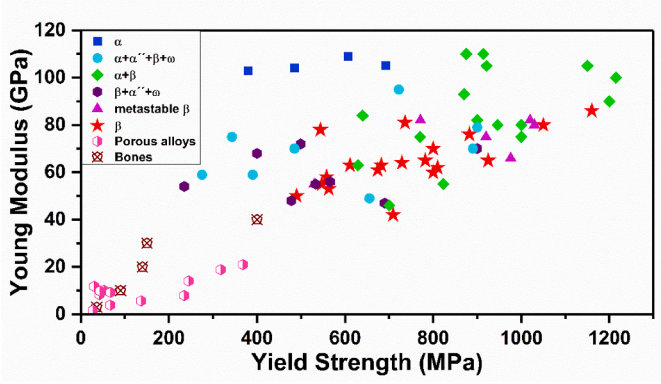


**Fig. 45.** A plot showing the modulus of elasticity, E (GPa) versus Yield Strength, YS (MPa) [620–622].

four passes, with finely ground grains and homogenous microstructures. In addition, a low elastic modulus of around 59 GPa was attained [598].

To enhance the hardness of the TNTZ alloy, Kheradmandfard et al. [630] treated it using the ultrasonic nanocrystal surface modification (UNSM) technique. As a result, the surface hardness increased from 195 HV to 385 HV; nevertheless, as one moves away from the surface, the rate at which surface hardness increases diminishes. Both grain refinement as well as a working hardening phenomenon are attributed for the UNSM's increase in hardness.

Chauhan et al. [631] modified the surface microstructure of VT3-1 α-β-Ti alloy by laser surface heat treatment (LST). LST was performed using a variety of laser energies (100–250 W) and scanning velocities (150–500 mm/min). A laser-affected zone has been analyzed using Electron backscatter diffraction (EBSD), which has revealed a unique microstructure that changes with laser power and scanning speed. A nearly β-complete -containing microstructure was formed at the surface with a high hardness level of 750 HV at a lower scanning speed (150 mm/min) and higher laser power (200 W). Hardness is improved by obtaining dendritic microstructures and uniform elemental distributions. On the other hand, in their investigation about re-melting on Ti–35Nb–2Ta–3Zr, Zhang et al. [632] also employed a laser. Laser re-melting of the material resulted in a change from an equiaxed crystal to a needle-like structure, which caused an increase in the average microhardness value from 165 HV to 264 HV. Moreover, the ECAP technology can generate sizable homogeneous plastic stresses to improve mechanical behaviour and purify grains.

Successful plasma electrolytic oxidation (PEO) coating development on the Ti–39Nb–6Zr alloy was achieved by Chen et al. [633], investigated the alloy's electrochemical corrosion and wear behavior prior to as well as following modification in PBS solution. The findings demonstrated that the Ti–39Nb–6Zr alloy in the PBS solution greatly enhanced its corrosion and wear resistance following PEO surface treatment.

### 8.1.3. Fatigue

Fatigue fracture initiation is typically observed to take place at stress concentration locations and manufacturing flaws in the metallic component, including holes, fillets, welds, notches, pits, and surface defects from machining procedures [634]. Fatigue could also initiate in microstructural imperfections, such as grain boundaries and non-metallic inclusions [635]. Cyclical loading is a known factor in the failure of orthopaedic implants over the course of their lifespans [636]. Through the phenomena of corrosion-fatigue, the corrosive physiological environment intensifies the damage done by fatigue. Micro-motions at implant interfaces may result in fretting fatigue, which in turn may lead to implant failure [637]. Biomedical Ti alloys must have fatigue strengths at least equal to and ideally higher than Ti–6Al–4V (700 MPa) [638]. It is crucial to first characterize and then appropriately enhance the fatigue resistance of Ti alloys. The alloy Ti–29Nb–13Ta-4.6Zr has been extensively studied for its fatigue properties [602,639]. In general, single β phase microstructures lack the necessary fatigue strength for load-bearing orthopaedic applications. In single β phase conditions, the fatigue strengths of alloys such Ti–29Nb–13Ta-4.6Zr [602], Ti–24Nb–4Zr– 8Sn [596], Ti–35Nb-2.5Sn [640], and Ti–35Nb [564] are, respectively, 320, 375, 225, and 275 MPa. These fatigue strength values are undoubtedly lower than those for Ti–6Al–4V [638]. Precipitation strengthening, plastic deformation, particle reinforcing, and adjustment of the O content are methods to boost the fatigue strength of Ti alloys. To enhance strength while keeping a lower modulus, Nakai et al. [641] regulated the precipitation of the phase during the aging of cold rolled Ti–29Nb–13Ta-4.6Zr. Yield strength increased from 700 to 900 MPa and fatigue strength increased concurrently from 350 to 600 MPa after 10.8 ks of aging at 300 °C [641]. The ductility of the material reduced to almost zero when aged for longer than 10.8 years, so fatigue strength tests were not conducted. The improvement in both tensile and fatigue strength was achieved while maintaining a modulus of less than 80 GPa. This was due to the texture of phase [641]. Achieving high fatigue strength requires both a boost in strength after precipitation and considerable ductility. A cold-rolled Ti–29Nb–13Ta-4.6Zr with the maximum strength was obtained by aging it at 325 °C. Ti–29Nb–13Ta-4.6Zr aged at 450 °C produced a steel with a lower degree of strengthening but acceptable ductility [585]. As a result, the fatigue strength after aging at 450 °C was substantially higher than the fatigue strength after aging at 325 °C [585].

Investigations have also been made into the impact of corrosive body environments on the fatigue life of Ti alloys [582,585,640]. The high cycle fatigue strength of Ti alloys is reported to be comparable in both air and corrosive environments that mimic the conditions of the human body, as described in a few reports [582,585,640]. It is most likely due to Ti alloys' excellent corrosion resistance. In contrast to the fatigue response to an airy environment, the fatigue response to an environment with corrosive compounds is dependent on the processing history. After water quenching and furnace cooling, the fatigue strength of

solution-treated Ti–35Nb alloy was similar in air and 0.9% NaCl (275 MPa), but lower in NaCl (150 MPa) than in air (225 MPa)) [564]. After furnace cooling, the fatigue strength was lower than it had been after water quenching, despite the initial strength being higher.

In Fig. 46, the limit and sensitivity ($\sigma_f$/UTS) to fatigue of some titanium alloys is showed. As is expected, regardless of the type of alloy, test with R = 0.1 has a higher fatigue life than test with R = −1, and has lower fatigue sensitivity (higher values). In comparison to biphasic alloys, fatigue resistance is generally improved by ternary and quaternary titanium alloys, with oxygen control being a key component of the alloys. In addition, Ti alloys' resistance to fatigue is decreased by the presence of pores, as shown in Fig. 47. Although pores are thought to be places where cracks form, they also function as a mechanism for making fractures more difficult to break (R-curve - "stop-hole"). Given that the implant's resistance to wear, it will rise once the pores have been filled with the bone tissue that grows inward, therefore, the combination of a sufficient number of pores could be an intriguing solution for fatigue limit improvement.

### 8.1.4. Wear

It is assumed that a material's wear resistance will grow as hardness increases. The wear resistance of three β-Ti alloys with the compositions Ti–24Nb–4Zr–8Sn, Ti–29Nb–13Ta–7Zr, and Ti–35Nb–4Sn was studied by Chapala et al. [644]. Due to the alloy's high-volume fraction of the high hardness phase, Ti–35Nb–4Sn had the best wear resistance. Likewise, due to the earlier alloy's higher hardness, Ti–15Zr-7.5Mo has better wear resistance than Ti–15Zr–15Mo [645]. Wear occurs to implants under physiologically wet environments. Because of this, tribological characteristics are frequently assessed in simulated body fluid. A

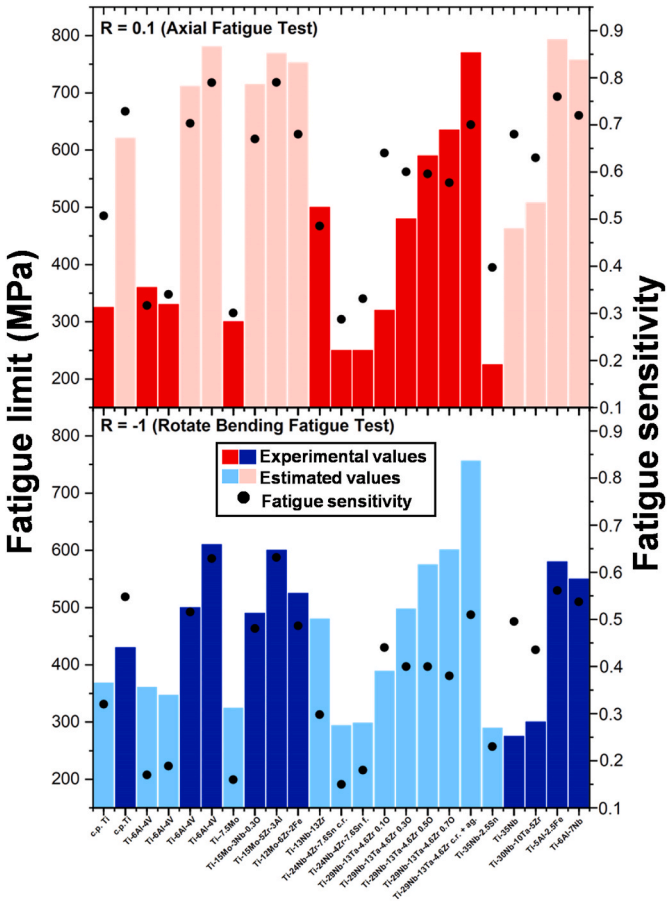


**Fig. 46.** Limit and sensitivity ($\sigma_f$/UTS) to fatigue of C.P. titanium and their alloys. Note: estimated values (using Goodman Equation) [570,585,593,602,639,640,642].

variety of studies have been conducted on tribo-corrosion, or pure wear behaviour in moist environments, while other studies evaluate the combined impact of wear and corrosion. Wet environments have the capability of speeding up as well as slowing down the wear rate of an alloy in a particular tribological system [646]. According to Yang et al. [547], in contrast to dry conditions, the wear rate of Ti–12Mo–6Zr–2Fe increased while that of Ti–6Al–4V decreased. In contrast, compared to dry conditions, the lubricating function of SBF decreased the wear of Ti–6Al–4V [547]. The wear rate of a Ti–29Nb–13Ta-4.6Zr disc against a ball of the same alloy was found to be higher in Ringer's solution than in a dry environment in another study [646]. Ringer's solution's presence made it possible to get rid of worn particles that was acting as a lubricant and speeding up wear. On the other hand, because the debris generated in Ringer's solution had no lubricating effect, the wear rate of a Ti–6Al–4V disc against a Ti–6Al–4V ball was lowered in comparison to air [646]. In comparison to Ti–6Al–4V, β-Ti alloys may have a reduced, equal, or greater wear rate. The tribological system has a significant influence on the wear response. Alumina or zirconia mating balls resulted in a higher and lower wear rate for Ti–29Nb–13Ta-4.6Zr, respectively, than Ti–6Al–4V [121]. Generally, β-Ti alloys' wear performance can be compared to Ti–6Al–4V. It is noteworthy that there is no literature that discusses the wear of several new compositions of titanium alloys.

The majority of the time, medicinal Ti alloys exhibit poor wear characteristics and are easily worn in the human body [647,648]. Large wear loss and high friction coefficients are regarded as negative aspects of tribological behaviour. Despite having a high corrosion resistance, the Ti alloys' protective oxide layer may become degraded during an infection or when in touch with biomolecules or physiological fluids that contain low oxygen. Several β-Ti alloys do not show a consistent trend in their wear rates when compared to Ti–6Al–4V. The tribological system has a major impact on how well β-Ti alloys resist wear [649]. The high volume fraction of the high hardness phase in the alloy is what gives the material its greatest wear resistance [644]. Clearly, the wear performance of Ti-based alloys remains an unresolved research issue, which offers numerous opportunities for improving its performance under, wear.

## 8.2. Corrosion resistance

Throughout their use in the human body, orthopaedic implants corrode. The physiological liquid which surrounds implants is a saline solution that contains $Na^+$, $Mg^{2+}$, $Cl^-$, $SO_4^{2-}$ and $HCO_3^{2-}$ ions [650]. Several factors contribute to the ability of metallic implants to resist corrosion. One such factor is the formation of a passive film, a stable, compact, and continuous oxide surface film that protects the underlying bare metal surface from corrosion [651]. Nevertheless, the passive layer may become dissolved locally, particularly by chloride ions, resulting in pits that spread rapidly and pitting corrosion. Implant composition should be carefully engineered and, as a result, must be highly corrosion resistant, to minimize adverse body reactions. When metal ions are liberated from an implant, they can elicit allergic reactions, cause localised tissue reactions, and raise the concentration of metal ions in bodily fluids, which can lead to toxicity [652]. This ion release is influenced by both the alloy's rate of corrosion and the solubility of the earliest corrosion products. To evaluate the long-term impacts of the porosity on the material's behaviour in physiological fluids, it is crucial to consider the corrosion process. Within seconds to minutes following implantation, the biomaterial's surface becomes covered in plasma/-tissue proteins. Monocytes attach to the protein-covered surface of the implant four to 8 h later and differentiate to macrophages, which generate a variety of growth factors, proinflammatory cytokines, and cytokines that promote fibrosis [29]. Additionally, damaging reactive oxygen species (ROS) are produced by surface-activated macrophages that might contribute to oxidative damage to the implant. Along with the locally elevated ROS content, neutrophils also produce lactic acid,

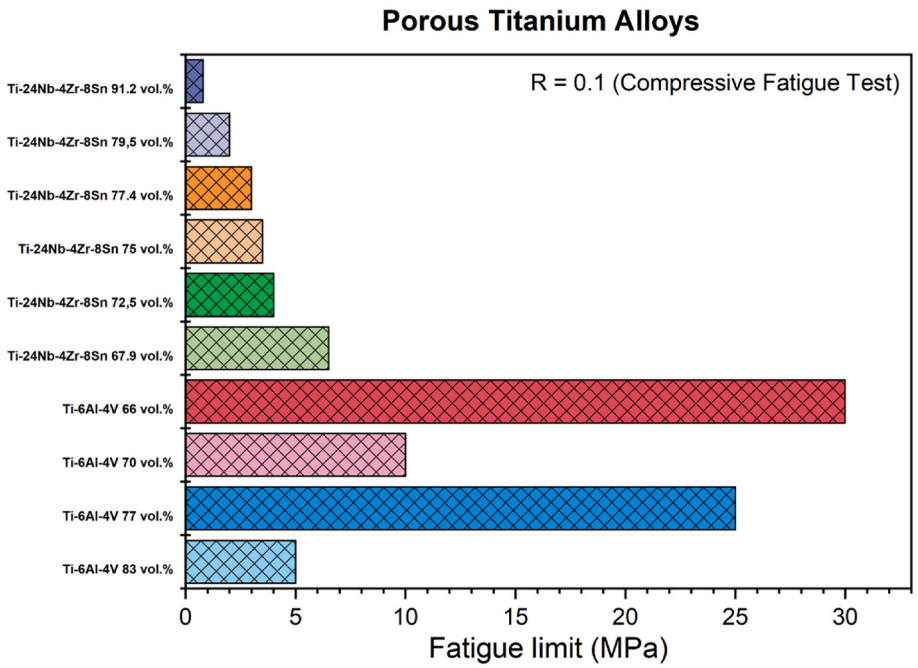


**Fig. 47.** Fatigue behavior of porous titanium alloys [337,643].

which reduces the pH of the surrounding microenvironment [653]. All these factors make metals more prone to corrosion. The composition of the implant is the core problem regarding corrosion resistance [654,655]. The question is how common alloying ingredients are employed in Ti alloys. According to Okazaki et al., adding Zr, Nb, Ta, and a tiny amount of Pd reduces the critical current density for passivation *Ic*. An upward trend in the *Ic* value was seen when Sn was employed in place of Zr in Ti alloys [656]. The obtained *Ic* values for Ti–Zr alloys were significantly lower than for Ti–6Al–4V ELI, although they were higher for Ti–Sn alloys. Whenever the final corrosion potential ($E_{corr}$) value drops along with the metal's porosity, porous metals become susceptible to localised corrosion [29]. It was hypothesised that relatively small, isolated pores produced by denser compacts would favor the trapping of electrolyte species and the depletion of oxygen, both of which are essential for maintaining a stable titanium oxide layer [29].

Ti alloys are the good choice for orthopaedic applications owing to their excellent corrosion resistance. Ti is corrosion resistant in a wide range of environments due to the stable thin $TiO_2$ layer that is formed on its surface [121]. β-Ti alloys have a remarkable resistance to corrosion, as shown by their low corrosion rates, which vary from $10^{-9}$ to $10^{-7}$ A/cm$^2$ [657]. Comparing a β-Ti alloy's corrosion resistance to Ti–6Al–4V or CP-Ti is a common way to evaluate its corrosion resistance. The corrosion resistance of β-Ti alloys may be superior to CP-Ti or Ti–6Al–4V [55], equal to Ref. [658], or worse to Ref. [659]. The rates of corrosion are influenced by several variables, including alloying elements, microstructure, and corrosive media. The relationship between alloying elements and corrosion resistance may be explained by their impact characteristics of the oxide layer in β-Ti alloys. The mechanism by which Nb improves the corrosion resistance of Ti–6Al–6Nb alloy is one such leading example [660]. The presence of lower valence $Ti^{+3}$ ions cause oxygen vacancies in the oxide, which are diminished by the higher valence $Nb^{+5}$ ions [660]. Thus, as the number of defects in the oxide layer decreases, corrosion resistance also increases [660]. The corrosion rate may also change due to phase transformation during thermomechanical treatment. After subjecting the Ti–32Nb–2Sn alloy to a surface mechanical attrition procedure, researchers noticed an increase in the corrosion rate because the microstructure's heterogeneity had grown [661]. Additionally, the corrosion media significantly affects how quickly alloys corrode [662]. This brings attention to a crucial point when assessing the corrosion rate of β-Ti alloys. It is important to highlight that the temperature used for the corrosion testing in simulated environments is either room temperature or that of a human being. Furthermore, the implants will encounter a different environment *in-vivo* than they will in an artificial environment that is simulated with a variety of electrolytes, such as simulated body fluid (SBF), Ringer's solution, phosphate buffer saline (PBS), Hank's balanced salt solution (HBSS). As a result, *in-vivo* animal tests are necessary to accurately assess the corrosion resistance of recently developed Ti alloys.

In this regard, the chemical composition of the alloy and the presence of pores have a significant impact on the corrosion resistance of Ti implants. Since allergic, toxic/cytotoxic, or carcinogenic species (such as Ni, Co, Cr, V, or Al) may be released into the body during corrosion processes, this is quite concerning in the case of metal implants and devices for *in-vivo* service [644]. In contrast to Ti–6Al–4V alloys, Ti–35Nb–7Zr–5Ta alloy does not contain any of these elements. Additionally, earlier research shows that Ti–Al–V and TNZT alloys display various levels of corrosion resistance in simulated fluids, including Hank's solution [663], Ringer's solution [664,665]. However, as they increase the surface area exposed to an aggressive environment, alloy porosity content, shape, and distribution also affect the corrosion properties of porous Ti and its alloys [666,667]. For instance, Xu et al. noticed that when Ti–10Mo alloy manufactured using powder metallurgy and the space holder technique was exposed to naturally aerated phosphate buffered saline solution, the corrosion rate increased exponentially from 1.6 g/m$^2$ day to 17.1 g/m$^2$ day when the porosity increased from 2.8 to 66.9% [667]. Additionally, crevice corrosion is driven on by high and interconnected porosities [668]. However, from a corrosion and protection perspective, an increase in porosity does not always result in a worsening of the implant's corrosion behaviour. Contrarily, there is broad agreement that increased porosity can be quite advantageous since it dramatically improves the infiltration and adherence of various coatings, which, in turn, significantly improves their corrosion protection compared to their totally dense counterparts [669].

### 8.2.1. *Electrochemical behavior*

Corrosion is a degradation process involving multiple simultaneous electrochemical reactions between oxidized (anode) and reduced

(cathode) regions placed in contact by a conductive medium (electrolyte) [670]. From section 2 (Table 1), Ti matrix possesses higher electronegativity than other more active metals such as Mg and Al. From the above, CP-Ti has been widely applied due to its high corrosion resistance. However, the mechanical characteristics of CP-Ti are not suitable for the high-impact or cyclic load required for articulation implants. The requirement for mechanically resistant, low-elastic-modulus, and non-toxic alloy systems is an immediate worldwide priority to attend to the increasing demand for implant procedures [671,672].

As seen in section 2, the corrosion susceptibility of Ti alloys is strongly influenced by their chemical composition and the natural oxide passivation layer on Ti. A $TiO_2$ surface passive layer forms when Ti encounters the air, improving the corrosion resistance [70]. However, the surface layer can be broken by atomic diffusion of alloying elements, like V [70]. Chemical heterogeneities might also trigger the formation of micro-galvanic couplings, i.e., regions with high electrochemical potential disparities. Micro-galvanic couplings encourage the breakage of the passive film [82] and corrosion losses. Since the passive oxide film limits the ionic and electronic migration across the oxide/body fluid interface, its breakage allows corrosion on the implant.

Besides chemical composition, the electrochemical performance is also determined by the microstructural features and the service environment, which are the focus of this section.

### 8.2.2. *Microstructural effect in corrosion behavior*

Pitting, also known as localized corrosion, may lead to premature implant failure. Defects in the microstructure, such as interfaces (grain boundaries, multiphasic borders, different defects transitions, etc.), chemical heterogeneities (inclusions, intermetallic particles, segregates, etc), pores, among others, are preferred pitting nucleation sites in Ti alloys [673–675]. The preferred attack is based on the higher energy and cation mobility at defects compared to the homogeneous inner grain regions [676]. In the case of porous structures, the pores reduce the oxygen supply, allow $Cl^-$ adsorption, and trigger higher electronic donor density [673]. The previous conditions accelerate the dissolution of the oxide film in the porous materials. The negative impact of pores on the corrosion resistance of NiTi and Ti–39Nb alloys has been reported [677,678].

Regarding interfaces in metallic materials, intergranular corrosion occurs preferentially at high-energy grain boundaries (HAGBs) than at low-energy grain boundaries (LAGBs) [679]. However, HAGBs also promote the atomic diffusion to form thick surface passive layers [673]. Considering that twin are less energetic than HAGBs [680], it may be interesting to study the effect of high-dense twined microstructures on the corrosion resistance compared to that in high-dense HAGBs Ti alloys. These systematic studies remain a future opportunity for research.

In general, corrosion resistance is associated to coarse (micrometric grained) alloys due to their lower defects (grain boundaries) density compared to nanostructured or ultrafine materials, i.e., coarse materials have less preferred sites for the corrosion [681]. However, low density of grain boundaries also decreases the sites for adherence of the surface passive layer compared to fine-grained systems [682–684]. The high density of grain boundaries and triple junctions (intersection of least-wise three different neighboring grains in nanostructured alloys results in better atomic diffusion and well-adhered passive layers [685]. Thus, nanostructured materials have more uniform and compact surface passive surface layers compared to those in coarse-grained alloys [684]. As a result, nano-grained materials have a low susceptibility to localized corrosion. One example is the wrought and EBM Ti–6Al–4V alloys, where the EBM showed better oxide film stability due to higher grain boundary density [686]. However, the high density of defects in fine-grained materials increases the surface energy and the chemical activity in non-passivating media [684].Therefore, grain size may have a dual effect on the electrochemical behavior of Ti alloys, being strongly dependent on the severity of the corrosive environment [683]. Nanostructured alloys may show low corrosion susceptibility in passivating environments, and increase it in non-passivating media [683].

Regarding multiphasic microstructures, the coexistence of different phases, such as HCP-α, BCC-β, HCP-α′, orthorhombic-α′’, or HCP-ω, encourage electrochemical potential disparities. The reason for such electrochemical disparities is the different chemical concentrations along the phases. It is expected that the β- and α-phases will have a higher concentration of β- and α-stabilizers (described in section 2), respectively. As a result, each phase will have different electrochemical potential and corrosion performance [687,688]. The galvanic activity might also trigger stress corrosion cracking (SCC) in Ti alloys, where the cathodic and anodic regions will be determined by the chemical composition of the present phases. As an example of the above, the β-Ti phase has been reported as more susceptible to corrosion than the α-Ti phase of V-bearing Ti alloys [70]. However, the β-phase was more electrochemically resistant than the α-Ti phase when Nb, Mo, and Zr β-stabilizers were present [77]. Besides multiphasic microstructures, galvanic couplings can also be formed by impurities on the microstructure.

The volume fraction and distribution of the cathodic and anodic regions through the microstructures also impact the corrosion performance of the alloy. Two parameters were described to study this effect size; 1) a critical dimension (λ) of the electrochemical cell big enough to affect the distribution of current density on the system, and 2) the path length between anode and cathode ($L$). If the ratio $\lambda/L$ is low, then a uniform current distribution might be expected through the system. Contrastingly, for large $\lambda/L$, the current density is not expected to be uniform, and the corrosion is controlled by the electrical resistance of the electrolyte [689]. Simulations on Al alloys have agreed with the previous phenomena [690]. From the above, if the anodic area is too small (below 0.5 μm for Al-alloys [690]), the ionic transportation is restricted, and local corrosion stabilizes. For much larger anodic than cathodic areas, there is not enough driving force to activate the anodic dissolution. Besides, a small inter-cathodic distance encourages local acidification. However, the previous simulation was based on Al alloys. Different crystallographic anisotropy, chemical composition, and activation energies may be expected for Ti alloys. Thus, systematic modeling and experimental studies about the anode/cathode effect size in Ti alloys remain a future opportunity for researchers.

### 8.2.3. *Effect of the environment*

The prosthetic materials are subjected to severe requirements to safeguard the safety of the patients. The shelf life and stability in the human environment are critical factors for their feasibility as biomedical materials. The body fluids can be a severely corrosive environment for many metallic materials. As a reference, serum and interstitial fluids can hold concentrations of $Cl^-$ of about 113–117 mEq $l^{-1}$ [692]. The body fluids are electrolytes rich in different ionic species, such as $Na^+$, $Ca^{2+}$, $PO_4^{3-}$, $SO_4^{2-}$, etc., that cause degradation on the implant surface. Furthermore, there is a high concentration of dissolved oxygen in the blood and intercellular spaces [691]. If the material is designed for dental applications, the ionic $F^-$ concentration also becomes a significant challenge. The aforementioned conditions constitute a severe corrosive media for implant materials. Thus, the implant material should be electrochemically stable under different *in-vitro* and *in-vivo* corrosive media, simulating the physiological body fluids or the oral environment.

As body fluids, which are almost water, will surround the implant, depending on the hydrophobicity, the water molecules might be dissociated, chemisorb (undissociated), or physiosorbed. Thus, the interactions between water-oxide may be covalent, ionic, or Van der Waals' types [691]. The hydrated oxide film surface is, therefore, an electrolyte medium. However, its electronic conductivity is inherent to its chemical bonding and structure. The $TiO_2$ is considered an *n*-type semiconductor.

$Cl^-$ rich electrolytes are other common corrosive media used to test biomedical Ti alloys. The potential-pH diagrams, also known as Pourbaix diagrams, are useful to predict the passivation or corrosion

behavior of Ti when immersed in a corrosive medium as a function of the pH. Examples of Pourbaix diagrams for Ti when immersed in water and chloride solutions at 25 °C and 37 °C can be found in the literature [692,693]. It should be mentioned that 37 °C corresponds to the average body core temperature [694] and is commonly used for simulating Ti alloys in body fluids environments. Examples of the above are the ion release assessments from Ti–In, Ti–34Nb–6Sn, and Ti–6Al–4V alloys at 37 °C in artificial saliva [59–61].

Ti alloys form a spontaneous protective oxide film of $TiO_2$ at specific pH and potentials that may vary with the corrosive media chemistry and the activated electrochemical reactions. As the electrochemical potential and available chemical species for electrochemical reactions vary for different Ti alloys, their Pourbaix diagrams may also vary.

#### 8.2.4. Microbial corrosion

Biofilms formed by bacteria may influence (accelerate or reduce) the implant degradation during service [695,696]. Biofilms produce corrosive metabolites, such as organic and inorganic acids [697–699], which assist on the formation of local oxygen/ion concentration cells. Those factors are responsible for the occurrence of microbiologically influenced corrosion (MIC), i.e., acceleration or inhibition of corrosion by microorganisms [697]. From the literature, the main pathogenic species influencing orthopedic implant infections are *S. aureus* (34%), *S. epidermis* (32%), Pseudomonas (8%), Enterococcus (5%), among others [95]. Raising or decreasing the corrosion rates by MIC depends on the type of pathogens involved and the characteristics of the media [700].

Surface roughness, chemical composition, microstructure, temperature, kind of pathogen, and nutrients content at the media influence the bacterial attachment and biofilm formation [697,701]. An example of affecting microstructural factors is porosity. *Staphylococcus aureus* was found to adhere and colonize the surface of porous Ti–6Al–4V alloy, changing the oxide layer composition due to the increment of metabolic products [702]. Besides, as explained in previous section 7.1., diverse defects may encourage pitting formation, as well as bacteria adherence.

MIC may involve high risk of implant failure due to the generation of pitting. Pitting breaks the Ti-rich oxide passive layer, allowing the infiltration of ions, such as $Cl^-$, $F^-$, etc. Furthermore, the kinetics and severity of MIC are still unpredictable. Regardless of the good corrosion resistance of Ti alloys, pitting by MIC is so far inevitable and frequently leads to premature implant failure or revision surgeries. The risk of infection from 0.5 to 5% of the total joint replacements is estimated to occur due to microbes [95]. Tailoring chemical composition can assist microbiologically influenced corrosion (MIC) mitigation on Ti alloys. Different β- or nearly β-Ti alloys have developed antimicrobial properties due to adding antimicrobial metallic elements [532,533,526,703].

Many metallic elements are reported as promising antimicrobial materials. They are an alternative against the microbes' multidrug resistance that has been encouraged by the extensive use of antibiotics [704]. Silver and copper are some of the most effective metals against multiple pathogens, including bacteria, viruses, fungi, and algae [705]. Both metals are efficient against several pathogens, including *Influenza H1N1, Candida albicans, Salmonella enterica, SARS-CoV-2, Escherichia coli, and Staphylococcus aureus,* among others [705–707]. However, Cu provides a more cost-efficient route than Ag. From the previous section 2.6., designing low-cost implant materials is a priority.

However, the implant material should compromise efficient mechanical properties, low toxicity, biocompatibility, and good corrosion performance. Thus, attention should be paid to certain trade-offs such as antimicrobial properties-corrosion. An example of the above is the addition of Cu and Ag in a Ti matrix, which generated galvanic pairs due to segregates or intermetallic phases [82].

### 8.3. In-vitro behavior of prosthesis based on β-Ti

The *in-vitro* evaluation of different aspects that prosthesis usually tackle is a key issue to prevent early failure. In this section will be detailed most critical strategies to investigate new insights into mechanisms, impact of alloy composition with coating and non-coating approaches as depicted in Fig. 48.

#### 8.3.1. Antibacterial properties

Due to the host tissue's inability to generate or sustain osseointegration, prosthetic joint bacterial infections and consequent aseptic loosening are among the most frequent complications following prosthesis or implant surgery [708–710]. Depending on the type of cell wall they possess, bacteria are either classified as Gram-positive or Gram-negative. The lack of a membrane in the peptidoglycan thick external layer of Gram-positive bacteria makes it extremely beneficial for antibiotic targeting. Gram-negative bacteria are wrapped by an outer cell membrane and cytoplasmic membrane, with a thinner layer of peptidoglycan (2–3 nm) in between them that is known as the periplasmic space. The oral cavity contains a complex microbial flora that is in homeostasis, however an imbalance carried on by surgery may imply the colonization of new pathogenic microorganisms, such as bacteria, that might easily infect this cavity. Gram-positive dental infections include *Eubacterium nodatum, Filifactor alocis, Slackia exigua, Parvimonas micra, Staphylococcus aureus, Staphylococcus Warneri, and Streptococcus intermedius*; the corresponding gram-negative, *Bacteroides fragilis, Prevotella intermedia, Porphyromona gingivalis, Treponema denticola, Tannerella forsythia, Aggregatibacter actinomycetemcomitans, Campylobacter rectus, Treponema socranskii, and Pseudomonas aeruginosa* are among examples. Moreover, *S. aureus* is a common bacterium in various prosthetic infections. *E. aureus aeruginosa, E. coli,* and *S. E. Epidermidis S. faecalis C. lutea* and *albicans* [711,712]. In this sense, following implant surgery, there is a phenomenon known as the "race for the surface," in which bacteria, macrophages, fibroblasts, and even platelets are drawn to the surface, especially when it is 50 nm or less away from the implant so they can adhere to it [713,714]. In a second step, the bacteria colonization spreads the formed and matured biofilm infection, affecting not only the implant but also the tissues after the bacteria proliferation [715]. In fact, the basis of bacterial reduction strategies is anti-adhesion to a metal surface, anti-colonization, anti-biofilm, or even anti-proliferative strategies. It is established that *S. aureus* can infect bone canaliculi, forming a bacterial reservoir that can result in chronic or recurrent infections like osteomyelitis [716]. The spread of bacterial


**Fig. 48.** Research activities concerning antibacterial behavior aspects.

biofilms can occur quite quickly; in one study that used a pig model, the bacterial biofilm had spread to the surroundings in just six days [715].

There are numerous established approaches for assessing the antibacterial activity of solid materials, the majority of which rely on one or more of the agar diffusion plate test, plate count method, or live/dead stain techniques [82]. For the agar diffusion method, a hot agar solution is poured onto sterilized Petri dishes, and then a suspension of bacteria is sprayed over the Petri dish. A test sample, a control sample, and a positive sample are each placed in contact with the agar separately. They are then incubated for 18–24 h at (37 ± 1) °C. The width of the inhibition zone, which is used to quantify antibacterial activity, ought to be up to 1 mm to qualify as having good antibacterial effects. In the plate-count method, a bacterial suspension (approx. 0.4 mL) is poured onto the sample, control sample, and the negative sample, and they are incubated at (35 ± 1) °C for 24 h. After the incubation, the active bacteria colonies are counted. The live/dead stain method evaluates bacterial adhesion, death, or biofilm formation. In this case, the bacterial suspension is dripped onto the samples, or the sample is immersed inside a bacterial suspension after incubation at 37 °C for 24 h.

The diagnosis of a prosthesis infection is frequently difficult to accomplish since it may require a joint aspiration and analysis of leukocyte, *D*-lactate, or protein levels [717,718], and it is challenging to be treated because it frequently entails high costs and loss of quality of life [719]. Unfortunately, the idiosyncrasy of bone tissue exhibiting a peculiar pharmacokinetic environment and undesirable metabolic reactions, facilitated by the infection, usually offer difficult circumstances to use clinical antibiotic therapy [720,721]. Furthermore, antibiotic resistance, which occurs as a result of their use and leads to a change in which they lose their ability to kill or stop bacterial growth, is also based on a number of mechanisms, including enzymatic inactivation or a decrease in membrane permeability, and is unfortunately growing to be a significant public threat on a global scale. Hence, antibiotic intake should be controlled to avoid excessive or misuse to ensure the success of antimicrobials in treating infections. To preserve the functionality of implanted devices exhibiting optimal characteristics at the biomaterial-tissue interface and to ensure that implanted devices remain functional in situ, several innovations dealing with surface treatments, based on coated or non-coated methodologies, or biofilm microbiology, have been developed to tackle these issues.

i. Coating methods:

It is known that antibacterial prosthesis containing metallic materials inhibits regular mechanism of bacteria. For instance, to increase wear resistance as well as antibacterial properties, TiN coatings have been fabricated [722,723], although they have not been clinically evaluated a decrease of bacteria is produced caused from the incorporation of hydroxyapatite (HAp) using a low-cost plasma spraying [724–726]. Other approaches including sol-gel methods with antibacterial entities, such as silver nanoparticles, could provoke undesirable chemical structures or delamination in numerous cases, but fortunately on the other hand, it implements mechanical properties and decrease the possible adherence of S. aureus bacteria in a rate of 99.3%, after 24 h [727]. Also, methods such as PVD (Physical Vapor Deposition) [347,348,728], easily suffers delamination, although they increase wear resistance, but the presence of silver in these cases guarantees the antimicrobial properties against methicillin-sensitive S. epidermidis [729]. Furthermore, bioactive glasses such as BGF18 has shown important anti-biofilm behavior at low concentrations (1.34 mg/mL) for P. aeruginosa and S. epidermidis, also promoting osseointegration mechanism [730]. Additionally, other approaches concerning antibiotic coatings have been developed, although resistance issues are always an important drawback, as already mentioned [718].

ii. Non-coating methods:

Another promising area of research to induce antibacterial properties is the use of acid etching on the Ti surface. CP-Ti and Ti–6Al–4V, has been used in this sense, also implemented with silver ions to exert this action, but unfortunately residual ions are commonly introduced in surrounding tissues [731]. It is well established that smoother surfaces implement bacteria growth, so studies to induce irregularities are appropriated. Laser Treatments, also with CP-Ti and Ti–6Al–4V has been evaluated and this is considered a promising research area to combat infections. Electrochemical anodization has accomplished good results *in-vivo*, but unfortunately is associated with a lack of uniformity although it displayed bactericidal properties when the fabricated nanotubes were combined with gentamicin/chitosan against *S. aureus* [732]. Interestingly, metals and alloys containing Ti and other metals such as Cu or Ag has been described to provide adequate antibacterial behavior [733–739]. More recent findings use stainless steel, or include other alloys with cobalt, zinc, or magnesium to induce antibacterial properties and that fulfill mechanical properties, corrosion resistance and biocompatibility as well [82,740]. In general, β-Ti alloys do not exhibit antibacterial characteristics, and after surgery the implants usually suffer infection [626]. Therefore, it is critical and significant to endow the antibacterial property of β-Ti alloys via surface implementation. In this sense, laser-nitrided surfaces could induce significant antibacterial effect as shown by Chang et al., that employed an automated fiber laser system (Micro Laser Systems) with Ti–30Nb–4Sn alloy to reduce the S. aureus biofilm coverage ten times [741]. Similar surface fabrication procedure using Ti–35Nb–7Zr–6Ta (TNZT) was evaluated with S. aureus, to show a decrease of the bacteria percentage from 5% to less than 1%, and it seems that TiN in the outermost surface oxide could improve biocompatibility and antibacterial behavior [530]. The fabrication of Ti–13Nb–13Zr–5Cu alloy proportioned good antibacterial property (S. aureus> 90%), due to the precipitation of the Ti2Cu phase [742]. Furthermore, Liu et al. prepared SLA–TiCu using a combined sandblasting and large-grits etching (SLA) methodology to increase antibacterial rate against S. aureus [743]. An alternative for surface Ti–Mo alloys to bear appropriated texture was used with an electron beam surface combined with a thermal treatment to enhanced antifouling against S. aureus, as it was described by Ferraris et al. [744]. Other alloys based on Ti–Mn–Cu alloys are potential candidates and have shown that the more content of Cu added, the less colonies of E. coli colonies are present around the implant. Furthermore, Ti5Cu and Ti–10Cu sintered alloys can be considered materials with antibacterial ability within the Food Safety Standard [529].

### 8.3.2. *Biocompatibility evaluation*

Ti alloys are simply made using non-toxic alloying ingredients to increase biocompatibility. However, it is crucial to evaluate the biocompatibility of new compositions and associated processing impacts [553]. The cytotoxicity of alloys is frequently assessed using the fibroblasts' viability. Investigations have revealed that various β-Ti alloy compositions are similarly biocompatible compared to either CP-Ti or Ti–6Al–4V. A limited number of studies claim that β-Ti alloys perform better than CP-Ti or Ti–6Al–4V in *in-vitro* osteogenic differentiation [745,746]. Alteration in the passive layer's characteristics and the emission of metal ions that promote osteogenic differentiation were both suggested as causes of the improvement [745,746]. The proposed alloys are assessed for their inflammatory response in addition to cell viability and differentiation. The inflammatory response of alloys is assessed by measuring the amounts of macrophage-released cytokines *in-vitro*. Low levels of inflammation are reported for β-Ti alloys, which are equivalent to CP-Ti and Ti–6Al–4V [747]. The adhesion of stem cells to severely deformed surfaces of aged Ti–32Nb–2Sn alloy, on the other hand, revealed a decrease, but proliferation and osteogenic differentiation were increased [661]. The increased focal adhesions of stem cells induced by roughness were attributed for the higher proliferation and differentiation. Generally, *in-vitro* experiments have proven that β-Ti alloys are biocompatible. It is crucial to understand that different

materials may have different biological responses when used *in-vivo*. The *in-vivo* reaction of only a few compositions of β-Ti alloys has been studied. The *in-vivo* bone tissue biocompatibility of β-Ti alloys is measured using variables including bone to tissue volume ratio, bone apposition ratio, bone implant contact, and new bone area. The majority of the time, the alloys are implanted in the femur (or tibia) of rabbits [748,749]. According to Prado et al. [617], Ti–35Nb–7Zr–5Ta had a higher bone to tissue volume ratio and more bone implant contact than CP-Ti. Similar to this, it was discovered that Ti–Mo based alloys had larger new bone areas at 26 weeks than Ti–6Al–4V [750]. Contrary to the alloys, Ti–6Al–4V showed a reduction in bone area with an increase in time from 12 to 26 weeks [750]. Due to their lower modulus than Ti–6Al–4V, the alloy did not experience bone loss [750]. However, several investigations [662,748,749] have revealed that CP-Ti/Ti–6Al–4V and β-Ti alloys exhibit comparable *in-vivo* responses. Overall, β-Ti alloys appear to meet the requirements established by CP-Ti or Ti–6Al–4V tested *in-vivo*. To determine the biocompatibility of β-Ti alloys, however, significant, and prolonged *in-vivo* testing is required. For instance, the release of metal ions after implantation and their potential harmful effects have not been studied.

i. *In-vitro* assessments

The studies concerning the biocompatibility describe all the appropriate biological requirements, host response and capacity of a prosthesis to be used as a medical device in a specific application. It is also one of the mandatory requirements for the clinical use of biomaterials to evaluate potential injurious and toxic effects of biological systems. Specifically, cell biocompatibility that compile numerous studies related to cell viability, apoptosis, differentiation, or migration. In the last decade, it has been described through a bionic perspective that the acquisition of similar human bone structure topography and morphology is critical to the potential biological activity of Ti implants, in terms of cell growth and osseointegration [751]. The micro-topography on the surface could be obtain via sandblasting, acid etching, anodizing, spin-coating, sputtering deposition, or introducing other active materials for an implementation [39,752,753]. Hence, Kheradmandfard et al., described a gradient nanostructure layer on the TNTZ surface bearing a microstructure composed of nanoflakes with a width of 60–200 nm, to demonstrate induced enhanced cell adhesion, osteoblast differentiation, excellent osseointegration using mesenchymal stem cells [630]. It was concluded that this micro-pattern favored excellent bone regeneration as well as biological activity. Recently Yao et al. have published that commercial purity Ti bearing an ultra-fine-grained structure, influences the increased osteoblast adhesion due to the increased number of grain boundary sites [754]. In the Ti alloys it has been widely described that the ions from some of the elements such as Cu or Ag could cause cytotoxicity [82]. If the alloy exerts no damage, it has been described that on the surfaces the cell should have a polygonal shape containing a numerous lamellipodia or filopodia [755]. Also, alloys could not only bear antibacterial atoms, but they could also contain Zn or Mg ion to promote stimulation for osteogenesis as well as viability, proliferation, and adhesion [756,757].

In general, β-Ti alloys made up of non-toxic elements (Nb, Ta, and Mo, Zr, Au, and Sn) are biocompatible devices and acceptable mechanical and chemical properties, with an elasticity comparable to cortical bone, with a superior cell response and osteo-compatibility, to be employed as implant [122]. The Ti–45Nb binary alloy with β-Ti phase exhibit good mechanical properties bearing convenient balance between low elastic modulus (64.3 GPa), high tensile strength (527 MPa) and high hardness (233.4 MPa), and a controlled chemical corrosion [662]. Also, it is known that both L929 and MG-63 cells presented good rates of attachment, proliferation, differentiation on the surface, influencing a good bone tissue compatibility, compared to that of pure Ti. In this sense, Chernozen et al. have described the preparation and comparison of hybrid composites based on β-alloy Ti−xNb and oxide nanotubes, to highlight that the best hMSC cell adhesion after 24 h was observed for the NTs, obtained at an anodization with an inner diameter of ~50 nm, also hMSC proliferation exhibit better results on flat substrates [758].

In conclusion, surface nanostructurization of NTs with a diameter of ~50 nm is more favorable than fabricated NTs with a larger inner diameter. Bai et al. have fabricated a Ti–45Nb binary alloy with β-Ti phase with appropriate mechanical and chemical performance (low elastic modulus, high tensile strength and high hardness, good corrosion resistance), that after *in-vitro* cytotoxicity evaluation, reflected that both L929 and MG-63 cells presented a convenient attachment, proliferation, differentiation, and what it has formed critical new bone and tissue formation (identical to pure Ti) [662]. With regard to Ti–25Nb–11Sn alloy disks, another example includes cell culture tests (L929 and MC3T3-E1) that showed good proliferation, similar relative cell growth ratios, and relative absorbance ratios when compared to Ti–6Al–4V alloy and CP-Ti, along with surface stability and appositional new bone formation around the rods, after histopathological examination [748]. This result suggests that the cytotoxicity is identical if compared to Ti–6Al–4V alloy or CP-Ti, already in the market. Moreover, new beta Ti–Mo–Nb alloy compositions lead to good biocompatibility in terms of adhesion, morphology, proliferation, no critical inflammatory response was described in RAW 264.7 macrophages and differentiation potential of MC3T3-E1 pre-osteoblasts if compared to CP-Ti [759]. Other combination for alloys such as Ti–25Nb–11Sn alloy has demonstrated that direct contact cell culture tests two types of cells exhibit good proliferation, compared to Ti–6Al–4V alloy and CP-Ti [748]. Besides, it was concluded that it is a bioinert material with bone tissue compatibility, good surface stability and has demonstrated appositional new bone formation in rods, one of the mail requirements for use in the orthopedic area. Also, Donaghy et al. described a fiber laser treatment for TNZT alloys that studies dealing with cell attachment, proliferation, and differentiation of MSCs promote significant decrease for bacteria adhesion [474]. In this case, the texture acquired is a critical feature that induce nano-topography to increase surface area that enables a more easily attachment of cells since this is related to the protein interactions, filaments, and tubules, which controls cell signaling and regulates cell functionality as well. The same author reported in 2019 that nitrided surfaces showed important antibacterial effect but offered no advantage to MSC response for beta TNZT alloys [760]. Ferraris et al., established that the procedure of electron beam technology applied to Ti15Mo alloys to obtain parallel grooves with 10 μm showed that they can support gingival fibroblast adhesion and alignment with no bacterial contamination [744]. Hence, this is an example that highlight that without the use of a lot of active agents, often associated to cytotoxicity and regulatory problems, the biological behavior could be improved. In summary, to validate the clinical translation of prosthesis based on β-Ti, is clear that more research is required on these topics.

ii. In-*vivo* assessments

In the early to mid-1960s, Branemark and his colleagues performed *in-vivo* tests on dogs and rabbits using Ti implants, and they observed that the implants were perfectly implanted into the bone without inflaming it. This marked the beginning of titanium's use in dental implants [761]. *In-vivo* studies are critical to implement prosthesis due to the limitations offered by the presence of multispecies such as pathogens, fibrinogen, fibronectin, collagen, plasma albumin, or immune system cell and diverse body fluids. However, in general to establish reliable *in-vivo* procedures is not an easy task, and it usually takes a long time, is also expensive and requires specialist manipulation. That could be presumably the reason why there are only few examples in the literature concerning these kinds of combined studies focused on the use of β-Ti alloys for example, in the case of the Ti–Cu alloy, an *in-vivo* study was carried out using rabbits [762]. Briefly, bacterium was implanted in the muscle and pathological observation, the white blood cell test and the plate-count method were analyzed to observe a general appearance.

Also, Niinomi et al. reported that TNTZ alloy can promote bone remodeling, although it has a low elastic modulus that inhibit its practical use for prosthesis [763]. In this case, the X-ray photographs of intramedullary rods show a clear bone formation as well as the pictures of extracted bone plates fixed to tibiae. An alternative alloy, the Ti–15Mo–1Bi, although does not exhibit appropriate mechanical properties if compared to others Ti Mo alloys, however the addition of Bi with antibacterial behavior has been used to implement its use in clinical [750]. Besides, *in-vivo* experiments employing 6 mm × 32 mm metal pin implanted into the epicondyle of rabbit femur, has shown excellent new bone growth (the new bone measured 249%), and better persistence of the deposited surrounded tissue, if compared to Ti–6Al–4V after 26 weeks. In summary, although only few examples of *in-vivo* experiments have been described, no drawbacks have been found when using β-Ti alloys, so new and exciting data would probably be expected to be compiled in the near future in this area.

## 9. Conclusion and future topics

Ti alloys is a metal with numerous advantageous properties, including light weight, substantial strength, and superior corrosion resistance. The strategy to obtain strength comparable to or even superior to Ti–6Al–4V while maintaining a low modulus is the main motivation behind β-Ti alloys development. The likelihood of cytotoxicity is diminished by using non-toxic constituent elements. The main motivation of ongoing research in the field of β -type Ti-based super elastic alloys is the need for a metallic implant material that unites super elasticity with biocompatibility comparable to that of pure Ti and Ti–6Al–4V alloys. It is crucial to evaluate how processing affects a broad range of material performance metrics, including biocompatibility, corrosion resistance, fatigue resistance, and tribological performance. Data on how processing influences the fatigue and tribological performance of β-Ti alloys is woefully missing in the literature. Furthermore, it is crucial to confirm the long-term biocompatibility of these metals utilizing ethical *in-vivo* tests using large animal models.

Future advancements in the investigation of β-Ti alloys for orthopedics can be made in the following crucial sectors:

1. New medical devices should be made using material computing science, to mimic the evolution of microstructures during processing and their impact on mechanical characteristics, sophisticated approaches, such as phase modeling, can be applied. A phase-field model, for instance, can be used to represent the rapid growth that takes place during aging treatments. Then, mechanical properties might be predicted using the developed microstructure. In order to create new β-Ti alloy compositions, first principle calculations might be expanded further.
2. To improve thermomechanical processing so that alloys have improved fatigue and wear resistance, research should be supported. This could be accomplished by creating high throughput approaches for determining acceptable microstructures.
3. Investigating whether peptides comprising the amino acids arginine, glycine, and aspartic acid (RGD), which have been demonstrated to regulate osteoblast adhesion, would encourage osteoblast differentiation when attached to a β-Ti surface.
4. Long-term biocompatibility must be determined using large animal models. These investigations may emphasize on the quantity of leached metal ions and their cytotoxic effects, corrosion rate, production of wear debris and consequent inflammatory response, osseointegration, and stress shielding effect. The performance of these materials should be assessed using commercially available medical device simulators in addition to *in-vivo* tests. Additionally, exploring new chemical entities currently in development could be an intriguing aspect to consider as a supplement to antibacterial properties when incorporated into coatings as a preventative measure.

Assuming ongoing research efforts are focused on eventually engineering high performance orthopedic devices, Ti alloys have the potential to become the next generation of materials for orthopedic applications.

## Author contributions

Amir A. Elhadad: Writing – original draft, Writing – review & editing. L. Romero-Resendiz: Conceptualization, editing. M. C. Rossi: Writing – original draft, Writing – review & editing. L. M. Rodríguez-Albelo: Writing – original draft, Writing – review & editing. Sheila Lascano: Writing – original draft, Writing – review & editing. Conrado R M Afonso: Writing – original draft, Writing – review & editing. A. Alcudia: Writing – original draft, Writing – review & editing. V. Amigó: Writing – original draft, Writing – review & editing. Yadir Torres: Conceptualization, Methodology, Project administration, Funding acquisition.

## Funding

This publication has been part of the following projects:

- *R+D+i* projects PDC2022-133369-I00 and PID2022-137911OB-I00, financed by MCIN/AEI/10.13039/501100011033/
- CNPq Universal Project #422015/2018-0 (C.R.M.A.);
- FAPESP (São Paulo Research Foundation) for financial support through “Projeto Temático” # 2018/18293-8, post doc Grant # 2021/03865-9 (M.C.R.)

## Data availability

No data was used for the research described in the article.

## Declaration of competing interest

The authors declare that they have no known competing financial interests or personal relationships that could have appeared to influence the work reported in this paper.

## References

[1] Amini AR, Laurencin CT, Nukavarapu SP. Bone tissue engineering: recent advances and challenges. Crit Rev Biomed Eng 2012;40.
[2] Kumar S, Kumar R. Role and selection consideration of metallic biomaterial: a study. i-Manager's Journal on Material Science 2021;9:13.
[3] Ho-Shui-Ling A, et al. Bone regeneration strategies: engineered scaffolds, bioactive molecules and stem cells current stage and future perspectives. Biomaterials 2018;180:143–62.
[4] Annar D, et al. Body structural and cellular aging of women with low socioeconomic status in Hungary: a pilot study. Am J Hum Biol 2022;34:e23662.
[5] Barranco V, Jiménez-Morales A, Hickman G, Galván J, Perry C. Triethylphosphite as a network forming agent enhances in vitro biocompatibility and corrosion protection of hybrid organic–inorganic sol–gel coatings for Ti6Al4V alloys. J Mater Chem B 2014;2:7955–63.
[6] Prasad K, et al. Metallic biomaterials: current challenges and opportunities. Materials 2017;10:884.
[7] Javaid M, Haleem A. Additive manufacturing applications in orthopaedics: a review. Journal of clinical orthopaedics and trauma 2018;9:202–6.
[8] Sallent I, et al. The few who made it: commercially and clinically successful innovative bone grafts. Front Bioeng Biotechnol 2020;8:952.
[9] Elhadad AA, Alcudia A, Begines B, Pérez-Soriano EM, Torres Y. A multidisciplinary perspective on the latest trends in artificial cartilage fabrication to mimic real tissue. Appl Mater Today 2022;29:101603.
[10] Morris MT, Tarpada SP, Cho W. Bone graft materials for posterolateral fusion made simple: a systematic review. Eur Spine J 2018;27:1856–67.
[11] Delgado-Pujol EJ, et al. Porous beta titanium alloy coated with a therapeutic biopolymeric composite to improve tribomechanical and biofunctional balance. Mater Chem Phys 2023;300:127559.
[12] Han Q, Wang C, Chen H, Zhao X, Wang J. Porous tantalum and titanium in orthopedics: a review. ACS Biomater Sci Eng 2019;5:5798–824.
[13] Saini M, Singh Y, Arora P, Arora V, Jain K. Implant biomaterials: a comprehensive review. World Journal of Clinical Cases: WJCC 2015;3:52.
[14] Barranco V, et al. Enhancing in vitro biocompatibility and corrosion protection of organic–inorganic hybrid sol–gel films with nanocrystalline hydroxyapatite. J Mater Chem B 2014;2:3886–96.

[15] Zhang L, et al. Structure design of porous TC4 alloy with excellent mechanical properties prepared by laser-powder bed fusion. Vacuum 2024;220:112818.
[16] Wang H, et al. Influence of bonding time during diffusion bonding of Ti–6Al–4V to AISI 321 stainless steel on metallurgical and mechanical properties. Vacuum 2024;222:113072.
[17] Hu J, Zhong X, Fu X. Enhanced bone remodeling effects of low-modulus Ti–5Zr–3Sn–5Mo–25Nb alloy implanted in the mandible of Beagle dogs under delayed loading. ACS Omega 2019;4:18653–62. https://doi.org/10.1021/acsomega.9b02580.
[18] Katti KS, Verma D, Katti DR. In: Revell Peter A, editor. Joint replacement technology. Woodhead Publishing; 2008. p. 81–104.
[19] El Hadad AA, et al. Biocompatibility and corrosion protection behaviour of hydroxyapatite sol-gel-derived coatings on Ti6Al4V alloy. Materials 2017;10:94.
[20] Mohammed MT, Khan ZA, Siddiquee AN. Beta titanium alloys: the lowest elastic modulus for biomedical applications: a review. Int. J. Chem. Mol. Nucl. Mater. Metall. Eng 2014;8:726.
[21] Parvizi J, Gehrke T. Definition of periprosthetic joint infection. J Arthroplasty 2014;29:1331.
[22] Nicholson W, Titanium J. Alloys for dental implants: a review. Prosthesis 2020;2:11.
[23] Izakovicova P, Borens O, Trampuz A. Periprosthetic joint infection: current concepts and outlook. EFORT open reviews 2019;4:482–94.
[24] Xie KY, et al. Nanocrystalline β-Ti alloy with high hardness, low Young's modulus and excellent in vitro biocompatibility for biomedical applications. Mater Sci Eng C 2013;33:3530–6.
[25] Bocchetta P, et al. Passive layers and corrosion resistance of biomedical Ti-6Al-4V and β-Ti alloys. Coatings 2021;11:487.
[26] Prakash C, Kansal H, Pabla B, Puri S. Multi-objective optimization of powder mixed electric discharge machining parameters for fabrication of biocompatible layer on β-Ti alloy using NSGA-II coupled with Taguchi based response surface methodology. J Mech Sci Technol 2016;30:4195–204.
[27] Pesode P, Barve S. A review—metastable β titanium alloy for biomedical applications. J Eng Appl Sci 2023;70:25.
[28] Shalabi M, Gortemaker A, Hof MVt, Jansen J, Creugers N. Implant surface roughness and bone healing: a systematic review. J Dent Res 2006;85:496–500.
[29] Pałka K, Pokrowiecki R. Porous titanium implants: a review. Adv Eng Mater 2018;20:1700648.
[30] Ko S, et al. Osteoconductivity of porous titanium structure on implants in osteoporosis. J Dent Res 2021;100:1178–85.
[31] Merheb J, et al. Influence of skeletal and local bone density on dental implant stability in patients with osteoporosis. Clin Implant Dent Relat Res 2016;18:253–60.
[32] Salimov F, et al. Evaluation of relationship between preoperative bone density values derived from cone beam computed tomography and implant stability parameters: a clinical study. Clin Oral Implants Res 2014;25:1016–21.
[33] Xiong Y, Qian C, Sun J. Fabrication of porous titanium implants by three-dimensional printing and sintering at different temperatures. Dent Mater J 2012;31:815–20.
[34] Wang X, et al. Topological design and additive manufacturing of porous metals for bone scaffolds and orthopaedic implants: a review. Biomaterials 2016;83:127–41.
[35] Hou C, et al. Additive manufacturing of functionally graded porous titanium scaffolds for dental applications. Biomater Adv 2022;139:213018. https://doi.org/10.1016/j.bioadv.2022.213018.
[36] Raza D, et al. Development and heat treatment of β-phase titanium alloy for orthopedic application. Mater Today Proc 2022;50:649–54.
[37] Karre R, Dey SR. In: Abdul-Ghani Olabi, editor. Encyclopedia of Smart materials. Elsevier; 2019. p. 512–27.
[38] Liu S, et al. Superelastic behavior of in-situ eutectic-reaction manufactured high strength 3D porous NiTi-Nb scaffold. Scripta Mater 2020;181:121–6.
[39] Barranco, V., Jiménez-Morales, A., Peon, E. & Galván, J. in *Journal of Physics: Conference series.* 012007 (IOP Publishing).
[40] Haase, F. et al. in *MATEC Web of Conferences.* 05008 EDP Sciences).
[41] Nam SM, et al. Effects of aluminum on the reduction of neural stem cells, proliferating cells, and differentiating neuroblasts in the dentate gyrus of D-galactose-treated mice via increasing oxidative stress. J Vet Sci 2016;17:127–36.
[42] Mouro VG, et al. How bad is aluminum exposure to reproductive parameters in rats? Biol Trace Elem Res 2018;183:314–24.
[43] Ochmański W, Barabasz W. Aluminum–occurrence and toxicity for organisms. Przegl Lek 2000;57:665–8.
[44] Alrabeah GO, Knowles JC, Petridis H. The effect of platform switching on the levels of metal ion release from different implant–abutment couples. Int J Oral Sci 2016;8:117–25.
[45] Imura H, et al. Vanadium toxicity in mice: possible impairment of lipid metabolism and mucosal epithelial cell necrosis in the small intestine. Toxicol Pathol 2013;41:842–56.
[46] Sánchez-Lara E, et al. A one-dimensional supramolecular chain based on [H 2 V 10 O 28] 4− units decorated with 4-dimethylaminopyridinium ions: an experimental and theoretical characterization. New J Chem 2019;43:17746–55.
[47] Sansone V, Pagani D, Melato M. The effects on bone cells of metal ions released from orthopaedic implants. A review. Clinical Cases in Mineral and Bone Metabolism 2013;10:34.
[48] Mirzajavadkhan A, Rafieian S, Hasan MH. Toxicity of metal implants and their interactions with stem cells: a review. International Journal of Engineering Materials and Manufacture 2020;5:2–11.
[49] Sawicka E, Długosz A. The role of 17β-estradiol metabolites in chromium-induced oxidative stress. Adv Clin Exp Med 2017;26:215–21.
[50] Murray FJ, Tyl RW, Sullivan FM, Tiwary AK, Carey S. Developmental toxicity study of sodium molybdate dihydrate administered in the diet to Sprague Dawley rats. Reprod Toxicol 2014;49:202–8.
[51] Murray FJ, Sullivan FM, Hubbard SA, Hoberman AM, Carey S. A two-generation reproductive toxicity study of sodium molybdate dihydrate administered in drinking water or diet to Sprague-Dawley rats. Reprod Toxicol 2019;84:75–92.
[52] Huat TJ, et al. Metal toxicity links to Alzheimer's disease and neuroinflammation. J Mol Biol 2019;431:1843–68.
[53] Kepp KP, Squitti R. Copper imbalance in Alzheimer's disease: Convergence of the chemistry and the clinic. Coord Chem Rev 2019;397:168–87.
[54] Correa D, et al. The effect of the solute on the structure, selected mechanical properties, and biocompatibility of Ti–Zr system alloys for dental applications. Mater Sci Eng C 2014;34:354–9.
[55] Hussein AH, Gepreel MA-H, Gouda MK, Hefnawy AM, Kandil SH. Biocompatibility of new Ti–Nb–Ta base alloys. Mater Sci Eng C 2016;61:574–8.
[56] Kreitcberg A, Brailovski V, Prokoshkin S. New biocompatible near-beta Ti-Zr-Nb alloy processed by laser powder bed fusion: process optimization. J Mater Process Technol 2018;252:821–9.
[57] Luo J, et al. Additively manufactured biomedical Ti-Nb-Ta-Zr lattices with tunable Young's modulus: mechanical property, biocompatibility, and proteomics analysis. Mater Sci Eng C 2020;114:110903.
[58] Li S, Nam T-h. Superelasticity and tensile strength of Ti-Zr-Nb-Sn alloys with high Zr content for biomedical applications. Intermetallics 2019;112:106545.
[59] Romero-Resendiz L, et al. Microstructural, mechanical, electrochemical, and biological studies of an electron beam melted Ti-6Al-4V alloy. Mater Today Commun 2022;31:103337.
[60] Correa-Rossi M, et al. Mechanical, corrosion, and ion release studies of Ti-34Nb-6Sn alloy with comparable to the bone elastic modulus by powder metallurgy method. Powders 2022;1:3–17.
[61] Romero-Resendiz L, Gómez-Sáez P, Vicente-Escuder A, Amigó-Borrás V. Development of Ti–In alloys by powder metallurgy for application as dental biomaterial. J Mater Res Technol 2021;11:1719–29.
[62] Dilea M, Mazare A, Ionita D, Demetrescu I. Comparison between corrosion behaviour of implant alloys Ti6Al7Nb and Ti6Al4Zr in artificial saliva. Mater Corros 2013;64:493–9.
[63] Marshall TA, Warren JJ, Hand JS, Xie X-J, Stumbo PJ. Oral health, nutrient intake and dietary quality in the very old. J Am Dent Assoc 2002;133:1369–79.
[64] Hemendinger RA, Armstrong III EJ, Brooks BR. Methyl Vitamin B12 but not methylfolate rescues a motor neuron-like cell line from homocysteine-mediated cell death. Toxicol Appl Pharmacol 2011;251:217–25.
[65] Schmalz G, Arenholt-Bindslev D, Pfüller S, Schweikl H. Cytotoxicity of metal cations used in dental cast alloys. Altern Lab Anim 1997;25:323–30.
[66] Gülden M, Mörchel S, Seibert H. Factors influencing nominal effective concentrations of chemical compounds in vitro: cell concentration. Toxicol Vitro 2001;15:233–43.
[67] Zhou Y, et al. Electrospun water-soluble carboxyethyl chitosan/poly (vinyl alcohol) nanofibrous membrane as potential wound dressing for skin regeneration. Biomacromolecules 2008;9:349–54.
[68] Sun D, et al. An investigation of the antibacterial ability and cytotoxicity of a novel cu-bearing 317L stainless steel. Sci Rep 2016;6:1–13.
[69] Batsanov SS. The concept of electronegativity. Conclusions and prospects. Russ Chem Rev 1968;37:332.
[70] Atapour M, Pilchak A, Frankel G, Williams J. Corrosion behavior of β titanium alloys for biomedical applications. Mater Sci Eng C 2011;31:885–91.
[71] Afzali P, Ghomashchi R, Oskouei RH. On the corrosion Behaviour of low modulus titanium alloys for medical implant applications: a review. Metals 2019;9:878.
[72] Lu J, et al. Effect of microstructure characteristic on mechanical properties and corrosion behavior of new high strength Ti-1300 beta titanium alloy. J Alloys Compd 2017;727:1126–35.
[73] Ibrahim KM, Moustafa MM, Al-Grafi MW, El-Bagoury N, Amin MA. Effect of solution heat treatment on microstructure and wear and corrosion behavior of a two phase β-metastable titanium alloy. Int J Electrochem Sci 2016;11:3206–26.
[74] Deng J, et al. Electrochemical behavior and microstructural characterization of lanthanum-doped titanium-zirconium-molybdenum alloy. J Alloys Compd 2018;763:687–94.
[75] He X, Noël J, Shoesmith D. Effects of iron content on microstructure and crevice corrosion of grade-2 titanium. Corrosion 2004;60:378–86.
[76] Zhang E, Wang X, Chen M, Hou B. Effect of the existing form of Cu element on the mechanical properties, bio-corrosion and antibacterial properties of Ti-Cu alloys for biomedical application. Mater Sci Eng C 2016;69:1210–21.
[77] Su B, et al. Annealed microstructure dependent corrosion behavior of Ti-6Al-3Nb-2Zr-1Mo alloy. J Mater Sci Technol 2021;62:234–48.
[78] Mareci D, Bocanu C, Aelenei N, Nemtoi G. Galvanic corrosion between Ti/Ti6Al4V and various dental alloys. Eurasian Chemico-Technological Journal 2004;6:221–6.
[79] Taher NM, Al Jabab AS. Galvanic corrosion behavior of implant suprastructure dental alloys. Dent Mater 2003;19:54–9.
[80] Grosgogeat B, Reclaru L, Lissac M, Dalard F. Measurement and evaluation of galvanic corrosion between titanium/Ti6Al4V implants and dental alloys by electrochemical techniques and auger spectrometry. Biomaterials 1999;20:933–41.
[81] Chen L-Y, Cui Y-W, Zhang L-C. Recent development in beta titanium alloys for biomedical applications. Metals 2020;10:1139.

[82] Zhang E, et al. Antibacterial metals and alloys for potential biomedical implants. Bioact Mater 2021;6:2569–612.
[83] Zhang LC, Chen LY. A review on biomedical titanium alloys: recent progress and prospect. Adv Eng Mater 2019;21:1801215.
[84] Davis P, et al. Phase separation in Ti-6Al-4V alloys with boron additions for biomedical applications: scanning kelvin probe force microscopy investigation of microgalvanic couples and corrosion initiation. Jom 2017;69:1446–54.
[85] Meng F, et al. Characterization of Ti powders mixed with TiO2 powders: thermal and kinetic studies. J Loss Prev Process Ind 2020;66:104184.
[86] Reding NS, Shiflett MB. Metal dust explosion hazards: a technical review. Ind Eng Chem Res 2018;57:11473–82.
[87] Gharagheizi F. An accurate model for prediction of autoignition temperature of pure compounds. J Hazard Mater 2011;189:211–21.
[88] Jacobson M, Cooper A, Nagy J. Explosivity of metal powders. In: Rapport d'étude RI 6561. US Bureau of Mines; 1964.
[89] Lee J, Nersisyan H, Won C. The combustion synthesis of iron group metal fine powders. J Solid State Chem 2004;177:251–6.
[90] Yavor Y, Goroshin S, Bergthorson JM, Frost DL. Comparative reactivity of industrial metal powders with water for hydrogen production. Int J Hydrogen Energy 2015;40:1026–36.
[91] Piskulich ZA, Mesele OO, Thompson WH. Activation energies and beyond. J Phys Chem 2019;123:7185–94.
[92] James W. Powder metallurgy methods and applications, vol. 7. ASM International; 2015.
[93] Froes F, Mashl S, Hebeisen J, Moxson V, Duz V. The technologies of titanium powder metallurgy. Jom 2004;56:46–8.
[94] Emelogu A, Marufuzzaman M, Thompson SM, Shamsaei N, Bian L. Additive manufacturing of biomedical implants: a feasibility assessment via supply-chain cost analysis. Addit Manuf 2016;11:97–113.
[95] Campoccia D, Montanaro L, Arciola CR. The significance of infection related to orthopedic devices and issues of antibiotic resistance. Biomaterials 2006;27:2331–9.
[96] Kolli RP, Joost WJ, Ankem S. Phase stability and stress-induced transformations in beta titanium alloys. Jom 2015;67:1273–80.
[97] Liang S. Review of the design of titanium alloys with low elastic modulus as implant materials. Adv Eng Mater 2020;22:2000555.
[98] Wang K. The use of titanium for medical applications in the USA. Mater Sci Eng, A 1996;213:134–7.
[99] Duan R, et al. A high strength and low modulus metastable β Ti-12Mo-6Zr-2Fe alloy fabricated by laser powder bed fusion in-situ alloying. Addit Manuf 2021;37:101708.
[100] Zhou L, et al. Effects of Ta content on phase transformation in selective laser melting processed Ti-13Nb-13Zr alloy and its correlation with elastic properties. Vacuum 2021;183:109798.
[101] Tendero I, et al. Laser surface modification in Ti-xNb-yMo alloys prepared by powder metallurgy. Metals 2021;11:367.
[102] Li Y-H, Chen R-B, Qi G-x, Wang Z-T, Deng Z-Y. Powder sintering of porous Ti–15Mo alloy from TiH2 and Mo powders. J Alloys Compd 2009;485:215–8.
[103] Min X, et al. Effect of oxygen content on deformation mode and corrosion behavior in β-type Ti-Mo alloy. Mater Sci Eng, A 2017;684:534–41.
[104] Nomura N, et al. Mechanical properties of porous Ti–15Mo–5Zr–3Al compacts prepared by powder sintering. Mater Sci Eng C 2005;25:330–5.
[105] Koizumi H, et al. Castability and mechanical properties of Ti-15Mo-5Zr-3Al alloy in dental casting. J Oral Sci 2018;60:285–92.
[106] Zhang L, Klemm D, Eckert J, Hao Y, Sercombe T. Manufacture by selective laser melting and mechanical behavior of a biomedical Ti–24Nb–4Zr–8Sn alloy. Scripta Mater 2011;65:21–4.
[107] Aydoğmuş T, AL-Zangana NJF, Kelen F. PROCESSING OF β-TYPE BIOMEDICAL Ti74Nb26 ALLOY BY COMBINATION OF HOT PRESSING AND HIGH TEMPERATURE SINTERING. Konya Mühendislik Bilimleri Dergisi 2020;8:269–81.
[108] Kulin S, Cohen M, Averbach B. Effect of applied stress on the martensitic transformation. JOM 1952;4:661–8.
[109] Olson G, Cohen M. A mechanism for the strain-induced martensitic transformations* nucleation of. J. LessCommon Met 1972;28:107–18.
[110] Motyka M. Martensite formation and decomposition during traditional and AM processing of two-phase titanium alloys—an overview. Metals 2021;11:481.
[111] Zhou YL, Niinomi M, Akahori T. Dynamic Young's modulus and mechanical properties of Ti− Hf alloys. Mater Trans 2004;45:1549–54.
[112] Kolli R, Devaraj A. A review of metastable beta Titanium alloys. Metals 2018;8(7):506.
[113] Dehghan-Manshadi A, Dippenaar RJ. Strain-induced phase transformation during thermo-mechanical processing of titanium alloys. Mater Sci Eng, A 2012;552:451–6.
[114] Mitchell A, Kawakami A, Cockcroft S. Beta fleck and segregation in titanium alloy ingots. High Temp Mater Process 2006;25:337–49.
[115] Mitchell A. Melting, casting and forging problems in titanium alloys. Mater Sci Eng, A 1998;243:257–62.
[116] Yin X, Liu J, Wang Q, Wang L. Investigation of beta fleck formation in Ti-17 alloy by directional solidification method. J Mater Sci Technol 2020;48:36–43.
[117] Ng C, Bermingham MJ, Dargusch M. Eliminating segregation defects during additive manufacturing of high strength β-titanium alloys. Addit Manuf 2021;39:101855.
[118] Ng C, Bermingham M, Yuan L, Dargusch M. Towards β-fleck defect free additively manufactured titanium alloys by promoting the columnar to equiaxed transition and grain refinement. Acta Mater 2022;224:117511.
[119] Morinaga M, et al. Theoretical design of beta-type titanium alloys. Titanium'92: science and technology. 1993. p. 217–24.
[120] Mohamed AHG, Mervat I, Kobayashi S. Low Young's modulus β-Ti alloys for biomedical applications. Adv Mater Res 2014;1024:308–11.
[121] Bahl S, Suwas S, Chatterjee K. Comprehensive review on alloy design, processing, and performance of β Titanium alloys as biomedical materials. Int Mater Rev 2021;66:114–39.
[122] Sidhu SS, Singh H, Gepreel MA-H. A review on alloy design, biological response, and strengthening of β-titanium alloys as biomaterials. Mater Sci Eng C 2021;121:111661.
[123] Sun P, Fang ZZ, Zhang Y, Xia Y. Review of the methods for production of spherical Ti and Ti alloy powder. Jom 2017;69:1853–60.
[124] Singh S, Ramakrishna S, Singh R. Material issues in additive manufacturing: a review. J Manuf Process 2017;25:185–200. https://doi.org/10.1016/j.jmapro.2016.11.006.
[125] Neikov OD, Gopienko VG. Production of titanium and titanium alloy powders. Handbook of non-ferrous metal powders. 2019. p. 549–70.
[126] Kroll W. The production of ductile titanium. Transactions of the Electrochemical Society 1940;78:35.
[127] Froes FH, Eylon D. Powder metallurgy of titanium alloys. Int Mater Rev 1990;35:162–84.
[128] Gopienko VG, Neikov OD. In: Handbook of non-Ferrous metal powders; 2009. p. 314–23.
[129] Platacis E, Kaldre I, Blumbergs E, Goldšteins L, Serga V. Titanium production by magnesium thermal reduction in the electroslag process. Sci Rep 2019;9:1–13.
[130] Olkhov YN, Ogurtsov SV. Thermodynamics of the titanium redox reaction from titanium tetrachloride by magnesium and the choice of optimal ways to intensify the titanium production. Investigations in Titanium Chloric Metallurgy 1969;302.
[131] Takeda O, Ouchi T, Okabe TH. Recent progress in titanium extraction and recycling. Metall Mater Trans B 2020;51:1315–28.
[132] Duan S, et al. Investigation of the oxidation behaviour of Ti and Al in Inconel 718 superalloy during electroslag remelting. Sci Rep 2018;8:1–14.
[133] Fang ZZ, Lefler HD, Froes FH, Zhang Y. Extractive metallurgy of titanium, vols. 1–10. Elsevier; 2020.
[134] Araci K, Mangabhai D, Akhtar K. In: Titanium powder metallurgy. Elsevier; 2015. p. 149–62.
[135] Agripa H, Botef I. Modern production methods for titanium alloys: a review. Titanium Alloys-Novel Aspects of Their Manufacturing and Processing vol. 10, 2019.
[136] Li Y, et al. Biomedical TiNbZrTaSi alloys designed by d-electron alloy design theory. Mater Des 2015;85:7–13.
[137] Suryanarayana C, Ivanov E. Advances in powder metallurgy: 3. Mechanochemical synthesis of nanocrystalline metal powders. Elsevier Inc. Chapters; 2013.
[138] Al-Naib UB, Vikraman D, Karuppasamy K. Recent advancements in the metallurgical engineering and Electrodeposition. BoD–Books on Demand; 2020.
[139] Withers JC. In: Titanium powder metallurgy. Elsevier; 2015. p. 33–49.
[140] Santos da Silva F, et al. Cold gas spray coatings: basic principles, corrosion protection and applications. Eclética Química Journal 2017;42(1):9–32. 2017.
[141] Vetter JM, Gross G, Bergmann HW. Production of metal powders by atomizing their melts with liquid gases. Met Powder Rep 1990;45:100–4. https://doi.org/10.1016/S0026-0657(10)80118-3.
[142] German RM. Powder metallurgy and particulate materials processing: the processes, materials, products, properties and applications. Metal Powder Industries Federation 2005. ISBN 0976205718, 9780976205715.
[143] Sahu S, Chakraborty A, Maurya D. Coriolis-induced liquid breakup and spray evolution in a rotary slinger atomizer: experiments and analysis. Int J Multiphas Flow 2021;135:103532.
[144] Yule AJ, Dunkley JJ. Atomization of melts: for powder production and spray deposition. USA: Oxford University Press; 1994.
[145] Oshida Y. Bioscience and bioengineering of titanium materials. Elsevier; 2010.
[146] Mellor I, Doughty G. Novel and emerging routes for titanium powder production-an overview. Key Eng Mater 2016;704:271–81.
[147] Minagawa K, Kakisawa H, Takamori S, Osawa Y, Halada K. Hybrid atomization method suitable for production of fine spherical lead-free solder powder. Nukleonika 2006;51:83–8.
[148] Riabov D, Hryha E, Rashidi M, Bengtsson S, Nyborg L. Effect of atomization on surface oxide composition in 316L stainless steel powders for additive manufacturing. Surf Interface Anal 2020;52:694–706.
[149] Persson F, Eliasson A, Jönsson PG. Oxidation of water atomized metal powders. Steel Res Int 2014;85:1629–38.
[150] Moll JH. Utilization of gas-atomized titanium and titanium-aluminide powder. JOM 2000;52:32–4. https://doi.org/10.1007/s11837-000-0030-3.
[151] Sun P, Fang ZZ, Zhang Y, Xia Y. Review of the methods for production of spherical Ti and Ti alloy powder. Jom 2017;69:1853–60.
[152] Dietrich S, Wunderer M, Huissel A, Zaeh MF. A new approach for a flexible powder production for additive manufacturing. Procedia Manuf 2016;6:88–95.
[153] Entezarian M, Allaire F, Tsantrizos P, Drew RAL. Plasma atomization: a new process for the production of fine, spherical powders. JOM 1996;48:53–5. https://doi.org/10.1007/BF03222969.
[154] Dion, C. A. D. & Proulx, F. (Google Patents, 2020.
[155] Zdujić M, Uskoković D. Production of atomized metal and alloy powders by the rotating electrode process. Sov Powder Metall Met Ceram 1990;29:673–83.
[156] Samal P, Newkirk J. Powder metallurgy methods and applications. ASM handbook of powder metallurgy 2015;7.

[157] Tang J, Nie Y, Lei Q, Li Y. Characteristics and atomization behavior of Ti-6Al-4V powder produced by plasma rotating electrode process. Adv Powder Technol 2019;30:2330–7.
[158] Kim Y, Kim E-P, Song Y-B, Lee SH, Kwon Y-S. Microstructure and mechanical properties of hot isostatically pressed Ti–6Al–4V alloy. J Alloys Compd 2014;603:207–12.
[159] Hata S, Oki K, Hashimoto T, Kuwano N. Microstructures of Ti 50 Al 45 Mo 5 alloy powders produced by plasma rotating electrode process. J Phase Equil 2001;22:386–93.
[160] Fang ZZ, et al. Powder metallurgy of titanium–past, present, and future. Int Mater Rev 2018;63:407–59.
[161] Nachtrab, W. T., Roberts, P. R. & Newborn, H. A. in Key engineering materials. 115-140 (Trans Tech Publ).
[162] Hinrichs F, et al. Flexible powder production for additive manufacturing of refractory metal-based alloys. Metals 2021;11:1723.
[163] Limberg W, Aust E, Ebel T, Gerling R, Oger B. Metal injection moulding of an advanced bone screw 7Nb alloy powder. Euro pm 2004;4.
[164] Amherd Hidalgo A, Ebel T, Frykholm R, Carreño-Morelli E, Pyczak F. High-oxygen MIM Ti-6Al-7Nb: microstructure, tensile and fatigue properties. Mater Today Commun 2023;34:104982. https://doi.org/10.1016/j.mtcomm.2022.104982.
[165] Technology, A. https://metalatomizer.com/, <https://metalatomizer.com > (.
[166] Faraji G, Kim HS, Kashi HT. Severe plastic deformation: methods, processing and properties. Elsevier; 2018.
[167] Chawake N, et al. Evolution of morphology and texture during high energy ball milling of Ni and Ni-5 wt% Cu powders. Mater Char 2016;120:90–6.
[168] Abdollahi Khabisi M, Khorsand H, Ganjeh E, Tahmasebi M, Siadati MH. Ball milling synthesis and effects of infrared heat treating on the nanocrystalline Ti/Zr/Cu/Ni system. Mater Lett 2023;330:133414. https://doi.org/10.1016/j.matlet.2022.133414.
[169] Frutos E, Sanguino P, Trindade B. In-situ development of Fe3C and TiC reinforcements during the mechanosynthesis of Cu–10Sn–15Ti/diamonds composite powders by high energy ball milling: microstructural, thermal, and mechanical characterization. Int J Refract Metals Hard Mater 2021;95:105433. https://doi.org/10.1016/j.ijrmhm.2020.105433.
[170] Aguilar C, et al. Effect of Sn on synthesis of nanocrystalline Ti-based alloy with fcc structure. Trans Nonferrous Metals Soc China 2020;30:2119–31.
[171] Pradeep NB, et al. Synthesis and characterization of mechanically alloyed nanostructured ternary titanium based alloy for bio-medical applications. J Mater Res Technol 2022;16:88–101.
[172] Wang H, Zhang HM, Cheng XW, Chang S, Mu XN. Effect of ball milling time on microstructure and mechanical properties of graphene nanoplates and TiBw reinforced Ti–6Al–4V alloy composites. Mater Sci Eng, A 2022;861:144240. https://doi.org/10.1016/j.msea.2022.144240.
[173] Li Z, et al. Synthesis, microstructure and properties of Ti (C, N)-(HfZrTaNbTi) C5-HEA high-entropy cermets by high-energy ball milling and spark plasma sintering. Ceram Int 2022;48:30826–37.
[174] Shkodich NF, et al. Refractory TaTiNb, TaTiNbZr, and TaTiNbZrX (X= Mo, W) high entropy alloys by combined use of high energy ball milling and spark plasma sintering: structural characterization, mechanical properties, electrical resistivity, and thermal conductivity. J Alloys Compd 2022;893:162030.
[175] Wang N. FeCoNiMnCuTi high entropy amorphous alloys and M50Ti50 (M = Fe, Cu, FeCoNiMnCu) amorphous alloys: novel and efficient catalysts for heterogeneous photo-Fenton decomposition of Rhodamine B. Surface Interfac 2022;33:102265. https://doi.org/10.1016/j.surfin.2022.102265.
[176] Volkova EG, et al. Alloying of Al2Au intermetallic compound with Cu by the ball milling technique. J Alloys Compd 2022;900:163429. https://doi.org/10.1016/j.jallcom.2021.163429.
[177] Aguilar C, et al. Evolution of synthesis of FCC nanocrystalline solid solution and amorphous phase in the Ti-Ta based alloy by high milling energy. J Alloys Compd 2021;854:155980. https://doi.org/10.1016/j.jallcom.2020.155980.
[178] Shkodich NF, et al. Crystallization of amorphous Cu50Ti50 alloy prepared by high-energy ball milling. J Alloys Compd 2018;741:575–9. https://doi.org/10.1016/j.jallcom.2018.01.062.
[179] Xia W, Zarezadeh Mehrizi M. Direct synthesis of NiAl intermetallic matrix composite with TiC and Al2O3 reinforcements by mechanical alloying of NiO–Al–Ti–C powder mixture. Ceram Int 2021;47:26863–8. https://doi.org/10.1016/j.ceramint.2021.06.095.
[180] Pang X, et al. Grain refinement effect of ZrB2 in laser additive manufactured metastable β-titanium alloy with enhanced mechanical properties. Mater Sci Eng, A 2022;857:144104. https://doi.org/10.1016/j.msea.2022.144104.
[181] de Araujo-Silva R, et al. Synthesis of β-Ti-Nb alloys from elemental powders by high-energy ball milling and their hydrogenation features. Int J Hydrogen Energy 2018;43:18382–91. https://doi.org/10.1016/j.ijhydene.2018.08.036.
[182] Hezil N, et al. Structural, and tribological properties of nanostructured α + β type titanium alloys for total hip. J Mater Res Technol 2022;19:3568–78. https://doi.org/10.1016/j.jmrt.2022.06.042.
[183] Suryanarayana C. Mechanical alloying and milling. Prog Mater Sci 2001;46:1–184.
[184] Veverková A, et al. Mechanical properties of Ti-15Mo alloy prepared by cryogenic milling and spark plasma sintering. Metals 2019;9:1280.
[185] Kristaly F, et al. Effects of milling temperature and time on phase evolution of Ti-based alloy. J Min Metall B Metall 2022;58:141–56.
[186] Froes FHS, Suryanarayana C, Russell K, Li CG. Synthesis of intermetallics by mechanical alloying. Mater Sci Eng, A 1995;192:612–23.
[187] Wu ZM, et al. The ball to powder ratio (BPR) dependent morphology and microstructure of tungsten powder refined by ball milling. Powder Technol 2018;339:256–63.
[188] Lü L, Lai MO. Mechanical alloying. Springer Science & Business Media; 1997.
[189] Sugimoto S, Niwa T, Nakanishi Y, Danjo K. Development of a novel ultra cryo-milling technique for a poorly water-soluble drug using dry ice beads and liquid nitrogen. Int J Pharm 2012;426:162–9.
[190] Zhou F, Nutt SR, Bampton CC, Lavernia EJ. Nanostructure in an Al-Mg-Sc alloy processed by low-energy ball milling at cryogenic temperature. Metall Mater Trans 2003;34:1985–92.
[191] Kozlík J, et al. Cryogenic milling of titanium powder. Metals 2018;8:31.
[192] Avar B, Ozcan S. Structural evolutions in Ti and TiO2 powders by ball milling and subsequent heat-treatments. Ceram Int 2014;40:11123–30. https://doi.org/10.1016/j.ceramint.2014.03.137.
[193] Ali S, Karunanithi R, Prashanth M, Rahman MA. X-ray peak broadening on microstructure, and structural properties of titanium and Ti-6Al-4V alloys. Mater Today Proc 2020;27:2390–3. https://doi.org/10.1016/j.matpr.2019.09.137.
[194] Nicula R, Lüthen F, Stir M, Nebe B, Burkel E. Spark plasma sintering synthesis of porous nanocrystalline titanium alloys for biomedical applications. Biomol Eng 2007;24:564–7. https://doi.org/10.1016/j.bioeng.2007.08.008.
[195] Nguyen T-T-N, He J-L. Preparation of titanium monoxide nanopowder by low-energy wet ball-milling. Adv Powder Technol 2016;27:1868–73. https://doi.org/10.1016/j.apt.2016.04.022.
[196] Takeda O, Uda T, Okabe TH. In: Treatise on process metallurgy. Elsevier Ltd; 2014. p. 995–1069.
[197] Ltd TTC. Titanium sponge. 2023.
[198] Okabe TH, Takeda O. Extractive metallurgy of titanium, vols. 65–95. Elsevier; 2020.
[199] Yolton C, Froes FHS. In: Titanium powder metallurgy. Elsevier; 2015. p. 21–32.
[200] Wei M, Chen S, Liang J, Liu C. Effect of atomization pressure on the breakup of TA15 titanium alloy powder prepared by EIGA method for laser 3D printing. Vacuum 2017;143:185–94.
[201] Brika SE, Letenneur M, Dion CA, Brailovski V. Influence of particle morphology and size distribution on the powder flowability and laser powder bed fusion manufacturability of Ti-6Al-4V alloy. Addit Manuf 2020;31:100929. https://doi.org/10.1016/j.addma.2019.100929.
[202] Cui Y, et al. Effects of plasma rotating electrode process parameters on the particle size distribution and microstructure of Ti-6Al-4 V alloy powder. Powder Technol 2020;376:363–72.
[203] Esteban P, Ruiz-Navas E, Bolzoni L, Gordo E. Low-cost titanium alloys? Iron may hold the answers. Met Powder Rep 2008;63:24–7.
[204] Yamanoglu R, Bahador A, Kondoh K. Fabrication methods of porous titanium implants by powder metallurgy. Trans Indian Inst Met 2021;74:2555–67.
[205] German RM. Progress in titanium metal powder injection molding. Materials 2013;6:3641–62.
[206] Pilliar R, Cameron H, Macnab I. Porous surface layered prosthetic devices. Biomed Eng 1975;10:126–31.
[207] Bram M, Stiller C, Buchkremer HP, Stöver D, Baur H. High-porosity titanium, stainless steel, and superalloy parts. Adv Eng Mater 2000;2:196–9.
[208] Singh R, Lee P, Dashwood R, Lindley T. Titanium foams for biomedical applications: a review. Mater Technol 2010;25:127–36.
[209] Jung H-D, Yook S-W, Kim H-E, Koh Y-H. Fabrication of titanium scaffolds with porosity and pore size gradients by sequential freeze casting. Mater Lett 2009;17:1545–7.
[210] Ferraris S, Spriano S. Porous titanium by additive manufacturing: a focus on surfaces for bone integration. Metals 2021;11:1343.
[211] Huang Y-M, et al. Three-dimensional printed porous titanium screw with bioactive surface modification for bone–tendon healing: a rabbit animal model. Int J Mol Sci 2020;21:3628.
[212] Zhang LC, Liu Y, Li S, Hao Y. Additive manufacturing of titanium alloys by electron beam melting: a review. Adv Eng Mater 2018;20:1700842.
[213] Liu Y, et al. Enhanced fatigue characteristics of a topology-optimized porous titanium structure produced by selective laser melting. Addit Manuf 2020;32:101060.
[214] Attar H, Ehtemam-Haghighi S, Soro N, Kent D, Dargusch MS. Additive manufacturing of low-cost porous titanium-based composites for biomedical applications: advantages, challenges and opinion for future development. J Alloys Compd 2020;827:154263.
[215] Chirico C, Tsipas S, Toptan F, Gordo E. Development of Ti–Nb and Ti–Nb–Fe beta alloys from TiH2 powders. Powder Metall 2019;62:44–53.
[216] Chirico C, Tsipas SA, Wilczynski P, Gordo E. Beta titanium alloys produced from titanium hydride: effect of alloying elements on titanium hydride decomposition. Metals 2020;10:682.
[217] Abkowitz S. In: Titanium science and technology. Springer; 1973. p. 381–98.
[218] Bolzoni L, Meléndez IM, Ruiz-Navas EM, Gordo E. Microstructural evolution and mechanical properties of the Ti–6Al–4V alloy produced by vacuum hot-pressing. Mater Sci Eng, A 2012;546:189–97.
[219] Froes F. Titanium sport and medical application focus. Mater Technol 2002;17:4–7.
[220] Kolli RP, Devaraj A. A review of metastable beta titanium alloys. Metals 2018;8:506.
[221] Bolzoni L, Ruiz-Navas EM, Gordo E. Quantifying the properties of low-cost powder metallurgy titanium alloys. Mater Sci Eng, A 2017;687:47–53.
[222] Amigó A, Vicente A, Afonso CR, Amigó V. Mechanical properties and the microstructure of β Ti-35Nb-10Ta-x Fe alloys obtained by powder metallurgy for biomedical applications. Metals 2019;9:76.

[223] Dehghan-Manshadi A, Kent D, StJohn D, Dargusch M. Properties of powder metallurgy-fabricated oxygen-containing beta Ti–Nb–Mo–Sn–Fe alloys for biomedical applications. Adv Eng Mater 2020;22:1901229.
[224] Li X, Ye S, Yuan X, Yu P. Fabrication of biomedical Ti-24Nb-4Zr-8Sn alloy with high strength and low elastic modulus by powder metallurgy. J Alloys Compd 2019;772:968–77.
[225] Jia M, Gabbitas B. Rapid synthesis of a near-β titanium alloy by blended elemental powder metallurgy (BEPM) with induction sintering. Metall Mater Trans 2015;46:4716–29.
[226] Luo S, et al. High oxygen-content titanium and titanium alloys made from powder. J Alloys Compd 2020;836:155526.
[227] Saito T, et al. Multifunctional alloys obtained via a dislocation-free plastic deformation mechanism. Science 2003;300:464–7.
[228] Furuta T, et al. Mechanical properties and phase stability of Ti-Nb-Ta-Zr-O alloys. Mater Trans 2007;48:1124–30.
[229] Málek J, Hnilica F, Bartáková S, Míka P, Veselý J. The effect of different forms of oxygen on properties of beta titanium alloys. Acta Polytechnica 2018;58:179–83.
[230] McCracken C, Barbis D, Deeter R. Key characteristics of hydride–dehydride titanium powder. Powder Metall 2011;54:180–3.
[231] Zhao D, et al. Sintering behavior and mechanical properties of a metal injection molded Ti–Nb binary alloy as biomaterial. J Alloys Compd 2015;640:393–400.
[232] Amigó A, Zambrano J, Martinez S, Amigó V. Microstructural characterisation of Ti–Nb–(Fe–Cr) alloys obtained by powder metallurgy. Powder Metall 2014;57:316–9.
[233] Mohan P, Amigó Mata A, Amigó V. Effects of Fe and Mo content on the microstructure and mechanical properties of Ti-Mo based alloys prepared by elemental blend and mechanical alloying technique. Trans Powder Metall Assoc India 2016;42:25–31.
[234] Elshalakany AB, et al. Microstructure and mechanical properties of Ti-Mo-Zr-Cr biomedical alloys by powder metallurgy. J Mater Eng Perform 2017;26:1262–71.
[235] Çaha I, et al. Corrosion and tribocorrosion behavior of Ti-40Nb and Ti-25Nb-5Fe alloys processed by powder metallurgy. Metall Mater Trans 2020;51:3256–67.
[236] Mohan P, Osman T, Amigo V, Mohamed A. Effect of Fe content, sintering temperature and powder processing on the microstructure, fracture and mechanical behaviours of Ti-Mo-Zr-Fe alloys. J Alloys Compd 2017;729:1215–25.
[237] Caha I, et al. Tribocorrosion-resistant Ti40Nb–TiN composites having TiO2-based nanotubular surfaces. ACS Biomater Sci Eng 2022;8:1816–28.
[238] Chirico C, Romero AV, Gordo E, Tsipas S. Improvement of wear resistance of low-cost powder metallurgy β-titanium alloys for biomedical applications. Surf Coating Technol 2022;434:128207.
[239] Rossi M, et al. Effect of alloying elements on laser surface modification of powder metallurgy to improve surface mechanical properties of beta titanium alloys for biomedical application. J Mater Res Technol 2021;14:1222–34.
[240] Batibay A, et al. Investigation and production of non-cytotoxic TixNbxSn (x= 5, 10, 15, 20) alloys by high-energy mechanical milling with antibacterial activity. Mater Today Commun 2023;37:106912.
[241] Yang Y, et al. Characterization on corrosion and antibacterial properties of a new functionally graded porous Ti–Mo–Cu alloys with improved cytocompatibility. Vacuum 2023;215:112353.
[242] Lario J, Vicente Á, Amigó V. Evolution of the microstructure and mechanical properties of a Ti35Nb2Sn alloy post-processed by hot isostatic pressing for biomedical applications. Metals 2021;11:1027.
[243] Lario J, Escuder ÁV, Segovia F, Amigó V. Electrochemical corrosion behavior of Ti–35Nb–7Zr–5Ta powder metallurgic alloys after Hot Isostatic Process in fluorinated artificial saliva. J Mater Res Technol 2022;16:1435–44.
[244] Guo Y, et al. High-strength near-beta titanium alloy fabricated by direct hot pressing of the machining swarf. J Mater Eng Perform 2022:1–11.
[245] Sun J, et al. The designed high-performance PM Ti-6Al-4V alloy via two-step pressureless sintering. J Alloys Compd 2024;976:173324.
[246] Kuang F, Pan Y, Zhang J, Wu X, Lu X. Microstructure, mechanical properties, and strengthening mechanism of high performance Ti-6Al-4V alloy by pressureless sintering and hot extrusion. J Alloys Compd 2023;951:169990.
[247] Chen T, et al. Ultrastrong Ti–6Al–4V composite with hierarchical microstructure through two-step ball milling and pressureless sintering. Scripta Mater 2023;236:115676.
[248] Guo L, Yang F, Lu B, Chen C, Guo Z. High-performance Ti-6554 alloy manufactured using irregular powder via vacuum pressureless sintering followed by forging. J Mater Eng Perform 2024;33:43–53.
[249] Franco AH, Silva CRM, Muterlle PV, Ferreira JL, Araújo JA. Influence of heat treatment on fatigue resistance of sintered Ti 35Nb 7Zr 5Ta β alloy. Adv Mater Res 2014;936:1290–7.
[250] Cai Q, et al. In situ investigation on densification mechanism of Ti-20Al-19Nb (at. %) alloy by TiH2-assisted pressureless sintering. J Mater Sci Technol 2023;165:170–86.
[251] Kafkas F, Ebel T. Metallurgical and mechanical properties of Ti–24Nb–4Zr–8Sn alloy fabricated by metal injection molding. J Alloys Compd 2014;617:359–66.
[252] Xu P, et al. Tensile toughening of powder-injection-molded β Ti-Nb-Zr biomaterials by adjusting TiC particle distribution from aligned to dispersed pattern. Appl Mater Today 2020;19:100630. https://doi.org/10.1016/j.apmt.2020.100630.
[253] Santos PF, et al. Fabrication of low-cost beta-type Ti–Mn alloys for biomedical applications by metal injection molding process and their mechanical properties. J Mech Behav Biomed Mater 2016;59:497–507.
[254] Santos PF, et al. Effects of Mo addition on the mechanical properties and microstructures of Ti-Mn alloys fabricated by metal injection molding for biomedical applications. Mater Trans 2017;58:271–9.
[255] Zhao D, et al. Microstructure and mechanical behavior of metal injection molded Ti–Nb binary alloys as biomedical material. J Mech Behav Biomed Mater 2013;28:171–82.
[256] Xu P, Pyczak F, Limberg W, Willumeit-Römer R, Ebel T. Superior fatigue endurance exempt from high processing cleanliness of Metal-Injection-Molded β Ti-Nb-Zr for bio-tolerant applications. Mater Des 2021;211:110141.
[257] Hernandez J, et al. Microstructures and hardness properties for β-phase Ti–24Nb–4Zr–7.9 Sn alloy fabricated by electron beam melting. J Mater Sci Technol 2013;29:1011–7.
[258] Liu Y, et al. Electron beam melted beta-type Ti–24Nb–4Zr–8Sn porous structures with high strength-to-modulus ratio. J Mater Sci Technol 2016;32:505–8.
[259] Reig L, Amigó V, Busquets DJ, Calero JA. Development of porous Ti6Al4V samples by microsphere sintering. J Mater Process Technol 2012;212:3–7.
[260] Reig L, Tojal C, Busquets DJ, Amigó V. Microstructure and mechanical behavior of porous Ti–6Al–4V processed by spherical powder sintering. Materials 2013;6:4868–78.
[261] Reig L, Amigó V, Busquets D, Calero JA, Ortiz J. Application of the zero-order reaction rate model and transition state theory to predict porous Ti6Al4V bending strength. Mater Sci Eng C 2012;32:1621–6.
[262] Zhang F, et al. Preparation of nano to submicro-porous TiMo foams by spark plasma sintering. Adv Eng Mater 2017;19:1600600.
[263] Dunand DC. Processing of titanium foams. Adv Eng Mater 2004;6:369–76.
[264] Oh I-H, Segawa H, Nomura N, Hanada S. Microstructures and mechanical properties of porosity-graded pure titanium compacts. Mater Trans 2003;44:657–60.
[265] Torres Y, Trueba P, Pavón J, Montealegre I, Rodríguez-Ortiz J. Designing, processing and characterisation of titanium cylinders with graded porosity: an alternative to stress-shielding solutions. Mater Des 2014;63:316–24.
[266] Amigó V, Reig L, Busquets D, Ortiz JL, Calero JA. Analysis of bending strength of porous titanium processed by space holder method. Powder Metall 2011;54:67–70.
[267] Torres Y, et al. Processing, characterization and biological testing of porous titanium obtained by space-holder technique. J Mater Sci 2012;47:6565–76.
[268] Torres Y, et al. Design, processing and characterization of titanium with radial graded porosity for bone implants. Mater Des 2016;110:179–87.
[269] Pavón J, Trueba P, Rodríguez-Ortiz J, Torres Y. Development of new titanium implants with longitudinal gradient porosity by space-holder technique. J Mater Sci 2015;50:6103–12.
[270] Kim SW, et al. Fabrication of porous titanium scaffold with controlled porous structure and net-shape using magnesium as spacer. Mater Sci Eng C 2013;33:2808–15.
[271] Rossi MC, et al. Evaluation of the influence of low Mg content on the mechanical and microstructural properties of β titanium alloy. J Mater Res Technol 2021;10:916–25.
[272] Rossi MC, et al. Evaluation of the physical and biological properties of Ti-34Nb-6Sn/Mg alloy obtained by powder metallurgy for use as biomaterial. Mater Res 2022;25.
[273] Kearns MW, Blenkinsop P, Barber A, Farthing T. Manufacture of a novel porous metal. Int J Powder Metall 1986;24:59–64. 1988.
[274] Greiner C, Oppenheimer SM, Dunand DC. High strength, low stiffness, porous NiTi with superelastic properties. Acta Biomater 2005;1:705–16.
[275] Oppenheimer SM, Dunand DC. Porous NiTi by creep expansion of argon-filled pores. Mater Sci Eng, A 2009;523:70–6.
[276] Davis N, Teisen J, Schuh C, Dunand D. Solid-state foaming of titanium by superplastic expansion of argon-filled pores. J Mater Res 2001;16:1508–19.
[277] Spoerke ED, et al. A bioactive titanium foam scaffold for bone repair. Acta Biomater 2005;1:523–33.
[278] Pease III L, Sansoucy R. Advances in powder metallurgy-1991: Proceedings of the powder metallurgy conference and exhibition, Chicago, IL, June 9-12, 1991. Princeton, NJ (United States); Metal Powder Industry, ISBN: 1878954083, 978-1878954084 1991.
[279] Schwartz D, Shih D, Lederich R, Martin R, Deuser D. Development and scale-up of the low density core process for Ti-64, vol. 521. MRS Online Proceedings Library (OPL); 1998.
[280] Dunand D, Teisen J. Superplastic foaming of titanium and Ti-6Al-4V. MRS Online Proc Libr 1998;521:231–6.
[281] Dunand D, Bedell C. Transformation-mismatch superplasticity in reinforced and unreinforced titanium. Acta Mater 1996;44:1063–76.
[282] Frary M, Schuh C, Dunand DC. Kinetics of biaxial dome formation by transformation superplasticity of titanium alloys and composites. Metall Mater Trans 2002;33:1669–80.
[283] Murray N, Dunand D. Effect of thermal history on the superplastic expansion of argon-filled pores in titanium: Part I kinetics and microstructure. Acta Mater 2004;52:2269–78.
[284] Murray N, Dunand D. Effect of thermal history on the superplastic expansion of argon-filled pores in titanium: Part II modeling of kinetics. Acta Mater 2004;52:2279–91.
[285] Oppenheimer S, Dunand DC. Solid-state foaming of Ti–6Al–4V by creep or superplastic expansion of argon-filled pores. Acta Mater 2010;58:4387–97.
[286] Nugroho, A., Leadbeater, G. & Davies, I. in IOP Conference series: materials science and engineering. 012096 (IOP Publishing).
[287] Chino Y, Dunand DC. Directionally freeze-cast titanium foam with aligned, elongated pores. Acta Mater 2008;56:105–13.
[288] Du W, et al. Fabrication and compressive properties of directional porous titanium scaffold by freeze casting TiH2 powders. J Alloys Compd 2022;894:162363.

[289] Li JC, Dunand DC. Mechanical properties of directionally freeze-cast titanium foams. Acta Mater 2011;59:146–58.
[290] Chang J-M, Liu G-L, Tung H-M. Effects of sintering temperature on the porosity and mechanical behavior of porous titanium scaffolds prepared by freeze-casting. J Mater Eng Perform 2019;28:5494–500.
[291] Jenei P, et al. Mechanical behavior of freeze-cast Ti foams with varied porosity. Mater Sci Eng, A 2022;855:143911.
[292] Jenei P, Choi H, Tóth A, Choe H, Gubicza J. Mechanical behavior and microstructure of compressed Ti foams synthesized via freeze casting. J Mech Behav Biomed Mater 2016;63:407–16.
[293] Choi H, Shil'ko S, Gubicza J, Choe H. Study of the compression and wear-resistance properties of freeze-cast Ti and Ti–5W alloy foams for biomedical applications. J Mech Behav Biomed Mater 2017;72:66–73.
[294] Weaver JS, Kalidindi SR, Wegst UG. Structure-processing correlations and mechanical properties in freeze-cast Ti-6Al-4V with highly aligned porosity and a lightweight Ti-6Al-4V-PMMA composite with excellent energy absorption capability. Acta Mater 2017;132:182–92.
[295] Sheng Y, et al. Thermal stability of gel foams stabilized by xanthan gum, silica nanoparticles and surfactants. Gels 2021;7:179.
[296] Li F, et al. Lamellar structure/processing relationships and compressive properties of porous Ti6Al4V alloys fabricated by freeze casting. J Mech Behav Biomed Mater 2020;101:103424.
[297] Li F, et al. Porous Ti6Al4V alloys with high strength-to-modulus ratio fabricated by unidirectional freeze casting of SiC fiber-containing slurry. Mater Sci Eng, A 2021;820:141584.
[298] Chen Z, Liu X, Shen T, Wu C, Zhang L. Template-assisted freeze casting of macroporous Ti6Al4V scaffolds with long-range order lamellar structure. Mater Lett 2020;264:127374.
[299] Wu CZ, et al. Customizing the pore structure and properties of freeze-cast porous titanium by zirconium acetate additive. Adv Eng Mater 2020;22:2000519.
[300] Trueba P, et al. Porous titanium cylinders obtained by the freeze-casting technique: influence of process parameters on porosity and mechanical behavior. Metals 2020;10:188.
[301] Sharma B, Vajpai SK, Ameyama K. An efficient powder metallurgy processing route to prepare high-performance β-Ti–Nb alloys using pure titanium and titanium hydride powders. Metals 2018;8:516.
[302] Ibrahim A, Zhang F, Otterstein E, Burkel E. Processing of porous Ti and Ti5Mn foams by spark plasma sintering. Mater Des 2011;32:146–53. https://doi.org/10.1016/j.matdes.2010.06.019.
[303] Mahundla M, Matizamhuka W, Yamamoto A, Shongwe M, Machaka R. Corrosion behaviour of Ti–34Nb–25Zr alloy fabricated by spark plasma sintering. Journal of Bio-and Tribo-Corrosion 2020;6:1–9.
[304] Yamanoglu R. Pressureless spark plasma sintering: a perspective from conventional sintering to accelerated sintering without pressure. Powder Metall Met Ceram 2019;57:513–25.
[305] Shongwe, M. B., Ramakokovhu, M. M., Lethabane, M. L. & Olubambi, P. A. in Proceedings of the world Congress on engineering.
[306] Matizamhuka W. Spark plasma sintering (SPS)-an advanced sintering technique for structural nanocomposite materials, vol. 116. Journal of the Southern African Institute of Mining and Metallurgy; 2016. p. 1171–80.
[307] Ayodele O, Shongwe M, Obadele B, Olubambi P. In: Spark plasma sintering of materials. Springer; 2019. p. 673–701.
[308] Guillon O, et al. Field-assisted sintering technology/spark plasma sintering: mechanisms, materials, and technology developments. Adv Eng Mater 2014;16:830–49.
[309] Suárez M, et al. Challenges and opportunities for spark plasma sintering: a key technology for a new generation of materials. Sintering applications 2013;13:319–42.
[310] Attar H, Calin M, Zhang L, Scudino S, Eckert J. Manufacture by selective laser melting and mechanical behavior of commercially pure titanium. Mater Sci Eng, A 2014;593:170–7.
[311] Attar H, et al. Selective laser melting of in situ titanium–titanium boride composites: processing, microstructure and mechanical properties. Acta Mater 2014;76:13–22.
[312] Liu Y, Li X, Zhang LC, Sercombe T. Processing and properties of topologically optimised biomedical Ti–24Nb–4Zr–8Sn scaffolds manufactured by selective laser melting. Mater Sci Eng, A 2015;642:268–78.
[313] Zanger F, Schulze V. Investigations on mechanisms of tool wear in machining of Ti-6Al-4V using FEM simulation. Procedia Cirp 2013;8:158–63.
[314] Sung, S. Y. & Kim, Y. J. in Materials science forum. 3601-3606 [Trans Tech Publ)].
[315] Attar H, et al. Mechanical behavior of porous commercially pure Ti and Ti–TiB composite materials manufactured by selective laser melting. Mater Sci Eng, A 2015;625:350–6.
[316] Elhadad AA, et al. Applications and multidisciplinary perspective on 3D printing techniques: recent developments and future trends. Mater Sci Eng R Rep 2023;156:100760.
[317] Standard A. F2792. 2012. standard terminology for additive manufacturing technologies. ASTM F2792-10e1; 2012. p. 24.
[318] Salmi M. Additive manufacturing processes in medical applications. Materials 2021;14:191.
[319] Gu D, et al. Material-structure-performance integrated laser-metal additive manufacturing. Science 2021;372:eabg1487.
[320] Busachi A, et al. Defining next-generation additive manufacturing applications for the Ministry of defence (MoD). Procedia CIRP 2016;55:302–7. https://doi.org/10.1016/j.procir.2016.08.029.
[321] Cheng H, et al. Manufacturability and mechanical properties of Ti-35Nb-7Zr-5Ta porous titanium alloys produced by laser powder-bed fusion. Addit Manuf 2024;86:104190.
[322] Liu S, Shin YC. Additive manufacturing of Ti6Al4V alloy: a review. Mater Des 2019;164:107552. https://doi.org/10.1016/j.matdes.2018.107552.
[323] Dutta B, Froes FS. The additive manufacturing (AM) of titanium alloys. Met Powder Rep 2017;72:96–106.
[324] Ni J, et al. Three-dimensional printing of metals for biomedical applications. Materials Today Bio 2019;3:100024.
[325] Ambrosi A, Pumera M. 3D-printing technologies for electrochemical applications. Chem Soc Rev 2016;45:2740–55.
[326] Bhavar V, et al. A review on powder bed fusion technology of metal additive manufacturing. Additive manufacturing handbook 2017:251–3.
[327] Rahmani R, Brojan M, Antonov M, Prashanth KG. Perspectives of metal-diamond composites additive manufacturing using SLM-SPS and other techniques for increased wear-impact resistance. Int J Refract Metals Hard Mater 2020;88:105192.
[328] Chua CK, Leong KF. 3D Printing and additive manufacturing: principles and applications (with companion media pack)-of rapid prototyping. World Scientific Publishing Company; 2014.
[329] Yap CY, et al. Review of selective laser melting: materials and applications. Appl Phys Rev 2015;2:041101.
[330] Riedlbauer D, et al. Macroscopic simulation and experimental measurement of melt pool characteristics in selective electron beam melting of Ti-6Al-4V. Int J Adv Des Manuf Technol 2017;88:1309–17.
[331] Galarraga H, Warren RJ, Lados DA, Dehoff RR, Kirka MM. Fatigue crack growth mechanisms at the microstructure scale in as-fabricated and heat treated Ti-6Al-4V ELI manufactured by electron beam melting (EBM). Eng Fract Mech 2017;176:263–80.
[332] Bruno J, Rochman A, Cassar G. Effect of build orientation of electron beam melting on microstructure and mechanical properties of Ti-6Al-4V. J Mater Eng Perform 2017;26:692–703.
[333] Trevisan F, et al. Additive manufacturing of titanium alloys in the biomedical field: processes, properties and applications. J Appl Biomater Funct Mater 2018;16:57–67.
[334] Herzog D, Seyda V, Wycisk E, Emmelmann C. Additive manufacturing of metals. Acta Mater 2016;117:371–92.
[335] Liu Y, et al. Microstructure, defects and mechanical behavior of beta-type titanium porous structures manufactured by electron beam melting and selective laser melting. Acta Mater 2016;113:56–67.
[336] Wang Q, et al. Effect of Nb content on microstructure, property and in vitro apatite-forming capability of Ti-Nb alloys fabricated via selective laser melting. Mater Des 2017;126:268–77.
[337] Liu Y, et al. Compressive and fatigue behavior of beta-type titanium porous structures fabricated by electron beam melting. Acta Mater 2017;126:58–66.
[338] Hao Y-L, Li S-J, Yang R. Biomedical titanium alloys and their additive manufacturing. Rare Met 2016;35:661–71.
[339] Zhang L, Yang G, Johnson BN, Jia X. Three-dimensional (3D) printed scaffold and material selection for bone repair. Acta Biomater 2019;84:16–33.
[340] Sing SL. Perspectives on additive manufacturing enabled beta-titanium alloys for biomedical applications. International Journal of Bioprinting 2022;8.
[341] Liu Y, Zhang Y, Zhang L. Transformation-induced plasticity and high strength in beta titanium alloy manufactured by selective laser melting. Materialia 2019;6:100299.
[342] Schaal H, Castany P, Gloriant T. Outstanding strain-hardening of a new metastable β-titanium alloy elaborated by in situ additive manufacturing L-PBF process. Mater Sci Eng, A 2023;875:145117.
[343] Hafeez N, et al. Mechanical behavior and phase transformation of β-type Ti-35Nb-2Ta-3Zr alloy fabricated by 3D-Printing. J Alloys Compd 2019;790:117–26.
[344] Yang K, Wang J, Tang H, Li Y. Additive manufacturing of in-situ reinforced Ti–35Nb–5Ta–7Zr (TNTZ) alloy by selective electron beam melting (SEBM). J Alloys Compd 2020;826:154178.
[345] Luo X, et al. Circumventing the strength–ductility trade-off of β-type titanium alloys by defect engineering during laser powder bed fusion. Addit Manuf 2022;51:102640.
[346] Ackers M, Messé O, Manninen N, Stryzhyboroda O, Hecht U. Additive manufacturing of TTFNZ (Ti-4.5 Ta-4Fe-7.5 Nb-6Zr), a novel metastable β-titanium alloy for advanced engineering applications. J Alloys Compd 2022;920:165899.
[347] Jeong Y, Son I, Choe H. Formation of surface roughness on the Ti-35Nb-xZr alloy using femtosecond laser for biocompatibility. Procedia Eng 2011;10:2393–8.
[348] Bautista-Ruiz J, Elhadad A, Aperador W. Fabrication of silver-doped titanium vanadium nitride (TiVN) coatings for biomedical applications. Mater Chem Phys 2024;326:129856. https://doi.org/10.1016/j.matchemphys.2024.129856.
[349] Ng C, Bermingham M, Kent D, Dargusch M. High stability and high strength β-titanium alloys for additive manufacturing. Mater Sci Eng, A 2021;816:141326.
[350] Nartu M, et al. Omega versus alpha precipitation mediated by process parameters in additively manufactured high strength Ti–1Al–8V–5Fe alloy and its impact on mechanical properties. Mater Sci Eng, A 2021;821:141627.
[351] Nagase T, Hori T, Todai M, Sun S-H, Nakano T. Additive manufacturing of dense components in beta-titanium alloys with crystallographic texture from a mixture of pure metallic element powders. Mater Des 2019;173:107771.
[352] Ferrandini PL, Cardoso FF, Souza SA, Afonso CR, Caram R. Aging response of the Ti–35Nb–7Zr–5Ta and Ti–35Nb–7Ta alloys. J Alloys Compd 2007;433:207–10.
[353] Afonso CR, Ferrandini PL, Ramirez AJ, Caram R. High resolution transmission electron microscopy study of the hardening mechanism through phase separation

in a β-Ti–35Nb–7Zr–5Ta alloy for implant applications. Acta Biomater 2010;6:1625–9.
[354] Nag S. Influence of beta instabilities on the early stages of nucleation and growth of alpha in beta titanium alloys. The Ohio State University; 2008.
[355] Lopes ES, Contieri RJ, Button ST, Caram R. Femoral hip stem prosthesis made of graded elastic modulus metastable β Ti Alloy. Mater Des 2015;69:30–6.
[356] Afonso CR, Amigó A, Stolyarov V, Gunderov D, Amigó V. From porous to dense nanostructured β-Ti alloys through high-pressure torsion. Sci Rep 2017;7:1–6.
[357] Afonso C, Ferrandini P, Londoño A, Caram R. HRTEM study of the hardening mechanism through phase separation in a β Ti-35Nb-7Zr-5Ta alloy for implant applications. Acta Biomater 2010;27:908–13.
[358] Ricci VP, et al. Assessment of anodization conditions and annealing temperature on the microstructure, elastic modulus, and wettability of β-Ti40Nb alloy. Thin Solid Films 2021;737:138949. https://doi.org/10.1016/j.tsf.2021.138949.
[359] de Mello MG, et al. Isothermal omega assisted alpha phase precipitation and microstructural evolution of an aged Ti-30Nb-3Fe alloy. Mater Res 2020;23.
[360] de Mello MG, Dainese BP, Caram R, Cremasco A. Influence of heating rate and aging temperature on omega and alpha phase precipitation in Ti35Nb alloy. Mater Char 2018;145:268–76.
[361] da Costa FH, Salvador CAF, de Mello MG, Caram R. Alpha phase precipitation in Ti-30Nb-1Fe alloys – phase transformations in continuous heating and aging heat treatments. Mater Sci Eng, A 2016;677:222–9. https://doi.org/10.1016/j.msea.2016.09.023.
[362] de Mello MG, Salvador CF, Cremasco A, Caram R. The effect of Sn addition on phase stability and phase evolution during aging heat treatment in Ti–Mo alloys employed as biomaterials. Mater Char 2015;110:5–13.
[363] Santos RF, Ricci VP, Afonso CRM. Continuous cooling transformation (CCT) diagrams of β Ti-40Nb and TMZF alloys and influence of cooling rate on microstructure and elastic modulus. Thermochim Acta 2022;717:179341.
[364] Correa DRN, et al. Growth mechanisms of Ca- and P-rich MAO films in Ti-15Zr-xMo alloys for osseointegrative implants. Surf Coating Technol 2018;344:373–82. https://doi.org/10.1016/j.surfcoat.2018.02.099.
[365] Dos Santos, L. U. Estudo dos efeitos da adição de oxigênio na estabilidade microestrutural e nas propriedades mecânicas de ligas do sistema Ti-Nb.
[366] Chaves JAM, dos Santos RFM, Ricci VP, de Giovanni Rodrigues A, Afonso CRM. An exploratory study of TiO2-based multicomponent nanotubes on TiFeNbSn ultrafine eutectic alloy. Surf Coating Technol 2021;407:126765. https://doi.org/10.1016/j.surfcoat.2020.126765.
[367] Correa D, et al. Growth mechanisms of Ca-and P-rich MAO films in Ti-15Zr-xMo alloys for osseointegrative implants. Surf Coating Technol 2018;344:373–82.
[368] Gonzalez ED, Fukumasu NK, Gobbi AL, Afonso CRM, Nascente PAP. Effects of Mg addition on the phase formation, morphology, and mechanical and tribological properties of Ti-Nb-Mg immiscible alloy coatings produced by magnetron co-sputtering. Surf Coating Technol 2020;400:126070. https://doi.org/10.1016/j.surfcoat.2020.126070.
[369] Afonso CRM, Ferrandini PL, Ramirez AJ, Caram R. High resolution transmission electron microscopy study of the hardening mechanism through phase separation in a β-Ti–35Nb–7Zr–5Ta alloy for implant applications. Acta Biomater 2010;6:1625–9. https://doi.org/10.1016/j.actbio.2009.11.010.
[370] Pynn R. Neutron scattering—a non-destructive microscope for seeing inside matter. Neutron applications in earth, energy and environmental sciences 2009:15–36.
[371] Goonetilleke D, Sharma N. In situ neutron powder diffraction studies. Physical Sciences Reviews 2021;6:20180155.
[372] Peng Y, et al. Recent progress of synchrotron X-ray imaging and diffraction on the solidification and deformation behavior of metallic materials. Acta Metall Sin 2022;35:3–24.
[373] Wang X-L. The application of neutron diffraction to engineering problems. Jom 2006;58:52–7.
[374] NIST. Neutron scattering lengths and cross sections, <https://www.ncnr.nist.gov/resources/n-lengths/> (.
[375] Ducreux CIP, Saleh AA, Gazder AA, Pereloma EV. An in-situ neutron diffraction investigation of martensitic transformation in a metastable β Ti-10V-2Fe-3Al alloy during uniaxial tension. J Alloys Compd 2021;869:159301.
[376] Zhanal P, et al. Transformation Pathway upon heating of metastable beta titanium alloy Ti-15Mo investigated by neutron diffraction. Materials 2019;12.
[377] Cho K, Morioka R, Harjo S, Kawasaki T, Yasuda HY. Study on formation mechanism of {332}< 113> deformation twinning in metastable β-type Ti alloy focusing on stress-induced α" martensite phase. Scripta Mater 2020;177:106–11.
[378] Cornelius TW, Thomas O. Progress of in situ synchrotron X-ray diffraction studies on the mechanical behavior of materials at small scales. Prog Mater Sci 2018;94:384–434.
[379] Castany P, et al. In situ synchrotron X-ray diffraction study of the martensitic transformation in superelastic Ti-24Nb-0.5 N and Ti-24Nb-0.5 O alloys. Acta Mater 2015;88:102–11.
[380] Cai S, Schaffer J, Ren Y. Stress-induced phase transformation and room temperature aging in Ti-Nb-Fe alloys. Mater Sci Eng, A 2017;680:13–20.
[381] Cai S, Schaffer J, Ren Y. Deformation of a Ti-Nb alloy containing α-martensite and omega phases. Appl Phys Lett 2015;106.
[382] Yang Y, et al. Characterization of the martensitic transformation in the superelastic Ti–24Nb–4Zr–8Sn alloy by in situ synchrotron X-ray diffraction and dynamic mechanical analysis. Acta Mater 2015;88:25–33.
[383] Zhu Z, et al. In situ synchrotron X-ray diffraction investigations of the physical mechanism of ultra-low strain hardening in Ti-30Zr-10Nb alloy. Acta Mater 2018;154:45–55.
[384] Sun F, et al. Investigation of early stage deformation mechanisms in a metastable β titanium alloy showing combined twinning-induced plasticity and transformation-induced plasticity effects. Acta Mater 2013;61:6406–17.
[385] Barriobero-Vila P, et al. An in situ investigation of the deformation mechanisms in a β-quenched Ti-5Al-5V-5Mo-3Cr alloy. Mater Sci Eng, A 2018;717:134–43.
[386] Warchomicka F, et al. In-situ synchrotron X-ray diffraction of Ti-6Al-4V during thermomechanical treatment in the beta field. Metals 2019;9:862.
[387] Neldam CA, Pinholt EM. Synchrotron μCT imaging of bone, titanium implants and bone substitutes–A systematic review of the literature. J Cranio-Maxillofacial Surg 2014;42:801–5.
[388] Xue G, et al. Initiation and propagation of small fatigue crack in beta titanium alloy observed through synchrotron radiation multiscale computed tomography. Eng Fract Mech 2022;263:108308.
[389] Grandfield K, et al. Atom probe tomography for biomaterials and biomineralization. Acta Biomater 2022;148:44–60.
[390] Seidman DN. Three-dimensional atom-probe tomography: advances and applications. Annu Rev Mater Res 2007;37:127–58.
[391] Gault B, et al. Atom probe tomography. Nature Reviews Methods Primers 2021;1:51.
[392] Karlsson J, Sundell G, Thuvander M, Andersson M. Atomically resolved tissue integration. Nano Lett 2014;14:4220–3.
[393] Wang X, et al. Biomineralization at titanium revealed by correlative 4D tomographic and spectroscopic methods. Adv Mater Interfac 2018;5:1800262.
[394] Coakley J, et al. Characterizing nanoscale precipitation in a titanium alloy by laser-assisted atom probe tomography. Mater Char 2018;141:129–38.
[395] Devaraj A, et al. Experimental evidence of concurrent compositional and structural instabilities leading to ω precipitation in titanium–molybdenum alloys. Acta Mater 2012;60:596–609.
[396] Coakley J, et al. Precipitation processes in the Beta-Titanium alloy Ti–5Al–5Mo–5V–3Cr. J Alloys Compd 2015;646:946–53.
[397] Devaraj A, et al. A low-cost hierarchical nanostructured beta-titanium alloy with high strength. Nat Commun 2016;7:1–8.
[398] Coakley J, et al. Microstructural evolution in a superelastic metastable beta-Ti alloy. Scripta Mater 2017;128:87–90.
[399] Chong Y, et al. Oxygen interstitials make metastable β titanium alloys strong and ductile. Acta Mater 2023;257:119165.
[400] Halpin J, et al. An in-situ approach for preparing atom probe tomography specimens by xenon plasma-focussed ion beam. Ultramicroscopy 2019;202:121–7.
[401] Rossi MC, Kuroda PAB, de Almeida LS, Rossino LS, Afonso CRM. A detailed analysis of the structural, morphological characteristics and micro-abrasive wear behavior of nitrided layer produced in α (CP–Ti), α+ β (Ti–6Al–4V), and β (TNZ33) type Ti alloys. J Mater Res Technol 2023;27:2399–412.
[402] Gao MC, Yeh J-W, Liaw PK, Zhang Y. High-entropy alloys: fundamentals and applications. Springer; 2016.
[403] Zhang Y, Zhou YJ, Lin JP, Chen GL, Liaw PK. Solid-solution phase formation rules for multi-component alloys. Adv Eng Mater 2008;10:534–8.
[404] Iijima Y, et al. Design and development of Ti–Zr–Hf–Nb–Ta–Mo high-entropy alloys for metallic biomaterials. Mater Des 2021;202:109548.
[405] Wang S-P, Xu J. TiZrNbTaMo high-entropy alloy designed for orthopedic implants: as-cast microstructure and mechanical properties. Mater Sci Eng C 2017;73:80–9.
[406] Motallebzadeh A, et al. Microstructural, mechanical and electrochemical characterization of TiZrTaHfNb and Ti1. 5ZrTa0. 5Hf0. 5Nb0. 5 refractory high-entropy alloys for biomedical applications. Intermetallics 2019;113:106572.
[407] Berger J, Jorge Jr A, Asato G, Roche V. Formation of self-ordered oxide nanotubes layer on the equiatomic TiNbZrHfTa high entropy alloy and bioactivation procedure. J Alloys Compd 2021;865:158837.
[408] Todai M, et al. Novel TiNbTaZrMo high-entropy alloys for metallic biomaterials. Scripta Mater 2017;129:65–8.
[409] Hori T, Nagase T, Todai M, Matsugaki A, Nakano T. Development of non-equiatomic Ti-Nb-Ta-Zr-Mo high-entropy alloys for metallic biomaterials. Scripta Mater 2019;172:83–7.
[410] Lilensten L, et al. Design and tensile properties of a bcc Ti-rich high-entropy alloy with transformation-induced plasticity. Materials Research Letters 2017;5:110–6.
[411] Wang L, Lu W, Qin J, Zhang F, Zhang D. Microstructure and mechanical properties of cold-rolled TiNbTaZr biomedical β titanium alloy. Mater Sci Eng, A 2008;490:421–6.
[412] Torrento JE, et al. Development of non-equiatomic Bio-HEAs based on TiZrNbTa-(Mo and Mn). Apl Mater 2022;10.
[413] Santos RF Md. Ligas beta Ti-Nb-Zr (-Ta-Mo) multiprincipais com baixo módulo de elasticidade. 2023.
[414] Vlcak P, Fojt J, Koller J, Drahokoupil J, Smola V. Surface pre-treatments of Ti-Nb-Zr-Ta beta titanium alloy: the effect of chemical, electrochemical and ion sputter etching on morphology, residual stress, corrosion stability and the MG-63 cell response. Results Phys 2021;28:104613.
[415] Rosales-Leal JI, et al. Effect of roughness, wettability and morphology of engineered titanium surfaces on osteoblast-like cell adhesion. Colloids Surf A Physicochem Eng Asp 2010;365:222–9.
[416] Liu X, Poon RW, Kwok SC, Chu PK, Ding C. Plasma surface modification of titanium for hard tissue replacements. Surf Coating Technol 2004;186:227–33.
[417] Cho S-A, Park K-T. The removal torque of titanium screw inserted in rabbit tibia treated by dual acid etching. Biomaterials 2003;24:3611–7.
[418] Bacchelli B, et al. Influence of a zirconia sandblasting treated surface on peri-implant bone healing: an experimental study in sheep. Acta Biomater 2009;5:2246–57.

[419] Guo CY, Matinlinna JP, Tang ATH. Effects of surface charges on dental implants: past, present, and future. International Journal of Biomaterials 2012;2012.
[420] Suzuki K, Aoki K, Ohya K. Effects of surface roughness of titanium implants on bone remodeling activity of femur in rabbits. Bone 1997;21:507–14.
[421] Rama K, et al. Surface roughness of implants: a review. Trends Biomater. Artif Organs 2011;25:112–8.
[422] Ban S, Iwaya Y, Kono H, Sato H. Surface modification of titanium by etching in concentrated sulfuric acid. Dent Mater 2006;22:1115–20.
[423] Vanzillotta P, Soares G, Bastos I, Simao R, Kuromoto N. Potentialities of some surface characterization techniques for the development of titanium biomedical alloys. Mater Res 2004;7:437–44.
[424] Santiago AS, Santos EA, Sader MS, Santiago MF, Soares GdA. Response of osteoblastic cells to titanium submitted to three different surface treatments. Braz Oral Res 2005;19:203–8.
[425] Takeuchi M, et al. Acid pretreatment of titanium implants. Biomaterials 2003;24:1821–7.
[426] Chou B-Y, Chang E. Interface investigation of plasma-sprayed hydroxyapatite coating on titanium alloy with ZrO2 intermediate layer as bond coat. Scripta Mater 2001;45:487–93.
[427] Yang G-l, He F-m, Yang X-f, Wang X-x, Zhao S-f. Bone responses to titanium implants surface-roughened by sandblasted and double etched treatments in a rabbit model. Oral Surgery, Oral Medicine, Oral Pathology, Oral Radiology, and Endodontology 2008;106:516–24.
[428] Juodzbalys G, Sapragoniene M, Wennerberg A. New acid etched titanium dental implant surface. Stomatologija, Baltic Dental and Maxillofacial Journal 2003;5:101–5.
[429] Liu X, Chu PK, Ding C. Surface modification of titanium, titanium alloys, and related materials for biomedical applications. Mater Sci Eng R Rep 2004;47:49–121.
[430] Park JY, Davies JE. Red blood cell and platelet interactions with titanium implant surfaces. Clin Oral Implants Res 2000;11:530–9.
[431] Kim H, et al. The biocompatibility of SLA-treated titanium implants. Biomed Mater 2008;3:025011.
[432] Massaro C, et al. Comparative investigation of the surface properties of commercial titanium dental implants. Part I: chemical composition. J Mater Sci Mater Med 2002;13:535–48.
[433] Fu L, Khor KA, Lim JP. The evaluation of powder processing on microstructure and mechanical properties of hydroxyapatite (HA)/yttria stabilized zirconia (YSZ) composite coatings. Surf Coating Technol 2001;140:263–8.
[434] Aparicio C, Padrós A, Gil F-J. In vivo evaluation of micro-rough and bioactive titanium dental implants using histometry and pull-out tests. J Mech Behav Biomed Mater 2011;4:1672–82.
[435] Gahlert M, et al. Osseointegration of zirconia and titanium dental implants: a histological and histomorphometrical study in the maxilla of pigs. Clin Oral Implants Res 2009;20:1247–53.
[436] Jiang B, et al. Structural stability of the metastable β-[(Mo 0.5 Sn 0.5)-(Ti 13 Zr 1)] Nb 1 alloy with low young's modulus at different states. Metall Mater Trans 2017;48:3912–9.
[437] Davies JE, Ajami E, Moineddin R, Mendes VC. The roles of different scale ranges of surface implant topography on the stability of the bone/implant interface. Biomaterials 2013;34:3535–46.
[438] Bodhak S, Bose S, Bandyopadhyay A. Role of surface charge and wettability on early stage mineralization and bone cell–materials interactions of polarized hydroxyapatite. Acta Biomater 2009;5:2178–88.
[439] Vanzillotta PS, Sader MS, Bastos IN, de Almeida Soares G. Improvement of in vitro titanium bioactivity by three different surface treatments. Dent Mater 2006;22:275–82.
[440] Le Guéhennec L, Soueidan A, Layrolle P, Amouriq Y. Surface treatments of titanium dental implants for rapid osseointegration. Dent Mater 2007;23:844–54.
[441] Park JY, Gemmell CH, Davies JE. Platelet interactions with titanium: modulation of platelet activity by surface topography. Biomaterials 2001;22:2671–82.
[442] Elias CN, Oshida Y, Lima JHC, Muller CA. Relationship between surface properties (roughness, wettability and morphology) of titanium and dental implant removal torque. J Mech Behav Biomed Mater 2008;1:234–42.
[443] Bjursten LM, et al. Titanium dioxide nanotubes enhance bone bonding in vivo. J Biomed Mater Res Part A: An Official Journal of The Society for Biomaterials, The Japanese Society for Biomaterials, and The Australian Society for Biomaterials and the Korean Society for Biomaterials 2010;92:1218–24.
[444] Wen H, Liu Q, De Wijn J, De Groot K, Cui F. Preparation of bioactive microporous titanium surface by a new two-step chemical treatment. J Mater Sci Mater Med 1998;9:121–8.
[445] Hoppe V, et al. Study of cytotoxic activity of Ti–13Nb–13Zr medical alloy with different surface finishing techniques. J Mater Sci 2021;56:17747–67.
[446] Lausmaa J. Mechanical, thermal, chemical and electrochemical surface treatment of titanium. Titanium in medicine; 2001. p. 231–66.
[447] Xue T, et al. Surface modification techniques of titanium and its alloys to functionally optimize their biomedical properties: thematic review. Front Bioeng Biotechnol 2020;8:603072.
[448] Burnat B, Parchańska-Kowalik M, Klimek L. The influence of chemical surface treatment on the corrosion resistance of titanium castings used in dental prosthetics. Arch Foundry Eng 2014;14.
[449] Iwaya Y, et al. Surface properties and biocompatibility of acid-etched titanium. Dent Mater J 2008;27:415–21.
[450] Conforto E, Aronsson B-O, Salito A, Crestou C, Caillard D. Rough surfaces of titanium and titanium alloys for implants and prostheses. Mater Sci Eng C 2004;24:611–8.
[451] Lario J, Amigó A, Segovia F, Amigó V. Surface modification of Ti-35Nb-10Ta-1.5Fe by the double acid-etching process. Materials 2018;11:494.
[452] Cochran D, Schenk R, Lussi A, Higginbottom F, Buser D. Bone response to unloaded and loaded titanium implants with a sandblasted and acid-etched surface: a histometric study in the canine mandible, vol. 40. Journal of Biomedical Materials Research: An Official Journal of The Society for Biomaterials, The Japanese Society for Biomaterials, and the Australian Society for Biomaterials; 1998. p. 1–11.
[453] Frank MJ, Walter MS, Lyngstadaas SP, Wintermantel E, Haugen HJ. Hydrogen content in titanium and a titanium–zirconium alloy after acid etching. Mater Sci Eng C 2013;33:1282–8.
[454] Matsuno H, Yokoyama A, Watari F, Uo M, Kawasaki T. Biocompatibility and osteogenesis of refractory metal implants, titanium, hafnium, niobium, tantalum and rhenium. Biomaterials 2001;22:1253–62.
[455] Jeong Y-H, Kim W-G, Choe H-C, Brantley WA. Control of nanotube shape and morphology on Ti–Nb (Ta)–Zr alloys by varying anodizing potential. Thin Solid Films 2014;572:105–12.
[456] Takesue S, Kikuchi S, Akebono H, Misaka Y, Komotori J. Effect of pre-treatment with fine particle peening on surface properties and wear resistance of gas blow induction heating nitrided titanium alloy. Surf Coating Technol 2019;359:476–84.
[457] Balza, J. et al. in IOP Conference series: materials science and engineering. 012004 (IOP Publishing).
[458] Rudawska A, Danczak I, Müller M, Valasek P. The effect of sandblasting on surface properties for adhesion. Int J Adhesion Adhes 2016;70:176–90.
[459] Qosim N, Supriadi S, Shamsuddin-Saragih A, Whulanza Y. Surface treatments of ti-alloy based bone implant manufactured by electrical discharge machining. Ing Univ 2018;22:59–70.
[460] Shah FA, Thomsen P, Palmquist A. Osseointegration and current interpretations of the bone-implant interface. Acta Biomater 2019;84:1–15.
[461] Baleani M, Viceconti M, Toni A. The effect of sandblasting treatment on endurance properties of titanium alloy hip prostheses. Artif Organs 2000;24:296–9.
[462] Yuda, A. W., Supriadi, S. & Saragih, A. S. in *AIP Conference Proceedings*. 020015 (AIP Publishing LLC).
[463] Stoilov M, et al. Effects of different titanium surface treatments on adhesion, proliferation and differentiation of bone cells: an in vitro study. J Funct Biomater 2022;13:143.
[464] Zambrano JC, Cárcel B, Pereira JC, Amigó V. Recubrimientos laser cladding de TiAl SOBRE Ti6Al4V: caracterización tribologica. Revista Latinoamericana de Metalurgia y Materiales 2016;36:45–53.
[465] Zhang F, et al. Microstructures and mechanical behavior of beta-type Ti-25V-15Cr-0.2 Si titanium alloy coating by laser cladding. Mater Sci Eng, A 2020;796:140063.
[466] Annamaria G, Massimiliano B, Francesco V. Laser polishing: a review of a constantly growing technology in the surface finishing of components made by additive manufacturing. Int J Adv Des Manuf Technol 2022;1–40.
[467] Ahmadi Z, Lee S, Shamsaei N, Mahjouri-Samani M. International solid Freeform fabrication symposium. University of Texas at Austin); 2019.
[468] Poole K. Mechanisms of bacterial biocide and antibiotic resistance. J Appl Microbiol 2002;92:55S–64S.
[469] Yasuyuki M, et al. Antibacterial properties of nine pure metals: a laboratory study using Staphylococcus aureus and Escherichia coli. Biofouling 2010;26:851–8.
[470] Gogniat G, Thyssen M, Denis M, Pulgarin C, Dukan S. The bactericidal effect of TiO2 photocatalysis involves adsorption onto catalyst and the loss of membrane integrity. FEMS Microbiol Lett 2006;258:18–24.
[471] Chen X, et al. Laser-modified black titanium oxide nanospheres and their photocatalytic activities under visible light. ACS Appl Mater Interfaces 2015;7:16070–7.
[472] Zhang X, Wang L, Levänen E. Superhydrophobic surfaces for the reduction of bacterial adhesion. RSC Adv 2013;3:12003–20.
[473] Fadeeva E, et al. Bacterial retention on superhydrophobic titanium surfaces fabricated by femtosecond laser ablation. Langmuir 2011;27:3012–9.
[474] Donaghy CL, et al. Fibre laser treatment of beta TNZT titanium alloys for load-bearing implant applications: effects of surface physical and chemical features on mesenchymal stem cell response and Staphylococcus aureus bacterial attachment. Coatings 2019;9:186.
[475] Laketić S, et al. Surface modifications of biometallic commercially pure Ti and Ti-13Nb-13Zr alloy by picosecond Nd: YAG laser. Int J Miner Metall Mater 2021;28:285–95.
[476] Chan C-W, et al. Enhancement of wear and corrosion resistance of beta titanium alloy by laser gas alloying with nitrogen. Appl Surf Sci 2016;367:80–90.
[477] Yue TM, Yu J, Mei Z, Man HC. Excimer laser surface treatment of Ti–6Al–4V alloy for corrosion resistance enhancement. Mater Lett 2002;52:206–12.
[478] Shah F, Grandfield K, Palmquist A. In: *Laser surface Modification of biomaterials* 253-280. Elsevier; 2016.
[479] Brown MS, Arnold CB. In: *Laser precision microfabrication* 91-120. Springer; 2010.
[480] Trtica M, et al. Laser-assisted surface modification of Ti-implant in air and water environment. Appl Surf Sci 2018;428:669–75.
[481] Ng, C.-H., Chan, C.-W., Man, H.-C., Waugh, D. & Lawrence, J. in Laser materials processing Conference, 34th international Congress on applications of laser & electro-optics (ICALEO).
[482] Wen H, Zeng C, Hemmasian Ettefagh A, Gao J, Guo S. Laser surface treatment of Ti-10Mo alloy under Ar and N2 environment for biomedical application. J Laser Appl 2019;31:022012.

[483] Mattox DM. Handbook of physical vapor deposition (PVD) processing. William Andrew; 2010.
[484] Vlcak P, Fojt J, Weiss Z, Kopeček J, Perina V. The effect of nitrogen saturation on the corrosion behaviour of Ti-35Nb-7Zr-5Ta beta titanium alloy nitrided by ion implantation. Surf Coating Technol 2019;358:144–52.
[485] Gordin D, et al. Design of a nitrogen-implanted titanium-based superelastic alloy with optimized properties for biomedical applications. Mater Sci Eng C 2013;33:4173–82.
[486] Jones J, Clare A. Bio-glasses: an introduction. John Wiley & Sons; 2012.
[487] Kenawy MH, El-Hadad A, Soliman IE, Ereiba KM. Bioactivity and characterization. Study of synthetic zirconia-silicate sol-gel glass powder. Middle East J Appl Sci 2016;6:329–40.
[488] Hirao K, Zhang Z, Morita H, Soga N. Effect of densification treatment on the mechanical properties of borate glasses. Zairyo 1991;40:400–4.
[489] Rahaman M. Tissue engineering using ceramics and polymers, vols. 67–114. Elsevier; 2014.
[490] Kasuga T, Nogami M, Niinomi M, Hattori T. Bioactive calcium phosphate invert glass-ceramic coating on β-type Ti–29Nb–13Ta–4.6 Zr alloy. Biomaterials 2003;24:283–90.
[491] Rawson, H. (Academic Press, London, 1960).
[492] Kasuga T, Hosoi Y, Nogami M, Niinomi M. Apatite formation on calcium phosphate invert glasses in simulated body fluid. J Am Ceram Soc 2001;84:450–2.
[493] Kasuga T, Abe Y. Calcium phosphate invert glasses with soda and titania. J Non-Cryst Solids 1999;243:70–4.
[494] Kasuga, T., Nogami, M. & Niinomi, M. in Structural biomaterials for the 21 st Century as held at the 2001 TMS annual meeting. 265-272.
[495] Kasuga T, Mizuno T, Watanabe M, Nogami M, Niinomi M. Calcium phosphate invert glass-ceramic coatings joined by self-development of compositionally gradient layers on a titanium alloy. Biomaterials 2001;22:577–82.
[496] da Rocha GVB, et al. An innovative strategy for bioactivation of β-Ti12Mo6Zr2Fe alloy surface by dip-coating method with potential application in the biomedical field. Appl Surf Sci 2022;603:154460.
[497] Colli A, Verhoye J-P, Leguerrier A, Gherli T. Anticoagulation or antiplatelet therapy of bioprosthetic heart valves recipients: an unresolved issue. Eur J Cardio Thorac Surg 2007;31:573–7.
[498] John R, et al. Improved survival and decreasing incidence of adverse events with the HeartMate II left ventricular assist device as bridge-to-transplant therapy. Ann Thorac Surg 2008;86:1227–35.
[499] Sin D-C, Kei H-L, Miao X. Surface coatings for ventricular assist devices. Expet Rev Med Dev 2009;6:51–60.
[500] Hayward JA, Chapman D. Biomembrane surfaces as models for polymer design: the potential for haemocompatibility. Biomaterials 1984;5:135–42.
[501] Lewis AL. Phosphorylcholine-based polymers and their use in the prevention of biofouling. Colloids Surf B Biointerfaces 2000;18:261–75.
[502] Chen H, Zhang Z, Chen Y, Brook MA, Sheardown H. Protein repellant silicone surfaces by covalent immobilization of poly (ethylene oxide). Biomaterials 2005;26:2391–9.
[503] Gunaydin S, et al. Clinical performance and biocompatibility of poly (2-methoxyethylacrylate)—coated extracorporeal circuits. Ann Thorac Surg 2002;74:819–24.
[504] Zhang F, Kang E, Neoh K, Wang P, Tan K. Surface modification of stainless steel by grafting of poly (ethylene glycol) for reduction in protein adsorption. Biomaterials 2001;22:1541–8.
[505] Stanfield JR, Bamberg S. Durability evaluation of biopolymer coating on titanium alloy substrate. J Mech Behav Biomed Mater 2014;35:9–17.
[506] Vandrovcova M, et al. Beta-titanium alloy covered by ferroelectric coating–physicochemical properties and human osteoblast-like cell response. Coatings 2021;11:210.
[507] Vaněk P, et al. Electrical activity of ferroelectric biomaterials and its effects on the adhesion, growth and enzymatic activity of human osteoblast-like cells. J Phys Appl Phys 2016;49:175403.
[508] Khare D, Basu B, Dubey AK. Electrical stimulation and piezoelectric biomaterials for bone tissue engineering applications. Biomaterials 2020;258:120280.
[509] Ben-Shlomo Y, et al. The national joint Registry 16th annual report 2019. 2020.
[510] Gil F, Planell Estany JA. Aplicaciones biomédicas del titanio v sus aleaciones. 1993. p. 9.
[511] Worthington RJ, Richards JJ, Melander C. Small molecule control of bacterial biofilms. Org Biomol Chem 2012;10:7457–74.
[512] Kłodzińska SN, et al. Utilizing nanoparticles for improving anti-biofilm effects of azithromycin: a head-to-head comparison of modified hyaluronic acid nanogels and coated poly (lactic-co-glycolic acid) nanoparticles. J Colloid Interface Sci 2019;555:595–606.
[513] Pérez-Tanoira R, et al. Prevention of biomaterial infection by pre-operative incubation with human cells. Surg Infect 2017;18:336–44.
[514] Yang X, et al. Recent progress on bioinspired antibacterial surfaces for biomedical application. Biomimetics 2022;7:88.
[515] Bolzoni L, Alqattan M, Peters L, Alshammari Y, Yang F. Ternary Ti alloys functionalised with antibacterial activity. Sci Rep 2020;10:1–13.
[516] Li Z, et al. Enhancement in mechanical properties, antimicrobial properties and osseointegration ability of porous TC4-5Cu alloys prepared via additive manufacturing. J Mater Res Technol 2024;29:3011–23.
[517] Yan Z, et al. Anodic etching surface treatment and antibacterial properties of Ti–Cu. Acta Metall Sin 2024;1–10.
[518] Chen M, et al. Enhanced mechanical, bio-corrosion, and antibacterial properties of Ti-Cu alloy by forming a gradient nanostructured surface layer. Surf Coating Technol 2023;465:129609.
[519] Yi C, et al. Antibacterial Ti-Cu alloy with enhanced mechanical properties as implant applications. Mater Res Express 2020;7:105404.
[520] Mao X, et al. The influence of copper content on the elastic modulus and antibacterial properties of Ti-13Nb-13Zr-x Cu alloy. Metals 2022;12:1132.
[521] Shirai T, et al. Prevention of pin tract infection with titanium-copper alloys. J Biomed Mater Res B Appl Biomater 2009;91:373–80.
[522] Kang M-K, Moon S-K, Kwon J-S, Kim K-M, Kim K-N. Antibacterial effect of sand blasted, large-grit, acid-etched treated Ti–Ag alloys. Mater Res Bull 2012;47:2952–5.
[523] Zhang E, et al. A new antibacterial titanium–copper sintered alloy: preparation and antibacterial property. Mater Sci Eng C 2013;33:4280–7.
[524] Bai B, Zhang E, Dong H, Liu J. Biocompatibility of antibacterial Ti–Cu sintered alloy: in vivo bone response. J Mater Sci Mater Med 2015;26:1–12.
[525] Zadorozhnyy VY, et al. Ti–Ag–Pd alloy with good mechanical properties and high potential for biological applications. Sci Rep 2016;6:1–9.
[526] Ou K-L, Weng C-C, Lin Y-H, Huang M-S. A promising of alloying modified beta-type Titanium-Niobium implant for biomedical applications: microstructural characteristics, in vitro biocompatibility and antibacterial performance. J Alloys Compd 2017;697:231–8.
[527] Lin H-I, et al. Functional studies of anodic oxidized β-Ti-28Nb-11Ta-8Zr alloy for mechanical, in-vitro and antibacterial capability. Sci Rep 2018;8:1–11.
[528] Liu X, et al. Biocompatibility evaluation of antibacterial Ti–Ag alloys with nanotubular coatings. Int J Nanomed 2019;14:457.
[529] Alqattan M, Peters L, Alshammari Y, Yang F, Bolzoni L. Antibacterial Ti-Mn-Cu alloys for biomedical applications. Regenerative biomaterials 2021;8:rbaa050.
[530] Donaghy CL, et al. Creating an antibacterial surface on beta TNZT alloys for hip implant applications by laser nitriding. Opt Laser Technol 2020;121:105793.
[531] Alberta LA, et al. Novel low modulus beta-type Ti–Nb alloys by gallium and copper minor additions for antibacterial implant applications. J Mater Res Technol 2022;20:3306–22.
[532] Tsutsumi Y, et al. Electrochemical surface treatment of a β-titanium alloy to realize an antibacterial property and bioactivity. Metals 2016;6:76.
[533] Zhang Y, et al. Fabrication of high strength, antibacterial and biocompatible Ti-5Mo-5Ag alloy for medical and surgical implant applications. Mater Sci Eng C 2020;106:110165.
[534] Adhikari J, Saha P, Sinha A. In: Balakrishnan Preetha, Sreekala MS, Thomas Sabu, editors. Fundamental biomaterials: metals. Woodhead Publishing; 2018. p. 299–321.
[535] Zysset PK, Guo XE, Hoffler CE, Moore KE, Goldstein SA. Elastic modulus and hardness of cortical and trabecular bone lamellae measured by nanoindentation in the human femur. J Biomech 1999;32:1005–12.
[536] Goia, T. S., Violin, K. B., Yoshimoto, M., Bressiani, J. C. & Bressiani, A. H. A. in Advances in science and technology. 259-263 (Trans Tech Publ).
[537] Mezour M, et al. Surface modification of CoCr alloys by electrochemical reduction of diazonium salts. RSC Adv 2018;8:23191–8.
[538] Lemons JE. Quantitative characterization and performance of porous implants for hard tissue applications: a symposium. ASTM International; 1987.
[539] Moore TA, Gibson L. Microdamage accumulation in bovine trabecular bone in uniaxial compression. J Biomech Eng 2002;124:63–71.
[540] Prando D, et al. Corrosion of titanium: Part 1: aggressive environments and main forms of degradation. J Appl Biomater Funct Mater 2017;15:e291–302.
[541] Mohan P, Rajak DK, Pruncu CI, Behera A, Amigó-Borrás V. Influence of β-phase stability in elemental blended Ti-Mo and Ti-Mo-Zr alloys. Micron 2021;142:102992.
[542] Rossi MC, et al. Study of the current density of the electrical resistance sintering technique on microstructural and mechanical properties in a β Ti-Nb-Sn ternary alloy. Appl Phys A 2021;127:1–19.
[543] Amigó-Mata A, Haro-Rodriguez M, Vicente-Escuder Á, Amigó-Borrás V. Development of Ti–Zr alloys by powder metallurgy for biomedical applications. Powder Metall 2022;65:31–8.
[544] Carrullo JZ, Borrás AD, Borrás VA, Navarro-Laboulais J, Falcón JP. Electrochemical corrosion behavior and mechanical properties of Ti–Ag biomedical alloys obtained by two powder metallurgy processing routes. J Mech Behav Biomed Mater 2020;112:104063.
[545] Chlebus E, Kuźnicka B, Kurzynowski T, Dybała B. Microstructure and mechanical behaviour of Ti–6Al–7Nb alloy produced by selective laser melting. Mater Char 2011;62:488–95.
[546] Jia M, Gabbitas B, Bolzoni L. Evaluation of reactive induction sintering as a manufacturing route for blended elemental Ti-5Al-2.5 Fe alloy. J Mater Process Technol 2018;255:611–20.
[547] Yang X, Hutchinson CR. Corrosion-wear of β-Ti alloy TMZF (Ti-12Mo-6Zr-2Fe) in simulated body fluid. Acta Biomater 2016;42:429–39.
[548] Lee S-H, et al. Biocompatible low Young's modulus achieved by strong crystallographic elastic anisotropy in Ti–15Mo–5Zr–3Al alloy single crystal. J Mech Behav Biomed Mater 2012;14:48–54.
[549] Nag S, Banerjee R, Stechschulte J, Fraser H. Comparison of microstructural evolution in Ti-Mo-Zr-Fe and Ti-15Mo biocompatible alloys. J Mater Sci Mater Med 2005;16:679–85.
[550] Mantshiu, A., Matizamhuka, W., Yamamoto, A., Shongwe, B. & Machaka, R. in *IOP Conference series: materials Science and engineering*. 012036 (IOP Publishing).
[551] Niinomi M, Nakai M. In: *Novel structured Metallic and inorganic materials* 61-76. Springer; 2019.
[552] Kumar P, Mahobia G, Mandal S, Singh V, Chattopadhyay K. Enhanced corrosion resistance of the surface modified Ti-13Nb-13Zr alloy by ultrasonic shot peening. Corrosion Sci 2021;189:109597.

[553] Acharya S, Panicker AG, Laxmi DV, Suwas S, Chatterjee K. Study of the influence of Zr on the mechanical properties and functional response of Ti-Nb-Ta-Zr-O alloy for orthopedic applications. Mater Des 2019;164:107555.
[554] Tane M, et al. Peculiar elastic behavior of Ti–Nb–Ta–Zr single crystals. Acta Mater 2008;56:2856–63.
[555] Cui W, Guo A, Zhou L, Liu C. Crystal orientation dependence of Young's modulus in Ti-Nb-based β-titanium alloy. Sci China Technol Sci 2010;53:1513–9.
[556] Barbas A, Bonnet AS, Lipinski P, Pesci R, Dubois G. Development and mechanical characterization of porous titanium bone substitutes. J Mech Behav Biomed Mater 2012;9:34–44. https://doi.org/10.1016/j.jmbbm.2012.01.008.
[557] Otawa N, et al. Custom-made titanium devices as membranes for bone augmentation in implant treatment: modeling accuracy of titanium products constructed with selective laser melting. J Cranio-Maxillofacial Surg 2015;43:1289–95. https://doi.org/10.1016/j.jcms.2015.05.006.
[558] Marin E, et al. Characterization of grade 2 commercially pure Trabecular Titanium structures. Mater Sci Eng C 2013;33:2648–56. https://doi.org/10.1016/j.msec.2013.02.034.
[559] Bhuiyan M, Chowdhury M, Parvin MS. Potential nanomaterials and their applications in modern medicine: an overview. ARC Journal of Cancer Science 2016;2:25–33.
[560] Pałka K, Szaraniec B. Analiza mikrostruktury spieków tytanowych z gradientem porowatości przy zastosowaniu rentgenowskiej mikrotomografii komputerowej. Engineering of Biomaterials 2012;15:26–30.
[561] Arifvianto B, Zhou J. Fabrication of metallic biomedical scaffolds with the space holder method: a review. Materials 2014;7:3588–622.
[562] Bidaux J-E, Closuit C, Rodriguez-Arbaizar M, Zufferey D, Carreño-Morelli E. Metal injection moulding of low modulus Ti–Nb alloys for biomedical applications. Powder Metall 2013;56:263–6.
[563] Fischer M, et al. Synthesis and characterization of Ti-27.5 Nb alloy made by CLAD® additive manufacturing process for biomedical applications. Mater Sci Eng C 2017;75:341–8.
[564] Cremasco A, et al. Effects of the microstructural characteristics of a metastable β Ti alloy on its corrosion fatigue properties. Int J Fatig 2013;54:32–7.
[565] Ozan S, Lin J, Li Y, Ipek R, Wen C. Development of Ti–Nb–Zr alloys with high elastic admissible strain for temporary orthopedic devices. Acta Biomater 2015;20:176–87.
[566] Schulze C, Weinmann M, Schweigel C, Keßler O, Bader R. Mechanical properties of a newly additive manufactured implant material based on Ti-42Nb. Materials 2018;11:124.
[567] Panigrahi A, et al. Mechanical properties, structural and texture evolution of biocompatible Ti–45Nb alloy processed by severe plastic deformation. J Mech Behav Biomed Mater 2016;62:93–105.
[568] Zhang J, et al. Influence of equiatomic Zr/Nb substitution on superelastic behavior of Ti–Nb–Zr alloy. Mater Sci Eng, A 2013;563:78–85.
[569] Vu NB, et al. In vitro and in vivo biocompatibility of Ti-6Al-4V titanium alloy and UHMWPE polymer for total hip replacement. Biomedical Research and Therapy 2016;3:1–11.
[570] Long M, Rack H. Titanium alloys in total joint replacement—a materials science perspective. Biomaterials 1998;19:1621–39.
[571] Ozan S, et al. Deformation mechanism and mechanical properties of a thermomechanically processed β Ti–28Nb–35.4 Zr alloy. J Mech Behav Biomed Mater 2018;78:224–34.
[572] Salvador CA, et al. Solute lean Ti-Nb-Fe alloys: an exploratory study. J Mech Behav Biomed Mater 2017;65:761–9.
[573] Oh JM, et al. High strength and ductility in low-cost Ti–Al–Fe–Mn alloy exhibiting transformation-induced plasticity. Mater Sci Eng, A 2020;772:138813.
[574] Zhao X, Niinomi M, Nakai M, Miyamoto G, Furuhara T. Microstructures and mechanical properties of metastable Ti–30Zr–(Cr, Mo) alloys with changeable Young's modulus for spinal fixation applications. Acta Biomater 2011;7:3230–6.
[575] Bahl S, Das S, Suwas S, Chatterjee K. Engineering the next-generation tin containing β titanium alloys with high strength and low modulus for orthopedic applications. J Mech Behav Biomed Mater 2018;78:124–33.
[576] Chen W, et al. Controlling the microstructure and mechanical properties of a metastable β titanium alloy by selective laser melting. Mater Sci Eng, A 2018;726:240–50.
[577] Li P, Ma X, Wang D, Zhang H. Microstructural and mechanical properties of β-type Ti–Nb–Sn biomedical alloys with low elastic modulus. Metals 2019;9:712.
[578] González M, Peña J, Gil F, Manero J. Low modulus Ti–Nb–Hf alloy for biomedical applications. Mater Sci Eng C 2014;42:691–5.
[579] Kuroda D, Niinomi M, Morinaga M, Kato Y, Yashiro T. Design and mechanical properties of new β type titanium alloys for implant materials. Mater Sci Eng, A 1998;243:244–9.
[580] Jiang B, et al. Effects of Nb and Zr on structural stabilities of Ti-Mo-Sn-based alloys with low modulus. Mater Sci Eng, A 2017;687:1–7.
[581] Chen J, et al. Effects of Nb on superelasticity and low modulus properties of metastable β-type Ti-Nb-Ta-Zr biomedical alloys. J Mater Eng Perform 2019;28:1410–8.
[582] Akita M, Nakajima M, Uematsu Y, Tokaji K, Kojima T. High-cycle fatigue properties of beta Ti alloy 55Ti–30Nb–10Ta–5Zr, gum metal. Fatig Fract Eng Mater Struct 2014;37:1223–31.
[583] Li Y, Wong C, Xiong J, Hodgson P, Wen C. Cytotoxicity of titanium and titanium alloying elements. J Dent Res 2010;89:493–7.
[584] Yilmazer H, et al. Mechanical properties of a medical β-type titanium alloy with specific microstructural evolution through high-pressure torsion. Mater Sci Eng C 2013;33:2499–507.
[585] Akahori T, Niinomi M, Fukui H, Ogawa M, Toda H. Improvement in fatigue characteristics of newly developed beta type titanium alloy for biomedical applications by thermo-mechanical treatments. Mater Sci Eng C 2005;25:248–54.
[586] Akahori T, et al. Mechanical properties of biocompatible beta-type titanium alloy coated with calcium phosphate invert glass-ceramic layer. Mater Trans 2005;46:1564–9.
[587] Narita K, Niinomi M, Nakai M, Hieda J, Oribe K. Development of thermo-mechanical processing for fabricating highly durable β-type Ti–Nb–Ta–Zr rod for use in spinal fixation devices. J Mech Behav Biomed Mater 2012;9:207–16.
[588] Nakai M, Niinomi M, Oneda T. Improvement in fatigue strength of biomedical β-type Ti–Nb–Ta–Zr alloy while maintaining low Young's modulus through optimizing ω-phase precipitation. Metall Mater Trans 2012;43:294–302.
[589] Yilmazer, H. et al. in Advanced materials research. 9-14 (Trans Tech Publ).
[590] Narita K, Niinomi M, Nakai M. Effects of micro-and nano-scale wave-like structures on fatigue strength of a beta-type titanium alloy developed as a biomaterial. J Mech Behav Biomed Mater 2014;29:393–402.
[591] Niinomi M, Akahori T, Katsura S, Yamauchi K, Ogawa M. Mechanical characteristics and microstructure of drawn wire of Ti–29Nb–13Ta–4.6 Zr for biomedical applications. Mater Sci Eng C 2007;27:154–61.
[592] Niinomi M. Material sience and engineering, A243; 1998. p. 231–6.
[593] Li S, Cui T, Hao Y, Yang R. Fatigue properties of a metastable β-type titanium alloy with reversible phase transformation. Acta Biomater 2008;4:305–17.
[594] Guo S, Chu A, Wu H, Cai C, Qu X. Effect of sintering processing on microstructure, mechanical properties and corrosion resistance of Ti–24Nb–4Zr–7.9 Sn alloy for biomedical applications. J Alloys Compd 2014;597:211–6.
[595] Sharman K, et al. Enhancement in mechanical properties of a β-titanium alloy by high-pressure torsion. J Mater Res Technol 2015;4:79–83.
[596] Zhang Z, Hao Y, Li S, Yang R. Fatigue behavior of ultrafine-grained Ti–24Nb–4Zr–8Sn multifunctional biomedical titanium alloy. Mater Sci Eng, A 2013;577:225–33.
[597] Zou L, Yang C, Long Y, Xiao Z, Li Y. Fabrication of biomedical Ti–35Nb–7Zr–5Ta alloys by mechanical alloying and spark plasma sintering. Powder Metall 2012;55:65–70.
[598] Lin Z, et al. Microstructure evolution and mechanical properties of a Ti–35Nb–3Zr–2Ta biomedical alloy processed by equal channel angular pressing (ECAP). Mater Sci Eng C 2013;33:4551–61.
[599] Kent D, Wang G, Yu Z, Ma X, Dargusch M. Strength enhancement of a biomedical titanium alloy through a modified accumulative roll bonding technique. J Mech Behav Biomed Mater 2011;4:405–16.
[600] Ma X-Q, Niu H-Z, Yu Z-T, Yu S, Wang C. Microstructural adjustments and mechanical properties of a cold-rolled biomedical near β– Ti alloy sheet. Rare Met 2018;37:846–51.
[601] Wan W, et al. Microstructure characterization and property tailoring of a biomedical Ti–19Nb–1.5 Mo–4Zr–8Sn alloy. Mater Sci Eng, A 2015;637:130–8.
[602] Liu H, Niinomi M, Nakai M, Obara S, Fujii H. Improved fatigue properties with maintaining low Young's modulus achieved in biomedical beta-type titanium alloy by oxygen addition. Mater Sci Eng, A 2017;704:10–7.
[603] Lan C, Wu Y, Guo L, Chen H, Chen F. Microstructure, texture evolution and mechanical properties of cold rolled Ti-32.5 Nb-6.8 Zr-2.7 Sn biomedical beta titanium alloy. J Mater Sci Technol 2018;34:788–92.
[604] Drob S, et al. Multifunctional "gum metal" titanium-based alloy: its long-term electrochemical behavior and macrophage response. Int J Electrochem Sci 2015;10:10738–55.
[605] Dai S, Wang Y, Chen F. Effects of annealing on the microstructures and mechanical properties of biomedical cold-rolled Ti–Nb–Zr–Mo–Sn alloy. Mater Char 2015;104:16–22.
[606] Li Y, Zou L, Yang C, Li Y, Li L. Ultrafine-grained Ti-based composites with high strength and low modulus fabricated by spark plasma sintering. Mater Sci Eng, A 2013;560:857–61.
[607] Ying-Long Z, Dong-Mei L. Microstructures and mechanical properties of Ti–Mo alloys cold-rolled and heat treated. Mater Char 2011;62:931–7.
[608] Khan M, Williams RL, Williams D. The corrosion behaviour of Ti–6Al–4V, Ti–6Al–7Nb and Ti–13Nb–13Zr in protein solutions. Biomaterials 1999;20:631–7.
[609] Nnamchi PS, Obayi C, Todd I, Rainforth M. Mechanical and electrochemical characterisation of new Ti–Mo–Nb–Zr alloys for biomedical applications. J Mech Behav Biomed Mater 2016;60:68–77.
[610] Yang G, Zhang T. Phase transformation and mechanical properties of the Ti50Zr30Nb10Ta10 alloy with low modulus and biocompatible. J Alloys Compd 2005;392:291–4.
[611] Abou Bakr Elshalakany, S. A. A. Amigó Mata, Ashraf K. Eessaa, P. Mohan, TA Osman & V. Amigó Borrás.
[612] Cojocaru V, Raducanu D, Gordin D, Cinca I. Texture in ultra-strength Ti–25Ta–25Nb alloy strips. J Alloys Compd 2013;576:170–6.
[613] Sing SL, Yeong WY, Wiria FE. Selective laser melting of titanium alloy with 50 wt % tantalum: microstructure and mechanical properties. J Alloys Compd 2016;660:461–70.
[614] Black J, Hastings G. Handbook of biomaterial properties. Springer Science & Business Media; 2013.
[615] Brailovski V, et al. Bulk and porous metastable beta Ti–Nb–Zr (Ta) alloys for biomedical applications. Mater Sci Eng C 2011;31:643–57.
[616] Wang X, Li Y, Xiong J, Hodgson PD. Porous TiNbZr alloy scaffolds for biomedical applications. Acta Biomater 2009;5:3616–24.
[617] do Prado RF, et al. In vitro and in vivo biological performance of porous Ti alloys prepared by powder metallurgy. PLoS One 2018;13:e0196169.
[618] Li B, Xie R, Lu X. Microstructure, mechanical property and corrosion behavior of porous Ti–Ta–Nb–Zr. Bioact Mater 2020;5:564–8.

[619] Lascano S, et al. Graphene-coated Ti-Nb-Ta-Mn foams: a promising approach towards a suitable biomaterial for bone replacement. Surf Coating Technol 2020; 401:126250.
[620] Torres Y, Pavón J, Rodríguez J. Processing and characterization of porous titanium for implants by using NaCl as space holder. J Mater Process Technol 2012;212:1061–9.
[621] Torres Y, Lascano S, Bris J, Pavón J, Rodriguez JA. Development of porous titanium for biomedical applications: a comparison between loose sintering and space-holder techniques. Mater Sci Eng C 2014;37:148–55.
[622] Muñoz S, et al. On the influence of space holder in the development of porous titanium implants: mechanical, computational and biological evaluation. Mater Char 2015;108:68–78.
[623] Itälä AI, Ylänen HO, Ekholm C, Karlsson KH, Aro HT. Pore diameter of more than 100 μm is not requisite for bone ingrowth in rabbits. J Biomed Mater Res: An Official Journal of The Society for Biomaterials, The Japanese Society for Biomaterials, and The Australian Society for Biomaterials and the Korean Society for Biomaterials 2001;58:679–83.
[624] Niinomi M, Nakai M, Hieda J. Development of new metallic alloys for biomedical applications. Acta Biomater 2012;8:3888–903.
[625] Nielsen LF. Elasticity and damping of porous materials and impregnated materials. J Am Ceram Soc 1984;67:93–8.
[626] Shao L, et al. β-Ti alloys for orthopedic and dental applications: a review of progress on improvement of properties through surface modification. Coatings 2021;11:1446.
[627] Zhu Y, et al. Influence of forging deformation and heat treatment on microstructure of Ti–xNb–3Zr–2Ta alloys. Mater Sci Eng C 2012;32:126–32.
[628] Wang L, et al. Tensile and superelastic behaviors of Ti-35Nb-2Ta-3Zr with gradient structure. Mater Des 2020;194:108961.
[629] Wang L, et al. Investigation of deformation mechanisms in β-type Ti-35Nb-2Ta-3Zr alloy via FSP leading to surface strengthening. Metall Mater Trans 2015;46: 4813–8.
[630] Kheradmandfard M, et al. Nanostructured β-type titanium alloy fabricated by ultrasonic nanocrystal surface modification. Ultrason Sonochem 2017;39: 698–706.
[631] Chauhan AS, et al. Laser surface treatment of α-β titanium alloy to develop a β-rich phase with very high hardness. J Mater Process Technol 2021;288:116873.
[632] Zhang T, et al. Effect of laser remelting on microstructural evolution and mechanical properties of Ti-35Nb-2Ta-3Zr alloy. Mater Lett 2019;253:310–3.
[633] Chen L, et al. Characterization of plasma electrolytic oxidation film on biomedical high niobium-containing β-titanium alloy. Surf Coating Technol 2018;352: 295–301.
[634] Griza S, Reis M, Reboh Y, Reguly A, Strohaecker T. Failure analysis of uncemented total hip stem due to microstructure and neck stress riser. Eng Fail Anal 2008;15:981–8.
[635] Guilhem Y, Basseville S, Curtit F, Stephan J-M, Cailletaud G. Investigation of the effect of grain clusters on fatigue crack initiation in polycrystals. Int J Fatig 2010; 32:1748–63.
[636] Pohler OE. Unalloyed titanium for implants in bone surgery. Injury 2000;31: D7–13.
[637] Niinomi M. Mechanical biocompatibilities of titanium alloys for biomedical applications. J Mech Behav Biomed Mater 2008;1:30–42.
[638] Rack H, Qazi J. Titanium alloys for biomedical applications. Mater Sci Eng C 2006;26:1269–77.
[639] Song X, Wang L, Niinomi M, Nakai M, Liu Y. Fatigue characteristics of a biomedical β-type titanium alloy with titanium boride. Mater Sci Eng, A 2015; 640:154–64.
[640] Azevedo TF, de Andrade CEC, dos Santos SV, Silva AS, Griza S. Fatigue and corrosion-fatigue strength of hot rolled Ti35Nb2. 5Sn alloy. Mater Des 2015;85: 607–12.
[641] Nakai M, Niinomi M, Oneda T. Improvement in fatigue strength of biomedical β-type Ti–Nb–Ta–Zr alloy while maintaining low Young's modulus through optimizing ω-phase precipitation. Metall Mater Trans 2012;43:294–302.
[642] Lin C-W, Ju C-P, Lin J-HC. A comparison of the fatigue behavior of cast Ti–7.5 Mo with cp titanium, Ti–6Al–4V and Ti–13Nb–13Zr alloys. Biomaterials 2005;26: 2899–907.
[643] Yavari SA, et al. Fatigue behavior of porous biomaterials manufactured using selective laser melting. Mater Sci Eng C 2013;33:4849–58.
[644] Chapala P, Acharyya SG, Shariff S, Bhattacharjee A. Studying the effect of composition on the in vitro wear behavior and elastic modulus of titanium-niobium-based alloys for biomedical implants. Biomedical Physics & Engineering Express 2018;4:027003.
[645] Correa D, et al. Tribocorrosion behavior of β-type Ti-15Zr-based alloys. Mater Lett 2016;179:118–21.
[646] Lee Y-S, Niinomi M, Nakai M, Narita K, Cho K. Differences in wear behaviors at sliding contacts for β-type and (α+ β)-type titanium alloys in Ringer's solution and air. Mater Trans 2015;56:317–26.
[647] Molinari A, Straffelini G, Tesi B, Bacci T. Dry sliding wear mechanisms of the Ti6Al4V alloy. Wear 1997;208:105–12.
[648] Cui W-f, Niu F-j, Tan Y-l, Qin G-w. Microstructure and tribocorrosion performance of nanocrystalline TiN graded coating on biomedical titanium alloy. Trans Nonferrous Metals Soc China 2019;29:1026–35.
[649] Eliaz N. Corrosion of metallic biomaterials: a review. Materials 2019;12:407.
[650] Bloyer DR, et al. Stress–corrosion crack growth of Si–Na–K–Mg–Ca–P–O bioactive glasses in simulated human physiological environment. Biomaterials 2007;28: 4901–11.
[651] Antunes RA, De Oliveira MCL. Corrosion processes of physical vapor deposition-coated metallic implants. Crit Rev Biomed Eng 2009;37.
[652] Comino-Garayoa R, et al. Allergies to titanium dental implants: what do we really know about them? A scoping review. Biology 2020;9:404.
[653] Przekora A, Ginalska G. In vitro evaluation of the risk of inflammatory response after chitosan/HA and chitosan/β-1, 3-glucan/HA bone scaffold implantation. Mater Sci Eng C 2016;61:355–61.
[654] Brooks EK, Brooks RP, Ehrensberger MT. Effects of simulated inflammation on the corrosion of 316L stainless steel. Mater Sci Eng C 2017;71:200–5.
[655] Manivasagam G, Dhinasekaran D, Rajamanickam A. Biomedical implants: corrosion and its prevention-a review. Recent patents on corrosion science, 2 2010, 40 - 54.
[656] Okazaki Y, Ito A, Tateishi T, Ito Y. Effect of alloying elements on anodic polarization properties of titanium alloys in acid solutions. Mater Trans, JIM 1994;35:58–66.
[657] Abd-elrhman Y, Gepreel MA-H, Abdel-Moniem A, Kobayashi S. Compatibility assessment of new V-free low-cost Ti–4.7 Mo–4.5 Fe alloy for some biomedical applications. Mater Des 2016;97:445–53.
[658] Yi R, et al. Precipitation hardening and microstructure evolution of the Ti–7Nb–10Mo alloy during aging. Mater Sci Eng C 2016;63:577–86.
[659] Bahl S, Krishnamurthy AS, Suwas S, Chatterjee K. Controlled nanoscale precipitation to enhance the mechanical and biological performances of a metastable β Ti-Nb-Sn alloy for orthopedic applications. Mater Des 2017;126: 226–37.
[660] Metikos-Huković M, Kwokal A, Piljac J. The influence of niobium and vanadium on passivity of titanium-based implants in physiological solution. Biomaterials 2003;24:3765–75.
[661] Bahl S, Meka SRK, Suwas S, Chatterjee K. Surface severe plastic deformation of an orthopedic Ti–Nb–Sn alloy induces unusual precipitate remodeling and supports stem cell osteogenesis through Akt signaling. ACS Biomater Sci Eng 2018;4: 3132–42.
[662] Bai Y, et al. Characterization, corrosion behavior, cellular response and in vivo bone tissue compatibility of titanium–niobium alloy with low Young's modulus. Mater Sci Eng C 2016;59:565–76.
[663] Assis SLd, Costa I. Electrochemical evaluation of Ti-13Nb-13Zr, Ti-6Al-4V and Ti-6Al-7Nb alloys for biomedical application by long-term immersion tests. Mater Corros 2007;58:329–33.
[664] Cvijović-Alagić I, Cvijović Z, Mitrović S, Panić V, Rakin M. Wear and corrosion behaviour of Ti–13Nb–13Zr and Ti–6Al–4V alloys in simulated physiological solution. Corrosion Sci 2011;53:796–808.
[665] Xu Y-f, et al. Corrosion behavior of Ti–Nb–Ta–Zr–Fe alloy for biomedical applications in Ringer's solution. Trans Nonferrous Metals Soc China 2015;25: 2556–63.
[666] Li Y-H, Rao G-B, Rong L-J, Li Y-Y. The influence of porosity on corrosion characteristics of porous NiTi alloy in simulated body fluid. Mater Lett 2002;57: 448–51.
[667] Xu W, et al. Effects of porosity on mechanical properties and corrosion resistances of PM-fabricated porous Ti-10Mo alloy. Metals 2018;8:188.
[668] Xie F, He X, Cao S, Mei M, Qu X. Influence of pore characteristics on microstructure, mechanical properties and corrosion resistance of selective laser sintered porous Ti–Mo alloys for biomedical applications. Electrochim Acta 2013; 105:121–9.
[669] Domínguez-Trujillo C, et al. Improvement of the balance between a reduced stress shielding and bone ingrowth by bioactive coatings onto porous titanium substrates. Surf Coating Technol 2018;338:32–7.
[670] Berradja A. Electrochemical techniques for corrosion and tribocorrosion monitoring: fundamentals of electrolytic corrosion. Corrosion Inhibitors, ISBN: 978-1-78984-715-4, 2019, DOI: 10.5772/intechopen.76742.
[671] Elani HW, et al. Does providing dental services reduce overall health care costs?: a systematic review of the literature. J Am Dent Assoc 2018;149:696–703. e692.
[672] Kurtz SM, Devine JN. PEEK biomaterials in trauma, orthopedic, and spinal implants. Biomaterials 2007;28:4845–69.
[673] Gai X, et al. Review on corrosion characteristics of porous titanium alloys fabricated by additive manufacturing. Journal of Shanghai Jiaotong University (Science) 2021;26:416–30.
[674] Punckt C, et al. Sudden onset of pitting corrosion on stainless steel as a critical phenomenon. Science 2004;305:1133–6.
[675] Yan F, Tao N, Pan C, Liu L. Microstructures and corrosion behaviors of an austenitic stainless steel strengthened by nanotwinned austenitic grains. Adv Eng Mater 2016;18:650–6.
[676] Macdonald D, Englehardt G. The point defect model for bi-layer passive films. ECS Trans 2010;28:123.
[677] Li Y-H, Rao G-B, Rong L-J, Li Y-Y, Ke W. Effect of pores on corrosion characteristics of porous NiTi alloy in simulated body fluid. Mater Sci Eng, A 2003;363:356–9.
[678] Fojt J, Joska L, Málek J. Corrosion behaviour of porous Ti–39Nb alloy for biomedical applications. Corrosion Sci 2013;71:78–83.
[679] Luo C, Zhou X, Thompson G, Hughes A. Observations of intergranular corrosion in AA2024-T351: the influence of grain stored energy. Corrosion Sci 2012;61:35–44.
[680] Donadille C, Valle R, Dervin P, Penelle R. Development of texture and microstructure during cold-rolling and annealing of FCC alloys: example of an austenitic stainless steel. Acta Metall 1989;37:1547–71.
[681] Cramer SD, Covino BS. Corrosion: fundamentals, testing and protection, vol. 13. ASM international; 2003.
[682] Abdulstaar M, Mhaede M, Wagner L, Wollmann M. Corrosion behaviour of Al 1050 severely deformed by rotary swaging. Mater Des 2014;57:325–9.

[683] Ralston K, Birbilis N. Effect of grain size on corrosion: a review. Corrosion 2010; 66. 075005-075005-075013.
[684] Gollapudi S. Grain size distribution effects on the corrosion behaviour of materials. Corrosion Sci 2012;62:90–4.
[685] Palumbo G, Thorpe S, Aust K. On the contribution of triple junctions to the structure and properties of nanocrystalline materials. Scripta Metall Mater 1990; 24:1347–50.
[686] Gai X, et al. Electrochemical behaviour of passive film formed on the surface of Ti-6Al-4V alloys fabricated by electron beam melting. Corrosion Sci 2018;145:80–9.
[687] Reccagni P, Guilherme L, Lu Q, Gittos M, Engelberg D. Reduction of austenite-ferrite galvanic activity in the heat-affected zone of a Gleeble-simulated grade 2205 duplex stainless steel weld. Corrosion Sci 2019;161:108198.
[688] Zhang Z, et al. Influence of microstructure and elemental partitioning on pitting corrosion resistance of duplex stainless steel welding joints. Appl Surf Sci 2017; 394:297–314.
[689] Waber JT. Study of a size effect in galvanic corrosion. Corrosion 1957;13:25–32.
[690] Yin L, Jin Y, Leygraf C, Birbilis N, Pan J. Numerical simulation of micro-galvanic corrosion in Al alloys: effect of geometric factors. J Electrochem Soc 2017;164: C75.
[691] Sridhar T, Rajeswari S. Biomaterials corrosion. Corrosion Rev 2009;27:287–332.
[692] Cramer SD, et al. ASM handbook, vol. 13. Materials Park, Ohio: ASM international; 2003.
[693] Bhola R, Bhola SM, Mishra B, Olson DL. Electrochemical behavior of titanium and its alloys as dental implants in normal saline. Res Lett Phys Chem 2009;3:574359.
[694] Goldstein L, Dewhirst M, Repacholi M, Kheifets L. Summary, conclusions and recommendations: adverse temperature levels in the human body. Int J Hyperther 2003;19:373–84.
[695] Enning D, Garrelfs J. Corrosion of iron by sulfate-reducing bacteria: new views of an old problem. Appl Environ Microbiol 2014;80:1226–36.
[696] Costerton JW, et al. Bacterial biofilms in nature and disease. Annu Rev Microbiol 1987;41:435–64.
[697] Reza, J. (Springer-Verlag London Limited, 2008.
[698] Loto C. Microbiological corrosion: mechanism, control and impact—a review. Int J Adv Des Manuf Technol 2017;92:4241–52.
[699] Coetser S, Cloete TE. Biofouling and biocorrosion in industrial water systems. Crit Rev Microbiol 2005;31:213–32.
[700] Rodin V, et al. Development of biological methods for controlling the aerobic microorganism–induced corrosion of carbon steel. Appl Biochem Microbiol 2000; 36:589–93.
[701] Crawford RJ, Webb HK, Truong VK, Hasan J, Ivanova EP. Surface topographical factors influencing bacterial attachment. Adv Colloid Interface Sci 2012;179: 142–9.
[702] Silva D, et al. The effect of Staphylococcus aureus on the electrochemical behavior of porous Ti-6Al-4V alloy. Bioelectrochemistry 2020;136:107622.
[703] Cai D, et al. A novel biomedical titanium alloy with high antibacterial property and low elastic modulus. J Mater Sci Technol 2021;81:13–25.
[704] Fernando S, Gunasekara T, Holton J. Antimicrobial nanoparticles: applications and mechanisms of action. 2018.
[705] Khodashenas B. The influential factors on antibacterial behaviour of copper and silver nanoparticles. Indian Chem Eng 2016;58:224–39.
[706] Sportelli MC, et al. Can nanotechnology and materials science help the fight against SARS-CoV-2? Nanomaterials 2020;10:802.
[707] Lee HJ, Song JY, Kim BS. Biological synthesis of copper nanoparticles using Magnolia kobus leaf extract and their antibacterial activity. J Chem Technol Biotechnol 2013;88:1971–7.
[708] Quinn J, McFadden R, Chan C-W, Carson L. Titanium for orthopedic applications: an overview of surface modification to improve biocompatibility and prevent bacterial biofilm formation. iScience 2020;23:101745. https://doi.org/10.1016/j.isci.2020.101745.
[709] Accioni F, Vázquez J, Merinero M, Begines B, Alcudia A. Latest trends in surface modification for dental implantology: innovative developments and analytical applications. Pharmaceutics 2022;14:455.
[710] Gaviria L, Salcido JP, Guda T, Ong JL. Current trends in dental implants. Journal of the Korean Association of Oral and Maxillofacial Surgeons 2014;40:50.
[711] Savić I, et al. Anaerobic bacteria in implants and homologous teeth 2-14 Years after implantation. Acta Stomatol Croat: International journal of oral sciences and dental medicine 2018;52:193–202.
[712] Grover H, Shukla S. Microbiology of dental implant: a review of literature. Int J Oral Implant Clin 2012;3:43–6.
[713] Gristina A, Naylor P, Myrvik Q. Infections from biomaterials and implants: a race for the surface. Med Prog Technol 1988;14:205–24.
[714] Havard H, Miles J. Biofilm and orthopaedic implant infection. J Orthop Trauma 2015;3:54–7.
[715] Jensen LK, et al. Early implant-associated osteomyelitis results in a peri-implanted bacterial reservoir. Apmis 2017;125:38–45.
[716] de Mesy Bentley KL, MacDonald A, Schwarz EM, Oh I. Chronic osteomyelitis with Staphylococcus aureus deformation in submicron canaliculi of osteocytes: a case report. JBJS case connector 2018;8:e8.
[717] Otto-Lambertz C, Yagdiran A, Wallscheid F, Eysel P, Jung N. Periprosthetic infection in joint replacement: diagnosis and treatment. Deutsches Ärzteblatt International 2017;114:347.
[718] Zoubos AB, Galanakos SP, Soucacos PN. Orthopedics and biofilm–what do we know? A review. Med Sci Mon Int Med J Exp Clin Res: international medical journal of experimental and clinical research 2012;18:RA89.
[719] Yermak K, Karbysheva S, Perka C, Trampuz A, Renz N. Performance of synovial fluid D-lactate for the diagnosis of periprosthetic joint infection: a prospective observational study. J Infect 2019;79:123–9.
[720] Thabit AK, et al. Antibiotic penetration into bone and joints: an updated review. Int J Infect Dis 2019;81:128–36.
[721] Vandenbroucke-Grauls CM, Kluytmans JA. Tracing the origins of antibiotic resistance. Nat Med 2022;28:638–40.
[722] Scarano A, Piattelli M, Vrespa G, Caputi S, Piattelli A. Bacterial adhesion on titanium nitride-coated and uncoated implants: an in vivo human study. J Oral Implantol 2003;29:80–5.
[723] Chouirfa H, Bouloussa H, Migonney V, Falentin-Daudré C. Review of titanium surface modification techniques and coatings for antibacterial applications. Acta Biomater 2019;83:37–54. https://doi.org/10.1016/j.actbio.2018.10.036.
[724] Shahali H, Jaggessar A, Yarlagadda PK. Recent advances in manufacturing and surface modification of titanium orthopaedic applications. Procedia Eng 2017; 174:1067–76.
[725] Feliu JrS, et al. Native oxide films on AZ31 and AZ61 commercial magnesium alloys–corrosion behaviour, effect on isothermal oxidation and sol–gel thin film formation. New trends in alloy development, characterization and application. Rijeka: IntechOpen; 2015. p. 97–123.
[726] Moussa H, et al. High toughness resorbable brushite-gypsum fiber-reinforced cements. Mater Sci Eng C 2021;127:112205.
[727] Ferraris S, Spriano S. Antibacterial titanium surfaces for medical implants. Mater Sci Eng C 2016;61:965–78. https://doi.org/10.1016/j.msec.2015.12.062.
[728] Shunzhi Y, Zhonghai L, Liwei H, Yantao Z, Tao F. Biocompatible MgO film on titanium substrate prepared by sol-gel method. Rare Met Mater Eng 2018;47: 2663–7.
[729] Fabritius M, et al. Antimicrobial silver multilayer coating for prevention of bacterial colonization of orthopedic implants. Materials 2020;13:1415.
[730] Marques DM, et al. Biomaterials for orthopedics: anti-biofilm activity of a new bioactive glass coating on titanium implants. Biofouling 2020;36:234–44.
[731] Ferraris S, et al. Antibacterial and bioactive nanostructured titanium surfaces for bone integration. Appl Surf Sci 2014;311:279–91. https://doi.org/10.1016/j.apsusc.2014.05.056.
[732] Feng W, et al. Controlled release behaviour and antibacterial effects of antibiotic-loaded titania nanotubes. Mater Sci Eng C 2016;62:105–12. https://doi.org/10.1016/j.msec.2016.01.046.
[733] Hou X, et al. Synthesis of Ag ion-implanted TiO2 thin films for antibacterial application and photocatalytic performance. J Hazard Mater 2015;299:59–66. https://doi.org/10.1016/j.jhazmat.2015.05.014.
[734] Yi C, Yuan Y, Zhang L, Jiang Y, He Z. Antibacterial Ti-35Nb-7Zr-xCu alloy with excellent mechanical properties generated with a spark plasma sintering method for biological applications. J Alloys Compd 2021;879:160473.
[735] Ke Z, et al. Characterization of a new Ti-13Nb-13Zr-10Cu alloy with enhanced antibacterial activity for biomedical applications. Mater Lett 2019;253:335–8.
[736] Luo R, et al. Novel function-structure-integrated Ti-Mo-Cu alloy combined with excellent antibacterial properties and mechanical compatibility as implant application. J Alloys Compd 2023;945:169323.
[737] Yuan Y, et al. Design of a new Ti-Mo-Cu alloy with excellent mechanical and antibacterial properties as implant materials. Mater Lett 2022;306:130875.
[738] Yuan Y, Ke Z, Zhang L, Jiang Y, He Z. Mechanical, corrosion and antibacterial properties of Ti-13Nb-13Zr-based alloys with various Cu contents. Mater Res Express 2021;8:115403.
[739] Fu S, Zhang Y, Qin G, Zhang E. Antibacterial effect of TiAg alloy motivated by Ag-containing phases. Mater Sci Eng C 2021;128:112266.
[740] Elhadad A, et al. 2D magnesium phosphate resorbable coating to enhance cell adhesion on titanium surfaces. Mater Chem Phys 2024;316:129114. https://doi.org/10.1016/j.matchemphys.2024.129114.
[741] Chang X, et al. Optimization of anti-wear and anti-bacterial properties of beta TiNb alloy via controlling duty cycle in open-air laser nitriding. J Mech Behav Biomed Mater 2020;110:103913.
[742] Shi A, et al. Development of a low elastic modulus and antibacterial Ti-13Nb-13Zr-5Cu titanium alloy by microstructure controlling. Mater Sci Eng C 2021;126: 112116. https://doi.org/10.1016/j.msec.2021.112116.
[743] Liu H, et al. Rough surface of copper-bearing titanium alloy with multifunctions of osteogenic ability and antibacterial activity. J Mater Sci Technol 2020;48: 130–9.
[744] Ferraris S, et al. Contact guidance effect and prevention of microfouling on a beta titanium alloy surface structured by electron-beam technology. Nanomaterials 2021;11:1474.
[745] Pilz S, et al. Metal release and cell biological compatibility of beta-type Ti-40Nb containing indium. J Biomed Mater Res B Appl Biomater 2018;106:1686–97.
[746] Ion R, et al. In vitro bio-functional performances of the novel superelastic beta-type Ti–23Nb–0.7 Ta–2Zr–0.5 N alloy. Mater Sci Eng C 2014;35:411–9.
[747] Sun Y, Song Y, Zuo J, Wang S, Gao Z. Biocompatibility evaluation of novel β-type titanium alloy (Ti–35Nb–7Zr–5Ta) 98 Si 2 in vitro. RSC Adv 2015;5:101794–801.
[748] Miura K, Yamada N, Hanada S, Jung T-K, Itoi E. The bone tissue compatibility of a new Ti–Nb–Sn alloy with a low Young's modulus. Acta Biomater 2011;7:2320–6.
[749] Guo Y, et al. The bone tissue compatibility of a new Ti35Nb2Ta3Zr alloy with a low Young's modulus. Int J Mol Med 2013;31:689–97.
[750] Lee JW, et al. In-vitro and in-vivo evaluation of a new Ti-15Mo-1Bi alloy. J Biomed Mater Res Part B: Applied Biomaterials: An Official Journal of The Society for Biomaterials, The Japanese Society for Biomaterials, and The Australian Society for Biomaterials and the Korean Society for Biomaterials 2009; 91:643–50.

[751] Kaur M, Singh K. Review on titanium and titanium based alloys as biomaterials for orthopaedic applications. Mater Sci Eng C 2019;102:844–62. https://doi.org/10.1016/j.msec.2019.04.064.
[752] Jirka I, et al. On the role of Nb-related sites of an oxidized β-TiNb alloy surface in its interaction with osteoblast-like MG-63 cells. Mater Sci Eng C 2013;33:1636–45. https://doi.org/10.1016/j.msec.2012.12.073.
[753] Liang H, et al. 3D-printed porous titanium scaffolds incorporating niobium for high bone regeneration capacity. Mater Des 2020;194:108890.
[754] Yao, C., Slamovich, E., Webster, T. J., Qazi, J. & Rack, H. in Ceramic Nanomaterials and Nanotechnology III Proceedings of the 106th Annual Meeting of the American Ceramic Society. 239.
[755] Ahmed KBA, Raman T, Veerappan A. Future prospects of antibacterial metal nanoparticles as enzyme inhibitor. Mater Sci Eng C 2016;68:939–47. https://doi.org/10.1016/j.msec.2016.06.034.
[756] Wang J, et al. Recommendation for modifying current cytotoxicity testing standards for biodegradable magnesium-based materials. Acta Biomater 2015;21:237–49.
[757] An S, Gong Q, Huang Y. Promotive effect of zinc ions on the vitality, migration, and osteogenic differentiation of human dental pulp cells. Biol Trace Elem Res 2017;175:112–21.
[758] Chernozem RV, et al. Comprehensive characterization of titania nanotubes fabricated on Ti–Nb alloys: surface topography, structure, physicomechanical behavior, and a cell culture assay. ACS Biomater Sci Eng 2020;6:1487–99.
[759] Neacsu P, et al. In vitro performance assessment of new beta Ti–Mo–Nb alloy compositions. Mater Sci Eng C 2015;47:105–13. https://doi.org/10.1016/j.msec.2014.11.023.
[760] Lubov Donaghy C, et al. Creating an antibacterial surface on beta TNZT alloys for hip implant applications by laser nitriding. Opt Laser Technol 2020;121:105793. https://doi.org/10.1016/j.optlastec.2019.105793.
[761] Brånemark P-I, et al. Intra-osseous anchorage of dental prostheses: I. Experimental studies. Scand J Plast Reconstr Surg 1969;3:81–100.
[762] Wang X, et al. Molecular characterization of ABHD5 gene promoter in intramuscular preadipocytes of Qinchuan cattle: roles of Evi1 and C/EBPα. Gene 2019;690:38–47. https://doi.org/10.1016/j.gene.2018.12.030.
[763] Niinomi M, Nakai M. Titanium-based biomaterials for preventing stress shielding between implant devices and bone. International journal of biomaterials 2011;2011.

Amir Elhadad: Amir Elhadad previously worked as an Assistant Professor at the Faculty of Science, Al-Azhar University in Cairo, Egypt. He received his Ph.D. from Carlos III University of Madrid, Spain, with a focus on designing novel coatings for biomedical applications. Currently, he is a Research Associate at the College of Dental Medicine, Qatar University.

Liliana Romero: Liliana Romero-Resendiz is currently an assistant professor at the National Autonomous University of Mexico, Mexico; senior Marie Curie research fellow at Bournemouth University, UK; and honorary research fellow at the University of Birmingham, UK. Her research interest includes the design and development of heterostructured alloys with improved strength-ductility trade-off for interdisciplinary applications, e.g., antimicrobial, structural, biomedical, etc.

Mariana Correa Rossi: Mariana Correa Rossi is currently works as a postdoctoral fellow at Federal university of São Carlos and develops studies of surface modifications of beta Ti alloys via electrochemical routes (anodization and oxidation by electrolytic plasma) in order to improve tribological and corrosive properties for biomedical applications. She has experience in manufacturing and characterization of porous and dense metallic materials. Also has experience using laser surface treatment to improve the microstructure and consequently mechanical and wear properties of the materials. She obtained two scholarship grants and at the moment is as researcher at Universitat Politécnica de Valencia.

Luisa Marleny Rodríguez-Albelo: L. M. Rodriguez-Albelo is lecturer at Department of Pharmaceutical Organic Chemistry, Faculty of Pharmacy, at University of Seville. Her current research interests include fabrication of metallic, ceramic, and polymeric porous materials, by powder metallurgy and additive manufacture, for biomedical purposes. Furthermore, her skills arise from the study of coordination polymers (metal-organic frameworks, MOFs) as porous nanomaterials.

Sheila Lascano: Sheila Lascano Farak has a PhD in Mechanical Engineering, and she is a member of the steering committee of the Postgraduate in Mechanical Engineering at UTFSM and director of the Multidisciplinary Research Group in Materials and Advanced Manufacturing Laboratory. Her research is focused on the development and characterization of new materials and the development of metallic biomaterials with controlled porosity, through powder metallurgy and FAST/SPS rapid sintering.

Conrado R M Afonso: Conrado is an Associate Professor of Materials Science and Metallurgical Engineering at the Universidade Federal de São Carlos (UFSCar) in Brazil and researcher at the Materials Science and Engineering Graduation Program (PPG-CEM). He is specialized in transmission electron microscopy, Beta Ti alloys for implant applications, laser additive manufacturing, surface modifications and characterization of advanced metallic materials. He is interested in nanostructured, complex and multiprincipal alloys and correlation of processing, microstructure, and mechanical properties.

Ana Alcudia: Ana Alcudia's research journey began after graduating in Chemical Sciences from the University of Seville in 1994, eventually leading to her current position as an Associate Professor in Organic and Medicinal Chemistry since 2011. She pursued her PhD in "Optimally Pure N-sulfinilimines: Application to the Synthesis of Aziridines and Aminoalcohols," earning outstanding qualifications and an Extraordinary Doctorate Award in 1999. Following this, she undertook a postdoctoral stay at Emory University, focusing on molybdenum complex synthesis and its applications to biological products. Her research took her to Johnson and Johnson Pharmaceuticals Laboratories and PharmaMar S.A. Later, she secured a postdoctoral research contract at CSIC.

Vicente Amigó: Vicente is Professor of Materials Science and Metallurgical Engineering at the Universitat Politècnica de València and researcher at the University Institute of Materials Technology. He is specialized in titanium alloys for biomedical applications and powder metallurgy of dense and porous alloys. He is interested in the microstructural, mechanical, chemical and biological characterisation of biomaterials.

Yadir Torres: Dr. Torres is a Full Professor at Seville University, serving as the Deputy Director of Postgraduate Studies and R&D + i at the Polytechnic School, and leading the research line on Advanced Porous Applications. His primary research areas and expertise lie in the design and manufacturing of custom-made porous materials, surface modification, as well as the bio-functional and tribo-mechanical behavior of materials for biomedical applications.